

# Development of a Beam-based Phase Feedforward Demonstration at the CLIC Test Facility (CTF3).

Jack Roberts  
New College, Oxford

Thesis submitted in fulfilment of the requirements for the degree of Doctor  
of Philosophy at the University of Oxford

Trinity Term, 2016

## Abstract

The Compact Linear Collider (CLIC) is a proposal for a future linear electron–positron collider that could achieve collision energies of up to 3 TeV. In the CLIC concept the main high energy beam is accelerated using RF power extracted from a high intensity drive beam, achieving an accelerating gradient of 100 MV/m. This scheme places strict tolerances on the drive beam phase stability, which must be better than  $0.2^\circ$  at 12 GHz. To achieve the required phase stability CLIC proposes a high bandwidth ( $>17.5$  MHz), low latency drive beam “phase feedforward” (PFF) system. In this system electromagnetic kickers, powered by 500 kW amplifiers, are installed in a chicane and used to correct the phase by deflecting the beam on to longer or shorter trajectories. A prototype PFF system has been installed at the CLIC Test Facility CTF3, the design, operation and commissioning of which is the focus of this work.

Two kickers have been installed in a pre-existing chicane at CTF3 for the prototype. New optics have been created for the line to take these changes in to account, incorporating new constraints to obtain the desired phase shifting behaviour. Three new phase monitors have also been installed, one for the PFF input and two to verify the system performance. To achieve a  $0.2^\circ$  correction a phase monitor resolution below  $0.14^\circ$  is required. A point by point resolution sampled at 192 MHz below  $0.13^\circ$  has been achieved after a series of measurements and improvements to the phase monitor electronics.

The performance of the PFF system depends on the correlation between the PFF input phase and the beam phase after the correction chicane. Preliminary measurements found only 40% correlation. The source of the low correlation was determined to be energy dependent phase jitter, which has been removed by further optics adjustments. A final correlation of 93% was achieved, improving the theoretical reduction in jitter using the PFF system from a factor 1.1 to a factor 2.7.

The performance and commissioning of the kicker amplifiers and PFF controller are also discussed. Beam based measurements are used to determine the optimal correction timing. With a maximum output of around 650 V the amplifiers facilitate a correction range of  $\pm 5.5 \pm 0.3^\circ$ . Finally, results from operation of the complete system are presented. A mean phase jitter of  $0.28 \pm 0.02^\circ$  is achieved, in agreement with the theoretical prediction of  $0.27 \pm 0.02^\circ$  for an optimal system in the given beam conditions. Current limitations of and possible future improvements to the PFF setup are also discussed.

# Acknowledgements

Acknowledgements.

# Contents

<b>1</b>	<b>Introduction</b>	<b>1</b>
1.1	Particle Physics . . . . .	1
1.2	Colliders . . . . .	2
1.3	Motivation for Future Linear Colliders . . . . .	3
1.4	The Compact Linear Collider (CLIC) . . . . .	4
1.4.1	Drive Beam Recombination . . . . .	7
1.5	Phase Feedforward for CLIC . . . . .	9
1.6	The CLIC Test Facility CTF3 . . . . .	11
1.7	The PFF Prototype at CTF3 . . . . .	12
1.7.1	Hardware . . . . .	14
1.7.2	Differences Between PFF at CTF3 and CLIC . . . . .	16
1.8	Definitions of Different Phase Statistics . . . . .	17
1.9	Thesis Overview . . . . .	18
<b>2</b>	<b>Design of the PFF Chicane</b>	<b>19</b>
2.1	Introduction to Optics . . . . .	19
2.2	Kicker Design . . . . .	21
2.3	TL2 . . . . .	23
2.3.1	Integration of PFF Hardware . . . . .	25
2.4	TL2 Optics Constraints . . . . .	26
2.4.1	Nominal Optics Constraints . . . . .	26
2.4.2	PFF Optics Constraints . . . . .	28
2.5	TL2 Optics Measurements . . . . .	30
2.5.1	Method . . . . .	30
2.5.2	Results with Original MADX Model . . . . .	31
2.5.3	Sources of Errors in MADX Model . . . . .	31
2.5.4	Corrections to MADX Model . . . . .	34
2.6	Matched TL2 Optics . . . . .	36
2.6.1	Matching Process . . . . .	39
2.6.2	PFF Optics . . . . .	40
<b>3</b>	<b>Phase Monitor Characterisation Performance</b>	<b>46</b>
3.1	Phase Monitor Design . . . . .	47
3.2	Phase Monitor Electronics . . . . .	50
3.3	Resolution Definition . . . . .	57
3.4	Digitisation of Phase Monitor Signals . . . . .	59

3.5	Fitting Method . . . . .	61
3.6	Characterisation of Phase Monitor Electronics . . . . .	62
3.6.1	Experimental Setup . . . . .	63
3.6.2	Results . . . . .	64
3.6.3	Mixer Performance . . . . .	64
3.6.4	Diode Performance . . . . .	71
3.6.5	Consequences for Routine Operation . . . . .	77
3.7	Calibrations . . . . .	78
3.7.1	Calibration on SiS Digitisers . . . . .	79
3.7.2	Calibration on FONT5a Board . . . . .	82
3.7.3	Variations in Calibration Constants Along the Pulse . . . . .	82
3.7.4	Zero Crossing . . . . .	84
3.8	Phase Shifter Noise . . . . .	86
3.9	Resolution Measurements . . . . .	90
3.9.1	Best Resolution . . . . .	92
3.9.2	With Sample Averaging . . . . .	92
3.9.3	Dependence of Resolution on LO Phase . . . . .	93
3.10	Bandwidth . . . . .	95
3.11	Comparison of Measured Phase Along Pulse . . . . .	95
3.12	Effect of Variations in Calibration Constant . . . . .	98
3.13	Dependence on Position . . . . .	98
<b>4</b>	<b>Phase Propagation</b>	<b>105</b>
4.1	Feedforward Algorithm . . . . .	105
4.2	Characteristics of Uncorrected Phase Jitter . . . . .	106
4.3	First Order Energy Dependences . . . . .	110
4.3.1	Beam Energy Variations . . . . .	110
4.3.2	Correlation between Phase and Energy . . . . .	113
4.3.3	R56 . . . . .	113
4.3.4	Effect of R56 in TL2 . . . . .	116
4.4	Mitigation of First Order Energy Dependence . . . . .	119
4.4.1	Matched Optics for TL1 . . . . .	119
4.4.2	Scans of R56 in TL1 . . . . .	124
4.5	Higher Order Energy Dependences . . . . .	130
4.5.1	Simulated Effect of $T_{566}$ on the Downstream Phase . . . . .	131
4.5.2	R56 Scans whilst Varying Beam Energy . . . . .	136
4.5.3	Mitigation of Higher Order Dependences . . . . .	146
4.6	Possible Other Sources of Phase Jitter . . . . .	147
4.7	Best Phase Propagation . . . . .	150
<b>5</b>	<b>Setup and Commissioning of the PFF System</b>	<b>156</b>
5.1	Feedforward Controller (FONT5a Board) . . . . .	156
5.1.1	Implementation of the PFF Correction in Firmware . . . . .	160
5.1.2	ADC Droop Correction . . . . .	165
5.2	Amplifier . . . . .	168

5.2.1	Design . . . . .	168
5.2.2	Linearity . . . . .	173
5.2.3	Amplifier Pulse Shape Characteristics . . . . .	174
5.3	Kicker and Optics Performance Verification . . . . .	178
5.3.1	Correction Range . . . . .	178
5.3.2	Orbit Closure . . . . .	181
5.4	Calculation and Application of the PFF Correction Output . . . . .	184
5.4.1	Gain Calculation . . . . .	184
5.4.2	Effect of Using Small Angle Approximation . . . . .	185
5.4.3	Channel Offset . . . . .	186
5.4.4	Verification of Correction Shape . . . . .	190
5.5	Derivation of Optimal Timing for the Correction Outputs . . . . .	191
5.5.1	Kicker Cable Lengths . . . . .	192
5.5.2	System Latency . . . . .	195
5.5.3	Absolute Timing . . . . .	196
5.5.4	Relative Kicker Timing . . . . .	201
<b>6</b>	<b>PFF System Performance</b>	<b>207</b>
6.1	Stabilisation of Phase Jitter . . . . .	207
6.1.1	Correction of Pulse Shape . . . . .	208
6.1.2	Correction of Mean Phase . . . . .	209
6.1.3	Phase Jitter Along the Pulse . . . . .	212
6.1.4	CLIC Pulse Length . . . . .	213
6.2	Limitations of the PFF System Performance . . . . .	214
6.2.1	Phase Monitor Resolution . . . . .	214
6.2.2	Beam Conditions . . . . .	215
6.2.3	Upstream Phase Drifts . . . . .	217
6.2.4	Gain Stability . . . . .	220
6.3	Achieved and Simulated Corrected Phase Jitter . . . . .	224
<b>7</b>	<b>Conclusions</b>	<b>232</b>
7.1	Summary . . . . .	232
7.2	Future Work . . . . .	234
<b>Bibliography</b>		<b>236</b>

# Glossary

**ADC** Analogue to Digital Converter.

**BPM** Beam Position Monitor.

**CLEX** CLIC Experimental Area at CTF3.

**CLIC** Compact Linear Collider.

**CR** Combiner Ring.

**DAC** Digital to Analogue Converter.

**DAQ** Data Acquisition system, usually referring to the LabVIEW application used to control the FONT5a board.

**DL** Delay Loop.

**Downstream Phase** Phase measured by Mon 3 in the TBL line, after the correction chicane.

**FONT5a Board** Digital PFF controller, provided by Oxford University.

**CT Line** Beam line connecting the linac and TL1 at CTF3. Where the upstream phase monitors are installed.

**CTF3** CLIC Test Facility 3.

**Jitter** Standard deviation.

**PFF** Phase Feedforward.

**TBL** Test Beam Line at CTF3 in CLEX. Where the downstream phase monitor is installed.

**TL1** Transfer line between the delay loop exit and the combiner ring entrance at CTF3.

**TL2** Transfer line between the combiner ring exit and CLEX at CTF3. Contains the PFF correction chicane.

**Upstream Phase** Phase measured by either Mon 1 or Mon 2 in the CT line. Used as the PFF input.

$\phi_u$ ,  $\phi_1$  or  $\phi_2$  Upstream phase (measured in either Mon 1 or Mon 2).

$\phi_d$  or  $\phi_3$  Downstream phase.

$\sigma_u$  Upstream phase jitter.

$\sigma_d$  Downstream phase jitter.

$\rho_{ud}$  Correlation between the upstream and downstream phase.

$\rho_{up}$  Correlation between the upstream phase and the beam energy.

$\rho_{dp}$  Correlation between the downstream phase and the beam energy.

$R_{56}$  First order transfer matrix coefficient describing the dependence of the phase on the beam energy.

$T_{566}$  Transfer matrix coefficient describing the second order dependence of the phase on the beam energy.

# Chapter 1

## Introduction

### 1.1 Particle Physics

Particle physics is the study of the building blocks of the universe. At its heart is the standard model [1], which defines a small number of fundamental particles, spin half fermions, that form the constituents of all visible matter in the universe, as well as integer spin bosons that mediate the forces between the fermions. Tables 1.1 and 1.2 list all the standard model fermions and bosons, respectively.

The fermions are split in to two types – leptons with an integer charge of -1 (charged leptons) or 0 (neutrinos), and quarks with fractional charges of +2/3 or -1/3. The fermions are also split in to three generations, each with a charged lepton, neutrino, positively charged quark and negatively charged quark. The mass of the particles increases with the generation, and all stable matter is comprised of the first generation particles. Every particle in the standard model has an associated anti-particle, with the same mass but opposite charge.

The fermions in the standard model interact via three fundamental forces – the electromagnetic force, mediated by the photon, the weak force, mediated by the W and Z bosons, and the strong force, mediated by the gluon. The strong force binds quarks together to form hadrons, which are either a quark—anti-quark pair (mesons), or a bound state of three quarks (hadrons). Protons are hadrons comprising of two up quarks and one down quark. Quarks also interact via the electromagnetic and weak forces. Leptons do not interact with the strong force – neutrinos only interact via the weak force, and the charged leptons interact via the weak and electromagnetic forces. The final component of the standard model is the Higgs field, which is responsible for giving particles their masses, and its associated Higgs boson [2].

The standard model has been the subject of extensive theoretical and experimental research over the last 50 years. This culminated in 2012 with the discovery of the final standard model particle yet to be observed experimentally, the Higgs Boson, at the Large Hadron Collider (LHC), CERN, Switzerland [3, 4]. Despite the incredible success of the standard model there are several known phenomena it cannot explain. For example, it does not include the gravitational force nor have viable particles or mechanisms to describe dark matter and dark

Generation	Leptons		Quarks	
1	Electron ( $e^-$ )	Electron neutrino ( $\nu_e$ )	Up ( $u$ )	Down ( $d$ )
2	Muon ( $\mu^-$ )	Muon neutrino ( $\nu_\mu$ )	Charm ( $c$ )	Strange ( $s$ )
3	Tau ( $\tau^-$ )	Tau neutrino ( $\nu_\tau$ )	Top ( $t$ )	Bottom ( $b$ )
Charge	-1		0	+2/3 -1/3

Table 1.1: Standard model fermions.

Force	Bosons
Electromagnetic	Photon ( $\gamma$ )
Weak	$W^\pm$ and $Z^0$ Bosons
Strong	Gluon ( $g$ )
Higgs Field	Higgs Boson ( $H^0$ )

Table 1.2: Standard model bosons.

energy, which are required to explain observations in cosmology such as the increasing rate of expansion of the universe [5]. The LHC and other experiments around the world aim to discover new particles or find discrepancies in the standard model to explain these effects.

## 1.2 Colliders

The driving force behind recent discoveries in particle physics has been colliders, in which two beams of particles are accelerated to high energy and then brought in to collision with one another. Longitudinal electric fields are used to accelerate the two beams, with the fields created by injecting RF (radio frequency) power in to cavities placed along the beam line. The source of the RF power is usually klystrons, devices in which a low power RF input is amplified using a low energy electron beam [6]. Due to the use of RF accelerating fields, the colliding beams are bunched with a frequency related to the RF frequency, rather than being continuous. Each bunch of particles can then experience the same accelerating field.

The interaction of the two beams when they are brought in to collision produces new particles that are observed in large detectors surrounding the interaction point (IP). The types of interaction that can take place and the particles that can be produced depends on the centre of mass energy of the collision. Colliding a single beam in to a fixed target reduces the available energy for the interaction as the final state must have high kinetic energy to conserve momentum. Colliding two opposing beams head on with zero net momentum therefore maximises the centre of mass energy available to produce new particles.

The rate at which a given interaction  $X$  occurs when the beams collide can be defined as:

$$R(X) = \mathcal{L}\sigma(X) \quad (1.1)$$

Where  $\sigma(X)$  is the cross-section for the interaction, defined from the standard model and including dependences on the collision energy, for example. The luminosity  $\mathcal{L}$  is a property

of the beam and can be defined as:

$$\mathcal{L} = H \frac{f N^2}{4\pi\sigma_x\sigma_y} \quad (1.2)$$

Where  $f$  is the frequency at which bunches collide,  $N$  is the number of particles in each bunch,  $\sigma_x$  and  $\sigma_y$  are the horizontal and vertical beam sizes respectively and  $H$  is a factor dependent on the electromagnetic interaction of the two beams close to the collision point. Small, dense beams and a high bunch crossing frequency are desirable to maximise the interaction rate.

## 1.3 Motivation for Future Linear Colliders

Colliders are typically either circular (synchrotrons) or linear (linacs) and use either electron or proton beams (and their associated anti-particles). The choice of collider shape and particle has many consequences for the properties of the resulting experiment.

In synchrotrons the two beams are bent around a path of fixed radius using magnetic fields (dipoles). The beams circulate the collider many times, being brought in to collision at one or several interaction points around the ring where detectors are placed. A large fraction of the ring can be filled with bunches, and with these bunches circulating at close to the speed of light synchrotrons therefore benefit from high luminosities thanks to their high bunch crossing frequency. For proton machines the highest achievable energy in a synchrotron is predominantly defined by the radius of the ring and the maximum sustainable field in the dipoles. Electron beams have other limitations, as described below. The LHC is a 27 km proton synchrotron with 8.3 T dipoles and a bunch crossing frequency of around 30 MHz that has reached a world record collision energy of 13 TeV [7].

Proton collisions present a number of challenges for the particle detectors and data analysis, however. Protons are not fundamental particles, but rather contain quarks and gluons. Therefore the interactions that occur in proton colliders are in reality between the constituents of the protons, rather than the protons themselves. The precise energy of each quark or gluon is not known, which leads to increased uncertainties in the measurements. In addition, strong interactions between the quarks and gluons lead to high background noise in the collision events, making particle identification in the detectors more difficult. As electrons are (in our current knowledge) fundamental and do not partake in the strong interaction the resulting collisions in an electron (or electron–positron) collider are much cleaner and the uncertainties smaller. This motivates research into a future high energy electron collider, where the properties of recently discovered heavy particles such as the Higgs boson and top quark, or any new particles discovered by the LHC in the coming years, could be studied with high precision.

Electron machines present a different challenge to protons due to their approximately 2000 times lower mass. Charged particles bent in a magnetic field emit radiation, known as synchrotron radiation, that depends on the bending radius,  $r$ , the particle's energy,  $E$ , and

the particle's rest mass,  $m_0$ , as follows [8]:

$$P \propto \frac{1}{r^2} \frac{E^4}{m_0^4} \quad (1.3)$$

Where  $P$  is the radiated power due to synchrotron radiation. For electrons the power radiated is roughly a factor  $2000^4$  larger than for a proton beam of the same energy, which limits the beam energies achievable in electron synchrotrons. For example, LEP, an electron–positron collider previously installed in the same 27 km tunnel as the LHC [9], achieved energies up to around 200 GeV, almost two orders of magnitude lower than is now achievable with protons in the LHC.

The only feasible way to achieve an electron collider with centre of mass energies significantly larger than what was achieved at LEP, for example at the TeV scale, is to use a linear collider (linac). In a linac particles are injected at one end of the beam line, accelerated in cavities placed along its whole length and then brought in to collision with an opposing beam from a second linac. The maximum achievable energy in a linac is defined by the length of the facility and the rate of acceleration (the peak field) in the cavities. As the particles only traverse the linac once the collision frequency is normally much lower than for synchrotrons, and thus very small, nanometre scale, beam sizes are required to provide adequate luminosity. The requirements for the accelerating cavities are also much more challenging compared to a synchrotron where the particles circulate through the cavities many times and a lower accelerating field can be accepted.

Currently there are two separate proposals for the design of a future electron–positron collider that addresses these challenges and could achieve centre of mass energies at the TeV scale – the International Linear Collider (ILC) [10] and the Compact Linear Collider (CLIC) [11]. The ILC uses superconducting RF cavities with an accelerating gradient up to 35 MV/m to achieve a 500 GeV collision energy with a facility approximately 30 km in length, with a possible future upgrade to 1 TeV with a longer facility. CLIC uses normal conducting cavities and a novel two beam acceleration concept to achieve an accelerating gradient of 100 MV/m and collision energies up to 3 TeV for a 50 km facility, similar in length to the ILC 1 TeV upgrade. Both the ILC and CLIC have large international collaborations and test facilities, with the ILC design at a more advanced stage having published its technical design report in 2013 [10]. This thesis presents a contribution towards proving the feasibility of the CLIC concept.

## 1.4 The Compact Linear Collider (CLIC)

The parameters of CLIC, summarised in Table 1.3, are chosen to optimise the cost of an electron–positron collider with a centre of mass energy of 3 TeV whilst providing similar or higher luminosity than the LHC. Superconducting RF cavities are limited in the peak fields they can achieve, and so room temperature normal conducting cavities are used to achieve an accelerating gradient of 100 MV/m. This reduces the site length, and associated civil engineering costs, by roughly a factor 3 compared to what would be necessary with a superconducting 3 TeV machine. Studies and cost optimisations of the cavities necessary to

Parameter	CLIC 3 TeV
Peak Luminosity [ $\text{cm}^{-2}\text{s}^{-1}$ ]	$5.9 \times 10^{34}$
Site Length [km]	48.4
Accelerating Gradient [MV/m]	100
RF Frequency [GHz]	12
Number of Bunches	312
Number of Particles per Bunch	$3.72 \times 10^9$
Bunch Separation [ns]	0.5
Bunch Length [ $\mu\text{m}$ ]	44
Beam Pulse Length [ns]	156
Repetition Rate [Hz]	50
Horizontal Beam Size at IP [nm]	40
Vertical Beam Size at IP [nm]	1
AC Power Consumption [MW]	582

Table 1.3: Parameters of the CLIC main beam for a collision energy of 3 TeV [11].

support the high peak fields, taking in to account the RF field breakdown rate for example, lead to the choice of a 12 GHz RF frequency with a beam pulse length of 156 ns [11]. Each accelerating cavity requires an RF input power of around 65 MW [11].

Conventional klystrons cannot produce the short pulse lengths and high peak powers required for CLIC. To achieve the necessary specifications with klystrons RF pulse compressors would have to be used to increase their output power and decrease their pulse length by roughly a factor 5 [11]. This would require a prohibitively large number of klystrons, approximately 35000, and yield a low RF power efficiency of about 40% [11]. To solve this problem CLIC proposes to use a novel two beam acceleration concept, in which the high energy main beam is accelerated using RF power extracted from a secondary, high intensity but low energy, drive beam.

Figure 1.1 shows the layout of the CLIC complex. The bottom half of the figure shows the generation of the main colliding beams. The electron and positron beams are generated in dedicated injectors at the bottom of the figure, where they are accelerated to an energy of 2.86 GeV. They are then transported to a series of damping rings, in which the effects of synchrotron radiation are used to decrease the beam size [12]. After leaving the damping rings they are accelerated further to 9 GeV before being transported to each end of the main linac. Here both beams are accelerated in 21 km linacs containing the 100 MV/m accelerating structures, reaching an energy of 1.5 TeV. Finally, the beam size is squeezed further in the beam delivery system (BDS), down to the nanometre sizes necessary to achieve high peak luminosity, before being brought in to collision at the interaction point.

The top half of the figure shows the beam lines involved in the generation of the high intensity drive beams. The drive beam accelerators are conventional linacs with an RF frequency of 1 GHz, a beam pulse length of 142  $\mu\text{s}$ , a beam current of 4.2 A and a final energy of 2.4 GeV. The longer beam pulse length and lower power requirements means klystrons can be used with high efficiencies, unlike the main beams. Following the linac the



Figure 1.1: Layout of the CLIC complex [11].

drive beams enter a series of “delay loops” and “combiner rings” in which the drive beam is interleaved with itself to increase its intensity by a factor 24 (to 100 A) in a series of shorter 240 ns beam pulses. This drive beam recombination process is described in Section 1.4.1.

The 100 A drive beam is then directed into 24 decelerator sections. Here a series of specially designed cavities, Power Extraction and Transfer Structures (PETS), are installed which decelerate, and extract power from, the drive beam. The PETS extract 90% of the energy of the drive beam [11], creating an RF pulse with the necessary properties to accelerate the main beam at 100 MV/m. The extracted RF power from the PETS is transferred to the main beam accelerating cavities via short waveguides.

### 1.4.1 Drive Beam Recombination

The combination process used to produce the high intensity drive beam pulses is a unique feature of CLIC. The intensity is increased by a factor 2 in the delay loop, a factor three in the first combiner ring (CR1) and a factor 4 in the second combiner ring (CR2) to give the overall increase of  $2 \times 3 \times 4 = 24$  in beam current.

Figure 1.2 shows the recombination process in the delay loop. Although the drive beam acceleration frequency is 1 GHz it is bunched at 0.5 GHz. At 240 ns intervals along the 142  $\mu$ s drive beam pulse the phase of the bunching is switched by 180° at 0.5 GHz. This phase switching is performed by sub-harmonic bunchers (SHBs) powered by travelling wave tubes (TWTs). As 180° at 0.5 GHz is a full 360° at the acceleration frequency of 1 GHz the phase switching has no effect on the acceleration of the drive beam.

At the entrance of the delay loop a 0.5 GHz RF deflector is used. The 240 ns sub-trains alternate between having bunches that arrive when the field in the RF deflector is positive or negative. Sub-trains arriving when the field is positive are deflected into the delay loop, whereas the remaining sub-trains bypass it. The length of the delay loop is also precisely tuned to be 240 ns, so that the sub-trains leaving the delay loop merge with the following sub-train bypassing the delay loop. The bunch frequency and beam current following the delay loop are therefore doubled to 1 GHz and 8.4 A respectively. The resulting beam structure consists of 240 ns pulses separated by 240 ns gaps.

A similar process takes place in the two combiner rings to give the final 12 GHz bunch frequency and 100 A beam current. Figure 1.3 shows the recombination of a factor 4 in CR2. RF deflectors are again used to inject the beam into the ring, this time with a higher frequency 3 GHz deflecting field to match the bunch frequency of the drive beam following CR1. The first drive beam sub-train entering CR2 circulates the ring for four turns. The length of the ring is chosen so that the second sub-train arrives just as the first sub-train has completed one turn in the ring, with a delay of one quarter of the 3 GHz wave length. Repeating this for a further two turns, interleaving a new sub-train with the beam in the ring after each turn, yields the factor 4 increase in bunch frequency and therefore beam current. CR1 operates in the same way, but the beam circulates for three turns and the required path length difference is one third of the 1 GHz wavelength.



Figure 1.2: Drive beam recombination in the delay loop [11].



Figure 1.3: Drive beam recombination in the second combiner ring [11].

## 1.5 Phase Feedforward for CLIC

In the CLIC BDS at the end of the main linacs the beam size is reduced to the nanometre sizes needed to achieve high peak luminosity. The beam is focused using magnets (mostly quadrupoles) whose focal length depends on the beam energy. Variations in beam energy therefore lead to imperfections in the focusing, which subsequently causes a growth in the beam size and a reduction in luminosity at the collision point. To keep this luminosity loss below 1% CLIC can tolerate a main beam energy spread (standard deviation or “jitter”) of 0.3% [11]. The term jitter is used to describe the standard deviation in the remainder of the thesis.

As the CLIC main beams are accelerated using RF power extracted from the drive beams, this energy stability requirement also places strict tolerances on the parameters of the drive beams. To limit the luminosity loss to below 1% a drive beam phase jitter of  $0.2^\circ$  at 12 GHz, a bunch charge jitter of 0.08% and a bunch length jitter of 1% or below are required [13], for example. To achieve this level of stability a number of correction systems will be required in the drive beam complex. This thesis presents work on the correction system required to achieve the necessary  $0.2^\circ$  at 12 GHz ( $\sim 45$  fs) drive beam phase stability — the Phase Feedforward (PFF) system.

The drive beam linac klystrons are expected to provide an RF power stability of 0.2% and an RF phase stability of  $0.05^\circ$  at 1 GHz [11]. After being accelerated in the linac and recombined in the delay loop and combiner rings this leads to a final beam phase stability of around  $2^\circ$  at 12 GHz. The PFF system must therefore reduce the drive beam phase jitter by an order of magnitude prior to the power extraction and transfer to the main beam in the decelerator sections. Each drive beam complex has 24 decelerator sectors (see Figure 1.1), and CLIC proposes to install a PFF system in each sector, for a total of 48 PFF systems across both drive beams [11]. Placing the PFF systems in the decelerator sectors minimises the possibility of additional phase errors being introduced between the correction and the power extraction.

Figure 1.4 shows a schematic of the layout of the decelerator sectors and the implementation of the PFF system inside them. At the entrance to each decelerator sector the beam is bent and redirected through a turnaround. Following the turnaround each decelerator contains a chicane in which the beam is directed on to a “C-shaped” trajectory using four dipole magnets. Finally, the drive beam is transported to the PETs, where its power is extracted and transferred to the main beam.

For the purposes of the PFF system sixteen electromagnetic kickers will be installed in the chicane, with two before and two after each dipole magnet. A voltage is applied to conducting strips inside the kickers in order to produce transversely deflecting electric and magnetic fields. The combination of four kickers around each dipole can horizontally deflect the beam by up to  $\pm 375 \mu\text{rad}$ . This assumes the use of one 500 kW amplifier to power each metre long, 50 mm aperture kicker [11]. The length of the beam’s trajectory through the chicane depends on the voltage applied to the kickers — if the polarity of the applied voltage is chosen to deflect the beam towards the outside of the chicane the trajectory is

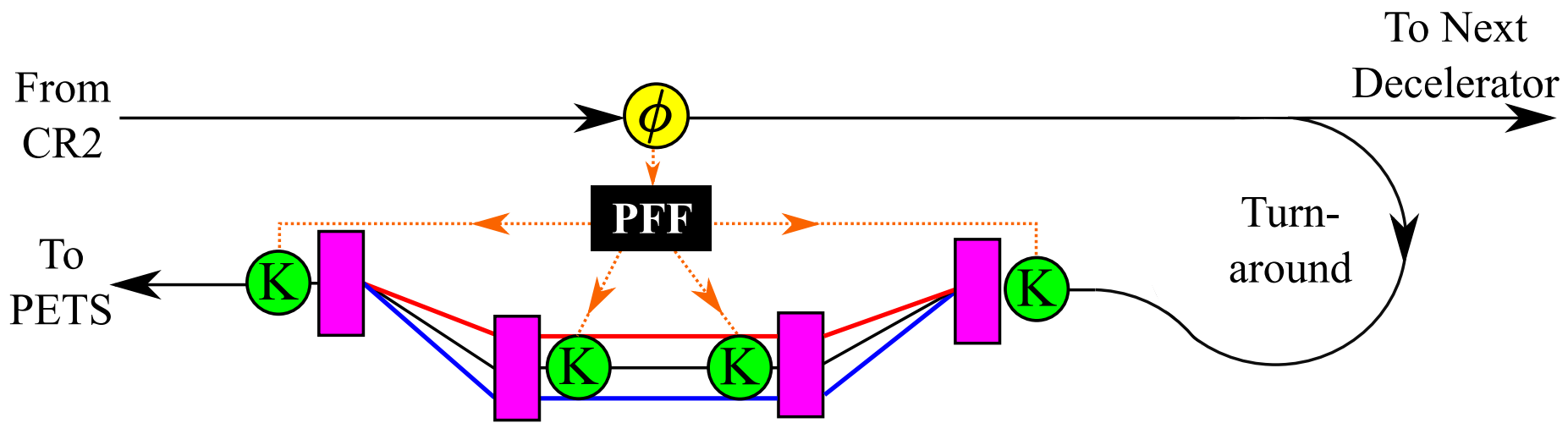


Figure 1.4: Schematic of the CLIC PFF system. The positions of the phase monitor ( $\phi$ ) before the turnaround, and the kickers (K) and dipoles (rectangles) in the chicane are shown. The box PFF represents the feedforward electronics, controls and kicker amplifiers. For the purposes of the diagram only four kickers are shown – the actual system would have 16 kickers, with two before and two after each dipole. Beam pulses arriving early at the phase monitor are directed on to longer trajectories in the chicane (blue), whereas pulses arriving late are directed on to shorter paths (red).

longer (blue), whereas the trajectory is shorter with the opposite polarity voltage applied and the beam directed towards the inside of the chicane (red).

This dependence of path length on the kicker voltage is used to correct the phase (with the phase being analogous to the arrival time or longitudinal position of the drive beam bunches). The drive beam phase is measured prior to the turnaround using a high precision phase monitor with a resolution of around  $0.1^\circ$  at 12 GHz ( $\sim 23$  fs). The measured phase is compared to a reference phase derived from the main beam, and the voltage to the kickers is varied depending on the relative phase offset between the two. If the drive beam arrives early it is directed on to a longer path and vice versa so that after the chicane the corrected phase is on reference.

Measuring the phase upstream of the correction location (feedforward rather than feedback) combined with the use of the turnaround gives the benefit of being able to apply the correction to the same beam pulse that was initially measured. This is possible despite the beam travelling at close to the speed of light as the path length of the signals between the phase monitors and the kickers is shorter than the trajectory of the beam. In other words the correction signals bypass the turnaround. The difference between the beam path length and the correction signal path length defines the available latency for the PFF hardware (signal processing, correction calculation and voltage generation).

The  $0.2^\circ$  phase stability must be maintained along the full combined beam pulse length, and thus the PFF correction will also be high bandwidth, able to correct variations along the pulse as well as any overall offsets in the mean pulse phase. The drive beam recombination and the properties of the main beam accelerating structures result in a filtering of the very high frequency phase jitter components [14]. The PFF system must have a bandwidth in excess of 17.5 MHz in order to remove the lower frequency components and achieve the required RF phase stability. The measurement from the phase monitors and the output of the kicker amplifiers must have bandwidths above 17.5 MHz to be able to achieve this.

## 1.6 The CLIC Test Facility CTF3

The CLIC design requires the use of many new concepts and technologies. Therefore, to prove the feasibility of CLIC the test facility CTF3 at CERN has been in operation since 2001 [15]. It aims to demonstrate the generation of a high intensity drive beam using the bunch recombination process, as well as the extraction of power from this drive beam and the use of the extracted power to accelerate another beam. CTF3 also hosts many related activities in areas such as the development of 12 GHz accelerating cavities and beam instrumentation, for example [16]. The main goals of CTF3 have been achieved and 2016 will be its last year of operation [17].

A diagram of the CTF3 facility is found in Figure 1.5, showing the layout of buildings (purple) and beam lines (red) with the names and extent of the main sections labelled in black. The source of the CTF3 beam, at the top left of the figure in the linac, is a thermionic electron gun [18] that produces a  $1.4 \mu\text{s}$  beam pulse with an intensity of 4 A and a repetition

rate of 0.8 Hz. The first 200 ns of the pulse contains a sharp energy transient and is eventually lost in the first bending sections of the facility, creating a usable pulse length of around 1.2  $\mu$ s. The continuous beam pulse from the gun is bunched at either 1.5 GHz or 3 GHz depending on the mode of operation.

The beam is accelerated along the linac in 3 GHz RF cavities powered by conventional klystrons combined with RF pulse compressors which double their output power [19]. The accelerating cavities are operated in the fully loaded mode, in which almost all the RF power sent to the cavity is absorbed by the beam for high power efficiency [20]. At the end of the linac the beam reaches an energy of approximately 135 MeV.

Following the linac the beam intensity can be increased by up to a factor 8 using the delay loop and combiner ring, which both function in the same way as described for CLIC in Section 1.4. Experiments at CTF3 are usually performed with either a 3 GHz factor 1 (4 A) or factor 4 (16 A) beam, or a 1.5 GHz factor 8 (28 A) beam. For the setups with 3 GHz bunching the delay loop is bypassed. The number of times the beam circulates around the combiner ring can be varied between 0.5 and 3.5 turns to give an increase in beam intensity by a factor 1, 2, 3 or 4. With 1.5 GHz beam a 1.5 GHz RF deflector [21] is used at the delay loop entrance to inject alternating 140 ns sub-trains in to the loop. The sub-trains exiting the loop merge with the 140 ns trains bypassing the loop to give a factor 2 increase in beam intensity. The intensity of this factor 2 beam can then also be increased by additional factor 4 in the combiner ring, to give the total increase of a factor 8.

Following the combiner ring the beam enters the transfer line TL2, which transports the beam to the CLIC experimental area (CLEX). In CLEX the CTF3 drive beam can be directed to two different beam lines - TBL (Test Beam Line) and TBM (Two Beam Module). In TBL a series of PETs are installed to test the extraction of power from the drive beam and to measure the properties of the produced RF power [22]. In TBM a prototype CLIC accelerating module is installed, in which RF power is extracted from the drive beam and used to accelerate a second beam, called CALIFES. The CALIFES beam also hosts many experiments independent from the CTF3 drive beam [23].

## 1.7 The PFF Prototype at CTF3

The phase feedforward system proposed for CLIC (Section 1.5) presents many challenges in terms of the required hardware latencies, resolutions, power and bandwidth. As a result, one of the key activities at CTF3 since 2013 has been the design, installation and operation of a prototype PFF system. The primary goal of the PFF prototype is to demonstrate the feasibility of the PFF concept, with the ultimate aim of reducing the CTF3 phase jitter to close to the CLIC requirement of 0.2° at 12 GHz, with a correction bandwidth above 17.5 MHz. The pursuit of this goal has required the development and installation of new hardware, as well as modifications and improvements to the setup and stability of the whole CTF3 drive beam complex.

The layout of the PFF prototype is shown in Figure 1.6. The overall concept is the same

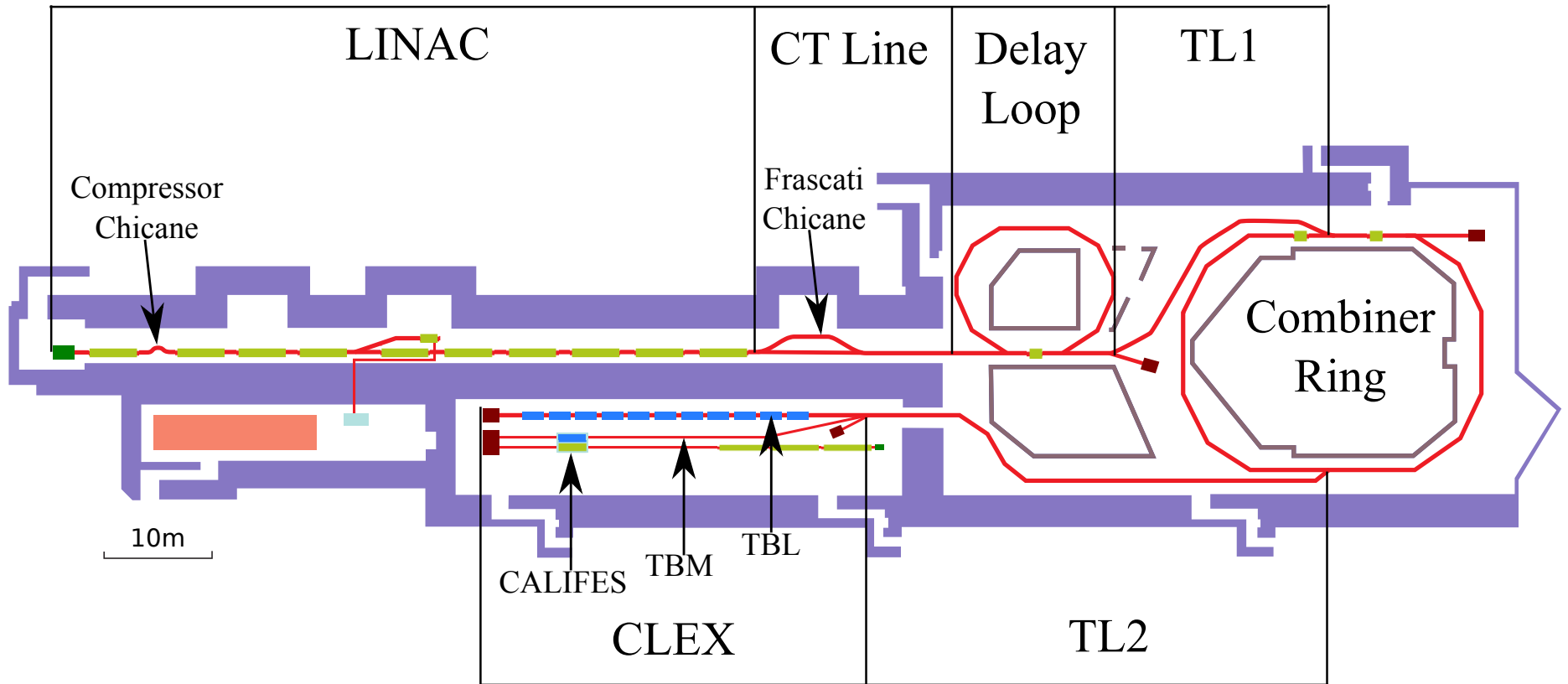


Figure 1.5: Layout of CTF3 with the main sections labelled.

as the CLIC proposal – the beam phase is measured prior to a turnaround and then corrected by changing the path length through a chicane using kickers. At CTF3 the PFF input is the phase measured in the CT line ( $\phi_1$  in the figure). The phase is then corrected using two kickers installed in the “dog-leg” shaped chicane in the TL2 transfer line. A 3 GHz, uncombined beam is used, bypassing the delay loop (DL) and completing only half a turn in the combiner ring (CR). With this setup the time of flight between the phase monitor ( $\phi_1$ ) and the first kicker (K1) is approximately 380 ns. Like the proposed CLIC system, the PFF prototype aims to apply the correction downstream (in TL2) to exactly the same pulse that was initially measured upstream (in the CT line), which is possible as the correction signals travel a shorter distance than the beam. The latency of the whole system, including the signal transit times in cables and hardware latencies, must therefore be less than 380 ns.

### 1.7.1 Hardware

The major hardware components of the PFF prototype are three phase monitors, two kickers, three sets of electronics for the phase monitors, a digitiser/feedforward controller and amplifiers to power the kickers (referred to as the kicker amplifiers). All the hardware components were designed, built and newly installed at CTF3 for the PFF prototype. The same components could be used at CLIC, with some important differences as described in Section 1.7.2. Each piece of hardware and its role is briefly introduced here, with more detail provided for each component in the remainder of the thesis.

The kickers and phase monitors are installed in the beam line at the locations shown in Figure 1.6, whereas the phase monitor electronics, feedforward controller and kicker amplifiers are installed in the CTF3 “klystron gallery”, on the floor above the accelerator hall, for easier access. The cable lengths between the phase monitors and their electronics, and between the amplifiers and the kickers, are therefore longer than they appear in Figure 1.6.

As already described, the first phase monitor ( $\phi_1$ ), in the CT line, provides the PFF input. The neighbouring second phase monitor ( $\phi_2$ ), also in the CT line, is used to cross-check and verify the performance of the phase monitors. The final phase monitor ( $\phi_3$ ), in the TBL line, measures the corrected phase jitter following the chicane in TL2. The phase monitors are designed by INFN, Italy [24] to give a resolution below 0.2° at 12 GHz with a bandwidth above 30MHz, also taking in to account the design of the phase monitor electronics, developed and built at CERN [24].

The processed signals from the first phase monitor are sent to the “FONT5a board”, the feedforward controller designed and built by the Oxford University group of the John Adams Institute (JAI) [25]. With a low latency of around 60 ns [26], the FONT5a board digitises the phase monitor signals, calculates the appropriate correction to apply and provides the drive signal for the kicker amplifiers.

The kicker amplifiers have also been designed and built by Oxford University/JAI, and provide the voltage that produces the electric and magnetic fields that deflect the beam when applied to the kickers. Each amplifier module provides a power of around 20 kW with a bandwidth close to 50 MHz for small variations [27].



Figure 1.6: Schematic of the PFF prototype at CTF3, showing the approximate location of the phase monitors ( $\phi_1$ ,  $\phi_2$  and  $\phi_3$ ) and the kickers (K1 and K2). The black box “PFF” represents the calculation and output of the correction, including the phase monitor electronics, feedforward controller and kicker amplifiers. A bunch arriving early at  $\phi_1$  is directed on to a longer path in the TL2 chicane using the kickers (blue trajectory), whereas a bunch arriving late will be directed on to a shorter path (red trajectory)

Finally, the two kickers that provide the correction were designed and built by INFN, Italy. They are installed prior to the first and last dipoles in the TL2 dog-leg chicane, and deflect the CTF3 beam through an angle of 1 mrad for an applied voltage of around 1.3 kV [28].

### 1.7.2 Differences Between PFF at CTF3 and CLIC

The goal of the prototype is to prove the general PFF concept and the feasibility of using it to achieve 0.2° drive beam phase stability. It is neither necessary nor possible for the proposed CLIC and CTF3 systems to be identical, and there are a number of differences between the two that are summarised here.

The most obvious difference between the applications at CTF3 and CLIC are the different beam energies and scale of the two complexes. CLIC will have a drive beam energy of 2.4 GeV, compared to the 135 MeV CTF3 drive beam. The CLIC PFF system therefore requires much higher power from the kicker amplifiers to deflect the beam by the same amount as the CTF3 prototype. CLIC requires up to 500 kW peak power from the amplifiers, compared to 20 kW at CTF3. Multiple amplifier modules with similar design to the CTF3 amplifiers could be combined to meet the CLIC power requirements [27].

The CLIC proposal requires 48 separate PFF systems, with one in each of the 24 decelerator sections for each of the two drive beams. Aside from the vast difference in the quantity of required hardware components, the CLIC application also presents the challenge of synchronising the reference timing of the 48 systems along the 50 km facility with femtosecond stability. This is not addressed in the CTF3 prototype but feasible solutions have been proposed [11].

Although both the CTF3 and CLIC schemes use chicanes to vary the beam trajectory the design of the chicanes used are different – with a four bend C-shaped chicane with sixteen PFF kickers proposed in the CLIC CDR, compared to the four bend dog leg chicane at CTF3 with two PFF kickers installed for the correction. The freedom to design a purpose built chicane with additional kickers in the CLIC design somewhat simplifies the challenges of obtaining a suitable layout for the prototype chicane at CTF3 using pre-existing beam lines (Chapter 2).

Another key difference is that at CTF3 the PFF prototype is operated on uncombined beam, bypassing the delay loop and completing only half a turn in the combiner ring. At CLIC the complete PFF system (including the PFF input) is placed after the drive beam recombination, and therefore would operate on combined beam. At CTF3 as the PFF input is placed prior to the delay loop any attempt to operate the PFF prototype with combined beam would be complicated by having to use the measured uncombined beam pulse to correct the combined pulse following the combiner ring. Nevertheless, operation of the prototype with combined beam could be possible and may be attempted in future tests.

The main effect of using the uncombined pulse at CTF3 rather than the combined pulse as foreseen for CLIC is that the beam pulse lengths are different. At CLIC 0.2° phase stability is needed across the 240 ns combined beam pulse. At CTF3 the uncombined pulse

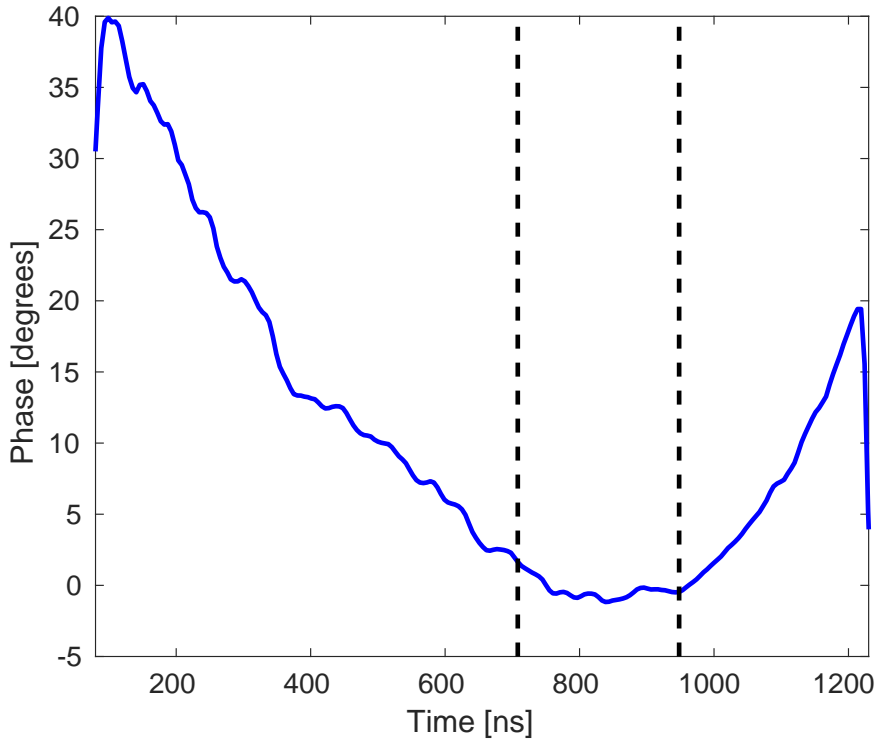


Figure 1.7: Phase sag along the  $1.2 \mu\text{s}$  CTF3 beam pulse. The dashed black lines mark show the  $240 \text{ ns}$  combined CLIC pulse length centred around the region where the phase sag is flattest.

is much longer, up to  $1.2 \mu\text{s}$ . It is therefore not necessary to demonstrate  $0.2^\circ$  phase stability across the full CTF3 pulse length to fulfil the CLIC requirements.

In fact, it is in any case impossible to demonstrate  $0.2^\circ$  phase stability across the full CTF3 pulse length with the PFF prototype due to the large phase sag that is present along the beam pulse. The RF pulse compression system at CTF3 [19] results in an approximately parabolic variation of roughly  $40^\circ$  along the pulse which would not be present at CLIC. The phase sag is much larger than the correction range of the PFF prototype, which is designed to remove smaller, fast offsets. The PFF correction is therefore focused on the flatter, central part of the pulse around the minimum in the phase sag, where the phase variations across the pulse length relevant for CLIC are within the correction range. This is shown in Figure 1.7.

## 1.8 Definitions of Different Phase Statistics

Throughout the thesis several terms will be used to describe different ways of measuring the phase, as well as other parameters. These terms are briefly summarised here for reference. All quoted phase values throughout the thesis are in degrees at 12 GHz.

CTF3 provides an uncombined beam pulse length of up to  $1.2 \mu\text{s}$ . It is useful to compare results both along the pulse and for the mean of the pulse. To calculate “mean” statistics,

the average of each beam pulse is taken. Usually this is not taken across the full pulse length, but rather across a region of several hundred nanoseconds near the mid-portion of the pulse where the beam is most stable and the phase sag is flattest. Mean statistics are usually plotted against time in units of the pulse number, with CTF3 operating at a repetition rate of 0.8 Hz, or one beam pulse every 1.25 s. The mean phase jitter represents the standard deviation of these mean values across the duration of a dataset.

Any statistic instead described as being “along the pulse” represents the measured values point by point along the beam pulse, typically sampled at a rate of a few hundred MHz. The time axes for plots of statistics along the pulse are either in units of nanoseconds, or simply the point number along the pulse (sample number). The phase jitter along the pulse represents the standard deviation of the measured phases at each individual sample point taken across the duration of a dataset.

Many of the discussions in the thesis also quote correlation coefficients, which in all cases are Pearson product-moment correlation coefficients [29].

## 1.9 Thesis Overview

This thesis documents the design, commissioning, operation and results of the PFF prototype at CTF3. In Chapter 2 the design of the TL2 chicane and the modifications to it that were necessary to achieve the desired phase shifting behaviour are described in more detail.

The performance of the PFF correction depends on the ability to precisely measure the beam phase, and so Chapter 3 presents the extensive work that has been completed to understand and maximise the precision of the new purpose built phase monitors that were installed at CTF3 for the PFF system.

As well as excellent precision in the measured phase, it is crucial to have high correlation between the phase at the end of the linac (the PFF input) and the phase at the correction location (TL2). With no correlation between the phases at these two points no improvement in phase jitter would be possible with the PFF system. Chapter 4 describes the process of understanding and improving this correlation.

Chapter 5 focuses on the setup of the remaining PFF hardware components and the commissioning of the complete PFF system. This includes the implementation of the PFF correction on the feedforward controller (the FONT5a board), the design and performance of the kicker amplifiers, as well as verifying the correction timing and correction range.

Chapter 6 then presents the best results that have been achieved with the PFF prototype to date following all the optimisations described in the rest of the thesis. An analysis of the current limitations of the system and possible future improvements to the PFF setup are also discussed. Finally, the conclusions from each chapter and suggestions for future work are summarised in Chapter 7.

# Chapter 2

## Design of the PFF Chicane

A basic beam line consists of focusing magnets (quadrupoles, as well as sextupoles and higher order magnets) and bending magnets (dipoles) connected by straight sections. A practical “real world” beam line must also include many diagnostic devices (such as beam position monitors, or BPMs) and additional elements (such as magnetic correctors) to be able to measure and remove the effects of small misalignments and imperfections in the beam line. The arrangement of devices along the line is referred to as the lattice. The collective settings (strengths) of each focusing element and the beam conditions they produce are referred to as the machine optics. The performance of the PFF system depends heavily on the lattice and optics of the correction chicane in the TL2 line at CTF3. This chapter describes the design of TL2, the modifications that have been made to its lattice for the PFF system and the derivation of suitable optics for the line taking in to account new constraints for the PFF system.

### 2.1 Introduction to Optics

This section presents basic aspects of lattice design and optics to introduce the terms used in the remainder of the thesis. Each element of a beam line can be expressed as a transfer matrix  $\mathbf{R}$  (sometimes also called a response matrix) that defines how it transforms the initial coordinates of a particle in the beam [8]:

$$\vec{x}_f = \mathbf{R}\vec{x}_0 \quad (2.1)$$

Where  $\vec{x}_0$  and  $\vec{x}_f$  are vectors describing the initial and final state of the particle. They are six dimensional vectors and the above equation can be expanded to become:

$$\begin{pmatrix} x_f \\ x'_f \\ y_f \\ y'_f \\ t_f \\ \Delta p_f/p_0 \end{pmatrix} = \begin{pmatrix} R_{11} & R_{12} & R_{13} & R_{14} & R_{15} & R_{16} \\ R_{21} & R_{22} & R_{23} & R_{24} & R_{25} & R_{26} \\ R_{31} & R_{32} & R_{33} & R_{34} & R_{35} & R_{36} \\ R_{41} & R_{42} & R_{43} & R_{44} & R_{45} & R_{46} \\ R_{51} & R_{52} & R_{53} & R_{54} & R_{55} & R_{56} \\ R_{61} & R_{62} & R_{63} & R_{64} & R_{65} & R_{66} \end{pmatrix} \begin{pmatrix} x_0 \\ x'_0 \\ y_0 \\ y'_0 \\ t_0 \\ \Delta p_0/p_{ref} \end{pmatrix} \quad (2.2)$$

In the transverse plane the vectors  $\vec{x}$  contain the horizontal and vertical offsets ( $x, y$ ) and divergences ( $x' = dx/ds, y' = dy/ds$ , where  $s$  is the longitudinal position along the beam line). The parameters  $(x, y, s)$  define a curvilinear set of coordinates that measure the position of the particle with respect to the nominal or reference orbit, following the trajectory of the beam through bending magnets, for example [8]. The final two longitudinal coordinates are the time offset ( $t$ ) and momentum offset ( $\Delta p_0/p_{ref}$ ) of the particle with respect to the reference or ideal particle. The time  $t$  is analogous to the phase of interest for the PFF system. The coefficients  $R_{ij}$  of the  $6 \times 6$  transfer matrix  $\mathbf{R}$  define how the final value of the  $i^{\text{th}}$  coordinate after passing through the element is influenced by the initial value of the  $j^{\text{th}}$  coordinate prior to the element.

The simplest and most widely used type of accelerator lattice is a FODO cell, consisting of an equally spaced focusing and defocusing quadrupole with equal strength [8]. For small horizontal or vertical offsets from the quadrupole centre the magnetic field linearly increases with the offset. The effect of a particle travelling through a quadrupolar field is analogous to a focusing lens with a focal length  $1/kl$  where  $l$  is the length of the quadrupole and  $k$  is the strength of the quadrupole dependent on its design. Using the thin lens approximation the transfer matrix for a quadrupole is defined as [30]:

$$\mathbf{R}_{\text{quad}} = \begin{pmatrix} 1 & 0 & 0 & 0 & 0 & 0 \\ \pm kl & 1 & 0 & 0 & 0 & 0 \\ 0 & 0 & 1 & 0 & 0 & 0 \\ 0 & 0 & \mp kl & 1 & 0 & 0 \\ 0 & 0 & 0 & 0 & 1 & 0 \\ 0 & 0 & 0 & 0 & 0 & 1 \end{pmatrix} \quad (2.3)$$

The final horizontal divergences of a particle after traversing a quadrupole, using the above matrix, are  $x'_f = x'_i \pm klx_i$  and  $y'_f = y'_i \mp kly_i$ . A quadrupole that focuses the beam in one plane therefore defocuses the beam in the other transverse plane. In a FODO cell a horizontally focusing quadrupole and horizontally defocusing quadrupole are used together to give a net focusing effect in both planes [30]. The complete effect of a FODO cell on a particle can be determined by multiplying the transfer matrices of each element:

$$\mathbf{R}_{\text{FODO}} = \mathbf{R}_F \times \mathbf{R}_{\text{drift}} \times \mathbf{R}_D \quad (2.4)$$

$$\vec{x}_f = \mathbf{R}_{\text{FODO}} \vec{x}_0 \quad (2.5)$$

Where  $R_F$  and  $R_D$  are the transfer matrices of the focusing and defocusing quadrupoles respectively and  $R_{\text{drift}}$  is the transfer matrix for the drift space between the quadrupoles.

The same approach can be used to construct the transfer matrix for any complete beam line, and several of the transfer matrix coefficients are of particular interest for the PFF system both in the TL2 and TL1 transfer lines at CTF3. These will be explained in more detail later in this chapter but include mostly the coefficients related to horizontally deflecting (or “kicking”) the beam, so the  $R_{2j}$  and  $R_{i2}$  terms including the horizontal divergence, and the coefficients related to the final beam phase, so the  $R_{5j}$  terms. At CTF3 optics and transfer matrices are calculated using a MADX model of the machine. MADX is one of the leading tools available for the design and simulation of particle accelerators [31]. All

the optics terms presented in this thesis use MADX coordinates and units [31]. In some cases these are slightly modified from the coordinates defined above, and these differences are explained later when relevant.

The previous discussion shows how the propagation of a single particle through a beam line can be modelled. The matrix formalism above can be adjusted to describe the trajectories of many particles by replacing the column vectors  $\vec{x}$  with matrices of many column vectors describing each particle. However, to understand the properties of a complete beam it is also useful to introduce the general solution to the transverse equations of motion (Hill's Equation) [32]:

$$x_i(s) = \sqrt{\beta_x(s)\epsilon_x} \cos[\mu_x(s) + \delta_{xi}] \quad (2.6)$$

Replacing  $x$  with  $y$  gives the equivalent solution in the vertical plane. The subscript  $i$  refers to the  $i^{\text{th}}$  particle. The transverse motion follows a modified harmonic oscillation with amplitude  $\sqrt{\beta_x(s)\epsilon_x}$ . The betatron (or beta) function  $\beta_x(s)$  varies along the beam line and depends on the lattice and optics, whilst the beam emittance  $\epsilon_x$  is a preserved quantity [33]. The phase advance  $\mu_x(s)$  defines the phase of the oscillation at each point along the lattice, with each particle having an initial phase offset  $\delta_{xi}$ .

The solution has a constant of motion known as the Courant-Snyder invariant [34]:

$$\gamma_x x^2 + 2\alpha_x x x' + \beta_x x'^2 = \epsilon_x \quad (2.7)$$

Where the explicit dependence on  $s$  of all the parameters apart from the emittance has been dropped for readability.  $\beta_x$ ,  $\alpha_x$  and  $\gamma_x$  are collectively known as the Twiss parameters, where the  $\alpha_x$  and  $\gamma_x$  functions relate to the beta function as follows [8]:

$$\alpha_x = -\frac{1}{2} \frac{d\beta_x}{ds} \quad (2.8)$$

$$\gamma_x = \frac{1 + \alpha_x^2}{\beta_x} \quad (2.9)$$

The Courant-Snyder invariant defines an ellipse with area  $\pi\epsilon_x$  in  $(x, x')$  phase space. All particles therefore follow elliptical trajectories in phase space as they progress through the beam line. At any point along the lattice one standard deviation of particles in a Gaussian beam are contained within an envelope of  $x(s) \leq \sqrt{\beta_x(s)\epsilon_x}$ . The beta function therefore defines the beam size at any point in the lattice (considering only transverse first order effects). In a FODO cell, for example, the optics is such that the beta function is minimum at the centre of the defocusing quadrupole and maximum at the centre of the focusing quadrupole [8].

## 2.2 Kicker Design

The two electromagnetic kickers provide the phase correction in the PFF system by deflecting the beam on to longer or shorter paths in the TL2 chicane. They have been designed and built by INFN, Italy [35], based on a similar design used at the DAΦNE collider [36]. A schematic of the kicker design is shown in Figure 2.1. It consists of two parallel conducting

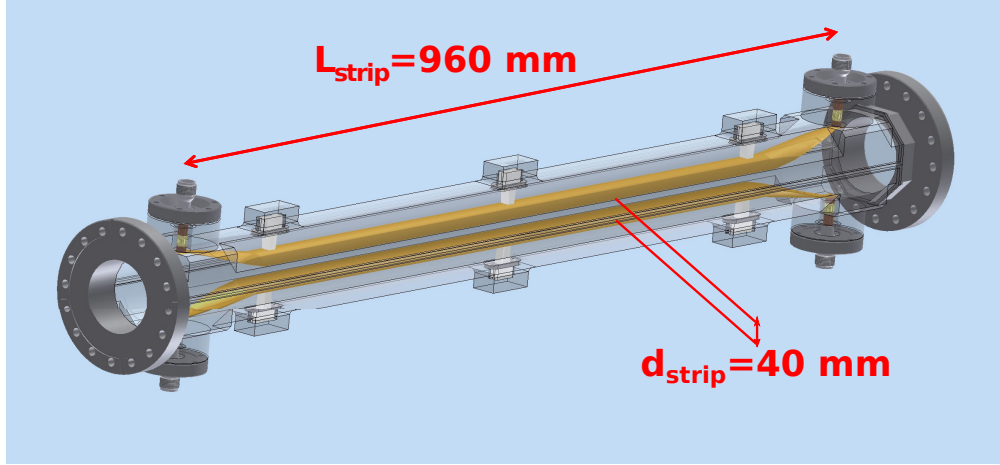


Figure 2.1: Technical drawing of the kicker design. The kicker is shown in a vertical orientation with the strips on the top and bottom. When installed in the beam line the kicker is oriented with the strips on the left and right, in order to create a horizontal electric field between the strips.

strips placed along the left and right side of the beam pipe. Each strip is approximately one metre in length and the horizontal separation between the strips is 40 mm. The strips are tapered at their ends to reduce coupling impedance (to reduce the voltage induced on the strips by the beam) [28].

At each end of each strip there is a transition to a  $50 \Omega$  HN-type connector. A voltage is applied to the downstream end of each kicker strip, with opposite polarity on each side, for example  $+V$  to the left strip and  $-V$  to the right strip. The voltage is produced by the amplifier discussed in Section 5.2, and the voltage leaving the upstream ends of the kicker strips is also terminated back at the amplifier. The applied voltage  $V(t)$  creates a horizontal, position independent, electric field and vertical magnetic field between the strips with related amplitudes as follows [37]:

$$E_x \sim V(t) \quad (2.10)$$

$$B_y \sim \frac{V(t)}{c} \quad (2.11)$$

Where  $c$  is the speed of light. By the Lorentz force an electron in the beam propagating with speed  $v$  from the upstream end of the kicker to the downstream end (in the opposite direction to the voltage applied to the strips) experiences the following horizontal force [37]:

$$F_x = e(E_x + vB_y) \sim e(1 + \beta)V(t) \sim 2eV(t) \quad (2.12)$$

Where  $e$  is the charge of an electron and  $\beta = v/c$ . The final expression holds for an ultra-relativistic particle where  $\beta \simeq 1$ , which is true for the CTF3 beam. In this case the forces resulting from the electric and magnetic fields have the same magnitude and direction. If the voltage were applied to the upstream end of the strip rather than the downstream end, the magnetic field would be in the opposite direction and the resulting electric and magnetic forces would cancel.

With the voltage correctly applied to the downstream end of the strips the force is as above and the kicker imparts a horizontal deflection to the beam. The kicker design gives

a horizontal deflection of 1 mrad for an applied voltage of  $\pm 1.26 \text{ kV}$  to each strip [28], assuming the CTF3 beam energy of around 135 MeV. This value together with the peak voltage output from the amplifier and the optics of the TL2 chicane (as described below) defines the maximum phase offset that can be corrected by the PFF system (Section 5.3.1).

## 2.3 TL2

The transfer line TL2 at CTF3 transports the beam from the exit of the combiner ring to the experimental area CLEX (see Figure 1.5). The whole line is approximately 45 m long and contains both vertical and horizontal chicanes to align the outgoing combiner ring beam line to the CLEX entrance. The PFF system attempts to correct the beam phase using the horizontal chicane at the end of TL2, where the two kickers are installed. Further details of the design of TL2 can be found in [38].

The diagram in Figure 2.2 shows a birds-eye view of the TL2 line and the lattice of the line. To interpret the diagram it is useful to introduce the device naming convention at CTF3. Devices have names of the form:

[CC].[QF][D][0840]

The first two letters refer to the section of the machine, with the prefix CC used for TL2. These are not included in the diagram to improve readability. In Chapters 3 and 4 the prefix CT is used to refer to the CT-line after the linac and transfer line TL1 prior to the combiner ring. The second group of letters refer to the type of device, the main ones being QF and QD for horizontally focusing and defocusing quadrupoles, BH and BV for horizontal and vertical dipoles, BP for beam position monitors (BPMs) and DH and DV for horizontal and vertical corrector magnets. The last letter indicates the type of that device, with four different designs of quadrupole used along the TL2 line (G-type, H-type, L-type and D-type), for example. The four final numbers indicate the position of that device along the line, in ascending order from the beginning to the end of the line.

The horizontal chicane of interest for the PFF system starts at the dipole CC.BHG0500 and ends at the dipole CC.BHG0800. The first (500) and last (800) dipoles bend the beam through  $+31^\circ$  and  $-31^\circ$  respectively. Inside the chicane there are two further dipoles of a different type – CC.BHH0600 and CC.BHH0700, which deflect the beam through  $+17^\circ$  and  $-17^\circ$  respectively. Some details on the differences between the two types of dipole are given in Section 2.5.3. The resulting overall chicane has a “dog leg” shape around 12 m in length, with three straight sections around 4 m in length between the bending magnets. Each straight section contains a triplet of quadrupoles and either one (in the first and last sections) or two (in the middle section) BPMs (of the BPI type [39]). Although the quadrupoles are labelled as horizontally focusing or defocusing the polarity of the current sent to each can be reversed so that it focuses in the opposite plane. The F or D labels refer to whether the magnet is horizontally focusing or defocusing when a positive current is sent to the quadrupole.



Figure 2.2: Lattice of the TL2 transfer line. The beam enters TL2 from the right hand side of the figure. Changes made to accommodate the PFF hardware are highlighted in yellow. Dipoles (BH or BV) and quadrupoles (QF or QD) are labelled below the line at their approximate positions. BPMs (BPI or BPM), correctors (DH or DV) and the PFF kickers (KH) are labelled above the line at their approximate positions. Adapted from [40]

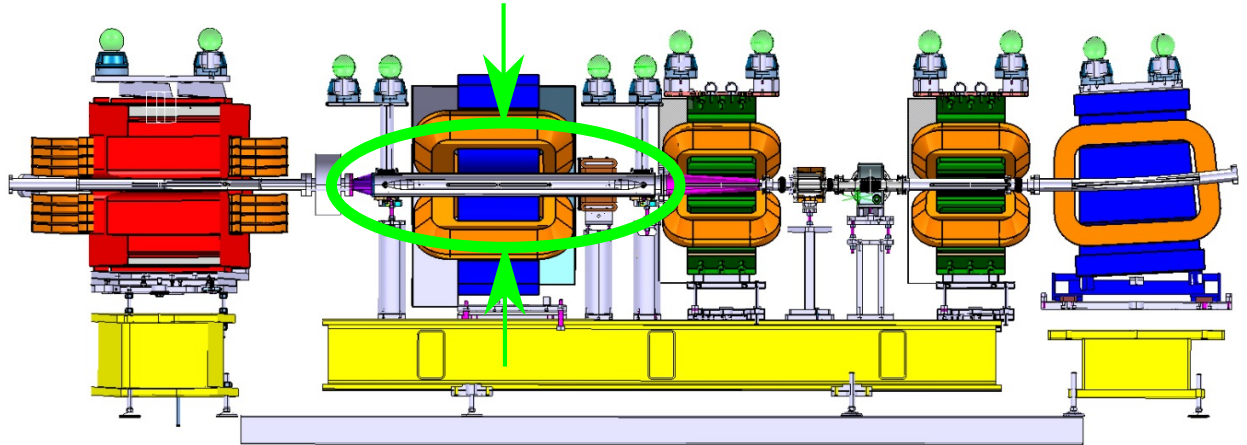


Figure 2.3: Schematic of the installation of the first kicker inside the quadrupole CC.QDH0490 (blue) before the first dipole in the chicane CC.BHG0500 (red). The kicker also passes through the aperture of the corrector CC.DHF0465 (brown) before the quadrupole [41].

Other features along the TL2 line that are important for the derivation of optics seen later in this chapter include the vertical chicane and two long drift spaces without focusing elements. The vertical chicane starts and ends at CC.BVA0300 and CC.BVB0400 respectively, and contains a triplet of quadrupoles. Between the quadrupole CC.QFD0840 (the last shown in the diagram) and CC.QFL0910, there is a long drift space of around 4 m with no focusing elements as the beam pipe passes through in to the neighbouring building where the CLEX area is located. Between the quadrupole CC.QFH0230 and CC.QFL0270 there is another long drift space, around 7 m. The Twiss beta and alpha functions entering these long drifts must be carefully chosen to avoid unrecoverable growth in the beam size.

### 2.3.1 Integration of PFF Hardware

Due to building and cost constraints the PFF prototype had to make use of the pre-existing layout of the TL2 horizontal chicane, with only minor modifications possible to accommodate the PFF hardware. These changes are highlighted in Figure 2.2.

As the chicane was already densely packed with quadrupoles and other devices the integration of the two kickers was not straightforward. To maintain the functionality of the lattice quadrupoles could not be removed, and thus instead the kickers have been installed inside wide aperture ‘H-type’ quadrupoles [42]. Two ‘L-type’ quadrupoles [42] (now CC.QDL0330 and CC.QDL0370) from the horizontal chicane were swapped with two ‘H-type’ quadrupoles (now CC.QDH0490 and CC.QDH0790) from the vertical chicane. The two PFF kickers, CC.KHD0480 and CC.KHD0780, are then installed inside the aperture of these quadrupoles, prior to the first and last dipole of the horizontal chicane. In addition, two magnetic correctors (now CC.DHF0465 and CC.DHF0765) were installed around the PFF kickers to facilitate a complementary, large range but low bandwidth, slow phase correction [43]. A schematic of the installation of the first kicker inside the quadrupole and corrector is shown in Figure 2.3. The kicker CC.KHD0480 will also be referred to as the first kicker (or K1),

and CC.KHD0780 as the second kicker (or K2). Apart from the quadrupoles and correctors two BPMs (now CC.BPI0435 and CC.BPI0735) also had to be moved slightly to vacate the area now occupied by the kickers.

## 2.4 TL2 Optics Constraints

To take in to account the changes made to the TL2 lattice new optics were needed. This section summarises the various optics constraints that must be met in TL2. These can be split in to two types – the nominal optics constraints, required to recover the same (or similar) beam conditions as before the changes, and the new optics constraints for operation of the PFF system, required to create the desired phase shifting behaviour in the chicane.

### 2.4.1 Nominal Optics Constraints

The nominal optics constraints are mostly put in place to minimise the transverse beam size along the line by restricting the magnitude of the dispersion and twiss functions. The final constraints, on the  $R_{56}$  transfer matrix coefficient, relates to the longitudinal stability of the beam.

#### Dispersion

The trajectory of a particle through a dipole depends on its energy, with lower energy particles following a smaller radius of curvature and high energy particles a larger radius. After a dipole the orbit of a particle though the following elements therefore depends on its energy. This effect is characterised using the horizontal and vertical dispersion,  $D_x$  and  $D_y$ , which are defined as follows (considering only the energy component of the beam orbit):

$$x(s) = D_x(s) \left( \frac{\Delta p}{p} \right) \quad (2.13)$$

$$y(s) = D_y(s) \left( \frac{\Delta p}{p} \right) \quad (2.14)$$

The dispersions  $D_x(s)$  and  $D_y(s)$  vary along the lattice and are equivalent to the transfer matrix coefficients  $R_{16} = D_x$  and  $R_{36} = D_y$ .

Optics are usually created so that there is no dispersion ( $D_x = D_y = 0$ ) in straight sections. However, inside chicanes and rings the dispersion can never always be zero. To give zero dispersion in the straight sections the dispersion must therefore be closed at the exit of all bending sections. Dispersion closure means that both the dispersion and its derivative ( $D'_x = dD_x/ds$ , and  $D'_y = dD_y/ds$ ) are zero at the exit from the chicane or ring. In TL2 this condition applies after the bend CC.BHH0200 at the start of the line and at the exit of the horizontal chicane (CC.BHG0800) for the horizontal dispersion, and at the exit of the vertical chicane (CC.BVB0400) for the vertical dispersion.

Parameter	Value
$\beta_x$	7.26 m
$\beta_y$	5.90 m
$\alpha_x$	-4.84
$\alpha_y$	-1.27

Table 2.1: Initial twiss parameters for the TL2 line, taken at the entrance to CC.QFH0210.

Within the bending sections the magnitude of the dispersion should be kept as small as possible whilst meeting the other optics constraints. At CTF3 there can be peak-to-peak energy offsets at around the  $\pm 1\%$  level [15]. Dispersion is then usually the largest contribution to the beam size, with a dispersion of 1 m giving excursions up to  $\pm 1$  cm in individual particle orbits, for example. The diameter of the beam pipe in bending sections at CTF3 is 10 cm in most cases, as opposed to 4 cm in straight sections, in order to minimise the effects of dispersion dependent beam size growth on the beam transport [15]. However, the second kicker installed in the chicane for the PFF system (CC.KHD0780) only has the normal 4 cm aperture (2 cm radius). Dispersion around the second kicker must therefore be kept well below 2 m to avoid losing a fraction of off-energy particles on the kicker strips.

## Twiss Functions

The twiss beta functions define the energy independent component of the transverse beam size and the alpha functions define the rate of change of the beta function along the line, as discussed in Section 2.1. The transverse beam size at any point in the lattice is related to the beta function and emittance via the relationship  $\sqrt{\beta_x(s)\epsilon_x}$  (and the vertical equivalent). At CTF3 the beam emittance is usually around  $0.5 \mu\text{m}$ , but may be up to a factor two larger than this in the horizontal plane depending on the beam setup [44]. With an emittance of  $0.5 \mu\text{m}$  a beta value of 50 m at one point in the lattice corresponds to a transverse beam size of 0.5 cm at that location, for example. The beta and alpha functions should be kept as small as possible to minimise the beam size along the line. Beta is usually kept below 50 m, but values up to 100 m can be accepted [45]. As mentioned previously there are long drift spaces with no focusing elements at the start and end of TL2, and it is most difficult to maintain low beta and alpha values following these regions.

At the start of TL2 the initial values of the twiss parameters are also constrained by the optics of the combiner ring. In other words, the beta and alpha values at the start of TL2 should be the same as the beta and alpha values at the exit of the combiner ring. This avoids discontinuities between sections in the complete CTF3 optics. The TL2 optics have usually been matched (Section 2.6) starting from CC.QFH0210, and the required initial conditions at this location are summarised in Table 2.1.

## R56

The dispersion describes how the transverse orbit of a particle is changed by its energy in bending sections as already discussed. These differences can also change the longitudinal path length of the particle's trajectory, thereby shifting the particle's phase (described by the time  $t$ , the fifth coordinate in the matrix formalism). This effect is described by the transfer matrix coefficient  $R_{56}$ :

$$t_f = t_i + R_{56} \left( \frac{\Delta p}{p} \right) \quad (2.15)$$

The  $R_{56}$  value between the entrance and exit of all bending sections at CTF3 is nominally zero so that there is no transformation of energy jitter into phase jitter. In TL2 this places the constraints for  $R_{56}$  to be zero between the entrance and exit of the vertical chicane (CC.BVA0300 to CC.BVB0400) and between the entrance and exit of the horizontal chicane (CC.BHG0500 to CC.BHG0800).

### 2.4.2 PFF Optics Constraints

All the additional PFF optics constraints place requirements on the transfer matrix coefficients between the two kickers, from the exit of the first kicker to the entrance of the second kicker. There are two sets of constraints, one to maximise the correction range of the PFF system and the other to ensure the PFF system does not degrade the orbit stability of the beam after the chicane.

#### Correction Range

The PFF system clearly requires the path length between the two kickers to depend on the applied kick. This difference in path length dependent on the voltage applied to the kickers is what shifts the time or phase of the beam to form the correction. The transfer matrix coefficient that relates the time variable to the deflection induced by the kickers is  $R_{52}$ :

$$t_{K2} = t_{K1} + R_{52} x'_{K1} \quad (2.16)$$

Where  $t_{K1}$  and  $t_{K2}$  are the time offset of the particle at the exit of the first kicker and at the entrance to the second kicker respectively.  $x_{K1}$  is the divergence at the exit of the first kicker resulting from the applied kick. MADX uses units of metres for its 'time' variable [31]. To convert these distances into 12 GHz degrees they must be multiplied by the constant factor  $360/\lambda_{12\text{GHz}}$ , where  $\lambda_{12\text{GHz}} = 2.5$  cm is the 12 GHz wavelength. Directly in terms of phase (in degrees) the equation above therefore becomes:

$$\phi_{K2} = \phi_{K1} + R_{52} \left( \frac{360}{\lambda_{12\text{GHz}}} \right) x'_{K1} \quad (2.17)$$

Where  $\phi_{K2}$  is the phase at the entrance to the second kicker (the corrected phase) and  $\phi_{K1}$  is the initial uncorrected phase at the exit of the first kicker. The maximum value of  $x'_{K1}$  is fixed by the peak voltage output from the kicker amplifiers and the design of the kickers

themselves. To obtain the largest possible correction range for the PFF system given the parameters of the hardware, the  $R_{52}$  transfer matrix coefficient should be as large as possible. For example, with  $R_{52} = 1$  m and a maximal kick of  $x'_{K1} = \pm 1$  mrad, the correction range of the PFF system would be  $\pm 14.4$  degrees.

The path length difference in the chicane largely results from differing trajectories in the dipoles. In this way it is somewhat analogous to the dispersion, which describes the energy dependent difference in beam orbit after dipoles. This has the unfortunate consequence of leading to optics with high  $R_{52}$  values also tending to have high peak dispersion values in the chicane. The PFF optics must therefore be a compromise that achieves a reasonable correction range whilst keeping the dispersion small enough to avoid beam losses in the chicane.

## Orbit Closure

The PFF system should not change the beam orbit after the chicane, which means the beam position and divergence after the second kicker must be independent of the applied kicks. In other words, the second kicker must close the horizontal orbit bump created by the first kicker. To understand the further constraints this places on the optics the position,  $x_{K2}$ , and divergence  $x'_{K2}$  of the beam at the entrance to the second kicker will be considered first. These can be expressed as:

$$x_{K2} = R_{11}x_{K1} + R_{12}x'_{K1} \quad (2.18)$$

$$x'_{K2} = R_{21}x_{K1} + R_{22}x'_{K1} \quad (2.19)$$

Where  $x_{K1}$  and  $x'_{K1}$  are the position and divergence at the exit of the first kicker, and  $R_{11}$ ,  $R_{12}$ ,  $R_{21}$  and  $R_{22}$  are transfer matrix coefficients for the optics between the exit of the first kicker and the entrance to the second kicker. The beam position at the exit of the first kicker is proportional to the applied kick:

$$x_{K1} = mx'_{K1} \quad (2.20)$$

Here  $m$  is a constant that depends on the properties of the kicker and also on the strength of the quadrupole CC.QDH0490 within which the kicker is installed (Section 2.3.1). Substituting this expression in to the equations for  $x_{K2}$  and  $x'_{K2}$  gives:

$$x_{K2} = \left( R_{11} + \frac{R_{12}}{m} \right) x_{K1} \quad (2.21)$$

$$x'_{K2} = (mR_{21} + R_{22})x'_{K1} \quad (2.22)$$

As stated  $x_{K2}$  and  $x'_{K2}$  are defined above at the entrance to the second kicker. The requirement for the PFF chicane optics is that the position and divergence at the exit of the second kicker are zero independent of the applied kicks. However, a derivation of the exact expression for the optics requirements between the kickers in order to close the orbit at the exit of the second kicker is complicated by the fact that the quadrupole around the second kicker, CC.QDH0790, can have a different strength to the quadrupole around the first kicker.

For the purpose of the discussion here the simplified case where CC.QDH0790 has the same strength but opposite polarity (focuses in the opposite plane) as CC.QDH0490 will

be considered. The ideal case where the two kickers can be powered with the same magnitude voltage but opposite polarity is also assumed. With these conditions, the second quadrupole/kicker effectively have precisely the opposite effect on the beam as the first quadrupole/kicker. To close the orbit after the second kicker the position and divergence at the entrance to the second kicker must therefore meet the following criteria:

$$x_{K2} = -x_{K1} \quad (2.23)$$

$$x'_{K2} = x'_{K1} \quad (2.24)$$

Comparing these two expressions to the previously derived equations for  $x_{K2}$  and  $x'_{K2}$  then yields the following optics constraints:

$$R_{11} + \frac{R_{12}}{m} = -1 \quad (2.25)$$

$$mR_{21} + R_{22} = +1 \quad (2.26)$$

There are many possible solutions to these expressions, with the simplest example being  $R_{11} = -1$ ,  $R_{12} = 0$ ,  $R_{21} = 0$  and  $R_{22} = 1$ . However, the optics matching (Section 2.6) allows the quadrupoles CC.QDH0490 and CC.QDH0790 to have different strengths. MADX is then used to model the actual beam orbit in the chicane and the figure of merit is for the simulated orbit to be closed after the second kicker, rather than for the above constraints to be met. Nevertheless, the optics eventually created do satisfy Equations 2.25 and 2.26 within several percent (Section 2.6.2).

## 2.5 TL2 Optics Measurements

As seen above there are many optics constraints in TL2 that must be met both to ensure that the beam can be transported efficiently in to the CLEX area as well as to obtain the desired behaviour in the horizontal chicane for the PFF system. MADX can be used to create optics that meet these criteria (Section 2.6), but they will be of no use if the model of TL2 does not accurately describe the actual characteristics of the line. As such, a series of measurements has been taken to determine and improve the accuracy of the TL2 MADX model. Measurements of this type had not previously been completed for the TL2 line at CTF3, thus any errors identified in the model are not limited to only the hardware changes made for the PFF system.

### 2.5.1 Method

The TL2 line includes 12 magnetic correctors, as shown in Figure 2.2 (plus one at the end of TL2 in the CLEX area, which is not shown in the figure). An electric current can be applied to horizontal or vertical coils on the corrector, creating independently adjustable horizontal and vertical fields that deflect the beam. The primary purpose of the correctors is to compensate differences in beam orbit resulting from small misalignments of devices along the line. However, they can also be used to test the accuracy of the TL2 model.

Measurements were taken in which the current applied to one of the correctors was changed, causing the beam to be deflected on to a new trajectory along the rest of the line. The new orbit is observed in the BPMs downstream of the corrector, with a total of 12 BPMs in TL2 (also shown in Figure 2.2). The position offset in each BPM depends on the transfer matrix between the corrector and that BPM, and therefore on the focusing properties of all the magnetic elements between the corrector and the BPM. By deflecting the beam with each corrector along the line, and in both planes, the response of the whole line as well as individual parts of the line can be determined.

The same process can then be repeated in the MADX model, applying a current to one of the correctors and creating a simulated deflected orbit. All the BPMs are included in the model, allowing the real measured position in each BPM to be compared to the simulated position from the MADX model. Any difference between the two highlights inaccuracies in the modelled properties of the TL2 lattice.

### 2.5.2 Results with Original MADX Model

Figures 2.4 and 2.5 show an example of the results obtained with the original version of the TL2 MADX model, in the horizontal and vertical planes respectively. One of the first correctors in TL2, CC.DHF0175 (or the equivalent CC.DVF0175 in the vertical plane), is used, so the results are sensitive to errors in the model along the full length of the line. Three lines are shown in each figure – the red line labelled “Measurement” corresponds to the actual measured position in the BPMs, the dashed blue line “Model” shows the simulated position in the BPMs from MADX, and the final black line “Full” shows the simulated MADX orbit propagated through all elements along the line (not restricted to only the BPM positions). In a perfect model of the line the blue “Model” and red “Measurement” lines would be identical.

In the horizontal plane there is good agreement between the model and the measurement in the three BPMs following the corrector (up until CC.BPM0275). After this point the response in the model is clearly completely different to the measurement. For example, the measured position shifts by 10 mm between CC.BPM0275 and CC.BPM0365 in the measurement, but only 6 mm in the model. Towards the end of the line the model is close to being the inverse of the measurement. There is also poor agreement between the model and the measurement in the vertical plane, with a large difference already visible at CC.BPM0275 in this case. The peak-to-peak vertical orbit offset in the model is roughly a factor two larger than the measurement.

### 2.5.3 Sources of Errors in MADX Model

The results described above immediately demonstrated large discrepancies between the model and the actual response of TL2. Based on previous experience from corrections made to the MADX model for other sections of CTF3 [46] two key areas were identified to investigate to try to improve the model — the properties of the “L-type” quadrupoles in



Figure 2.4: Horizontal orbit due to a kick from the corrector CC.DHF0175 (red) compared to the expected orbit in the original MADX model of TL2. The black line shows the MADX orbit propagated through all elements along the line, and the dashed blue line the orbit restricted to only the BPM positions.

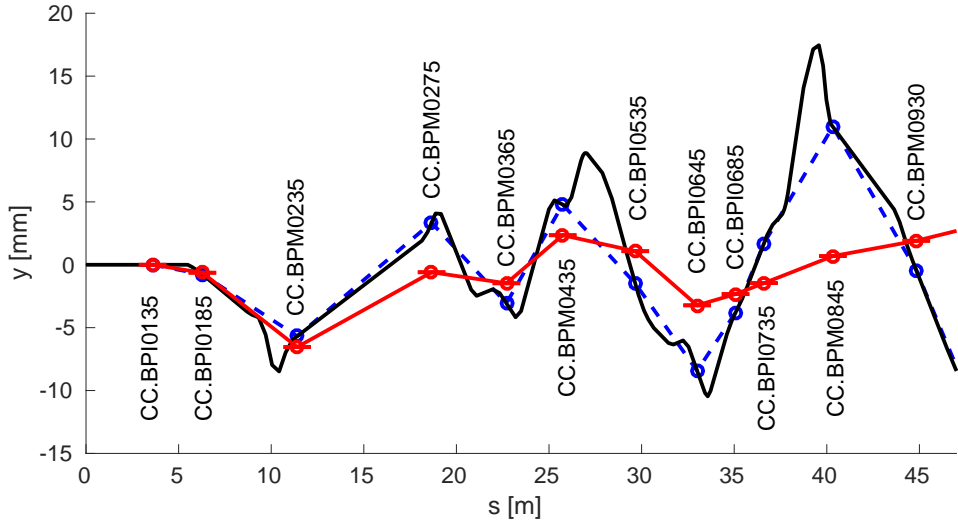


Figure 2.5: Vertical orbit due to a kick from the corrector CC.DHF0175 (red) compared to the expected orbit in the original MADX model of TL2. The black line shows the MADX orbit propagated through all elements along the line, and the dashed blue line the orbit restricted to only the BPM positions.

TL2, and the focusing effects from the dipoles in TL2.

### Quadrupole Strengths

16 out of the 27 quadrupoles in TL2 are of the “L-type”, with labels of the form CC.QDLxxxx or CC.QFLxxxx. This includes all the quadrupoles in the horizontal chicane apart from the two wide aperture “H-type” quadrupoles within which the PFF kickers are installed. These quadrupoles were reclaimed from the CELSIUS project in Uppsala, Sweden [47]. In the MADX model of TL2 the focusing strength of these magnets,  $K_1$  is defined by the following parameters:

$$K_1 = \frac{FQL \times I}{E} \quad (2.27)$$

Where  $FQL = 31.78$  is a constant defined by the properties of the quadrupole,  $I$  is the current delivered to the quadrupole from its power supply (a larger focusing effect) and  $E$  is the beam energy. The  $K_1$  value is analogous to the constant  $k$  in the quadrupole transfer matrix previously seen in Equation 2.3. This must be multiplied by the 30 cm active magnetic length of the quadrupole to determine the equivalent focal length of the quadrupole.

As the properties of the “L-type” quadrupoles were not measured in place at CERN prior to their use in CTF3 there was a large uncertainty on the correct value of  $FQL$  to use. Changing the  $FQL$  value was therefore a good candidate to try to reduce errors in the MADX model.

### Dipole Focusing

Although the primary purpose of dipole magnets is to bend the beam they also give focusing effects that depend on the design of the magnet, and in particular the orientation of the pole faces. The seven dipoles in TL2 can be roughly split into two types in terms of the focusing effects they are expected to produce — sector magnets (SBENDs) and rectangular magnets (RBENDs). Figure 2.6 compares the geometry of the pole faces for SBEND and RBEND dipoles. In SBEND magnets the ends of the pole faces are oriented such that the reference trajectory of the beam (black) enters and leaves the magnet perpendicular to the pole face. Alternatively, in RBEND dipoles the pole faces at the entrance and exit of the magnet are parallel to each other. In this case the reference trajectory forms an angle  $\theta/2$  with the pole faces, where  $\theta$  is the angle through which the beam is deflected by the magnet [30]. In TL2 the CC.BHH0200, CC.BHG0500, CC.BHH0600, CC.BHH0700 and CC.BHG0800 dipoles are RBENDs, and the CC.BVA0300 and CC.BVB0400 dipoles are SBENDs [42].

The first focusing effect from dipoles relates to the path length of the beam through the magnet. In SBEND magnets this length depends on the position offset in the (horizontal or vertical) bending plane. Particles entering the magnet experience the dipole field for a longer length on one side of the reference trajectory, and a shorter length on the other side of the reference trajectory, producing a focusing effect in the bending plane. This is also shown in Figure 2.6. In RBEND magnets the length of the trajectory is the same for all incoming position offsets, so this focusing effect is not present.

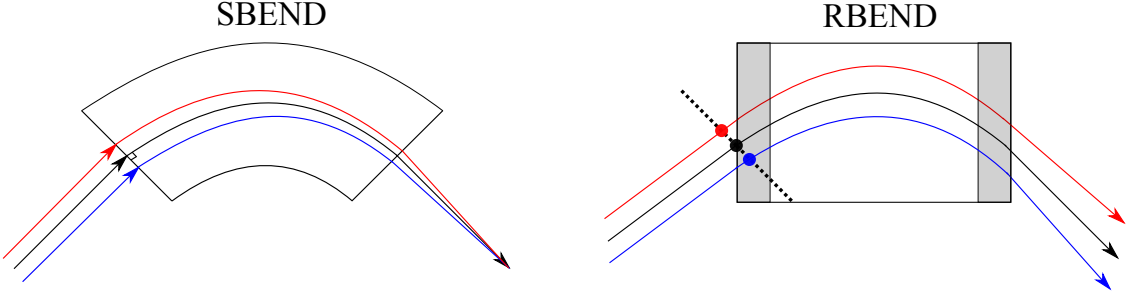


Figure 2.6: Geometry of SBEND and RBEND dipoles.

Another way in which dipoles produce focusing effects is via their fringe fields. The fringe fields describe the increase in magnetic field from zero to the peak bending field as the beam approaches the entrance to the dipole, and from the peak field back to zero as the beam leaves the dipole. The extent and rate of increase of the fringe fields depends on the design of the dipole, in particular the pole separation. In MADX the nature of the fringe fields is defined by the variables HGAP, the pole separation, and FINT, which describes the shape of the increase up to the peak field (e.g. linear) [31].

In RBEND magnets, where the reference orbit is not perpendicular to the pole faces, the longitudinal position along the trajectory where a particle enters the fringe field linearly depends on its transverse position offset in the bending plane. This is shown in Figure 2.6, where the grey shaded areas mark the region of the fringe fields. The red trajectory enters the fringe fields later than the blue trajectory. This creates a position dependent focusing effect which is defocusing in the bending plane and focusing in the other transverse plane, similar to a quadrupole [48]. In the ideal case this type of focusing is not present in SBEND magnets.

Finally, higher order field errors in the dipole can lead to further focusing terms. MADX allows a quadrupole field coefficient ( $K_1$ ) to be added to a dipole to model this effect. In other sections of CTF3 it was found that the default MADX parameters did not give a good approximation of the dipole focusing terms [46]. The FINT, HGAP and  $K_1$  parameters for each of the 7 dipoles in TL2 are therefore also good candidates to try to correct the MADX model of TL2.

#### 2.5.4 Corrections to MADX Model

By varying the parameters of the dipole focusing and the L-type quadrupole strengths described above it has been possible to find a solution that gives much better agreement between the corrector kick measurements and the expected response in the MADX model. The new values for the parameters do not necessarily represent their true real world characteristics (for example the dipole pole separation), but are rather a set of values that adjusts the simulated MADX focusing in a way that matches the actual behaviour. An iterative process was used, with a mixture of automatic optimisations via algorithms in MATLAB and MADX and manual interventions to drive the calculated adjustments towards a reasonable solution and away from any local minima.



Figure 2.7: Horizontal orbit due to a kick from the corrector CC.DHF0175 (red) compared to the orbit in the MADX model of TL2 with the L-type quadrupole strengths increased by 7%. The black line shows the MADX orbit propagated through all elements along the line, and the dashed blue line the orbit restricted to only the BPM positions.

The first adjustment made was to the modelled strength of the L-type quadrupoles. As the majority of quadrupoles along TL2 are of this type the focusing and calculated transfer matrices in the MADX model are very sensitive to any change in their strength. It was quickly determined that the focusing strength of the L-type quadrupoles needed to be increased to improve the agreement between the measurement and the model. Figure 2.7 shows an example of a horizontal kick from the corrector CC.DHF0175 with an optimal increase of 7% in the L-type quadrupole strength. This can be directly compared to the original model in Figure 2.4. By increasing the focusing from the L-type quadrupoles the largest discrepancies between the MADX model and the measurement are removed. In particular the region from inside the vertical chicane (CC.BPM0365) to inside the horizontal chicane (CC.BPI0735) originally showed large differences including sign flips in the horizontal plane. With the adjusted L-type strength these are removed and the agreement is excellent.

Figures 2.8 and 2.9 then show an example of adjusting the focusing of the four dipoles in the horizontal chicane (the outer 500/800 pair and inner 600/700 pair) to remove remaining differences between the measurement and the model. In this case the beam is kicked from the CC.DVF0525 corrector just after the first dipole in the horizontal chicane, making the measurement insensitive to any optics errors prior to CC.DVF0525 in the line. In both figures the 7% increase in the L-type quadrupole strength has been applied in the MADX model. With the quadrupole correction in place but no adjustment to the dipole focusing, in Figure 2.8, the simulated orbit has the same overall shape as the measured orbit inside the chicane (up until CC.BPI0735). However, there are still offsets between the two and these eventually lead to a large discrepancy between the model and the measurement still being present in the two BPMs following the chicane (CC.BPIM0845 and CC.BPM0930), which is also seen in Figure 2.7.

Device	Parameter	Original Value	Corrected Value
CC.BHH0200	HGAP	0 m	0.084 m
	FINT	0	0.79
	K1	0 m <sup>-2</sup>	0 m <sup>-2</sup>
CC.BVA0300 & CC.BVB0400	HGAP	0 m	0 m
	FINT	0	0
	K1	0 m <sup>-2</sup>	-0.125 m <sup>-2</sup>
CC.BHG0500 & CC.BHG0800	HGAP	0 m	0.06 m
	FINT	0	0.4
	K1	0 m <sup>-2</sup>	0.15 m <sup>-2</sup>
CC.BHH0600 & CC.BHH0700	HGAP	0 m	0.06 m
	FINT	0	0.2
	K1	0 m <sup>-2</sup>	0.425 m <sup>-2</sup>
L-type Quadrupoles	FQL	31.78	34.03

Table 2.2: Changes made to the dipole focusing and quadrupole strength parameters in the TL2 MADX model in order to improve the agreement with the kick measurements.

By adjusting the HGAP, FINT and quadrupole K1 component of the dipoles in the horizontal chicane a solution is found that reduces the difference between the model and the measurement in the chicane, and then also gives much better agreement between the two after the chicane. This is shown in Figure 2.9. Repeating this process with correctors prior to the vertical chicane, and prior to the CC.BHH0200 bend at the start of TL2, yields the focusing parameters for the seven dipoles in the line summarised in Table 2.2. The largest quadrupolar component of  $K1 = 0.425 \text{ m}^{-2}$  for the CC.BHH0600 and CC.BHH0700 dipoles corresponds to a focusing strength of roughly 2% of a typical quadrupole magnet in TL2.

Figures 2.10 and 2.11 compare the measured horizontal and vertical orbit to the new MADX model of TL2 with all the corrections from Table 2.2 in place. The same corrector, CC.DHF0175, and data are used as for the examples from the original model in Figures 2.4 and 2.5. The new version of the model is a clear improvement. In both the horizontal and vertical planes the measured and modelled beam orbit now agree along the full length of the line within a small margin of error. With the original MADX model the mean absolute difference between the measured and simulated positions in the ten BPMs following CC.DHF0175 was  $3.9 \pm 1.0 \text{ mm}$  in the horizontal plane and  $3.1 \pm 0.8 \text{ mm}$  in the vertical plane. The corrected model reduces these differences by an order of magnitude, to  $0.2 \pm 0.1 \text{ mm}$  in the horizontal plane and  $0.3 \pm 0.1 \text{ mm}$  in the vertical plane.

## 2.6 Matched TL2 Optics

With the corrected MADX model of TL2 in place the new optics for the PFF system were created. The optics were obtained using MADX matching libraries [31], in which many desired constraints can be defined for the line (each with its own weight) and then one of several optimisation algorithms can be used to change the quadrupole strengths and derive

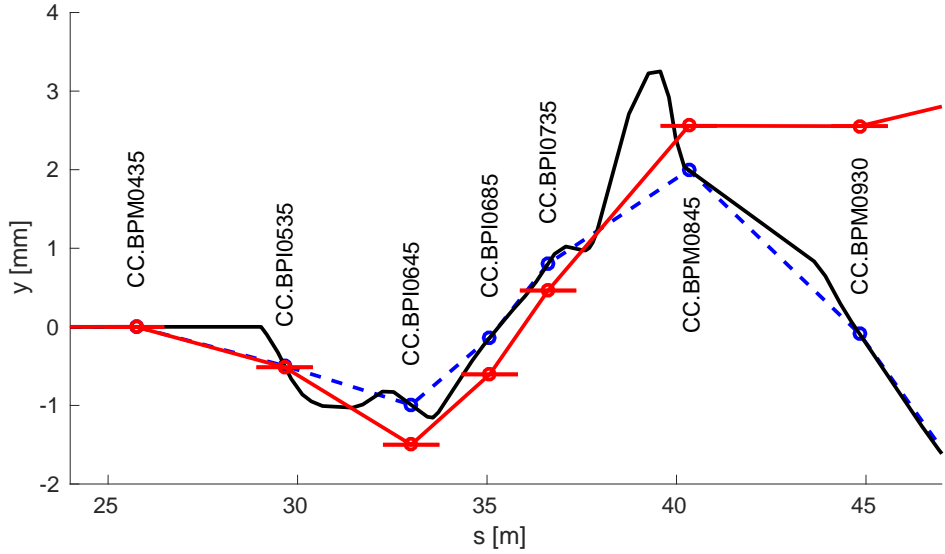


Figure 2.8: Vertical orbit due to a kick from the corrector CC.DVF0525 (red) with the default MADX model of the dipole focusing. The black line shows the MADX orbit propagated through all elements along the line, and the dashed blue line the orbit restricted to only the BPM positions.

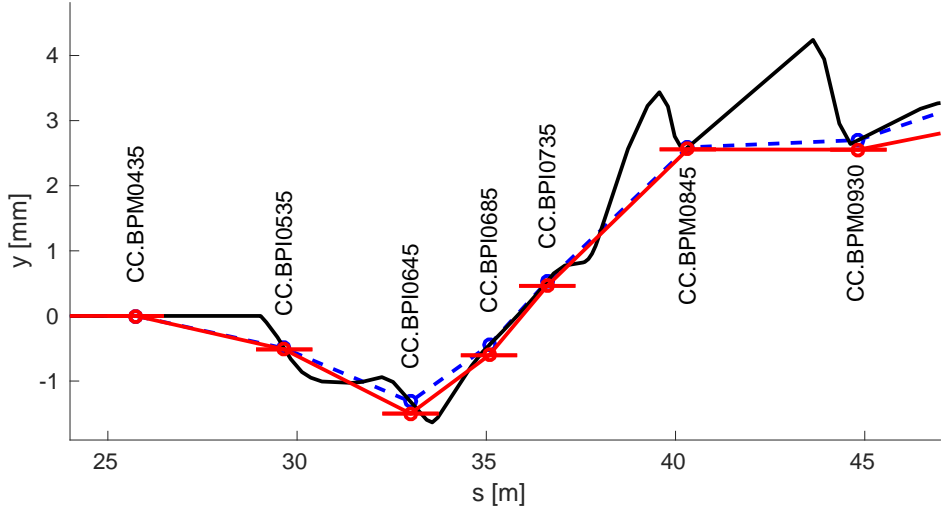


Figure 2.9: Vertical orbit due to a kick from the corrector CC.DVF0525 (red) with the corrected MADX model of the dipole focusing. The black line shows the MADX orbit propagated through all elements along the line, and the dashed blue line the orbit restricted to only the BPM positions.

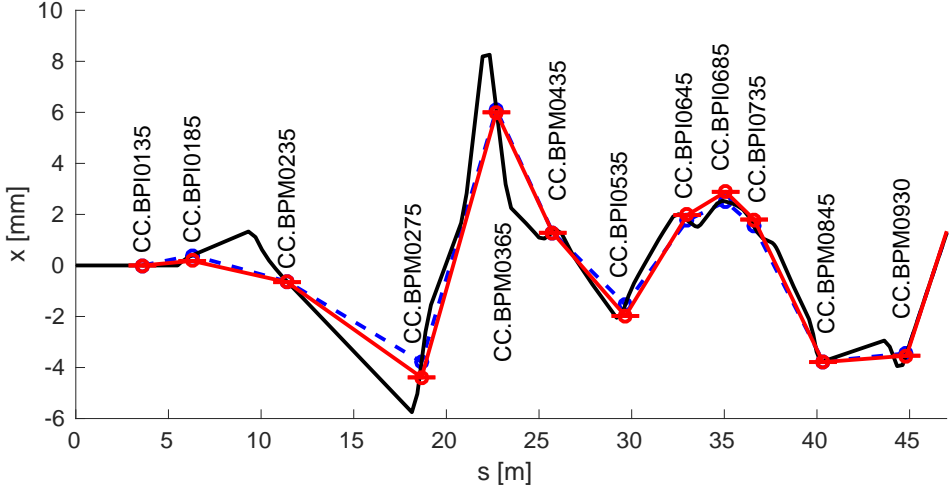


Figure 2.10: Horizontal orbit due to a kick from the corrector CC.DHF0175 (red) compared to the corrected MADX model of TL2. The black line shows the MADX orbit propagated through all elements along the line, and the dashed blue line the orbit restricted to only the BPM positions.

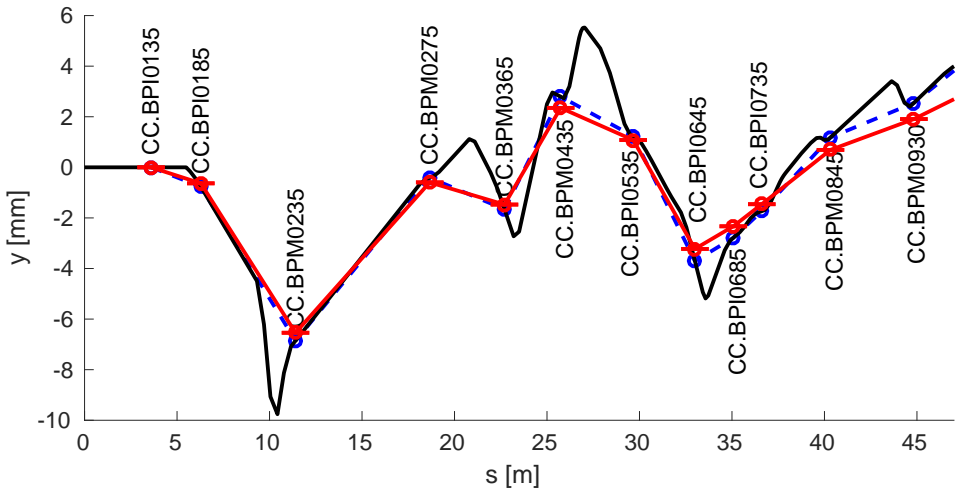


Figure 2.11: Vertical orbit due to a kick from the corrector CC.DVF0175 (red) compared to the corrected MADX model of TL2. The black line shows the MADX orbit propagated through all elements along the line, and the dashed blue line the orbit restricted to only the BPM positions.

an optics that meets those constraints. Two sets of optics were created for TL2 – a nominal set of optics containing only the constraints from Section 2.4.1, and a set of PFF optics containing the additional  $R_{52}$  and orbit closure related constraints for the PFF system from Section 2.4.2. Without the additional PFF constraints roughly a factor two smaller maximum dispersion and beta values can be achieved in the nominal optics. However, the beam quality achieved with the PFF optics has been sufficient to use routinely at CTF3 (including for non-PFF running), and so only this optics is documented here.

### 2.6.1 Matching Process

For the purposes of the matching TL2 was split in to three parts – from the beginning of the line to the exit of the vertical chicane (CC.BHH0210 to CC.BVB0400), from the exit of the vertical chicane to the exit of the horizontal chicane (CC.BVB0400 to CC.BHG0800) and the end of the line (from CC.BHG0800 and in to CLEX). The middle section, containing the PFF kickers and horizontal chicane, is the most critical for the PFF system.

At the beginning of each matching section the initial twiss parameters for that part of the lattice must be defined in MADX. At the start of the first section this is fixed by the properties of the beam leaving the combiner ring (Table 2.1). The initial and final twiss functions of the middle section containing the horizontal chicane were left as free parameters to allow the greatest degree of flexibility for meeting the constraints in the chicane. The optics for the middle section is therefore created first, with the resulting initial and final twiss parameters forming additional matching constraints that must be met at the end of the first section and the start of the final section.

Suitable initial values for the quadrupole strengths (defined by the current sent to each quadrupole from its power supply) must also be chosen to ensure the matching algorithms can converge to a good solution in a reasonable amount of time. For this purpose the currents from the prior optics for TL2 (before the modifications for the PFF system and the model corrections) were used.

To accurately simulate the effect of a kick applied at the PFF kickers they must be modelled together with the quadrupoles within which they are installed but this can not be directly defined in MADX. Instead the quadrupole definition in MADX has been split in to quarters, with zero length kicker elements inserted between each quadrupole quarter [45]. Each kicker element provides a quarter of the angular deflection of the complete kicker. This allows the focusing effect of the quadrupole on the applied kick to be approximated.

All the constraints for each section (taken from Section 2.4) are implemented in the matching scripts. The largest weight is given to achieving a non-zero  $R_{52}$  value between the kickers, as without this the optics would be of no use for the PFF system. The next strongest constraints are placed on the dispersion, both ensuring the dispersion is closed and keeping the dispersion well below 2 m around the second kicker. The remaining constraints, for example on the orbit closure,  $R_{56}$  and maximum twiss functions, are also included but with lower weights as a useful PFF demonstration could still be achieved if they are not precisely met.

As there are relatively few variables (quadrupoles) compared to the number of constraints it is not straightforward to match optics that meet most of the constraints. The final derivation of the optics in the following section required many matching steps, with the weights altered between each step to drive the optics closer to the desired solution. The matched quadrupole currents and twiss parameters for each matching section are used as the initial conditions for the following matching iteration. Ultimately a compromise had to be accepted that met most, but not all, of the constraints as described below.

### 2.6.2 PFF Optics

The PFF optics for TL2 that has been used for all the tests presented in this thesis is presented here. Tables 2.3 lists the matched quadrupole currents to apply and Table 2.4 summarises the optics constraints and their matched values. Figures 2.12 to 2.17 plot various optical parameters of interest along the line from CC.QFH0210 to CC.QDL0920. In these plots the position of the two chicanes (vertical and horizontal) are marked by dotted red lines, and the position of the two PFF kickers are marked by dotted green lines. In addition, underneath each figure the position of all quadrupoles, dipoles and the PFF kickers along the line are indicated. Blue convex lenses indicate focusing quadrupoles and blue concave lenses defocusing quadrupoles. Red rectangles mark the position of dipoles, and green squares the position of the two PFF kickers.

Figures 2.12 and 2.13 shows the twiss alpha and beta functions along TL2. The largest beta and alpha functions in both the horizontal and vertical planes are found in the region around the beginning of the vertical chicane, as a result of the long drift space between CC.QFH0230 and CC.QFL0270 (2 m to 9 m on the horizontal axis) preceding it. In this area the maximum beta value is 72.1 m, and the maximum alpha is 75.9. The alpha value is above the desired target of keeping alpha below a magnitude of 30 everywhere along the line. This constraint is primarily placed to minimise the strength of focusing in the line in order to reduce the effect of any remaining optics errors in the model. The vertical chicane therefore becomes a sensitive area for achieving good beam transport through TL2. However, in the rest of the line the beta (up to 32 m) and alpha functions (up to 18) are much smaller than their constrained maximums.

Figure 2.14 shows the horizontal and vertical dispersion along the line. The dispersions and their derivatives are closed at the  $10^{-5}$  level in the vertical chicane, and the  $10^{-6}$  level in the horizontal chicane. This leaves no residual dispersion in the straight sections, as desired. In the vertical chicane the dispersion reaches a peak magnitude of 0.11 m, whilst in the horizontal chicane the peak is 1.16 m. Both are much smaller than the constrained maximums. In addition, the dispersion in the region of the second kicker (K2), which is an aperture restriction as described previously, is 0.98 m and much smaller than the constrained maximum of 2 m.

The key constraint that is not met in the matched PFF optics is  $R_{56}$ , where a non-zero value had to be accepted in order to meet the remaining constraints. As seen in Figure 2.15 the  $R_{56}$  transfer matrix coefficient across the horizontal chicane is -0.18 m. This leads to additional energy dependent phase jitter following the chicane that is not present prior to

the chicane, which has severe consequences for the performance of the PFF system. The extent and mitigation of this effect is the focus of Chapter 4.

The last two figures, 2.16 and 2.17, show the effect of kicking the beam with the PFF kickers. A deflection of +1 mrad is applied from the first kicker, and -1 mrad from the second kicker. This leads to a peak horizontal orbit offset of 3.5 mm inside the horizontal chicane. The orbit is closed at the  $10^{-7}$  level following the chicane, so that the beam's trajectory following the PFF system is independent of the applied kick. The values from the approximated orbit closure expressions in Equations 2.25 and 2.26 are -1.03 and 1.04 respectively (with  $R_{11} = 1.2$ ,  $R_{12} = -0.9$ ,  $R_{21} = -0.7$ ,  $R_{22} = 1.3$  and  $m = 0.4$ ). The 3–4% difference from the expected values of -1 and +1 is explained by the 4% stronger strength of CC.IQDH0790 compared to CC.IQDH0490, which was not taken in to account in the derivation of the simplified equations.

Finally, the  $R_{52}$  value between the two kickers is 0.74 m. This defines the phase shift resulting from kicking the beam in the chicane, which is the key figure of merit for the PFF system. As shown in Figure 2.17 a kick of 1 mrad provides a phase shift of  $-10.6^\circ$  in this optics. This is converted in to the actual range of the PFF system taking in to account the specifications of the kicker amplifiers in Chapter 5. Verifications of the performance of the optics are presented in Chapters 4 and 5.

Quadrupole	Current
CC.IQFH0210	47.00 A
CC.IQDH0220	48.83 A
CC.IQFH0230	31.75 A
CC.IQFL0270	14.44 A
CC.IQDL0280	24.96 A
CC.IQDL0330	24.57 A
CC.IQFH0350	40.07 A
CC.IQDL0370	24.57 A
CC.IQDL0430	0.16 A
CC.IQFL0450	0.17 A
CC.IQDH0490	-6.05 A
CC.IQFL0530	21.94 A
CC.IQDL0550	27.57 A
CC.IQFL0570	30.19 A
CC.IQFL0620	-1.16 A
CC.IQDL0650	-10.46 A
CC.IQFL0680	-5.96 A
CC.IQFL0730	-7.77 A
CC.IQDL0750	-14.81 A
CC.IQDH0790	6.32 A
CC.IQDD0820	63.49 A
CC.IQFD0840	76.53 A
CC.IQFL0910	-11.97 A
CC.IQDL0920	-12.84 A

Table 2.3: Quadrupole power supply currents to set in the new PFF TL2 optics for a beam energy of 135 MeV.

Parameter	Constraint	Value
$\beta_x$	Max < 100 m	55.3 m at CC.QFL0270
$\beta_y$	Max < 100 m	72.1 m at CC.QDL0330
$ \alpha_x $	Max < 30	43.3 at CC.QFL0270
$ \alpha_y $	Max < 30	75.9 at CC.QFL0330
$ D_x $	Max < 2.5 m	1.16 m at CC.QDL0650
$ D_y $	Max < 1 m	0.11 m at CC.QDL0330
$ D_x $	$\ll 2$ m at K2	0.98 m
$D_x$	0 m at CC.BHG0800	$9 \times 10^{-7}$ m
$D'_x$	0 at CC.BHG0800	$-6 \times 10^{-6}$
$D_y$	0 m at CC.BVB0400	$4 \times 10^{-5}$ m
$D'_y$	0 at CC.BVB0400	$-6 \times 10^{-5}$
$ R_{52} $	$\gg 0$ m from K1 to K2	0.74 m
$x$	0 m after K2	$3 \times 10^{-7}$ m (1 mrad kick)
$x'$	0 after K2	$-5 \times 10^{-7}$ (1 mrad kick)
$R_{56}$	0 m from CC.BHG0500 to CC.BHG0800	-0.18 m

Table 2.4: Summary of constraints and their matched values in the new TL2 PFF optics.

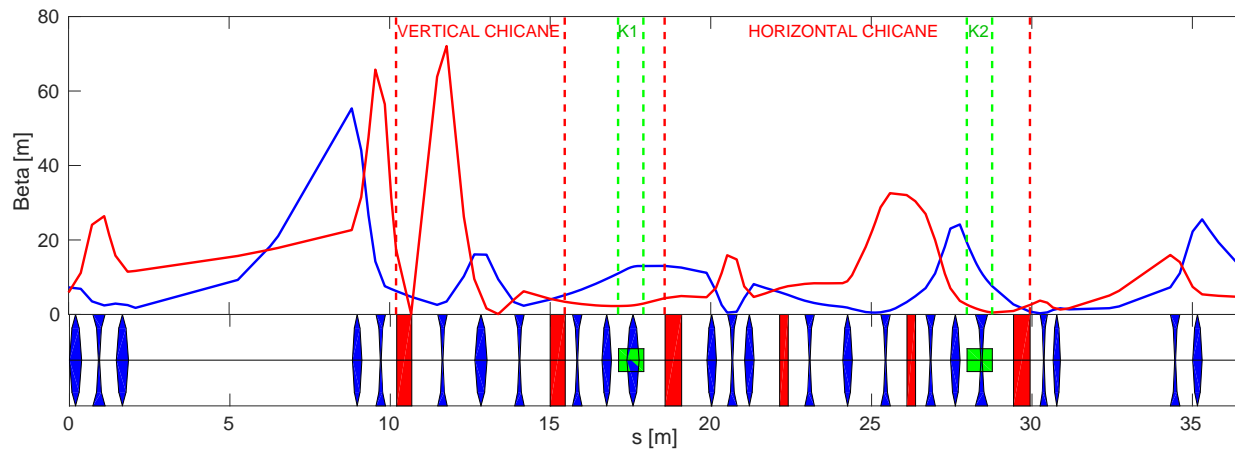


Figure 2.12: Horizontal (blue) and vertical (red) beta functions in the new TL2 optics. Blue convex lenses indicate focusing quadrupoles and blue concave lenses defocusing quadrupoles. Red rectangles mark the position of dipoles, and green squares the position of the two PFF kickers.

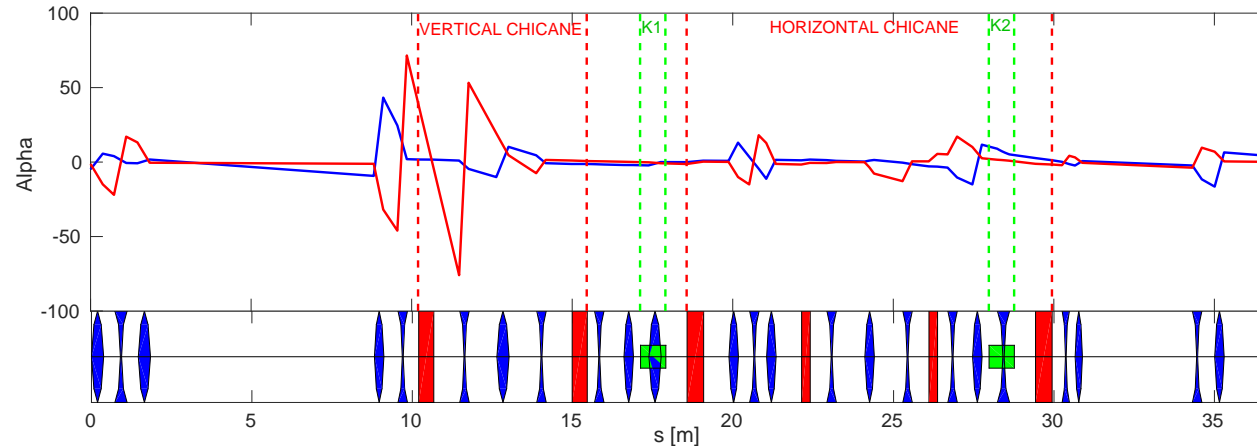


Figure 2.13: Horizontal (blue) and vertical (red) alpha functions in the new TL2 optics. Blue convex lenses indicate focusing quadrupoles and blue concave lenses defocusing quadrupoles. Red rectangles mark the position of dipoles, and green squares the position of the two PFF kickers.

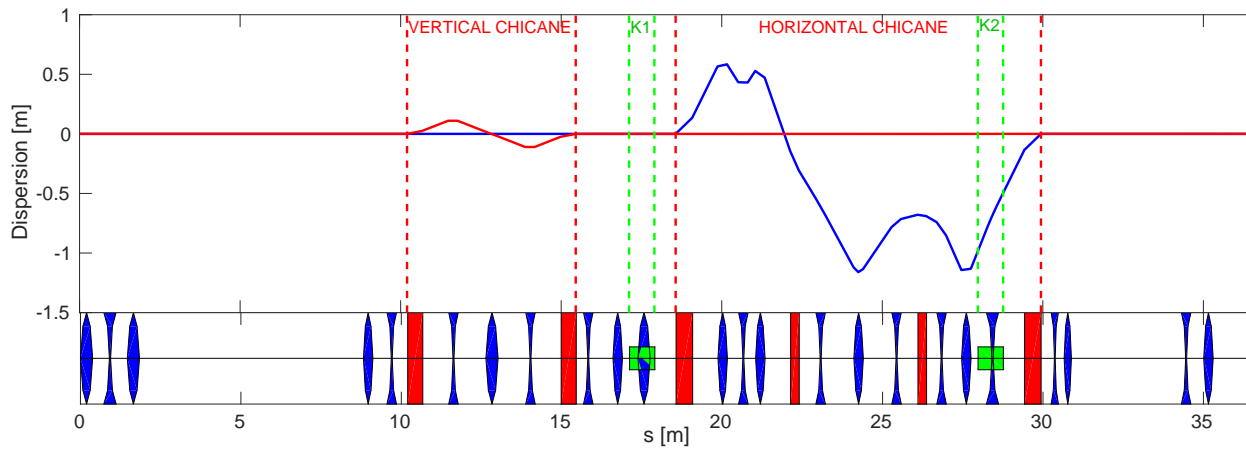


Figure 2.14: Horizontal (blue) and vertical (red) dispersion in the new TL2 optics. Blue convex lenses indicate focusing quadrupoles and blue concave lenses defocusing quadrupoles. Red rectangles mark the position of dipoles, and green squares the position of the two PFF kickers.

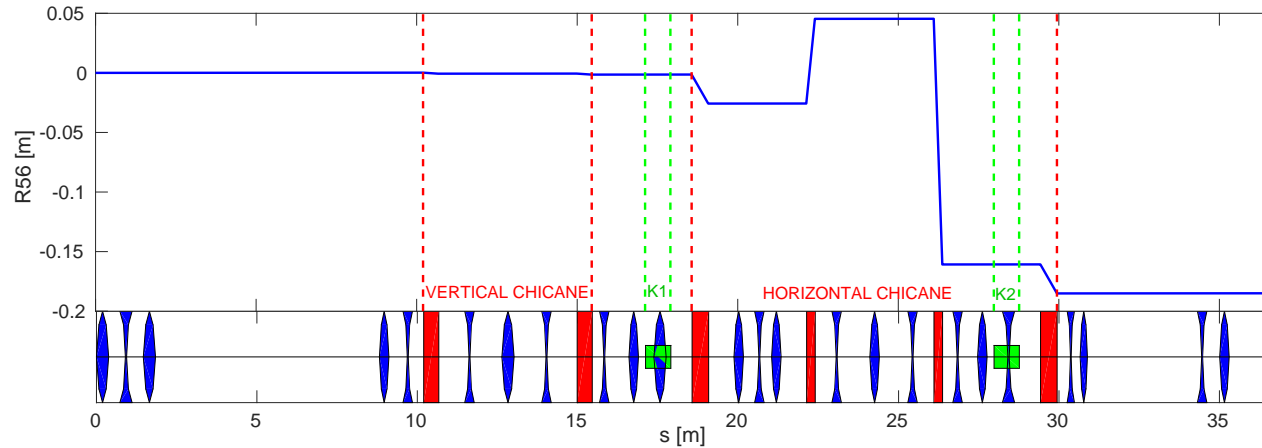


Figure 2.15:  $R_{56}$  in the new TL2 optics. Blue convex lenses indicate focusing quadrupoles and blue concave lenses defocusing quadrupoles. Red rectangles mark the position of dipoles, and green squares the position of the two PFF kickers.

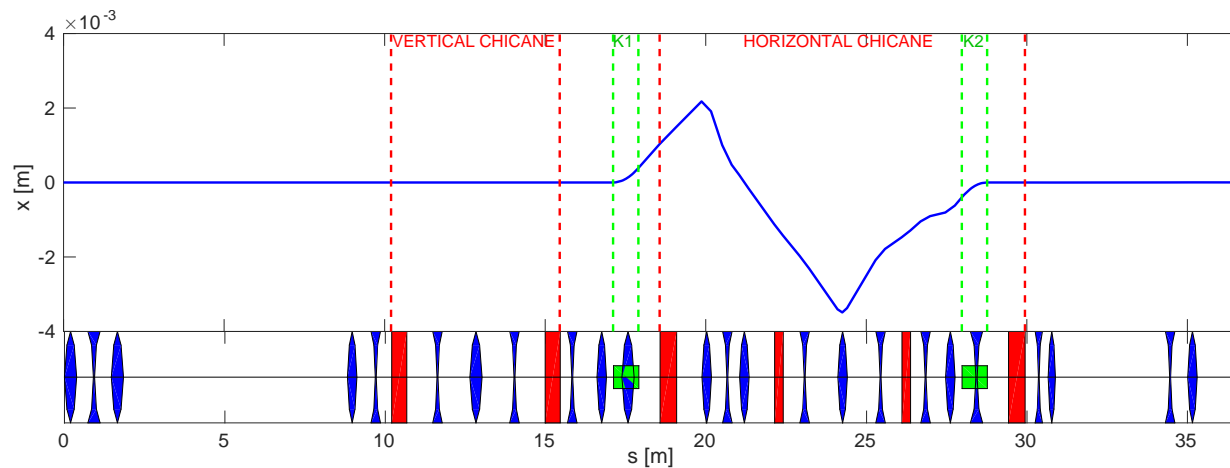


Figure 2.16: Horizontal orbit in the TL2 chicane with a 1 mrad kick from the PFF kickers. Blue convex lenses indicate focusing quadrupoles and blue concave lenses defocusing quadrupoles. Red rectangles mark the position of dipoles, and green squares the position of the two PFF kickers.

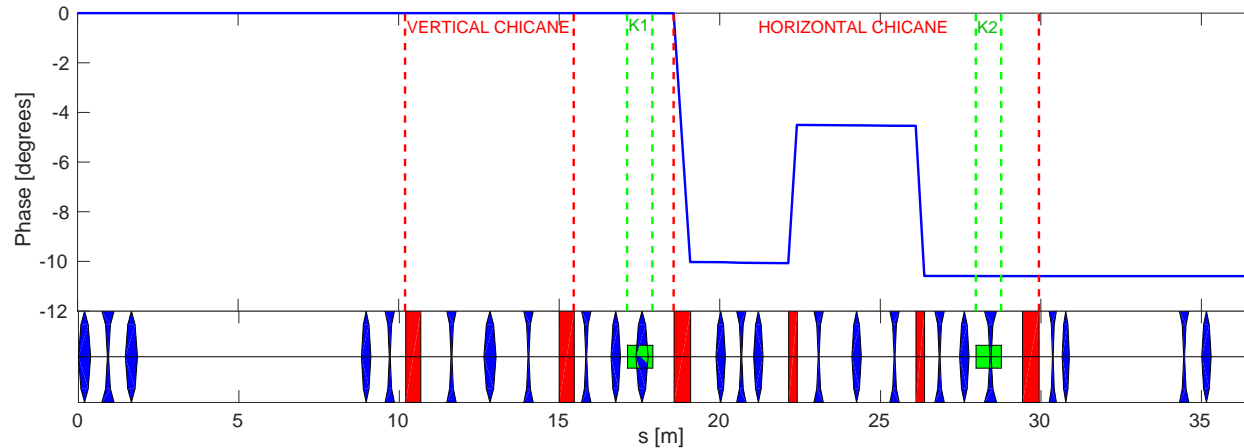


Figure 2.17: Phase in the TL2 chicane with a 1 mrad kick from the PFF kickers. Blue convex lenses indicate focusing quadrupoles and blue concave lenses defocusing quadrupoles. Red rectangles mark the position of dipoles, and green squares the position of the two PFF kickers.

# Chapter 3

## Phase Monitor Characterisation Performance

In order to successfully correct the phase with the PFF system it is clearly necessary to be able to accurately measure the phase, whilst meeting the low latency and high bandwidth requirements of the correction. Purpose-built phase monitors for the PFF system have been designed and constructed by INFN, Italy [24]. Three of these monitors are currently installed at CTF3 — two in the CT line at the end of the linac and one after the TL2 chicane in the TBL line. The approximate positions of the monitors are shown on the layout of the PFF system in Figure 1.6. The two “upstream” phase monitors in the CT line will be referred to as Mon 1 and Mon 2 (Mon 1 being upstream of Mon 2 in the beam line) in this chapter. The “downstream” phase monitor in TBL will be referred to as Mon 3. Mon 1 is normally used as the PFF correction input, with the neighbouring Mon 2 used for performance cross-checks. Mon 3 is then used to measure the effect of the PFF correction. In the rest of the thesis the phase measurements are generally simply referred to as being from either one of the upstream phase monitors, or the downstream monitor.

The chapter begins with an overview of the design and installation of the phase monitors themselves as well as the associated electronics. The electronics were provided as a “black box”, with the design and construction completed prior to author’s involvement in the project. The role of the author has been to maximise the performance of the existing electronics design, with the main focus of the chapter being the operational procedures, performance measurements and changes that have been necessary to achieve this. A resolution, or sensitivity to phase, of below  $0.14^\circ$  was achieved (Section 3.9), as derived to be necessary to be able to achieve the targeted  $0.2^\circ$  corrected phase jitter with the PFF system in Section 3.3. Several effects have also been identified that can still degrade the accuracy of the phase measurement, such as the position dependence seen in Section 3.13, and suggestions for further investigations are given, should an improvement in phase monitor performance be needed in the future.



Figure 3.1: Technical drawing of the phase monitor cavity design [51]. The length and internal diameter of the monitor are shown. Around the centre of the monitor are the four evenly spaced RF feedthroughs.

### 3.1 Phase Monitor Design

The phase monitors are cylindrical cavities with an external device length of approximately 19 cm and an internal diameter of 23 mm, as shown in Figure 3.1. When a charged beam traverses a cavity the interaction of the beam with the cavity walls creates electromagnetic fields inside the cavity. The amplitude of the induced fields depends both on the bunch charge and the bunch length [49]. Small ridges (called notch filters) in the cavity, see Figure 3.2, create a volume resonating at 12 GHz (the CLIC drive beam frequency) that contains the beam induced fields and reflects any stray 12 GHz fields, preventing them from disturbing the signal. Four rectangular slots, arranged in horizontal and vertical pairs, around the mid-point of the cavity are then used to extract the beam induced resonant fields. The fields leaving the cavity are transported in short rectangular waveguides before a transition to a  $50 \Omega$  coaxial cable via an RF feedthrough [50]. The output of the phase monitor cavities is therefore four 12 GHz signals whose time structure depends on the arrival time, or phase, of the drive beam bunches.

The solutions to Maxwell's equations in cavities such as this give a discrete set of transverse electric (TE) and transverse magnetic (TM) modes dependent on the geometry of the cavity [52]. TE modes are characterised by having only transverse electric field components, and no longitudinal electric field component, whereas TM modes have only transverse mag-



Figure 3.2: Schematic of phase monitor design [24].

netic field components and no longitudinal magnetic field component. Each TM and TE mode has an associated cutoff frequency dependent on the number of half-period variations,  $n$  and  $m$ , in the field horizontally and vertically across the cavity respectively. The amplitude of the 12 GHz signals output from the cavity will contain components of each TM and TE mode with a cutoff frequency below 12 GHz. For cylindrical cavities the cutoff frequency of the TM modes are defined as [52]:

$$f_{nm} = \frac{c}{2\pi} \frac{p_{nm}}{a} \quad (3.1)$$

And for the TE modes as:

$$f_{nm} = \frac{c}{2\pi} \frac{p'_{nm}}{a} \quad (3.2)$$

Here  $a$  is the radius of the cavity,  $p_{nm}$  is the  $m^{\text{th}}$  zero of the Bessel function  $J_n(x)$ , and  $p'_{nm}$  is the  $m^{\text{th}}$  zero of the derivative of the Bessel function  $J'_n(x)$  [53]. The beam pipe around the location of the phase monitors at CTF3 is usually 4 cm in diameter, and a cavity of this size would support six separate TM or TE modes with a cutoff frequency below 12 GHz [50]. It is for this reason that the phase monitor diameter was reduced to 23 mm, where only two modes are present: TM01 at 4.98 GHz ( $n = 0$ ,  $m = 1$ ,  $p_{01} = 2.4$ ) and TE11 at 3.74 GHz ( $n = 1$ ,  $m = 1$ ,  $p'_{11} = 1.8$ ).

TM01 is referred to as the monopole mode and TE11 as the dipole mode. The induced field distribution resulting from a bunch entering the cavity for both modes is shown in Figure 3.3. The precise expressions for each field distribution can be found in [54]. When the beam has been correctly setup it should enter the phase monitor cavity close to its centre. For small (horizontal or vertical) offsets between the beam position and the cavity centre there is no dependence of the monopole mode amplitude on the incoming beam position. However, the amplitude of the dipole mode does depend on the beam position, even for small offsets from the cavity centre. This means the amplitude of any of the four individual RF outputs from the monitor will have a position dependence. This property is used in cavity beam position monitors (BPMs) [54], but is undesirable for a phase monitor where the measurement should be position independent. For a 1 mm beam position offset the dipole mode is expected to have around 10% the amplitude of the monopole mode [55].



Figure 3.3: Field distribution of Monopole (TM01) and dipole (TE11) modes in the phase monitor cavities. The dipole mode has both horizontal and vertical components - only the horizontal component is shown.

Monitor	Power
Mon 1	27.6 dBm
Mon 2	29.8 dBm
Mon 3	24.5 dBm

Table 3.1: Power of the phase monitor signals (hybrid sum outputs) measured in the klystron gallery prior to being processed by the phase monitor electronics.

To remove the unwanted dipole mode the horizontal and vertical pairs of outputs from the cavities are combined, as the mode is symmetric and has equal magnitude but opposite sign on each side of the cavity. The CTF3 beam is generally more stable in the vertical plane (the majority of bends in the beam line are horizontal, so energy related orbit jitter resulting from dispersion is larger in the horizontal plane), thus the vertical pair of RF feedthroughs from the monitors are normally used. The two outputs are summed using 180 degree hybrids [55] installed next to the phase monitor cavities in the machine hall. The horizontal pair is also instrumented in the same way but the outputs are typically not used. For an ideal (perfectly symmetric) cavity and hybrid this would create an output with only the position independent monopole mode present. In reality small misalignments, for example in the waveguides and RF feedthroughs, cause slight asymmetries in the cavity and signal combination which leaves a small residual dipole component. The signal combination in the hybrids is expected to reduce the dipole amplitude by a further 20 dB at a 1 mm offset, giving a final amplitude around 1% of the monopole mode [55]. The remaining position dependence of the phase measurement is discussed in Section 3.13.

Figure 3.4 shows the installation of the upstream phase monitors in the CT line. The installation allows up to three phase monitors to be installed neighbouring each other, with the current two monitors installed in the first and third slots leaving approximately a 20 cm gap between the two. The connections between the four RF feedthroughs on the monitors and the hybrids fixed underneath the monitors can be seen in the figure, with the hybrids combining the horizontal pairs visible and two further hybrids placed on the other side of the beam line for the vertical pairs. The outputs from the hybrids are routed up to the klystron gallery on the floor above the accelerator hall, where they are processed and used for the PFF inputs. The complete phase monitor setup including the cables and electronics adds around 50 ns to the overall PFF latency [56]. For reference the power level of the three phase monitor signals as measured once they reach the klystron gallery are quoted in Table 3.1. These are useful to interpret the results of Section 3.6, for example.

## 3.2 Phase Monitor Electronics

The output of the phase monitor cavities (or more precisely the combined output from the hybrids) is a sinusoidal signal with a frequency of  $\omega_{RF} = 11.994$  GHz (the precise CLIC combined drive beam bunch frequency is 11.994 GHz rather than 12 GHz). This can be expressed as follows:

$$RF(t) = A_{RF}(t) \cos[\omega_{RF}t + \phi(t)] \quad (3.3)$$



Figure 3.4: Annotated picture of the two upstream phase monitors installed in the machine.

Where  $A_{RF}(t)$  is the time dependent amplitude (voltage) of the phase monitor signal and  $\phi(t)$  is the time dependent beam phase of interest for the PFF system. The beam based signals from the phase monitors are referred to as the RF signals.

This high frequency signal cannot be digitised directly, so it is multiplied by a similar reference signal to create a lower frequency output that can be digitised, whilst preserving the beam phase information. Mixers are the devices that perform this multiplication. The reference signal is referred to as the local oscillator or LO input, and it is usually a continuous sinusoidal signal with constant amplitude  $A_{LO}$  and frequency  $\omega_{LO}$ :

$$LO(t) = A_{LO} \cos[\omega_{LO} t] \quad (3.4)$$

The multiplication of the RF and LO signals on the mixer creates an output with the following dependence on each input:

$$\text{Mixer}(t) = RF(t) \times LO(t) \quad (3.5)$$

$$\text{Mixer}(t) = A_{RF}(t)A_{LO} \cos[\omega_{RF}t + \phi(t)] \cos[\omega_{LO}t] \quad (3.6)$$

Using trigonometric identities this can be expressed in terms of a high frequency component, with a frequency of  $(\omega_{LO} + \omega_{RF})$ , and a low frequency component, with a frequency of  $(\omega_{LO} - \omega_{RF})$ :

$$\text{Mixer}(t) = \frac{A_{RF}(t)A_{LO}}{2} \{ \cos[(\omega_{LO} + \omega_{RF})t + \phi(t)] + \cos[(\omega_{LO} - \omega_{RF})t + \phi(t)] \} \quad (3.7)$$

The high frequency component can then easily be removed using a low pass filter, so that the mixer output becomes:

$$\text{Mixer}(t) = \frac{A_{RF}(t)A_{LO}}{2} \cos[(\omega_{LO} - \omega_{RF})t + \phi(t)] \quad (3.8)$$

Finally, by using a reference LO signal with the same frequency as the RF signal, which is the case for the phase monitor electronics presented here, this simplifies to:

$$\text{Mixer}(t) = \frac{A_{RF}(t)A_{LO}}{2} \cos[\phi(t)] \quad (3.9)$$

The resulting mixer output is therefore a low frequency signal that depends only on the amplitude of the RF signal and the phase (as well as the constant LO amplitude).

To use the mixer output to calculate the phase, the voltage of the RF signal,  $A_{RF}$ , must be known. This can be determined by splitting the RF signal between the mixer and a diode detector, whose output is dependent on the power of the signal (the square of the voltage):

$$\text{Diode}(t) = A_{RF}(t)^2 \quad (3.10)$$

The phase can then be reconstructed from the mixer and diode outputs as follows:

$$\frac{\text{Mixer}(t)}{\sqrt{\text{Diode}(t)}} = A \cos[\phi(t)] \quad (3.11)$$

$$\phi(t) = \arccos \left[ \frac{\text{Mixer}(t)}{A \sqrt{\text{Diode}(t)}} \right] \quad (3.12)$$

LO	Power
LO 1	22.6 dBm
LO 2	23.6 dBm
LO 3	25.5 dBm

Table 3.2: Power of the LO inputs to the phase monitor electronics.

Where  $A$  is a calibration constant dependent on the relative amplitudes of the mixer and diode outputs. The electronics for the three PFF phase monitors use mixers and diodes as described above to produce signals that are dependent on the phase and amplitude of the output from the phase monitor cavities. Figure 3.5 shows the front panel of one of the sets of the electronics, showing the RF and LO inputs and mixer and diode outputs. The mixer and diode outputs are digitised, with the phase calculation above performed after the digitisation rather than by the phase monitor electronics themselves.

In order to avoid non-linearities and achieve the target resolution (Section 3.3), multiple mixers and diodes are used within each set of electronics. Non-linearities in the response of mixers and diodes are typically worse at higher input powers [57], but higher input powers are desirable to improve the signal to noise ratio of the output. With a single mixer and diode a compromise must therefore be made between the accuracy (linearity) and resolution (noise) of the electronics. To be able to operate the mixers at low power whilst maintaining a good signal to noise ratio eight separate mixers and diodes are used in each set of electronics [57]. The RF and LO inputs are split between the eight mixers and diodes, and then the eight outputs of each type are added together to create the final mixer and diode outputs from the electronics. Figure 3.7 shows a simplified example of this with two mixers and diodes.

Figure 3.7 also shows all the elements present in the generation of the LO reference signal for the electronics. The LO signal for all three sets of electronics is generated from a common 3 GHz source that is locked to the timing of the CTF3 drive beam (which has a 3 GHz acceleration frequency). The 3 GHz signal is split into three to provide the LO input for each set of electronics. After the split each LO chain includes a phase shifter, bandpass filter, frequency multiplier and an amplifier. The phase shifters are required for the calibration process as discussed in Section 3.7. Initially these were 3 GHz digital phase shifters of type [58], but these were later replaced with passive mechanical phase shifters to reduce noise on the LO (Section 3.8). The mechanical shifters are of type [59], and can be changed in units of 0.02 degrees at 4 GHz. After the shifters, a bandpass filter [60] removes any unwanted out of frequency noise in the LO signal, the frequency multiplier [61] increases the frequency of the LO to 11.994 GHz and finally the amplifier [62] is used to boost the power of the LO signals to the level seen in Table 3.2. The LO is designed to have a stability of 5 fs, or 0.02 degrees at 12 GHz [57].

Figure 3.6 shows the complete phase monitor electronics installation in the racks in the klystron gallery.



Figure 3.5: Front panel of the phase monitor electronics boxes containing the mixers and diodes. The connectors labelled LO and RF take the signals from the LO source and the phase monitors respectively. The connectors labelled  $A^2$  and  $A \sin(\phi)$  are the diode and mixer outputs respectively.



Figure 3.6: Annotated picture of the phase monitor electronics rack in the klystron gallery.



Figure 3.7: Simplified schematic of the phase monitor electronics setup. The components involved in the generation of the LO are shown in blue, the phase monitor beam signal in green and the outputs in red. For the purposes of the diagram only two individual mixers and diodes are shown. In the actual design the input signals are split between eight mixers and diodes, and then combined in the same way to create the two outputs. The outputs are digitised on either the FONT5a board or the SiS digitisers.

### 3.3 Resolution Definition

The performance of the PFF system clearly depends on the resolution with which the phase can be measured. Many of the measurements in this chapter are therefore focused on the phase monitor resolution, or more precisely on the resolution of the combined phase monitor and electronics setup. The resolution is defined as the noise between the measured phase and the true beam phase, which can be calculated by comparing the difference between the measured phase of two monitors. This is why two phase monitors, Mon 1 and Mon 2 are installed neighbouring each other in the upstream system in the CT line. The beam phase should be identical in these two monitors thus their measurements can always be compared to derive the resolution.

The precise derivation of the resolution dependent on the measurement of two monitors is as follows. First, the measured phase,  $\phi_x(t)$  and  $\phi_y(t)$ , in two monitors at time  $t$  can be defined as:

$$\phi_x(t) = \phi_b(t) + n_x(t) \quad (3.13)$$

$$\phi_y(t) = \phi_b(t) + n_y(t) \quad (3.14)$$

Here  $\phi_b(t)$  is the true beam phase and  $n_x(t)$  and  $n_y(t)$  is the noise on the measurement at that time. The time dependence will not be written explicitly from this point. These equations assume the beam phase is identical in each monitor, as should be the case for Mon 1 and Mon 2. The variance of each phase monitor measurement can then be derived from the equations above by adding the variance of the beam phase and the noise in quadrature:

$$\sigma_x^2 = \sigma_b^2 + \sigma_{nx}^2 \quad (3.15)$$

$$\sigma_y^2 = \sigma_b^2 + \sigma_{ny}^2 \quad (3.16)$$

Here  $\sigma_x$  and  $\sigma_y$  are the phase jitters measured by each phase monitor,  $\sigma_b$  is the true beam phase jitter and  $\sigma_{nx}$  and  $\sigma_{ny}$  are the phase monitor resolutions. The covariance terms are not considered as it is assumed the beam phase and the noise are uncorrelated. Assuming the magnitude (standard deviation) of the noise,  $\sigma_n$ , is the same for each phase monitor, this can be simplified to  $\sigma_x^2 = \sigma_y^2 = \sigma_b^2 + \sigma_n^2$ .

The quantity of interest for calculating the phase monitor resolution is the jitter in the difference between the two measured phases,  $\sigma_{x-y}$ . The variance of the difference between two correlated variables is defined as:

$$\sigma_{x-y}^2 = \sigma_x^2 + \sigma_y^2 - 2\sigma_x\sigma_y\rho_{xy} \quad (3.17)$$

$$(3.18)$$

Here  $\rho_{xy}$  is the correlation between the phase measurement of  $x$  and  $y$ . Substituting in the previously derived expressions for  $\sigma_x$  and  $\sigma_y$  this becomes:

$$\sigma_{x-y}^2 = 2(\sigma_b^2 + \sigma_n^2)(1 - \rho_{xy}) \quad (3.19)$$

The correlation coefficient  $\rho_{xy}$  depends on the covariance between  $x$  and  $y$ ,  $\text{cov}[x, y]$ , as follows:

$$\rho_{xy} = \frac{\text{cov}[x, y]}{\sigma_x \sigma_y} = \frac{\text{cov}[x, y]}{\sigma_b^2 + \sigma_n^2} \quad (3.20)$$

$$(3.21)$$

Here the covariance is defined as:

$$\text{cov}[x, y] = \frac{1}{N} \sum_{i=1}^N \phi_{xi} \phi_{yi} \quad (3.22)$$

$$(3.23)$$

Substituting in the expressions for  $\phi_x$  and  $\phi_y$  above and separating the terms in the sum then gives the following expression for the covariance of  $x$  and  $y$ :

$$\begin{aligned} \text{cov}[x, y] &= \frac{1}{N} \sum_{i=1}^N (\phi_{bi} + n_{xi})(\phi_{bi} + n_{yi}) \\ \text{cov}[x, y] &= \frac{1}{N} \sum_{i=1}^N \phi_{bi}^2 + \frac{1}{N} \sum_{i=1}^N \phi_{bi} n_{xi} + \frac{1}{N} \sum_{i=1}^N \phi_{bi} n_{yi} + \frac{1}{N} \sum_{i=1}^N n_{xi} n_{yi} \end{aligned} \quad (3.24)$$

The first term is the definition of the variance of the beam phase,  $\sigma_b^2$ . The remaining terms are the covariance between the beam phase and the monitor noises, and the covariance between the two monitor noises. Assuming the noise is uncorrelated all these terms are zero. The remaining equation for the covariance between  $x$  and  $y$  is therefore simply:  $\text{cov}[x, y] = \sigma_b^2$ . Finally, the correlation between the phase measurement of  $x$  and  $y$  becomes:

$$\rho_{xy} = \frac{\sigma_b^2}{\sigma_b^2 + \sigma_n^2} \quad (3.25)$$

Substituting this expression for the correlation in to the derived equation for the variance between the two phase measurements gives the following simple dependence on the phase monitor resolution:

$$\begin{aligned} \sigma_{x-y}^2 &= 2(\sigma_b^2 + \sigma_n^2) \left( 1 - \frac{\sigma_b^2}{\sigma_b^2 + \sigma_n^2} \right) \\ \sigma_{x-y}^2 &= 2\sigma_n^2 \end{aligned} \quad (3.26)$$

Finally, the resolution is defined as:

$$\sigma_n = \frac{\sigma_{x-y}}{\sqrt{2}} \quad (3.27)$$

In terms of a resolution calculation these equations only apply to the two upstream phase monitors, for which the assumption that the beam phase is identical in each monitor (made in Equations 3.13 and 3.14) is valid. All the resolution values quoted in this chapter use this equation and the difference between the measurement of Mon 1 and Mon 2.

However, as the PFF system can also be thought of as subtracting two phases (removing the upstream phase from the downstream phase) the same equations can be directly applied

Digitiser	No. ADCs	Resolution	Input Range	Sampling Rate
SiS 3320	8	12-bit	$\pm 2.5$ V	up to 250 MHz
FONT5a	9	14-bit (13-bit used)	$\pm 0.5$ V	up to 400 MHz

Table 3.3: Specifications of the ADCs on the FONT5a board and SiS digitisers.

to determine the limitations that the phase monitor resolution places on the PFF performance. Equation 3.26 shows that the lowest possible measured corrected downstream phase jitter is a factor  $\sqrt{2}$  times larger than the phase monitor resolution. In order to reduce the measured downstream phase jitter to the CLIC target of  $0.2^\circ$  the phase monitor resolution must therefore be better than  $0.14^\circ$ . Equation 3.25 shows that with this  $0.14^\circ$  resolution and a typical beam phase jitter of  $0.8^\circ$  (Section 4.2) the measured correlation between two phase monitor measurements would be 97%.

## 3.4 Digitisation of Phase Monitor Signals

The mixer and diode outputs from the phase monitor electronics are digitised for the signals to be processed and used for the PFF correction and offline data analysis. Two different types of analogue to digital converters (ADCs) have been used to digitise the phase monitor signals — the Texas Instruments ADS5474 ADCs [63] on the purpose-built FONT5a board used as the PFF controller, and a commercially available SiS 3320 digitiser [64]. The design and use of the FONT5a board is discussed in more detail in Section 5.1. Table 3.3 summarises the specifications of each type of ADC.

The SiS digitisers are used in addition to the FONT5a board as the PFF correction (running on the FONT5a board) is operated as a standalone system independent from other acquisition systems at CTF3. The PFF algorithm requires only the signals from one of the upstream phase monitors to be connected to the FONT5a board, with the convention being to use Mon 1. Mon 2 and Mon 3 are then normally connected to the SiS digitisers instead. The SiS digitisers are setup with the same trigger and sampling frequency (192 MHz) used for other signals at CTF3, and data from them can be acquired together with other devices using the standard systems in place at CTF3. This allows the Mon 2 and Mon 3 signals to be easily compared to other measurements, such as beam position signals, which has been indispensable for optimising the setup of the PFF system and in particular the phase propagation (Chapter 4). The FONT5a board is usually used with an independently sourced 357 MHz clock.

Digitising the phase monitor signals contributes additional noise to the overall phase monitor electronics setup. The purpose of this section is to ensure that the digitiser noise makes only a negligible contribution to the resolution on the phase measurement. The main parameters of interest needed to determine this are the input range and resolution of the ADCs, with the SiS ADCs being 12-bit with a range of  $\pm 2.5$  V and the FONT5a ADCs being 13-bit with an input range of  $\pm 0.5$  V. The full 5 V peak-to-peak input range of the SiS ADCs is therefore split across  $2^{12} = 4096$  values, or ADC ‘counts’, with each count corresponding

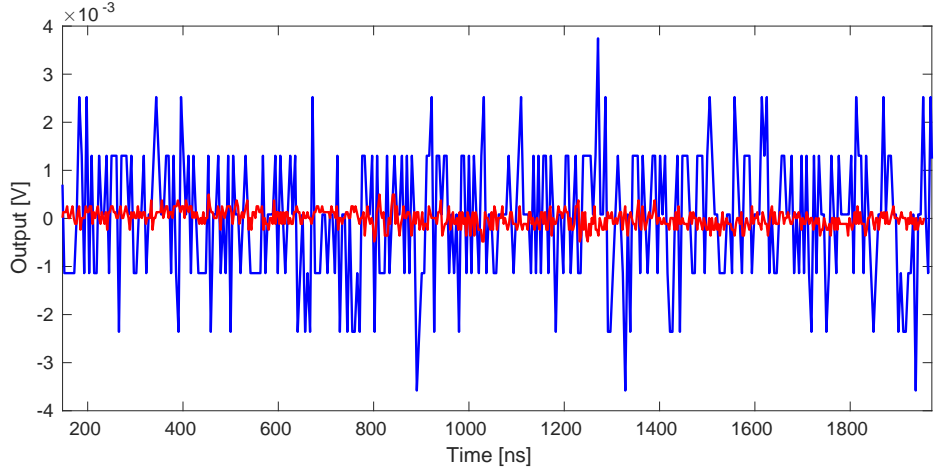


Figure 3.8: Comparison of noise on the output of the SiS (blue) and FONT5a (red) ADCs.

to roughly 1.2 mV. The equivalent 1 V peak-to-peak range and  $2^{13} = 8192$  counts of the FONT5a board corresponds to a factor 10 lower interval of 0.12 mV per ADC count. This already indicates that the FONT5a board should give a much smaller contribution to the phase resolution than the SiS digitisers.

Figure 3.8 shows the ADC noise, converted from counts in to an equivalent voltage, for both the SiS and FONT5a ADCs. As expected the noise on the FONT5a board is much lower than on the SiS digitisers. The actual ADC jitter values are  $1.47 \pm 0.04$  counts or  $0.179 \pm 0.005$  mV on the FONT5a board, and  $1.11 \pm 0.03$  counts or  $1.36 \pm 0.03$  mV on the SiS digitisers. These values can be converted in to an equivalent phase jitter using the phase reconstruction method described later in Section 3.6.5 and the monitor calibration constants determined in Section 3.7. For reference the peak output of the three phase monitor mixers varies between approximately 400 mV and 500 mV, which is well matched to the input range of the FONT5a ADCs. Taking the worst case scenario of Mon 3, which gives the lowest output voltage, the ADC jitter corresponds to  $0.025 \pm 0.001^\circ$  on the FONT5a board but  $0.198 \pm 0.005^\circ$  on the SiS digitisers. These values are summarised in Table 3.4.

As derived in the Section 3.3 the phase resolution must be better than  $0.14^\circ$  in order to achieve a corrected downstream phase jitter of  $0.2^\circ$  with the PFF system. The below  $0.03^\circ$  contribution of ADC noise on the FONT5a board is therefore insignificant compared to the resolution requirements. However, although it does not directly impact the PFF performance the  $0.2^\circ$  ADC jitter on the SiS digitisers would greatly degrade the resolution of the measurements of Mon 2 and Mon 3 usually connected to the SiS digitisers and used for offline data analysis of the PFF results.

The high phase jitter contribution from the SiS digitisers originates from the roughly 500 mV maximum mixer output being much lower than the SiS ADC range of  $\pm 2.5$  V. In order to rectify this the mixer outputs are boosted by roughly a factor 2.5 in voltage using an amplifier prior to the SiS digitisers. The specifications of the amplifier used are documented in [65]. With the amplifier in place the peak signal level sent to the SiS digitisers is around 1 V, and the equivalent phase jitter is reduced to  $0.078 \pm 0.002^\circ$ . This no longer prevents  $0.14^\circ$  resolution from being achieved on measurements using the SiS digitisers, as proven

Digitiser	Jitter [counts]	Jitter [mV]	Phase Jitter [degrees]
FONT5a	$1.47 \pm 0.04$	$0.179 \pm 0.005$	$0.0245 \pm 0.0007$
SiS 3320	$1.11 \pm 0.03$	$1.36 \pm 0.03$	$0.198 \pm 0.005$
SiS 3320 Amplified	$1.11 \pm 0.03$	$1.36 \pm 0.03$	$0.078 \pm 0.002$

Table 3.4: ADC jitter on the FONT5a board, SiS digitisers and with the mixer outputs amplified prior to the SiS digitisers expressed in terms of ADC counts, volts and equivalent phase jitter.

later in Section 3.9. A small further improvement in measured resolution could be achieved using a different amplifier and boosting the peak output voltage closer to 2 V.

### 3.5 Fitting Method

Due to the dependence of the mixer output on  $\cos(\phi)$  as seen in Section 3.2, many of the measurements in this chapter require a sinusoidal fit of the form:

$$y = A \sin(bx + c) + d \quad (3.28)$$

The use of sine rather than cosine makes no difference to the fitted amplitude,  $A$ , and offset,  $d$  which are usually the only parameters of interest in this chapter. It is also convenient to consider a mixer output of zero to correspond to zero phase (rather than  $90^\circ$  as in Equation 3.11). All the fits of this type have been performed using a weighted nonlinear least squares fit implemented in MatLab fitting libraries [66]. Each data point is weighted by the inverse of its standard error squared.

Care must be taken to select suitable initial values for the four parameters in the fit in order to avoid local minima and ensure a reasonable fit. This is particularly important for a sinusoidal fit as there are many solutions with different frequencies and phase offsets that can match the data. The frequency,  $b$ , is the most critical parameter but usually this is already known, being defined by the properties of the phase monitors and electronics, for example. Initial values for the three remaining parameters are estimated as follows:

$$A = \frac{\max(y) - \min(y)}{2} \quad (3.29)$$

$$d = \frac{\max(y) + \min(y)}{2} \quad (3.30)$$

$$c = \arcsin\left(\frac{y - d}{A}\right) - bx \quad (3.31)$$

The amplitude,  $A$ , and offset,  $d$ , of the sine curve are simply estimated by comparing the minimum and maximum output. These initial values are therefore highly biased by any large outliers around the minimum and maximum output, but this is rarely the case for the application here and these simple estimators are sufficient. Rearranging Equation 3.28 gives the expression for  $c$  above. Due to its use of arcsin the equation is only valid in the first and fourth quadrants, between  $-\pi/2$  and  $+\pi/2$  where the gradient of the sine curve is positive.

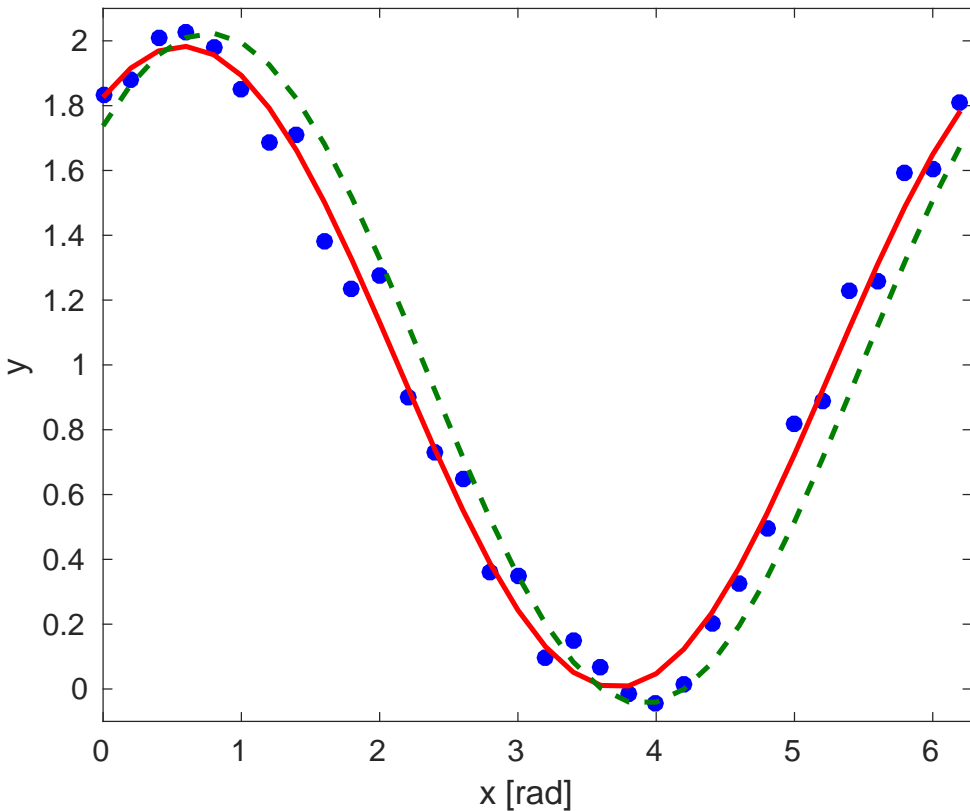


Figure 3.9: Example sine fit (red) to generated data with added random noise (blue markers). The dashed green line shows the initial conditions used for the fit with estimated values for the four fit parameters.  $x$  and  $y$  are defined as in Equation 3.28

The  $y$  value at each data point is compared to its neighbours to determine whether it is on the rising slope, in order to meet this criteria. The initial value of  $c$  is the mean value calculated across all the data points that meet this criteria.

Figure 3.9 and Table 3.5 show the results of an example fit using this approach. An initial distribution of points with  $y = \sin(x + 1) + 1$  is used ( $A = b = c = d = 1$ ), with random noise added. An approximate value for  $b$  is assumed to be known (from the phase monitor electronics specifications, as described), thus  $b = 1$  is directly used as its initial estimated value. The initial estimates for  $A$  and  $d$  are within a few percent of their true value. The initial estimate for  $c$  is within 20% of the correct value. After fitting all four parameters are in agreement with the expected values.

## 3.6 Characterisation of Phase Monitor Electronics

Measurements have been made using a 12 GHz signal generator to determine the performance of the three sets of phase monitor electronics independently from the phase monitors themselves. In particular, these tests were focused on identifying the saturation and cross-talk characteristics of the output mixer and diode signals in order to determine a suitable

Parameter	Value	Initial	Fit
$A$	1	1.03	$0.99 \pm 0.02$
$b$	1	1	$1.00 \pm 0.02$
$c$	1	0.81	$1.00 \pm 0.06$
$d$	1	0.99	$0.99 \pm 0.02$

Table 3.5: Initial estimates and final fitted values for the four sinusoidal fit parameters for a distribution generated with  $A = b = c = d = 1$  (plus random noise).

input power range to use during normal operation.

### 3.6.1 Experimental Setup

Two changes were made to the setup shown in Figure 3.7 for these tests. Firstly, a 12 GHz sinusoidal output from an RF signal generator is used as the RF input for the mixers, replacing the beam induced phase monitor signals. The signal generator output is amplified, allowing the input power to the mixers to be varied in a wide range between 0 and 33dBm, or between 0.2 and 10.0 V in terms of voltage. This range encompasses the input power usually provided by the phase monitor signals (Table 3.1). The precise power output to the mixer is verified between each measurement using a power meter.

Secondly, the diode outputs were amplified during these tests (using the same amplifier introduced in Section 3.4) by a factor 10 in voltage to reduce digitiser noise in the measurement. The non-amplified peak diode output corresponds to 170 mV, rather than the 1.7 V seen in the plots in this section. The  $\pm 500$  mV mixer outputs have not been amplified. Usually the mixer output is amplified and the diode not amplified, as in Figure 3.7.

There are some differences between the properties of the generated signal and the beam signal that would be used in normal operation. Firstly, unlike the pulsed beam signal the used generated signal is continuous. It has been verified that the response of the mixers is equivalent for both the continuous and pulsed signals, at least in terms of output power and saturation levels [67]. The cross-talk properties are difficult to characterise with beam based measurements alone, but assumed to be similar.

Secondly, the phase of the generated signal does not vary with time, compared to the beam signal which has a large phase sag of around  $40^\circ$  along the pulse and much larger phase jitter. If the signal generator was used at the same frequency as the beam and LO signals, 11.994 GHz, the mixer output would therefore be constant as it depends only on the static phase of the signal generator as per Equation 3.9. Instead, a generated signal with a slightly lower frequency of 11.991 GHz has been used. From Equation 3.8 it can be seen that in this case the mixer output voltage is sinusoidal, with a frequency equal to the frequency difference between the LO and RF inputs, or  $11.994 - 11.991$  GHz = 3 MHz, with the setup used here. This has the benefit of being able to see the response of the electronics to all input phases in one measurement, rather than having to take multiple measurements varying the LO phase shifter between each one.

### 3.6.2 Results

Figures 3.10–3.15 show the mixer and diode outputs for all three sets of electronics at each of the input power levels from the signal generator. All mixer outputs show a sinusoidal oscillation with a frequency of 3 MHz, or around 60 samples at the sampling frequency of 192 MHz, as expected. An oscillation with the same frequency is also visible on the diode outputs, with the largest amplitude for the 2nd set of electronics. This is the first hint of the non-ideal characteristics of the electronics. Finally, the output of the mixer and diode increases with the input power, as expected. At high input powers the outputs begin to saturate. The characteristics of the mixers are discussed in Section 3.6.3 and the diodes in Section 3.6.4.

### 3.6.3 Mixer Performance

#### Sinusoidal Characteristics

Figure 3.16 shows fits to the response of all mixer outputs at an input power of 27 dBm, close to the typical input power from the beam signals. The phase offset (displacement in peaks) between the output of each mixer holds no significance for the electronics performance. This is set only by the relative phase between the signal generator and the LO at the time the measurement was started. For normal operation with beam the LO phase shifters are changed to match the phasing of each set of electronics (Section 3.7).

The reconstruction of the phase from the mixer output depends on the mixer output being sinusoidal. In particular the maximum mixer output is critical due to the dependence on the amplitude in Equation 3.12. Each set of electronics has a different output amplitude due to slight differences in the LO power for each set of electronics and between the individual components used. At an input power of 27 dBm Mixer 1 has a higher peak output of 510 mV, compared to 410 mV and 380 mV for Mixer 2 and Mixer 3 respectively.

Overall, the agreement between the actual mixer output and the sinusoidal fits at this input power is good. However, there is some distortion away from the ideal sine curve that is most visible around the maximum and minimum mixer output. Figure 3.17 shows the residuals between the mixer outputs and the sine fits for the full mixer output range (from minimum to maximum, or equivalently phase offsets between  $\pm 90^\circ$ ). In the figure, the plotted residual is the difference between the fit and the data expressed in terms of an equivalent phase offset,  $\Delta\phi$ , using:

$$\Delta\phi(t) = \arcsin\left(\frac{V_{MIXER}(t) - V_{FIT}(t)}{A}\right) \quad (3.32)$$

Here  $V_{MIXER}(t)$  and  $V_{FIT}(t)$  are the mixer voltage and fitted voltage at sample  $t$  respectively, and  $A$  is the fitted mixer amplitude. On the falling slope between the peaks there is only a slight deviation about the ideal sinusoidal behaviour. The deviation from ideal is at the level of  $0.25 \pm 0.03^\circ$  and  $0.30 \pm 0.04^\circ$  for the first and third mixers, with a slightly larger effect of  $0.45 \pm 0.04^\circ$  for the second mixer. This applies within  $\pm 80^\circ$  of the zero crossing in

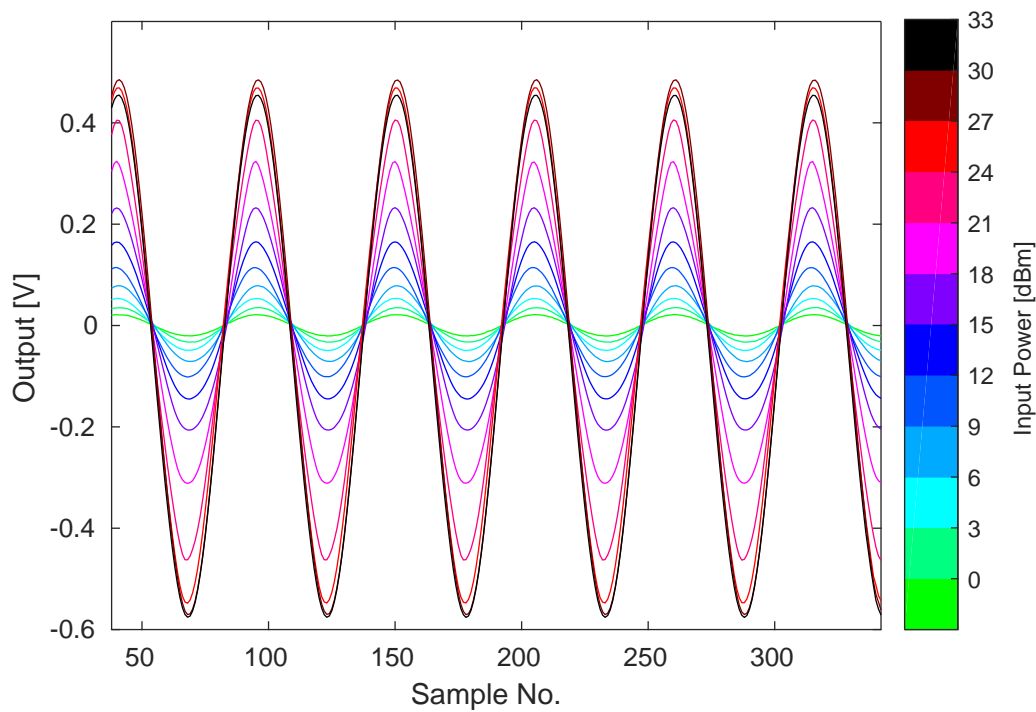


Figure 3.10: Response of Mixer 1 to signal generator input.

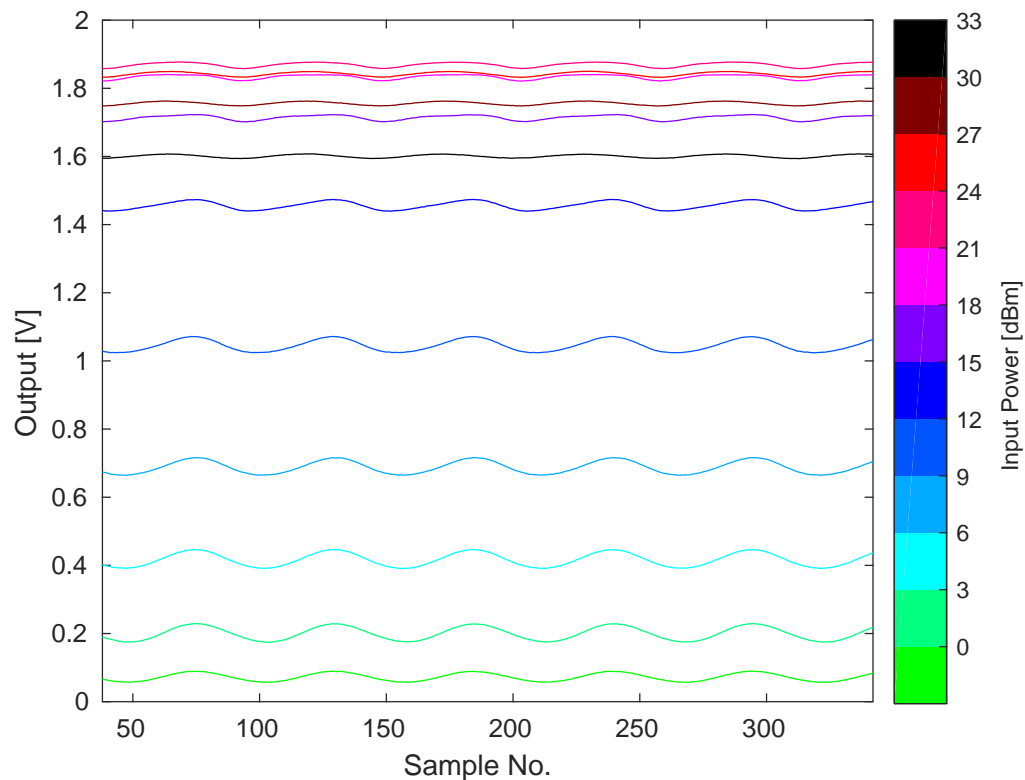


Figure 3.11: Response of Diode 1 to signal generator input.

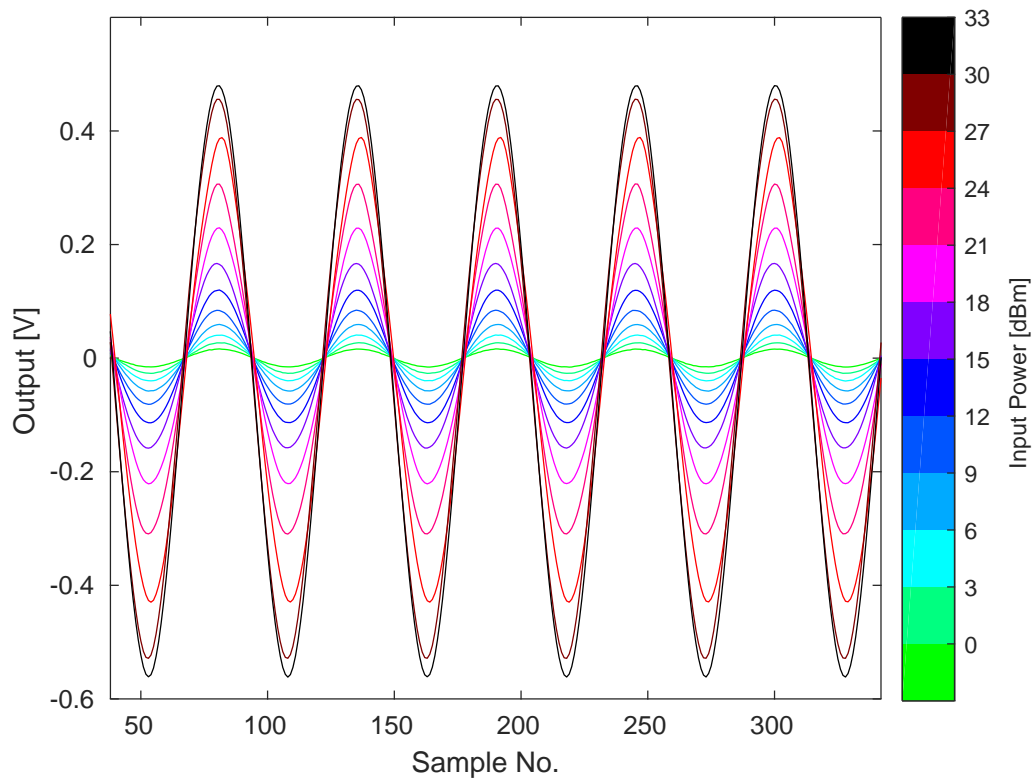


Figure 3.12: Response of Mixer 2 to signal generator input.



Figure 3.13: Response of Diode 2 to signal generator input.



Figure 3.14: Response of Mixer 3 to signal generator input.



Figure 3.15: Response of Diode 3 to signal generator input.

the mixer output. Outside this range, close to the maximum or minimum mixer output, the deviation from the sine fit rapidly increases, reaching several degrees for each mixer. For operation with the beam this means that the accuracy of the phase measurement cannot be guaranteed when the LO phase is set so that the mixer is giving close to its maximum or minimum output. This is also true for other reasons, as seen in Section 3.9. The PFF system can only correct small offsets at the level of around  $\pm 5^\circ$  (Section 5.3.1), so the non-ideal response close to peak output is not an issue for the PFF performance.

However, for input powers in the range from 15–21 dBm the non-ideal characteristics of the mixers are larger. One example of this is shown in Figure 3.18, at an input power of 18 dBm. If input powers in this range are used calibrations of the mixer response should normally be restricted to around the zero crossing so that the fitted amplitude gives the best approximation to the true behaviour for small phase offsets.

### Dependence on Input Power

The mixer output is expected to depend linearly on the input voltage, and the diode on the square of the input voltage. Both these dependences must hold in order to use Equation 3.12 and obtain a phase measurement that does not depend on the input voltage to the electronics (therefore making the calculated phase insensitive to any possible variations in power along the pulse from the beam signal, for example). For these measurements the input voltage can be calculated using the known input power and  $50\ \Omega$  impedance of the electronics.

Figure 3.19 shows the dependence of the mixer output amplitudes on the input voltage. As seen previously the first mixer gives a larger output than the other two mixers. The 2nd and 3rd mixers give a similar response up to an input voltage of 3.5 V (24 dBm). Linear fits to the mixer outputs restricted to the range between 0.45 V and 1.75 V (6 dBm to 18 dBm) are also shown in the figure. All three mixers give a linear response up to an input voltage of around 3 V (23 dBm), after which the effects of saturation begin to appear. At an input voltage of 5 V (27 dBm) the first and third mixers are almost fully saturated with almost no remaining power dependence in the output. The second mixer begins to enter saturation at the same voltage as the other two mixers but retains a strong power dependence up to a higher input voltage of 7 V (30 dBm).

### Asymmetry in Output

One final interesting property of the mixers is that the output is not symmetric about zero, in other words the maximum output voltage is different to the absolute value of the minimum output voltage. This is perhaps most visible looking back to the Mixer 1 output at all power levels in Figure 3.10, where the maximum output is around  $+0.45\ V$  but the minimum output is around  $-0.55\ V$ .

Figure 3.20 shows how the mixer amplitude at maximum and minimum output varies with the input voltage. The asymmetry is largest for Mixer 1 and smallest for Mixer 3. The effect appears to increase in magnitude with the input voltage, with approximately a

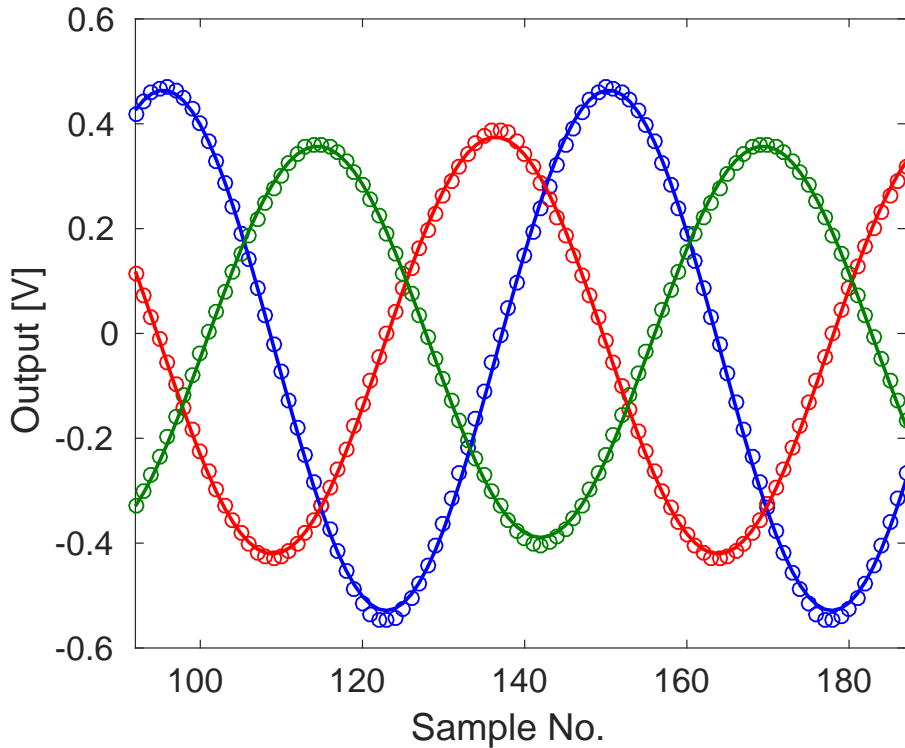


Figure 3.16: Sinusoidal fit to mixer responses at 27 dBm input power. Blue: Mixer 1, Red: Mixer 2 and Green: Mixer 3. Markers show the data points and the lines are sinusoidal fits to the data.

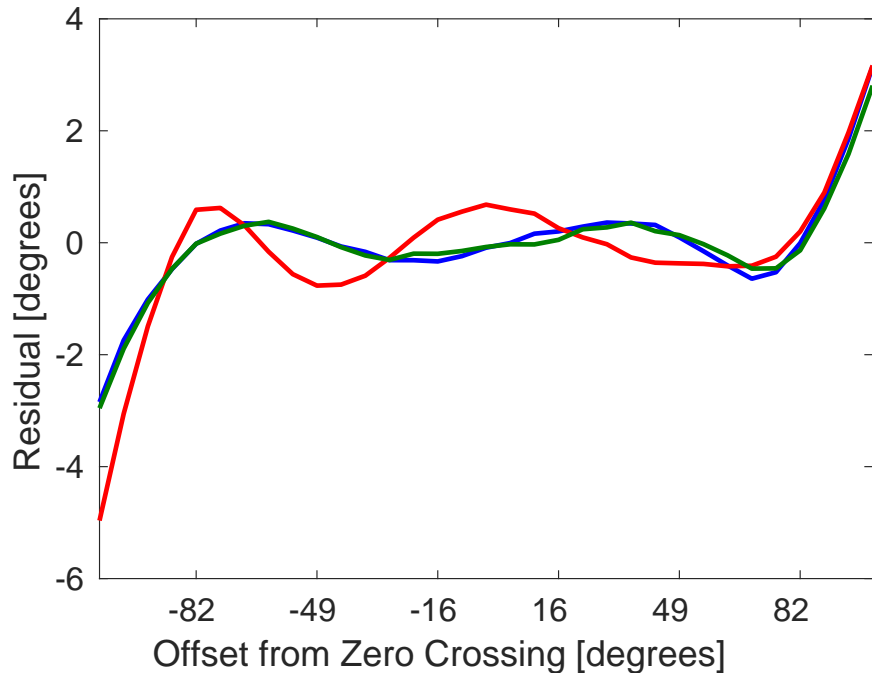


Figure 3.17: Residuals to sinusoidal fit at 27dBm. Blue: Mixer 1, Red: Mixer 2 and Green: Mixer 3. Markers show the data points and the lines are sinusoidal fits to the data.

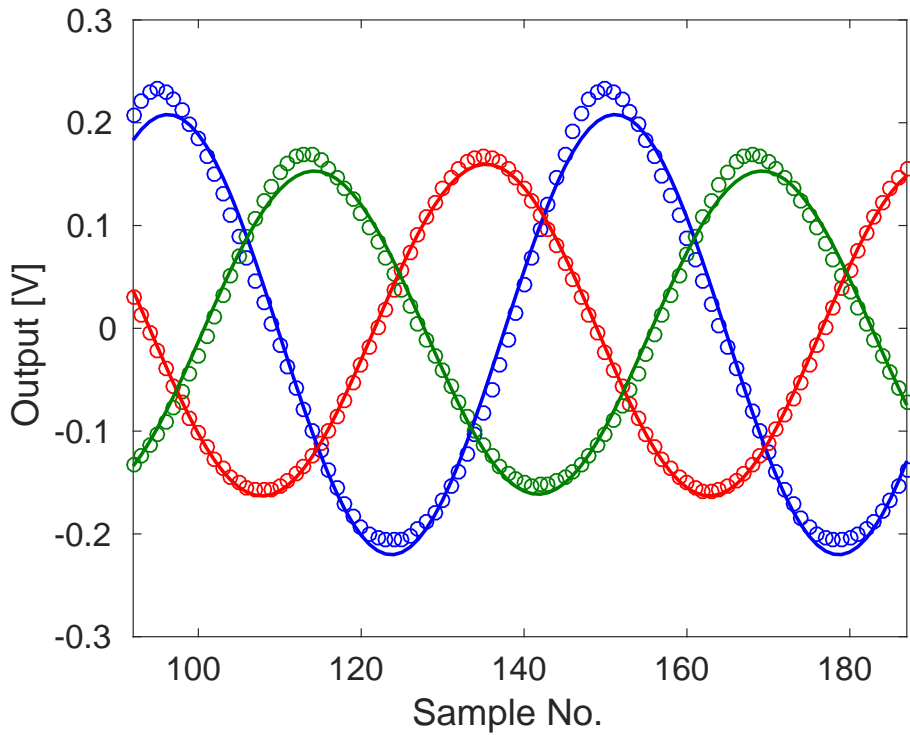


Figure 3.18: Sinusoidal fit to mixer responses at 18 dBm input power. Blue: Mixer 1, Red: Mixer 2 and Green: Mixer 3.



Figure 3.19: Linear fit (dashed lines) to the mixer output voltage vs. the input voltage (solid lines with markers). Blue: Mixer 1, Red: Mixer 2 and Green: Mixer 3. The linear fit is restricted to the region marked by vertical black lines.

100 mV asymmetry on Mixer 1 at an input of 10 V, but only several mV at low input powers. For each mixer the amplitude at maximum output is larger for input voltages up to 2.5 V (21 dBm). Above 2.5 V input voltage this flips, with the minimum mixer amplitude being larger than the maximum amplitude.

For input voltages between 0.45 V and 1.25 V (6 dBm to 15 dBm) the mixer asymmetry has an approximate quadratic dependence on the input voltage, as shown in Figure 3.21. Outside this range there is no simple relationship that can explain the dependence of the asymmetry on the input voltage. One explanation for the asymmetry in the mixer outputs is cross-talk coming from the diode signals. Above 15 dBm the diodes enter saturation, as discussed in Section 3.6.4, which may explain why the quadratic fit to the mixer asymmetry is only valid at power levels up to this value.

Taking the power dependent asymmetry into account the actual mixer response can be modified from Equation 3.9 to become:

$$\text{Mixer}(t) = m_1 A(t) \sin[\phi(t)] + m_2 A(t)^2 + m_3 A(t) + m_4 \quad (3.33)$$

Here  $A(t)$  is the input voltage at time  $t$ , and  $m_1$ ,  $m_2$ ,  $m_3$ , and  $m_4$  are calibration constants needed to describe the power dependence.

### 3.6.4 Diode Performance

#### Dependence on Input Power

The dependence of the three diode outputs on the input power is shown in Figure 3.22. The square root of the diode output is plotted, as the output voltage is expected to vary linearly with input power. It is immediately apparent that the diode signals saturate at much lower input voltages than the mixer signals. All three diodes are almost fully saturated at an input of 2 V (20 dBm), with the effects of saturation already beginning to appear above 1.25 V (15 dBm). Figure 3.23 shows a linear fit to the square root of the diode, using the range of input voltages between 0.45 V and 1.25 V (6–15 dBm). Even below saturation the response of  $\text{sqrt}(\text{Diode})$  is not well approximated by a linear dependence as desired. However, in the range from 0.30 V to 1.25 V (3 dBm to 15 dBm) a quadratic fit to the diode output directly (not  $\text{sqrt}(\text{Diode})$ ) does give a good approximation to the true dependence of the diodes on the input voltage. This is shown in Figure 3.24.

#### Cross-Talk

As seen previously in Figures 3.11, 3.13 and 3.15 the diode outputs show a sinusoidal oscillation. In the same way that there is cross-talk from the diode on the mixer outputs, there will also be cross-talk from the mixers on the diode outputs. Figure 3.25 shows a sinusoidal fit to the cross-talk on Diode 1 at an input power of 6 dBm. It has the same characteristics as the mixer output, including the slight distortion away from ideal sinusoidal behaviour around the peaks. However, as the diodes enter saturation the oscillation is initially distorted, and



Figure 3.20: Mixer maximum output voltage (dashed lines with upward triangle markers) and minimum output voltage (dashed lines with downward triangle markers) vs. the input voltage. Solid lines with circular markers show the average of the minimum and maximum. Blue: Mixer 1, Red: Mixer 2 and Green: Mixer 3.

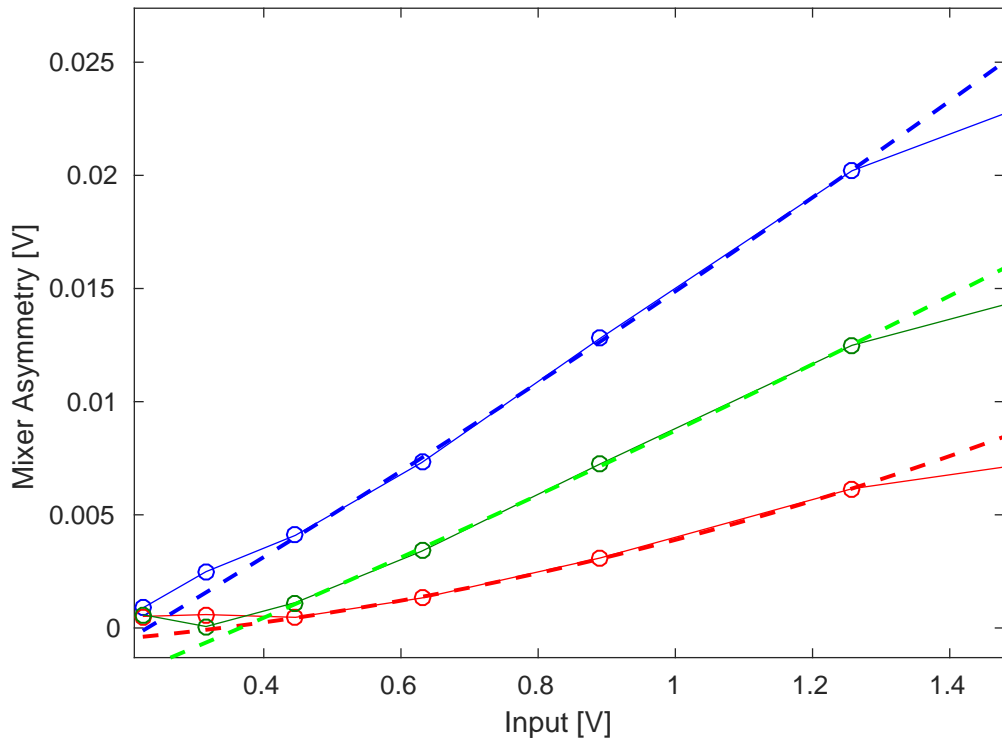


Figure 3.21: Relative amplitude of cross-talk on the mixer from the diode vs. the input voltage. Blue: Mixer 1, Red: Mixer 2 and Green: Mixer 3. Lines with circular markers are the measured data, and dashed lines quadratic fits to the data.

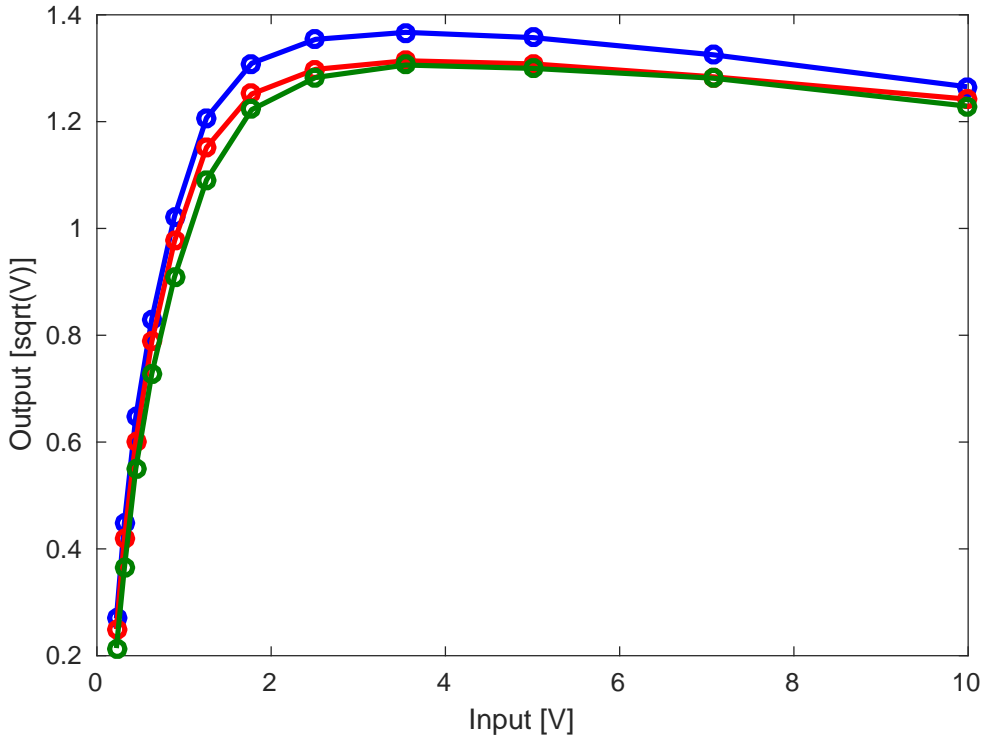


Figure 3.22: Square root of the diode output vs. the input voltage. Blue: Diode 1, Red: Diode 2 and Green: Diode 3.

then has a much smaller amplitude when the diode output is fully saturated. One example of this is shown for the Diode 1 output at 18 dBm in Figure 3.26. The peaks around the maximum output are clearly non-sinusoidal in this case.

Figure 3.27 shows the dependence of the relative amplitude of the cross-talk on the input power. The relative amplitude of the cross-talk is the fitted amplitude of the sinusoidal oscillation on the diode divided by the mean diode output. Up until the diode outputs are fully saturated the relative amplitude of the cross-talk is around a factor two larger for the second diode. For example, at an input power of 12 dBm the relative cross-talk is at around the level of 30% for the second diode, or 15% for the first and third diode outputs. Up to input powers of 15 dBm the relative cross-talk is always above 10%.

Finally, Figure 3.28 compares the oscillation on the diode to the oscillation on the mixer. It can be seen that there is a phase shift between the two, which adds a further complication to the necessary phase reconstruction method. Taking in to account the actual characteristics of the diodes, including the cross-talk and quadratic dependence on the input power, the expected expression for the diode output from Equation 3.10 can be modified to:

$$\text{Diode}(t) = d_1 A(t)^2 + d_2 A(t) + d_3 + d_4 A(t) \sin[\phi(t) + \delta] \quad (3.34)$$

Here  $d_1, d_2, d_3$  are calibration constants describing the actual power dependence of the diode output, and  $d_4$  and  $\delta$  are calibration constants describing the cross-talk from the mixer.

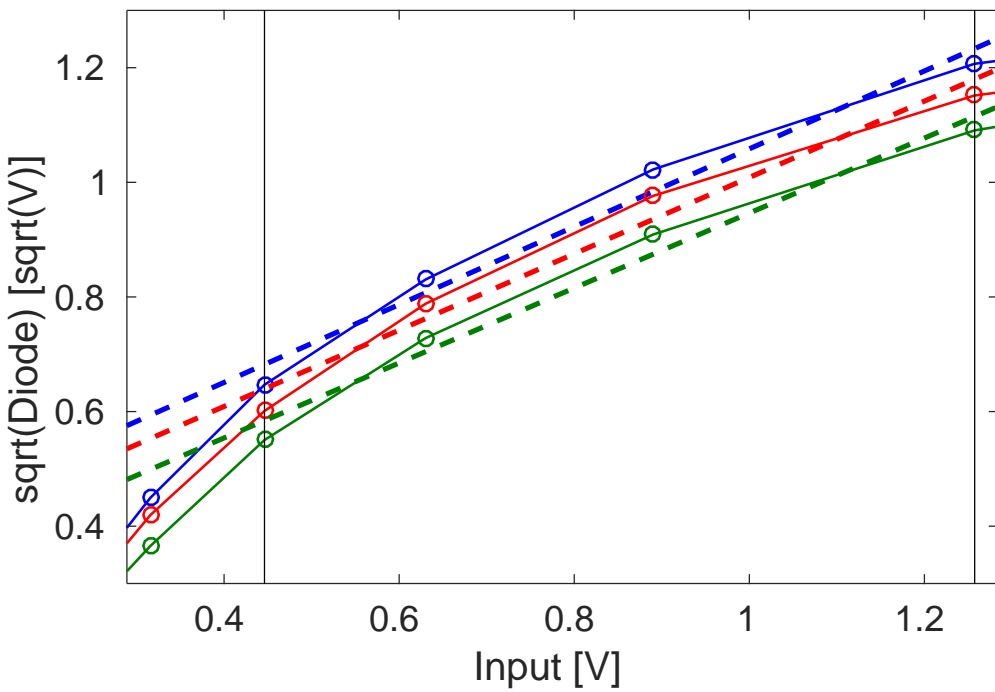


Figure 3.23: Linear fits (dashed lines) to the square root of the diode output (solid lines with circular markers) vs. the input voltage. The fits are restricted to the region marked by vertical black lines. Blue: Diode 1, Red: Diode 2 and Green: Diode 3.

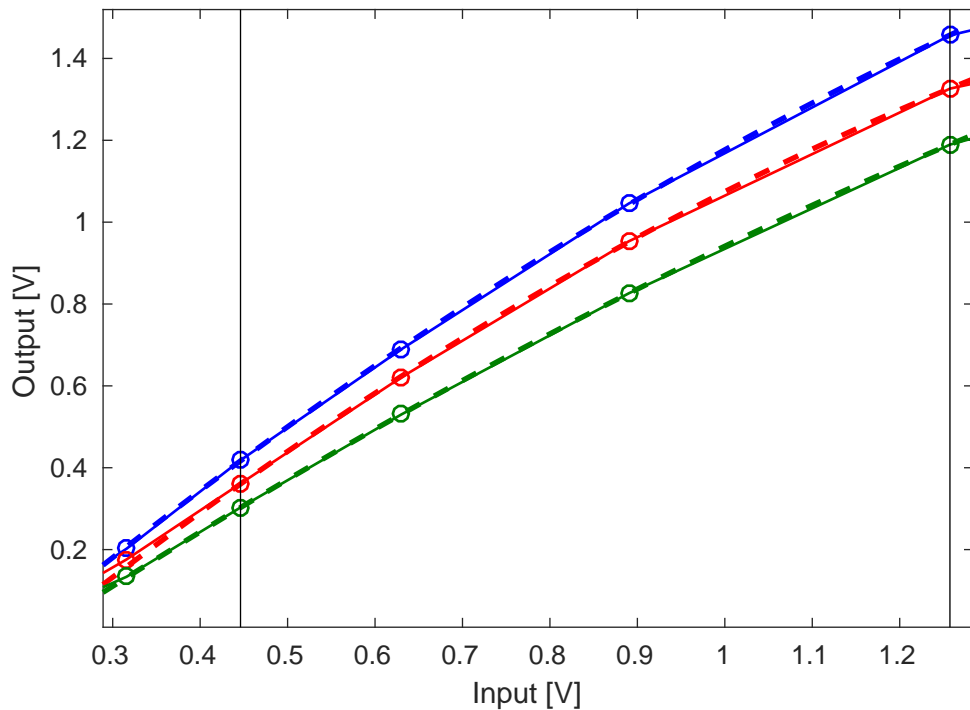


Figure 3.24: Quadratic fits (dashed lines) to the diode output (solid lines with circular markers) vs. the input voltage. The fits are restricted to the region marked by vertical black lines. Blue: Diode 1, Red: Diode 2 and Green: Diode 3.



Figure 3.25: Sinusoidal fit (black line) to cross-talk on Diode 1 at 6 dBm input power (blue markers).

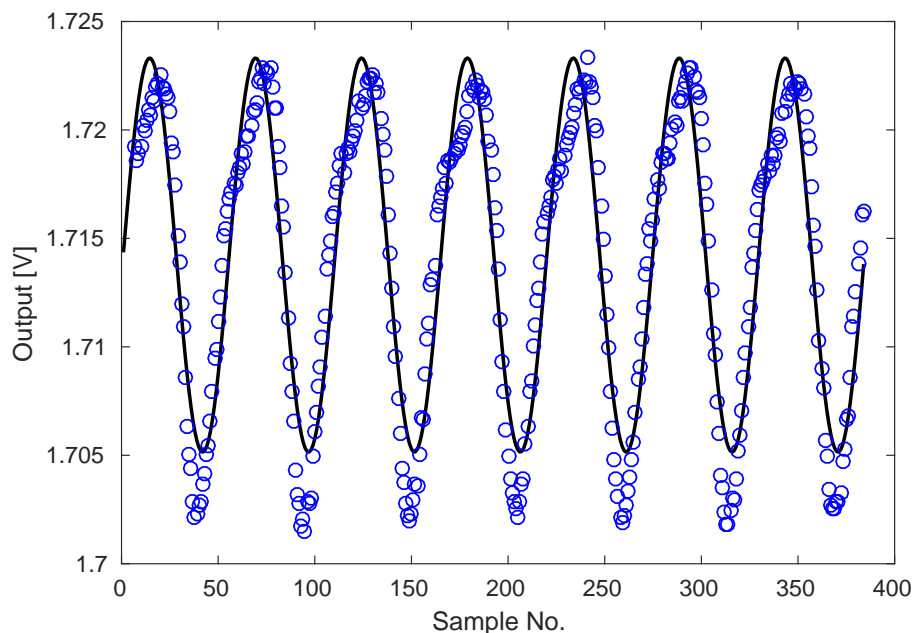


Figure 3.26: Sinusoidal fit (black line) to cross-talk on Diode 1 at 18 dBm input power (blue markers).



Figure 3.27: Dependence of the relative amplitude of cross-talk on the diode versus the input power. Blue: Diode 1, Red: Diode 2 and Green: Diode 3.



Figure 3.28: Comparison of the oscillation on Mixer 1 (red) and Diode 1 (blue), showing a relative phase offset between the two.

### 3.6.5 Consequences for Routine Operation

The results of the signal generator tests have several consequences for the setup of the electronics and phase reconstruction during normal operation with the beam induced signals from the phase monitors. Firstly, in order to maximise the signal to noise ratio and yield the best possible resolution on the phase measurement the highest possible input power below saturation should normally be used. The degradation of the phase resolution with the input power is seen for beam based measurements in Section 3.9.3. However, the diodes begin to enter saturation much earlier than the mixers, at around 15 dBm rather than 23 dBm. This means that in order to be able to use the diode measurement as part of the phase reconstruction the input power would have to be limited to below 15 dBm, 8 dBm lower than would be ideal for the mixer performance. There is no way to use different input powers for the mixers and diodes without a complete redesign of the electronics.

Secondly, the modifications that the cross-talk on the mixer and diode make in Equations 3.33 and 3.34 above makes the needed calculation to reconstruct the phase much more complex than the ideal case using  $\text{Mixer}/\sqrt{\text{Diode}}$  in Equation 3.12. In particular, the dependence of the diode output on  $\sin(\phi + \delta)$  means there is no simple expression that can be derived to create an input power independent phase measurement. An iterative process would have to be used to estimate the phase instead, converging towards the true diode output without cross-talk after each iteration using the estimated phase value. This may be possible in offline data analysis but would be difficult to implement in the PFF algorithm whilst still meeting latency requirements.

Due to these reasons, and with no possibility to make modifications to the electronics, the decision was eventually taken to not include the diode measurement in the phase reconstruction process. For operation with the beam this means making the assumption that the output power from the phase monitors is constant along the pulse, and that the jitter in the output power is small. This is a good approximation, as seen later in Section 3.7.3. To reduce the sensitivity to any slow drifts in the output power due to changes in the beam conditions calibrations are taken at regular intervals between measurements, as discussed in Section 3.7).

With this treatment of the electronics, the phase is reconstructed as follows:

$$\text{Mixer}(t) = A \sin[\phi(t)] + d \quad (3.35)$$

$$\phi(t) = \arcsin\left(\frac{\text{Mixer}(t) - d}{A}\right) \quad (3.36)$$

Two calibration constants are needed –  $A$  and  $d$ .  $A$  is the fitted amplitude of the sinusoidal mixer output, and  $d$  is the asymmetry or offset between the maximum and minimum mixer output. This is a simplified form of Equation 3.33 given the assumption that the power is constant. In reality both  $A$  and  $d$  have a power dependence.

As any variations in input power are not removed by this method there is a benefit to operating the mixer in a region where the power dependence of the output is reduced. The best phase resolution achieved to date has been achieved with input powers to the electronics in the range between 24.5 dBm and 27 dBm. Operating in this range also has the benefit

of reducing the deviation from ideal sinusoidal behaviour at lower input powers as seen in Section 3.6.3.

The remainder of this chapter presents the performance of the complete phase monitor and electronics system for normal operation with the beam. All the beam based measurements in the remainder of this chapter and the rest of the thesis use the phase reconstruction approach described here. Although the diodes are no longer directly used as part of the phase measurement they are still useful for the purposes of the time alignment of signals and for monitoring whether there have been any large changes in input power. The PFF firmware on the FONT5a feedforward controller has also been changed to add the option to not include the diode in the correction calculation (Section 5.1.1).

## 3.7 Calibrations

The first step in using the phase monitor measurements is to calibrate the mixer outputs. Calibrations of the phase monitor signals are typically taken on a daily basis during data taking periods, as well as additional calibrations when there have been any changes in beam conditions or to the setup of the electronics. These are needed to determine the calibration constants, amplitude and offset, required to calculate the phase from the mixer output (Equation 3.36). This section presents typical calibration results for all three phase monitors and discusses aspects such as the stability of the calibration along the pulse and determining the optimal set point for the LO phase shifters.

Calibrations are performed using the LO phase shifters. By varying the LO phase shifter the phase between the LO and the beam signal is changed. During a calibration the phase shifters are moved through  $360^\circ$  at 12 GHz so that the response of the mixer to all phase offsets between the beam and LO can be determined. Normally calibrations are taken at 12 shifter settings across the full  $360^\circ$  range, with 10 pulses acquired at each setting and the whole scan taking approximately 10 minutes. These choices are a compromise between having enough points for a good quality fit whilst reducing the possibility of large drifts in beam phase during the scan which would degrade the fit results. All the calibrations presented use the electronics setup with the mechanical LO phase shifters in place (see Section 3.8). The settings on these phase shifters approximately correspond to degrees at 4 GHz, thus a phase shifter change of 120 units corresponds to  $360^\circ$  at 12 GHz.

A calibration using both the SiS digitiser and FONT5a setup will be shown. During operation of the PFF system Mon 1 is usually connected to the FONT5a board as the correction input, whilst Mon 2 and Mon 3 are connected to the SiS digitisers where they can be acquired together with other signals at CTF3. The difference in measured output voltage between the two systems results from the use of an amplifier before the SiS digitisers to reduce noise in that setup (Section 3.4). Also, when using the FONT5a board the mixer outputs are attenuated by 1 dB to avoid saturating the FONT ADCs. The calibration constants from Mon 1 on the FONT5a board are needed for the PFF gain calculation in Section 5.1.1. Measurements of the upstream and downstream phase following this chapter use Mon 2 and Mon 3 on the SiS digitisers and their respective calibration constants, unless

Monitor	$A$ (amplitude)	$d$ (offset)
Mon 1	$1167 \pm 10$ mV	$86 \pm 9$ mV
Mon 2	$1064 \pm 6$ mV	$69 \pm 7$ mV
Mon 3	$990 \pm 12$ mV	$150 \pm 10$ mV

Table 3.6: Fit parameters from the calibration at sample 605 on the SiS digitisers for each monitor.

indicated otherwise.

### 3.7.1 Calibration on SiS Digitisers

Figures 3.29–3.31 show the mixer output as a function of time for all phase shifter settings in an LO scan, for each phase monitor respectively. Away from the minimum and maximum output each mixer shows the expected phase sag along the beam pulse resulting from the RF pulse compression used at CTF3 [19]. The shape of the phase sag as seen on the mixer changes sign depending on whether the LO phase places the mixer on the rising or falling slope of its sinusoidal output. Usually the mixers are operated on the falling slope where the measured phase sag is ‘u’-shaped, rather than ‘n’-shaped, as this is also the convention for other phase dependent signals at CTF3 [45].

Near the minimum or maximum mixer amplitude the beam phase sag causes a much smaller variation in the mixer output voltage along the pulse. The phase resolution close to the peaks in the mixer output is therefore greatly reduced, as seen in Section 3.9.3. LO phase scans are used to not only calculate the calibration constants but also to determine the phase shifter settings that zero the mixer output, where the resolution is maximal. This process is documented in Section 3.7.4.

The noisier appearance of the output on Mon 3 is not an effect of the phase monitors or phase monitor electronics but is rather caused by real differences between the beam phase upstream (Mon 1, Mon 2) and downstream (Mon 3). Reducing the differences between the upstream and downstream phase is the focus of Chapter 4.

Figure 3.32 shows the result of fitting the mixer output versus the phase shifter setting at sample 605 (see Figures 3.29–3.31). The mixer response is sinusoidal as expected and as seen previously in the signal generator tests. In the signal generator tests there was some visible distortion away from the sinusoidal fit around the peaks at some input power levels (Section 3.6.3). There is no visible effect for the input power of the phase monitor signals (Table 3.1). Differences in the peak output of each monitor are expected due to differences in the input power from each phase monitor as well as differences between the sets of electronics. Small offsets between the data and the fit at some shifter settings are caused by drifts in the beam phase during the scan (particularly for Mon 3 where the beam is less stable), as well as human error in setting the shifter values.

The fitted values of the mixer amplitude,  $A$ , and offset,  $d$ , are found in Table 3.6. These values are used to calculate the beam phase as per Equation 3.36.



Figure 3.29: Mon 1 mixer output along the pulse for each LO phase shifter setting during the calibration.



Figure 3.30: Mon 2 mixer output along the pulse for each LO phase shifter setting during the calibration.



Figure 3.31: Mon 3 mixer output along the pulse for each LO phase shifter setting during the calibration.



Figure 3.32: Fits (solid lines) to the mixer output for each phase monitor (markers) vs. the LO phase shifter setting. The data shown is for sample 605 on the SiS digitisers. Blue: Mon 1, Red: Mon 2 and Green: Mon 3.

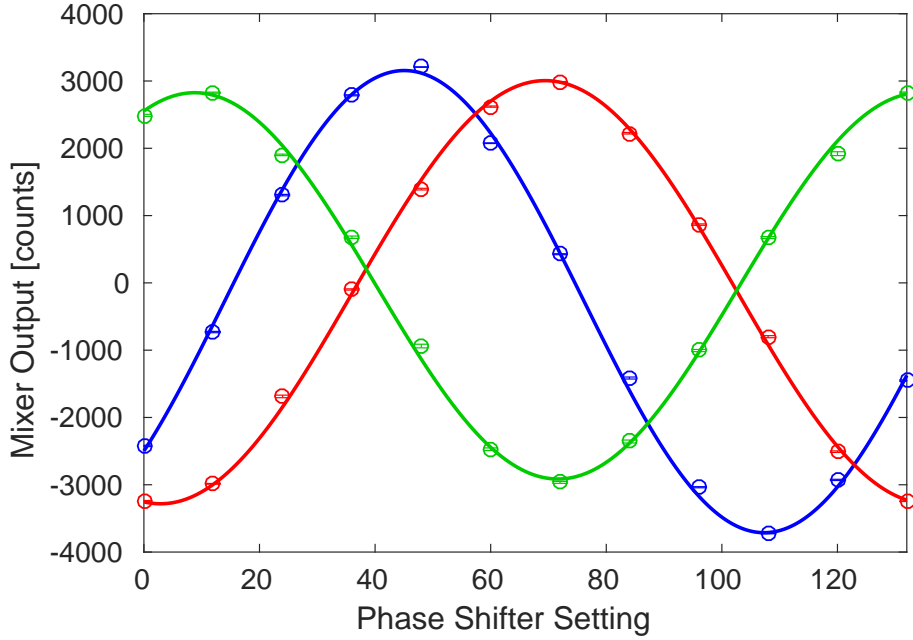


Figure 3.33: Results of a calibration performed on the FONT5a board. Solid lines are sinusoidal fits to the data (markers). Blue: Mon 1, Red: Mon 2 and Green: Mon 3.

### 3.7.2 Calibration on FONT5a Board

Figure 3.33 and Table 3.7 show the results of a calibration performed in exactly the same way but on the FONT5a board. The FONT5a board ADCs flip the sign of the input [68], so a positive ADC output in counts corresponds to a negative input voltage and vice-versa. This explains the inverted polarity of the resulting sine curves on the FONT5a board in Figure 3.33, compared to the SiS digitisers in Figure 3.32. For operation of the PFF system this difference must be taken in to account either by operating the mixer on the rising slope as seen on the FONT5a board (which in reality is the falling slope, as desired), or alternatively by using negative gain values for the correction output. The fitted values for  $d$  in Table 3.7 are also negative rather than positive as a result of this sign flip. Apart from these differences the overall shape of the mixer output follows the sinusoidal dependence as expected.

The FONT5a ADC outputs are 13-bit, or  $\pm 4096$  counts, with an input range of  $\pm 500$  mV (Section 5.1). The fitted Mon 1 output, with 1 dB attenuation added after the mixer, of between -3712 counts and +3156 counts therefore corresponds to an input voltage range of between +453 mV and -385 mV. Without the attenuator, which reduces the voltage by roughly 10%, the Mon 1 mixer would saturate the ADC at its peak output. As the contribution of digitiser noise is small on the FONT5a board (Section 3.4) a 1 dB attenuator is also added to the Mon 2 and Mon 3 outputs so that the overall setup for each monitor is the same in this measurement. However, during normal operation of the PFF system Mon 2 and Mon 3 are connected to the SiS digitisers, with their mixer outputs then being amplified rather than attenuated.

Monitor	$A$ (amplitude)	$d$ (offset)
Mon 1	$3434 \pm 41$ counts	$-278 \pm 34$ counts
Mon 2	$3144 \pm 16$ counts	$-138 \pm 17$ counts
Mon 3	$2870 \pm 43$ counts	$-44 \pm 44$ counts

Table 3.7: Fit parameters from the calibration for each monitor on the FONT5a board.

### 3.7.3 Variations in Calibration Constants Along the Pulse

The calibration results on both the SiS digitisers and FONT5a board have been presented at one sample number around the middle of the pulse close to where the phase sag along the pulse is flattest. In this section the variation in the fitted calibration constants along the pulse is discussed. This is particularly important after taking the decision to not use the diodes, as the intended purpose of using the diodes was to normalise the mixer response to give an output independent of the input power. Without using the diodes any variations in input power along the pulse will also create differences in the calibration constants along the pulse.

The current implementation of the PFF algorithm on the FONT5a board uses the mixer multiplied by a single gain value that is constant along the full pulse length to create the correction output (Section 5.1.1). It therefore cannot take in to account any variations in calibration constants along the pulse. Offline data analysis is usually performed in the same way so that the quoted resolutions are representative of the values that apply to the implementation of the PFF correction. The effect of taking in to account the variations in calibration parameters along the pulse seen here is shown in Section 3.12.

Figures 3.34 and 3.35 show the variation in the fitted calibration amplitude and offset across the full pulse length, using the same calibration on the SiS digitisers presented in Section 3.7.1. Differences in both the amplitude and offset along the pulse are visible. These are summarised in Table 3.8 in terms of the standard deviation of the fitted parameter values along the pulse.

The stability of the fitted amplitude along the pulse is similar for the upstream monitors (Mon 1 and Mon 2), with a variation of around 8 mV in both cases. As the downstream beam is less stable than the upstream beam the variations in fitted amplitude along the pulse are larger for Mon 3, at the 15 mV level. In terms of a relative difference these values correspond to roughly a 0.7% variation in fitted amplitude for Mon 1 and Mon 2, or 1.5% for Mon 3. With further optimisation of the downstream beam, as documented in Chapter 4, it should be possible to achieve similar Mon 3 amplitude stability to that seen for Mon 1 and Mon 2.

Absolute stability in the fitted offset along the pulse is similar to that of the amplitude but therefore much larger as a relative difference at the level of several percent. The variation in fitted offset along the pulse is smallest for Mon 2 at around 3 mV. For both Mon 1 and Mon 3 the variation is around a factor two larger, at 6 mV.

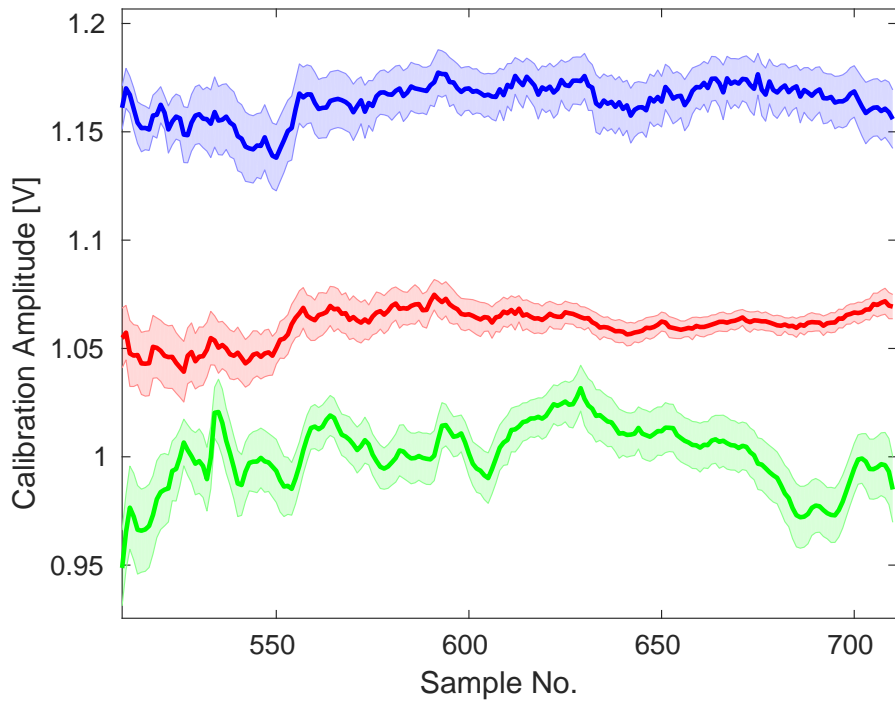


Figure 3.34: Variation in fitted amplitude along the pulse for each phase monitor. Blue: Mon 1, Red: Mon 2 and Green: Mon 3.

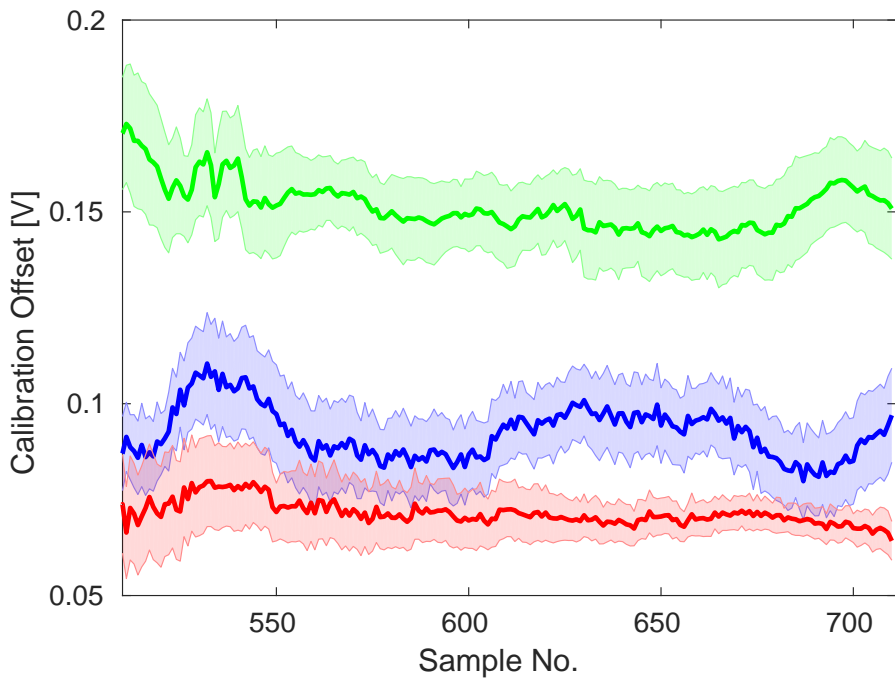


Figure 3.35: Variation in fitted offset along the pulse for each phase monitor. Blue: Mon 1, Red: Mon 2 and Green: Mon 3.

Monitor	$A$ (amplitude)	$d$ (offset)
Mon 1	$8.3 \pm 0.4$ mV	$6.7 \pm 0.3$ mV
Mon 2	$7.7 \pm 0.4$ mV	$3.0 \pm 0.3$ mV
Mon 3	$14.7 \pm 0.7$ mV	$6.1 \pm 0.3$ mV

Table 3.8: Standard deviation in calibration fit parameters along the pulse.

### 3.7.4 Zero Crossing

The full fit to the calibration result that is performed is:

$$\text{Mixer} = A \sin(bx + c) + d \quad (3.37)$$

Here  $x$  is the phase shifter setting.  $A$  and  $d$  are the calibration constants used to reconstruct the phase, with their values already quoted in Table 3.6. The remaining fit parameters  $b$  and  $c$  convert the phase shifter setting in to the phase offset between the LO and the beam. As the shifter readings are approximately in 4 GHz degrees, the expected value for  $b$  that converts the shifter value in to 12 GHz radians is  $(12/4) * (\pi/180) \simeq 50$  mrad/unit.

To obtain the best resolution for the measurement the mixers should be operated where the dependence of the output voltage on the phase is maximal. This means maximising the partial derivative of the mixer output with respect to the phase shifter setting:

$$\frac{\partial \text{Mixer}}{\partial x} = Ab \cos(bx + c) \quad (3.38)$$

This is maximised when  $bx + c = n\pi$ , where  $n$  is any positive or negative integer. The optimal phase shifter settings therefore meet this criteria:

$$x = \frac{n\pi - c}{b} \quad (3.39)$$

And with this phase shifter set point the mixer output is  $\text{Mixer} = A \sin(n\pi) + d = d$ . In the case where there is no offset between the minimum and maximum mixer output ( $d = 0$ ) the optimal point to operate the mixers is at zero output. Because of this the optimal shifter setting will be referred to as the zero crossing. In reality the small asymmetry in the mixer output means the optimal shifter setting is where mixer output is  $d$ . The effect of operating the mixers away from the zero crossing on the resolution is shown in Section 3.9.3.

In addition, as previously mentioned the convention is to operate the mixers on the falling slope where the partial derivative in Equation 3.38 is negative. The phase shifter settings are obtained using the smallest positive integer  $n$  that leads to this criteria being met. Table 3.9 shows an example of values for the fit parameters  $b$  and  $c$  and the calculated phase shifter settings to be on the zero crossing for each monitor. These values are taken from the same calibration and sample number presented in Section 3.7.1 (on the SiS digitisers). In Figure 3.32 it can be seen that the calculated phase shifter settings for the zero crossing are close to zero mixer output for each phase monitor.

Due to the large phase sag along the beam pulse it is clearly not possible to be at the zero crossing of the mixer for the full pulse length. For the PFF system the region of interest

Monitor	$b$	$c$	Zero Crossing
Mon 1	$50.8 \pm 0.5$ mrad/unit	$2.29 \pm 0.04$ rad	$16.7 \pm 0.9$ units
Mon 2	$47.4 \pm 0.5$ mrad/unit	$1.36 \pm 0.04$ rad	$37.5 \pm 0.8$ units
Mon 3	$51.3 \pm 0.6$ mrad/unit	$4.02 \pm 0.04$ rad	$105.5 \pm 1.5$ units

Table 3.9: Phase shifter setting to obtain the zero crossing for each mixer output and the fit parameters needed to calculate them.

is the central portion of the pulse where the phase sag is flattest. The shifters are therefore set to zero the mixer output in this region, giving best resolution in the central part of the pulse but slightly degraded resolution near the start and end of the pulse. In addition to this, slow drifts in the beam phase, particularly downstream, mean that the shifters must routinely be changed to stay at the zero crossing. With the current setup using mechanical phase shifters this must be done by hand, with no possibility to implement an automatic feedback on the shifter settings, for example.

## 3.8 Phase Shifter Noise

In the first tests with all three phase monitors in their final positions at CTF3 the measured phase resolution was far in excess of the  $0.14^\circ$  derived to be necessary to achieve a  $0.2^\circ$  corrected downstream phase jitter in Section 3.3. Figure 3.36 shows a typical example of the measured resolution along the pulse at that time with an achieved resolution of around  $0.4^\circ$ , three times larger than required. The lowest downstream phase jitter that could be achieved with the PFF system in these conditions is above  $0.55^\circ$ , only about 30% smaller than the initial upstream phase jitter at CTF3 (Chapter 4). To be able to achieve a large reduction in downstream phase jitter with the PFF prototype the source of the poor phase monitor resolution had to be identified and removed.

The first hint towards identifying the cause of the degraded resolution came by comparing the measured phase jitter from Mon 1 and Mon 2, with one example shown in Figure 3.37. Note that for all the results in this section it is not the absolute value of the phase jitter (which depends mostly on the beam conditions in that dataset) that is important but rather the difference between the measured phase jitter in each monitor. The measured phase jitter along the pulse in Mon 2 with a mean of  $1.38 \pm 0.01^\circ$  is 1.7 times larger than the  $0.83 \pm 0.01^\circ$  phase jitter in Mon 1. Jitter values from this and all the other datasets presented in this section are shown in Table 3.10. As Mon 1 and Mon 2 are neighbouring each other in the beam line the actual phase jitter in the two should be close to identical.

The overall phase monitor and electronics setup can be roughly split in to three parts – the RF signal from the beam (dependent on the phase monitors themselves and the hybrids), the LO reference signal and the mixers. An issue with any one of these parts could explain the larger phase jitter measured from Mon 2 (usually connected to Mixer 2 and LO 2) compared to the phase jitter from Mon 1 (usually connected to Mixer 1 and LO 1). To determine whether the issue was with the RF signal of one of the monitors measurements

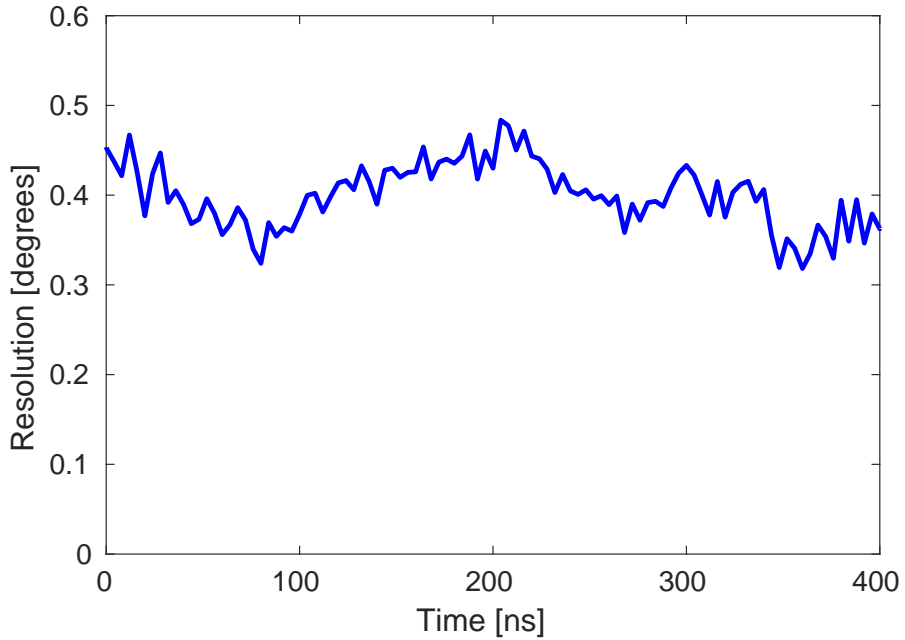


Figure 3.36: Phase monitor resolution for the initial setup using digital phase shifters in the phase monitor electronics.

were taken with Mon 1 and Mon 2 swapped between the three mixers.

Figure 3.38 shows the measured phase jitter along the pulse when Mon 2 is moved on to Mixer 1 (and LO 1) and with Mon 1 moved on to Mixer 2 (and LO 2). The colours in all the plots in this section correspond to the mixer used in the measurement – blue for Mixer 1, red for Mixer 2 and green for Mixer 3. With the phase monitors swapped the higher measured phase jitter stays with Mixer 2 with the same ratio of 1.7, in this case  $1.48 \pm 0.01^\circ$  on Mixer 2 (connected to Mon 1) and  $0.89 \pm 0.01^\circ$  on Mixer 1 (connected to Mon 2). This rules out that the difference in phase jitter is coming from the phase monitors themselves, and suggests the problem is with either Mixer 2 or the reference signal LO 2 for that mixer. The same exercise can then be repeated with Mon 2 moved on to Mixer 3 (and LO 3) and the nominal setup used for Mon 1. Mixer 3 gives similar results to Mixer 2, with 1.7 times larger phase jitter than Mixer 1. This is seen in Figure 3.39. The remaining task is therefore to identify whether the additional source of noise is from Mixer 2 or LO 2, and from Mixer 3 or LO 3.

This was determined by swapping the LO reference signals between the mixers. Figure 3.40 shows the measured phase jitter with LO 2 connected to Mixer 1, and LO 1 connected to Mixer 2. In this case the lower measured phase jitter stays with LO 1, with  $1.10 \pm 0.01^\circ$  jitter on Mixer 2 (with LO 1) and  $1.68 \pm 0.01^\circ$  on Mixer 1 (with LO 2). In Figure 3.41 the same is seen with LO 3 connected to Mixer 1, and LO 1 connected to Mixer 3, with the lower phase jitter coming from Mixer 3 (LO 1) in this case. In Table 3.10 it can also be seen that the lowest phase jitter in every dataset always comes from the phase monitor for which LO 1 was used.

In this way an issue with LO 2 and LO 3 was identified. The generation of the LO reference signals (Section 3.2) consists of a 3 GHz source that is common to all three signals,



Figure 3.37: Phase jitter along the pulse with the nominal electronics setup – Mon 1 connected to the first mixer, and Mon 2 connected to the second mixer. Blue: Mon 1, Mixer 1 and LO 1. Red: Mon 2, Mixer 2 and LO 2.



Figure 3.38: Phase jitter along pulse with Mon 2 connected to the first mixer (blue) and Mon 1 connected to the second mixer (red).



Figure 3.39: Phase jitter along pulse with Mon 1 connected to the first mixer and Mon 2 connected to the third mixer. Blue: Mon 1, Mixer 1 and LO 1. Green: Mon 2, Mixer 3 and LO 3.

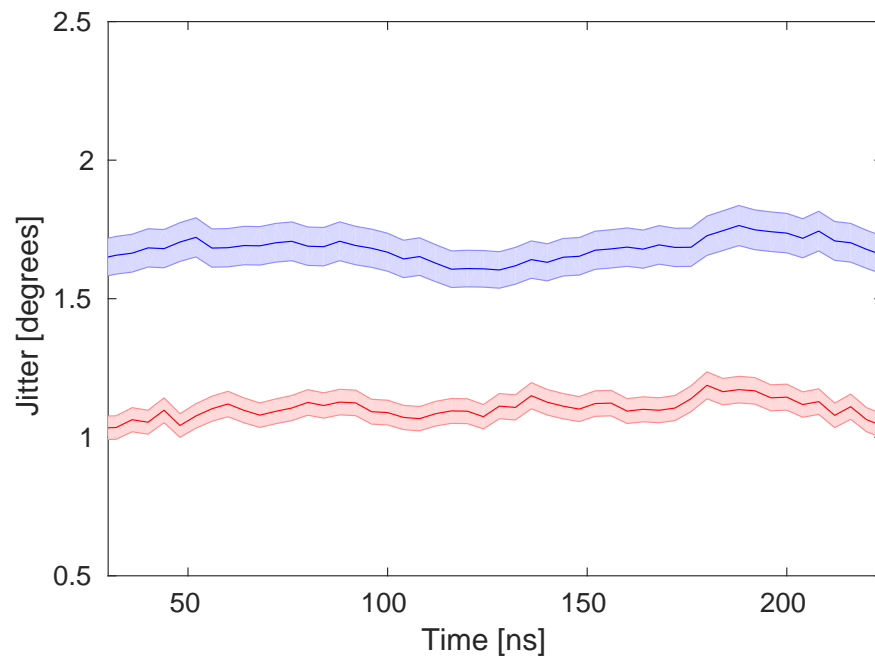


Figure 3.40: Phase jitter along pulse with the LO swapped between the first mixer and the second mixer. Blue: Mon 1, Mixer 1 and LO 2. Red: Mon 1, Mixer 2 and LO 1.

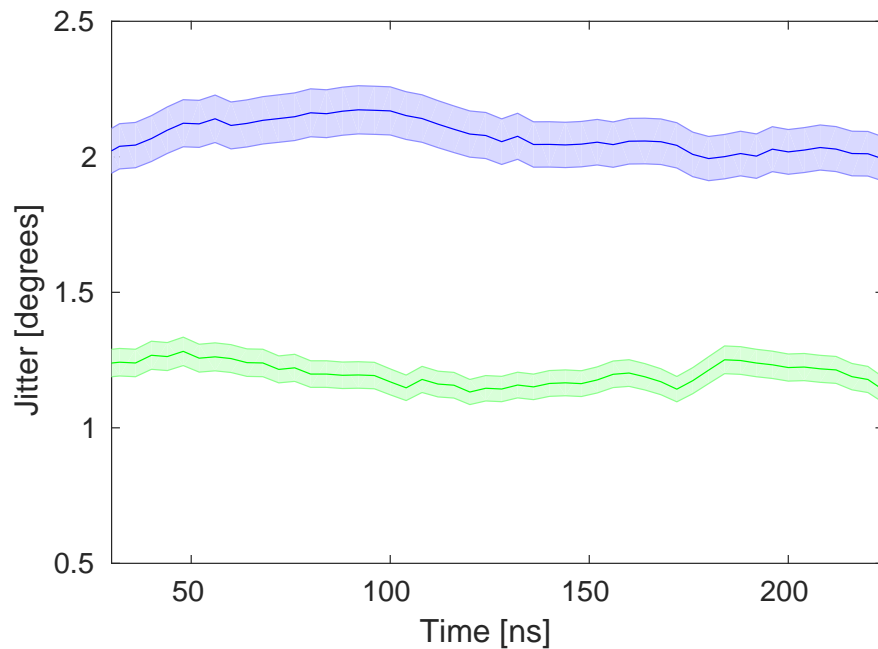


Figure 3.41: Phase jitter along pulse with the LO swapped between the third mixer and the first mixer. Blue: Mon 1, Mixer 1 and LO 3. Green: Mon 2, Mixer 3 and LO 1.

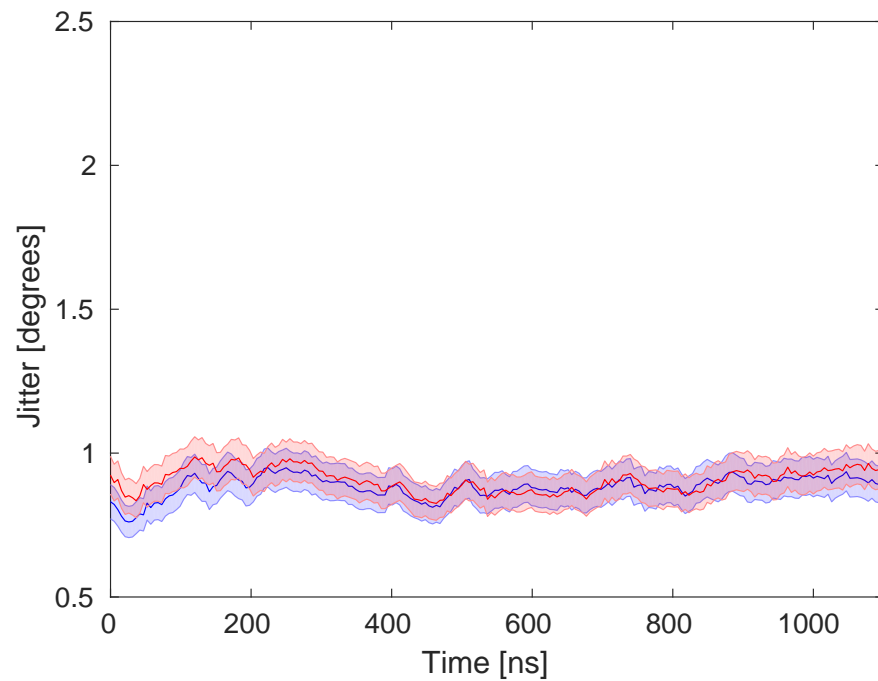


Figure 3.42: Phase jitter along pulse after installation of the mechanical phase shifters. Blue: Mon 1, Mixer 1 and LO 1. Red: Mon 2, Mixer 2 and LO 2.

Mon 1			Mon 2		
Mixer	LO	Jitter	Mixer	LO	Jitter
1	<b>1</b>	<b><math>0.83 \pm 0.01^\circ</math></b>	2	2	$1.38 \pm 0.01^\circ$
2	2	$1.48 \pm 0.02^\circ$	1	<b>1</b>	<b><math>0.89 \pm 0.01^\circ</math></b>
1	<b>1</b>	<b><math>1.15 \pm 0.01^\circ</math></b>	3	3	$1.91 \pm 0.01^\circ$
1	2	$1.68 \pm 0.01^\circ$	2	<b>1</b>	<b><math>1.10 \pm 0.01^\circ</math></b>
1	3	$2.07 \pm 0.01^\circ$	3	<b>1</b>	<b><math>1.20 \pm 0.01^\circ</math></b>

Table 3.10: Comparison of phase jitter along the pulse for each measurement with different setups of the electronics. Each row corresponds to the results of one dataset. The left hand side of the table shows the results from Mon 1 in that dataset, and the right hand side of the table the results from Mon 2. Bold text indicates the lower jitter value in that dataset, all of which use LO 1.

plus separate phase shifters, frequency multipliers (to create the 12 GHz reference) and amplifiers for each LO signal. The digital phase shifters were thought to be the most likely culprit to be adding noise in to the system, and preliminary tests replacing one of the digital phase shifters with a mechanical alternative provided an immediate improvement in resolution. Finally, all three digital shifters were replaced with mechanical phase shifters (the specifications of the shifters were introduced in Section 3.2). With this setup the measured phase jitter for Mon 1 and Mon 2 is the same irrespective of which mixer or LO the signal is connected to, as shown in Figure 3.42. The final achieved resolution is presented in Section 3.9.

## 3.9 Resolution Measurements

This section presents resolution measurements with the mechanical phase shifters in place and the same overall electronics setup that was used to achieve the best PFF results in Chapter 6. All measurements use the upstream phase monitors Mon 1 and Mon 2. Although there is no way to directly verify the resolution of the downstream phase monitor Mon 3 in-situ, an upper limit can be placed based on the achieved correlations between the measured upstream and downstream phase. The achieved phase propagation in Chapter 4 with  $0.74^\circ$  measured downstream phase jitter and 93% upstream-downstream phase correlation suggest the Mon 3 resolution must be better than  $0.2^\circ$  using Equation 3.25.

### 3.9.1 Best Resolution

Figure 3.43 shows the best phase resolution that has been achieved to date sample by sample along the pulse. Each point corresponds to the phase jitter in the difference between the measured Mon 1 and Mon 2 phase divided by the square-root of two as per Equation 3.27. The resolution is quite stable along the pulse, with a mean value of  $0.126 \pm 0.001^\circ$ . This is below the  $0.14^\circ$  needed to be able to theoretically achieve a  $0.2^\circ$  correction with the PFF prototype, as derived in Section 3.3. The achieved resolution corresponds to a theoretical

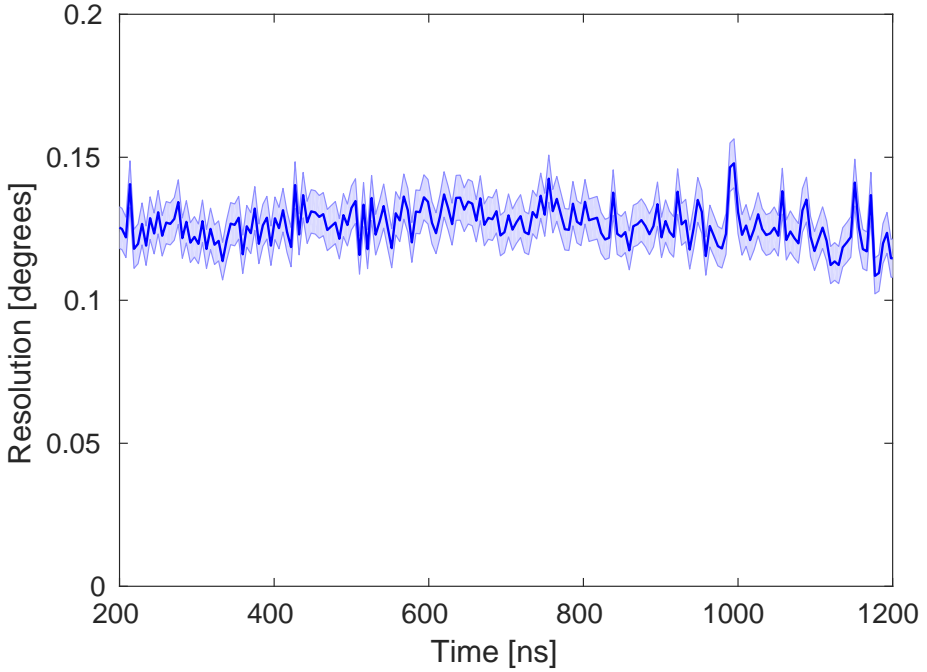


Figure 3.43: Best achieved phase monitor resolution measured point by point along the pulse (sampled at 192 MHz on the SiS digitisers).

limit of around  $0.18^\circ$  in the corrected downstream phase jitter.

### 3.9.2 With Sample Averaging

The phase monitor signals are digitised with a much higher sampling rate, 357 MHz on the FONT5a board or 192 MHz on the SiS digitisers, than the targeted PFF correction bandwidth of 30 MHz. This means the results from several samples could be averaged to reduce noise on the measurement whilst maintaining the same correction bandwidth. For example, for a measurement on the SiS digitisers, such as those shown here, 5 samples can be averaged to effectively create a signal with 38.4 MHz sampling rate, reduced from the initial 192 MHz. The effect of doing this is shown in Figure 3.44. The resolution is decreased from  $0.126 \pm 0.001^\circ$  as seen previously to  $0.108 \pm 0.001^\circ$  with 5 samples averaged. Currently the phase propagation (Chapter 4) is the main limiting factor for the PFF performance rather than the phase monitor resolution. However, it would be possible to implement sample averaging in the PFF firmware on the FONT5a board if deemed necessary for future tests [68].

### 3.9.3 Dependence of Resolution on LO Phase

The process of setting the mixers at their zero crossing after calibrations was documented in Section 3.7.4. This is necessary to operate the mixers where their output voltage is most sensitive to variations in the phase (close to the peaks of the mixer output there is negligible

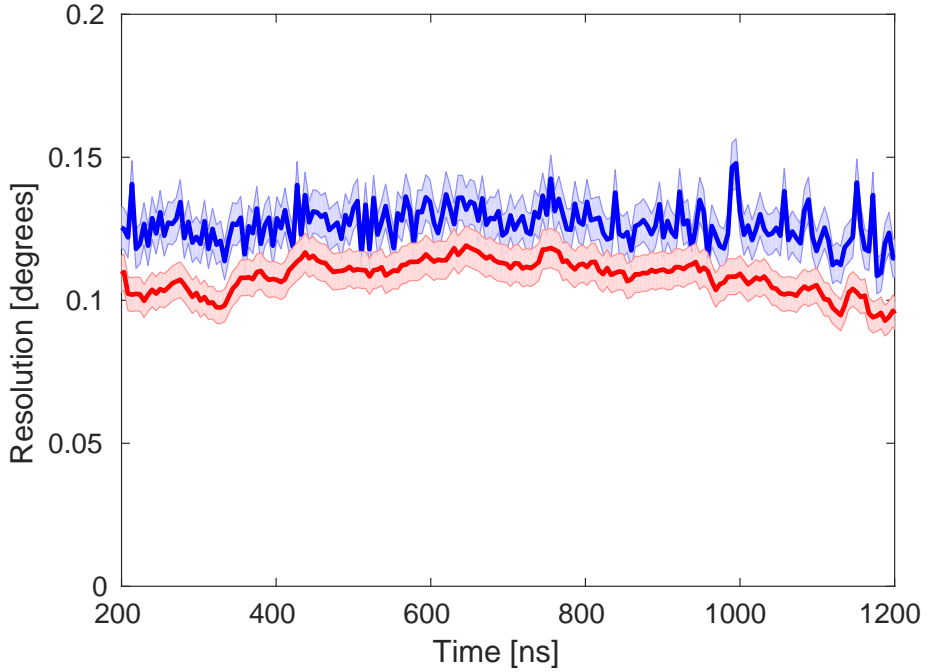


Figure 3.44: Effect of averaging 5 samples on the measured phase monitor resolution (red). The initial resolution with no averaging is shown in blue for comparison.

change in output voltage for small changes in phase). The dependence of the phase resolution on the beam phase across the full  $\pm 180^\circ$  range is shown in Figure 3.45. The plotted phase is the offset between the LO phase shifter setting and the calculated optimal setting. More than  $50^\circ$  away from the zero crossing there is a large degradation in resolution, reaching above 1 degree at the  $+90^\circ$  peak.

However, for the PFF system the phase resolution only needs to be guaranteed within its correction range, which is calculated to be  $\pm 5.5^\circ$  in Section 5.3.1. In Figure 3.46 it is seen that there is no noticeable degradation in resolution in the range between  $\pm 15^\circ$ . Therefore, providing the mixers have been correctly set at their zero crossings, this is not an issue for the PFF system.

## 3.10 Bandwidth

The overall targeted bandwidth for the prototype PFF correction is 30 MHz, which means each individual hardware component must have a bandwidth in excess of 30 MHz. To estimate the bandwidth of the phase measurement the delay loop has been used to create a sharp jump in the phase mid-way along the pulse. Normally the delay loop (whose length is 140 ns) is used with 1.5 GHz beam at CTF3, with seven 180 degree phase switches in the bunching at 140 ns intervals. Alternating 140 ns sub-trains are deflected in to the delay loop with a 1.5 GHz RF deflector, and then recombine with the 140 ns sub-trains bypassing the delay loop to double the drive beam current (Section 1.6). If the delay loop is instead used with 3 GHz beam alternating bunches, rather than sub-trains, enter the delay loop. The



Figure 3.45: Dependence of the phase monitor resolution on the phase offset between the beam and the LO, for the full  $360^\circ$  range.



Figure 3.46: Dependence of the phase monitor resolution on the phase offset between the beam and the LO, for offsets between  $\pm 20^\circ$ .

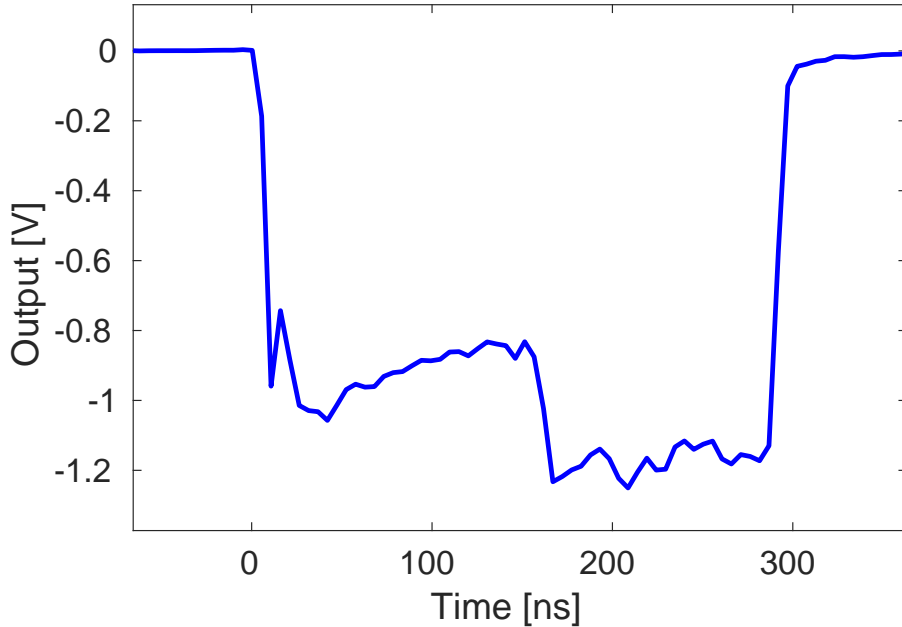


Figure 3.47: Response of Mixer 3 to a jump in phase in the middle of the pulse.

first 140 ns of the pulse after the delay loop contains only bunches that bypassed the loop, so is a 1.5 GHz beam with half the initial beam current. After the first 140 ns there is a fast transition back to 3 GHz beam with the same initial current as delayed bunches merge with the bypassing bunches. By varying the length of the delay loop (using a wiggler [69]) the phase of the bunches leaving the delay loop can be changed, also creating a fast phase jump at the transition to 3 GHz beam.

Figure 3.47 shows the response of the Mon 3 mixer to a beam pulse with a phase step setup in this way. The first 140 ns of the pulse contains only bunches bypassing the delay loop, as described, followed by the fast transition to 3 GHz beam and the phase step. The time taken for the mixer output to respond to the fast phase change can be related to the bandwidth by this approximate relationship [70]:

$$\text{BW} = \frac{350}{t} \quad (3.40)$$

Where BW is the bandwidth in MHz and  $t$  is the rise time of the signal in ns. The transition between the two phase states as seen on the mixer output occurs between 156.6 ns and 167.0 ns, a rise time of 10.4 ns corresponding to a bandwidth of approximately 34 MHz. In addition, the falling edge of the mixer output at the end of the pulse also takes around a 10 ns, also leading to a bandwidth estimate in the region of 35 MHz.

### 3.11 Comparison of Measured Phase Along Pulse

It has been shown that the phase jitter is at the same level in Mon 1 and Mon 2 after the installation of mechanical phase shifters (Section 3.8), and that the achieved resolution

is better than the level needed to be able to theoretically achieve a  $0.2^\circ$  PFF correction (Section 3.9.1). Nevertheless there are several remaining effects that have been identified which may limit the PFF performance in a way not described by the resolution. These are the focus of the remainder of this chapter, starting with differences between the measured shape of the phase along the pulse, discussed here. Neither the phase jitter nor the resolution are sensitive to any static differences in the measured phase in each monitor. For the PFF system to remove not only phase jitter but also to flatten the phase sag along the pulse the shape of the upstream and downstream phase must be the same.

Figure 3.48 shows an example of the measured phase along the pulse in all three monitors, as well as a fourth phase measurement taken from one of the power extraction and transfer structures (PETS) in the TBL line after Mon 3 [71]. The PETS measurement provides an independent cross-check of the response and calibration of the three PFF monitors. All four phase measurements show approximately the same overall phase sag of around  $45^\circ$  along the full pulse length, as desired.

Nevertheless, there are differences between the measurements. As described later in Chapter 4 there are many mechanisms by which the beam phase can change between the upstream and downstream monitors. Small discrepancies between the Mon 1 and Mon 2 phase compared to the Mon 3 and PETS phase are therefore not unexpected. A detailed comparison between the upstream and downstream phase is left to Chapter 4 rather than being discussed here.

However, as Mon 1 and Mon 2 are neighbouring each other in the beam line their measurements are expected to agree almost perfectly but this is not the case. Figure 3.49 shows the difference between the Mon 1 and Mon 2 phase along the pulse. The offset between the two has almost a linear dependence on the time along the pulse, varying by close to  $10^\circ$  across the full pulse length. Possible explanations could be an error in the fitted calibration amplitude or a time offset between the two signals. The fact that the Mon 2 phase is lower at one end of the pulse but higher at the other means that the difference is not simply a scale factor between the two, and therefore cannot be described by an error in calibration amplitude. Neither can it be explained by differences in the calibration constants along the pulse, as seen in Section 3.12. Similarly, by observing small variations along the pulse, for example at the end of the pulse after a time of 1000 ns in Figure 3.48, it can be seen that the two measurements are well aligned in time.

If there was a real difference in the phase sag between monitors (rather than it being a measurement effect) or if there was an issue with Mon 1, used as the PFF correction input, it would not be possible to completely flatten the phase sag along the pulse with the PFF system. The excellent flattening of the pulse that has in reality been achieved with the PFF system (Chapter 6) suggests this may be an issue affecting only Mon 2, as the correction input is based solely on Mon 1. Although the effect is not yet understood, recent measurements have suggested the source of the difference may be intermittent noise on the LO phase used by the second mixer, and not present or at least much weaker on the first and third LO sources used for Mon 1 and Mon 3 [72]. The noise appears to be correlated with the phase and power of the two klystrons nearest the phase monitor electronics in the klystron gallery, suggesting a possible grounding issue in the electronics.

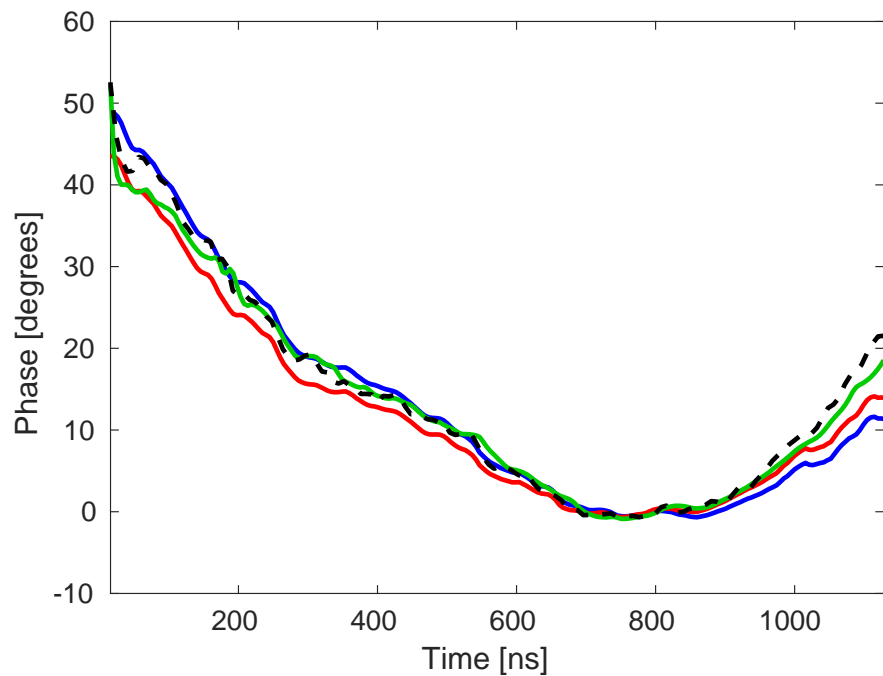


Figure 3.48: Comparison of phase along the pulse in the three PFF phase monitors and an alternative downstream phase measurement from a PETs. Blue: Mon 1, Red: Mon 2, Green: Mon 3 and Dashed Black: PETs.

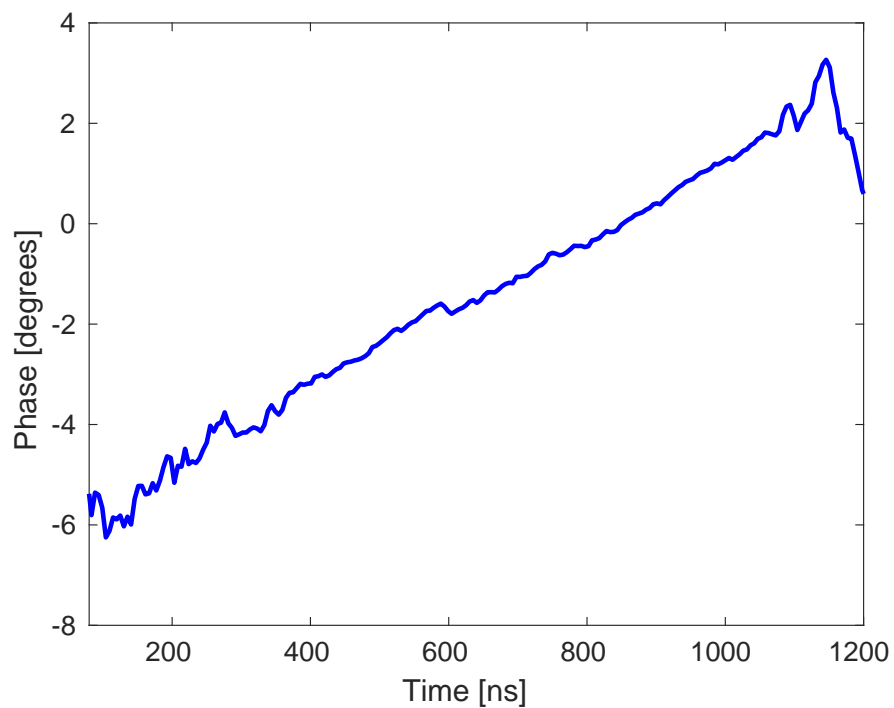


Figure 3.49: Difference between the measured Mon 1 and Mon 2 phase along the pulse.

## 3.12 Effect of Variations in Calibration Constant

In Section 3.7.3 it was shown how the calibration parameters vary along the pulse. In the PFF algorithm, and usually also in data analysis, single values for each calibration constant are used across the full pulse length. This will lead to small discrepancies between the measured phase and the true beam phase. Examples of the size of this effect are shown in Figures 3.50, for Mon 2, and in Figure 3.51 for Mon 3, comparing the measured phase along the pulse when using single value calibration constants or varying calibration constants along the pulse. In the range between 650 ns and 900 ns around the middle of the pulse where the phase sag is flattest (the part of interest for the PFF system) using a varying calibration constant along the pulse makes almost no difference to the measured upstream phase, with residuals of below 0.2° between the two calibration methods. This is unsurprising as the calibration constants normally used are calculated from one sample in this range. Outside this range the difference between the two reaches a peak of 1.5° near the start of the pulse.

For the downstream phase the differences are larger, including up to 1° offsets between the two methods in the range of interest for the PFF system. However, the example shown is without fully optimised downstream beam conditions achieved in Chapter 4 and so represents a worst case scenario for normal PFF operation. The PFF correction quality also does not directly depend on the downstream phase measurement (apart from for the gain calculation, as derived in Section 4.1), so these differences can be removed in offline analysis if deemed necessary.

## 3.13 Dependence on Position

As discussed in Section 3.1 the phase monitor output from the two vertical RF feedthroughs are summed in hybrids, and it is this sum signal that is connected to the mixers. This reduces, but does not remove completely, the dependence of the phase monitor signal power on the beam position in the monitor. In this section the remaining position dependence of the phase measurement is determined. Understanding the magnitude of the effect is particularly important considering the diodes are no longer used to power normalise the mixer output as originally intended.

The magnetic corrector placed roughly 1 m prior to Mon 1 (labelled CT.DHD0360) has been used to scan the beam position in the upstream phase monitors both horizontally and vertically. The position of the corrector with respect to the phase monitors can be seen in Figure 3.4. Around 1 m following Mon 2 there is a quadrupole (CT.QFF0420) followed by a BPM (CT.BPM0430). Distances between the elements are shown in Table 3.11. For the purposes of this measurement the quadrupole is turned off so that the whole 3.5 m length of beam line between the corrector and the BPM is a drift space. It is then straightforward to reconstruct the position offset in the two phase monitors based on the BPM measurement without having to rely on the MADX model to take in to account the effect of the quadrupole on the beam orbit.

In these conditions a position offset of  $x_{430}$  measured in the BPM (in horizontal or



Figure 3.50: Effect of using a varying calibration constant on the upstream phase. Top: Phase with a constant calibration constant (blue) and phase with a varying calibration constant (red). Bottom: The difference between the two.

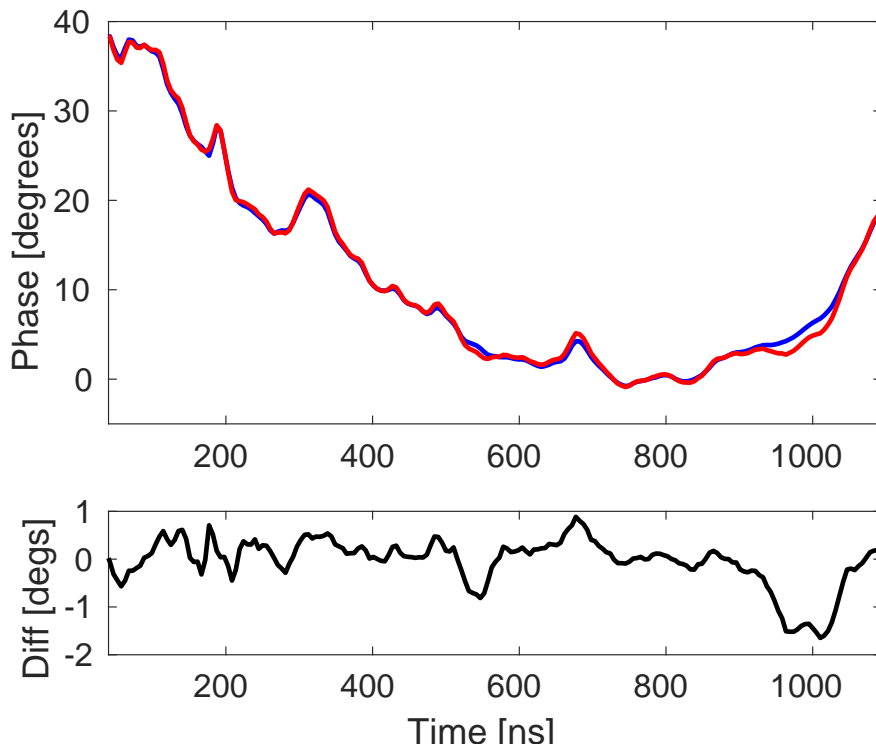


Figure 3.51: Effect of using a varying calibration constant on the downstream phase. Top: Phase with a constant calibration constant (blue) and phase with a varying calibration constant (red). Bottom: The difference between the two.

Device	Distance From CT.0360	Label
Mon 1	104.5 cm	$s_{M1}$
Mon 2	144.5 cm	$s_{M2}$
CT.BPM0430	357.0 cm	$s_{430}$

Table 3.11: Distance of the upstream phase monitors and following BPM CT.0430 to the corrector CT.0360 before the phase monitors.

vertical) corresponds to the following position offsets,  $x_{M1}$  and  $x_{M2}$ , in each phase monitor:

$$x_{M1} = r_{M1}x_{430} \quad (3.41)$$

$$x_{M2} = r_{M2}x_{430} \quad (3.42)$$

Here  $r_{M1}$  and  $r_{M2}$  are the position offsets in the phase monitors per unit position offset in the BPM, given by:

$$r_{M1} = \frac{s_{M1}}{s_{430}} \quad (3.43)$$

$$r_{M2} = \frac{s_{M2}}{s_{430}} \quad (3.44)$$

And were  $s_{M1}$ ,  $s_{M2}$  and  $s_{430}$  are the distances between the corrector and the phase monitors ( $s_{M1}$ ,  $s_{M2}$ ) or BPM ( $s_{430}$ ). Substituting in the values from Table 3.11 gives values of  $r_{M1} = 0.29$  and  $r_{M2} = 0.41$ .

Figure 3.52 shows the results of a horizontal position scan in the upstream phase monitors, with the phase plotted against the horizontal position in the BPM. Position scans of this type require a long time to complete in order to be able to acquire enough statistics at multiple corrector settings. The scan presented represents a data taking period of around one hour, for example. This means real drifts in beam phase (aside from any position dependent effects on the monitor signals) are unavoidable during the scan. The first impression of Figure 3.52 is that the only visible change in measured phase is due to actual drifts in beam phase rather than being as a result of the changes in position. However, Figure 3.53 shows the response of the phase monitor diode signals to the horizontal position in the BPM during the scan. Even though the diodes are heavily saturated a dependence of their output, and so a dependence of power, on the position is visible. This suggests there should also be a visible effect on the phase.

To remove the effects of drifts in the beam phase the difference between the measured Mon 1 and Mon 2 phase can be considered instead. The true beam phase,  $\phi_b$ , should be identical in Mon 1 and Mon 2, so any differences between their measurements  $\phi_{M1}$  and  $\phi_{M2}$  during the scan can be modelled as coming from the beam position in the monitor, as follows:

$$\phi_{M1} = \phi_b + c_{M1}x_{M1} \quad (3.45)$$

$$\phi_{M2} = \phi_b + c_{M2}x_{M2} \quad (3.46)$$

Here  $c_{M1}$  and  $c_{M2}$  are constants expressing the phase shift per unit position offset in each monitor. The difference between the measured phase in Mon 1 and Mon 2 is therefore given



Figure 3.52: Mon 1 (blue) and Mon 2 (red) phase dependence on the horizontal position during the scan.



Figure 3.53: Mon 1 (blue) and Mon 2 (red) diode dependence on the horizontal position during the scan.

by:

$$\phi_{M2} - \phi_{M1} = c_{M2}x_{M2} - c_{M1}x_{M1} \quad (3.47)$$

$c_{M1}$  and  $c_{M2}$  cannot be determined individually from the scan results alone using this approach, so instead it will be approximated that the strength of the position dependence is the same in Mon 1 and Mon 2. Letting  $c_{M1} = c_{M2} = c$  finally gives:

$$\phi_{M2} - \phi_{M1} = c(x_{M2} - x_{M1}) \quad (3.48)$$

$$c = \frac{\phi_{M2} - \phi_{M1}}{x_{M2} - x_{M1}} \quad (3.49)$$

The expressions for  $x_{M1}$  and  $x_{M2}$  in terms of the BPM position  $x_{430}$  derived earlier can then be substituted in to give:

$$c = \frac{\phi_{M2} - \phi_{M1}}{x_{430}(r_{M2} - r_{M1})} \quad (3.50)$$

The gradient of the phase difference versus the position offset in the BPM,  $(\phi_{M2} - \phi_{M1}) / x_{430}$ , is the only remaining parameter left to calculate in order to estimate  $c$ .

Figure 3.54 shows how the difference between the Mon 1 and Mon 2 phase measurement depends on the horizontal position in the BPM during the scan. By removing the actual beam phase drifts the dependence of the phase measurements on the beam position becomes clear. The fitted gradient is  $-0.22 \pm 0.01^\circ$  per mm offset in the BPM. Using Equation 3.50 this corresponds to a phase shift of  $-1.84 \pm 0.07^\circ$  per mm offset in the phase monitors themselves.

Exactly the same process can be repeated in the vertical plane, and the results of doing this are shown in Figure 3.55. Although the effect is smaller there is still a visible dependence of the phase on the vertical position, in this case with a gradient of  $0.06 \pm 0.01^\circ$  per mm offset in the BPM corresponding to  $0.53 \pm 0.07^\circ$  per mm vertical offset in the phase monitors.

The position dependence of the measurement appears large when quoted like this but it must be remembered that millimetre scale changes in beam orbit are rare during normal operation. Orbit jitter at CTF3 around the location of the upstream phase monitors is typically at the 0.02 mm level. Taking the calculated position dependence of Mon 1 and Mon 2 this corresponds to only an additional measured phase jitter of roughly  $0.04^\circ$ , using the larger dependence in the horizontal plane. This is only a small contribution to the overall phase monitor resolution of around  $0.13^\circ$  as seen in Section 3.9. However, it is important to consider that any change in beam setup that alters the trajectory through the monitors will lead to a change in output power and therefore a change in calibration constants. Calibrations are always repeated when the CTF3 setup is changed to take this in to account. Position scans around the region of the downstream phase monitor Mon 3 would be much more difficult to perform and have not yet been attempted. The effect should be of a similar magnitude, although the downstream beam is less stable than upstream so the contribution to measured phase jitter is likely to be slightly larger.



Figure 3.54: Fit (black line) to the measured difference between the Mon 1 and Mon 2 phase (blue markers) versus the horizontal position.



Figure 3.55: Fit (black line) to the measured difference between the Mon 1 and Mon 2 phase (blue markers) versus the vertical position.

# Chapter 4

## Phase Propagation

The PFF system uses the upstream phase measurement to correct the downstream phase. In this scheme any differences between the initial upstream phase and the downstream phase cannot be removed by the PFF system. The PFF system is therefore very sensitive to the “phase propagation”, or the extent to which the upstream phase predicts the actual downstream phase. As, at CTF3, the upstream and downstream phase monitors are separated by roughly 150 m of beam line there are many potential sources that may change the downstream phase with respect to the upstream phase. This chapter derives the requirements that the PFF system places on the phase propagation before describing its original status during the first PFF tests and the extensive work that has been needed to improve it.

### 4.1 Feedforward Algorithm

In the PFF system the voltage sent to the kickers in the TL2 chicane (see Figures 1.6 and 2.2) is varied depending on the upstream phase. The corrected downstream phase,  $\phi_{PFF}$ , can therefore be simply modelled as subtracting the upstream phase,  $\phi_u$ , from the initial downstream phase  $\phi_d$ :

$$\phi_{PFF} = \phi_d - g\phi_u \quad (4.1)$$

Here  $g$  is the applied correction gain. The corrected downstream phase jitter,  $\sigma_{PFF}$ , can then be defined using the standard result of subtracting correlated variances [73]:

$$\sigma_{PFF}^2 = \sigma_d^2 + g^2\sigma_u^2 - 2g\rho_{ud}\sigma_u\sigma_d \quad (4.2)$$

Here  $\rho_{ud}$  is the correlation coefficient between the upstream phase and the downstream phase.

Setting the partial differential of Equation 4.2 with respect to the gain equal to zero yields an expression for the theoretical optimal gain value to apply:

$$\frac{\partial\sigma_{PFF}^2}{\partial g} = 2g\sigma_u^2 - 2\rho_{ud}\sigma_u\sigma_d = 0 \quad (4.3)$$

$$g = \rho_{ud} \left( \frac{\sigma_d}{\sigma_u} \right) \quad (4.4)$$

In the case where the phase propagation is perfect and the downstream phase is identical to the upstream phase the optimal gain factor is 1, as expected. Alternatively, if there is no correlation between the upstream and downstream phase the PFF system could only act to increase the downstream phase jitter, thus the optimal gain would be zero. If the downstream phase jitter is amplified with respect to the upstream phase jitter ( $\phi_d = \text{const} \times \phi_u$ ), this can be removed by the PFF system via the dependence of the optimal gain on the upstream–downstream phase jitter ratio.

Substituting the optimal gain value back in to Equation 4.2 gives an expression for the theoretical limit on the corrected downstream phase jitter using the PFF system:

$$\sigma_{PFF} = \sigma_d \sqrt{1 - \rho_{ud}^2} \quad (4.5)$$

With the optimal PFF setup the achievable corrected downstream phase jitter has no dependence on the upstream phase jitter. It depends only on the initial downstream phase jitter and most strongly on the upstream–downstream phase correlation. The dependence of the achievable corrected downstream phase jitter on the phase monitor resolution (Section 3.3) is implicit, as this contributes to the measured upstream–downstream phase correlation. If non-optimal gains are used there is also a dependence on the upstream phase jitter and the set gain value as per Equation 4.2. Figure 4.1 shows how the achievable corrected downstream phase jitter depends on the upstream–downstream phase correlation. A factor 2 reduction in the initial downstream phase jitter requires a correlation of 86.6%, for example.

Equations 4.2, 4.4 and 4.5 are used extensively in the remainder of this thesis to determine the beam conditions needed to achieve a  $0.2^\circ$  correction at CTF3, as well as to calculate the expected effect of the PFF system given the beam conditions and PFF setup.

## 4.2 Characteristics of Uncorrected Phase Jitter

This section summarises the status of the phase propagation during the first PFF tests to demonstrate why the work in this chapter was necessary and to provide a point of comparison to the improved conditions later achieved in Section 4.7.

### Mean Phase

Figure 4.2 compares the mean phase upstream and downstream across one dataset of 213 pulses, or roughly 5 minutes. The downstream phase jitter is more than double the upstream phase jitter — at  $1.86 \pm 0.09^\circ$  compared to  $0.81 \pm 0.04^\circ$  upstream (rms). Theoretically the PFF system could still remove the amplified downstream phase jitter providing the jitter is well correlated with the upstream phase, as derived in the previous section. Unfortunately, as shown in Figure 4.3, there is almost no correlation between the upstream and downstream phase, with a calculated coefficient of  $0.34 \pm 0.06$  in this case.

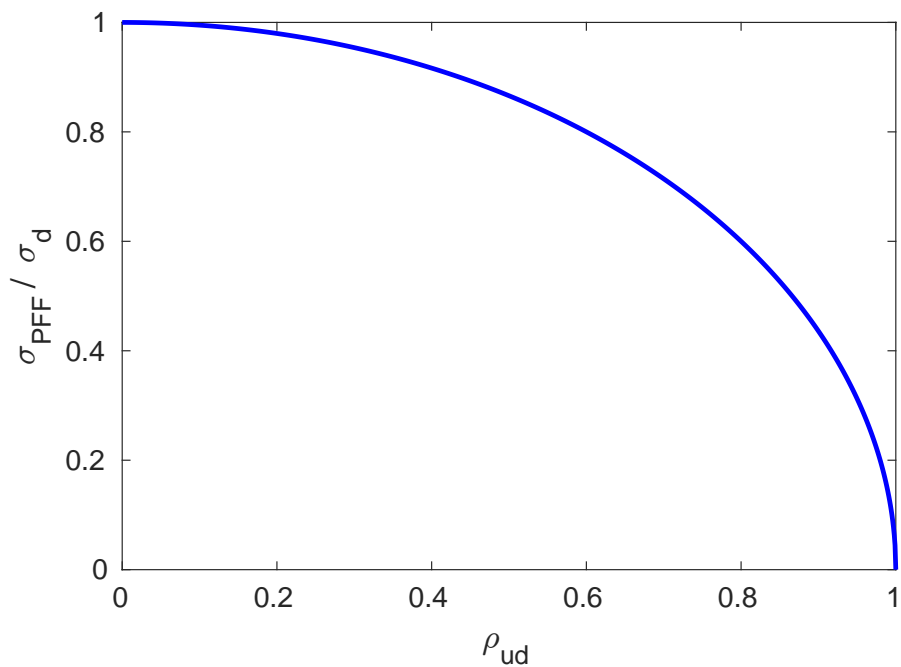


Figure 4.1: Dependence of the ratio between the theoretical corrected and initial downstream phase jitter ( $\sigma_{PFF}/\sigma_d$ ) on the initial upstream-downstream phase correlation ( $\rho_{ud}$ ).

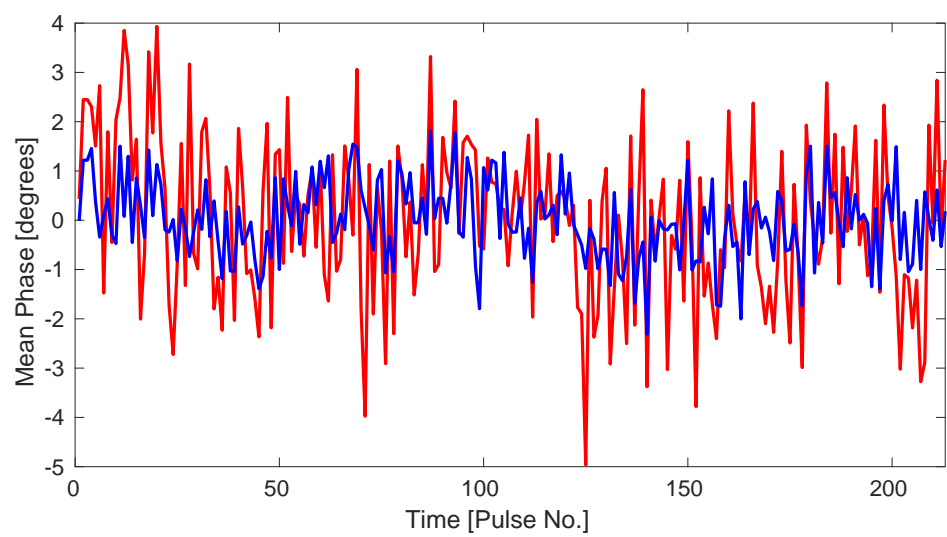


Figure 4.2: Mean phase jitter upstream (blue) and downstream (red) during early PFF tests.

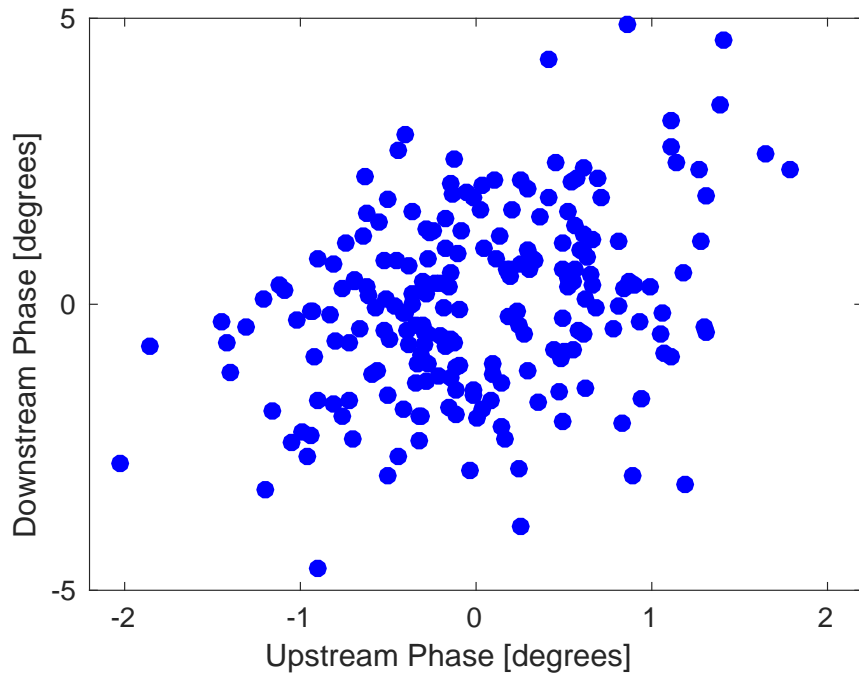


Figure 4.3: Correlation between the downstream phase and the upstream phase during early PFF tests.

### Phase Along Pulse

In addition to the differences in the mean phase there are also large discrepancies between the upstream and downstream phase along the pulse. Figure 4.4 shows one example of this. The overall phase sag along the pulse is approximately equivalent for both the upstream and downstream phase. However, there are many oscillations along the downstream phase, up to  $10^\circ$  peak-to-peak, that are not present upstream.

As well as the static variations in the downstream phase along the pulse, there are also large differences in the phase jitter along the pulse. An example is shown in Figure 4.5. The point by point upstream phase jitter along the pulse is quite flat at around 1 degree, slightly larger than the jitter on the mean. Alternatively, the downstream phase jitter has large variations along the pulse. In some regions the downstream jitter is a factor 4 higher than the upstream phase jitter, whilst in others it is only 50% higher.

### Consequences for the PFF System

The differences between the mean upstream and downstream phase, both on the mean and along the pulse, need to be removed to enable phase jitters close to the CLIC target to be achieved with the PFF prototype at CTF3. Using Equation 4.5, with the optimal PFF gain and  $0.34 \pm 0.06$  upstream–downstream phase correlation an initial downstream phase jitter of  $1.86 \pm 0.09^\circ$  could be reduced to  $1.51 \pm 0.09^\circ$ . This is only a modest improvement of around 20%, and far from the CLIC target of  $0.2^\circ$  phase stability.

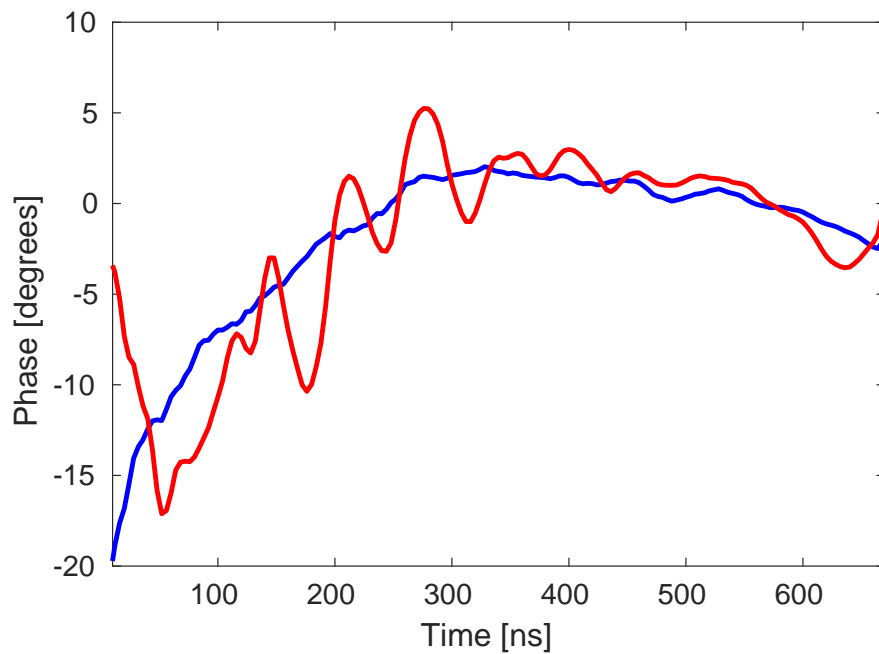


Figure 4.4: Mean upstream (blue) and downstream (red) phase along the pulse during early PFF tests, averaged across 213 pulses.

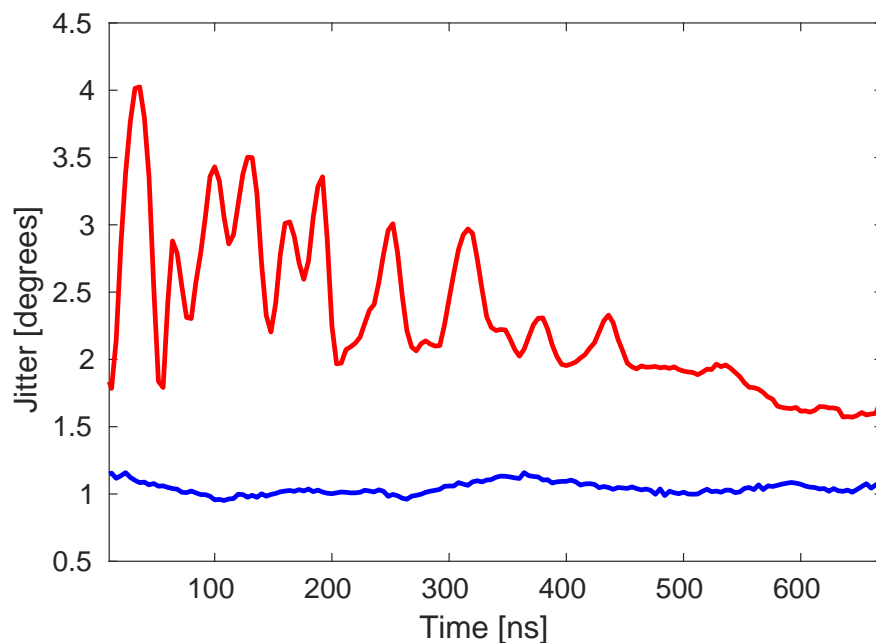


Figure 4.5: Upstream (blue) and downstream (red) phase jitter along the pulse during early PFF tests, across a dataset containing 213 pulses.

Assuming the initial downstream phase jitter could be reduced to the same level as the upstream phase jitter, to  $0.8^\circ$ , the upstream–downstream phase correlation required to theoretically achieve  $0.2^\circ$  corrected phase jitter is 97%. This chapter will describe the procedures developed to achieve this level of downstream phase jitter and correlation. The first effect investigated was the energy dependence of the downstream phase, for the reasons described in Section 4.3.

## 4.3 First Order Energy Dependences

The transfer matrix coefficient  $R_{56}$  defines the phase shift between two points in the lattice resulting from a beam energy offset (Section 2.4). Due to issues with meeting all the optics constraints for the PFF system a non-zero  $R_{56}$  value had to be tolerated in the TL2 chicane (Section 2.6). Therefore, a dependence of the downstream phase on the beam energy is expected, and this was the first place to look to try to understand and improve the poor upstream–downstream phase correlation and high downstream phase jitter.

### 4.3.1 Beam Energy Variations

The best way to measure variations in the beam energy at CTF3 is via the beam position in one of the chicanes or rings, where the position after a bending magnet depends on the beam energy. The beam position offset,  $\Delta x$ , in a BPM (beam position monitor) in these regions is linked to the relative energy offset,  $\Delta p/p$ , as follows:

$$\frac{\Delta p}{p} = \frac{\Delta x}{D_x} \quad (4.6)$$

Here  $D_x$  is the dispersion at that location given by the machine optics. Regions where  $D_x$  is non-zero are referred to as dispersive regions.

With the beam setup used for the PFF system operation (bypassing the Frsacati chicane and delay loop, see Figure 1.5) the first dispersive BPM after the CTF3 linac is the BPM CT.0608 in the transfer line TL1. TL1 is introduced in more detail in Section 4.4.1. The BPM CT.0608 is placed roughly 1 m after the first dipole magnet in TL1, with a horizontal dispersion of  $D_x = -0.61$  m at this point according to the CTF3 MADX model. There are no quadrupoles or other elements between the dipole and CT.0608, which reduces the sensitivity of this dispersion value to any inaccuracies in the model. All quoted energy measurements in this chapter are obtained using the horizontal position in BPM CT.0608, converted in to the energy using the Equation 4.6.

It should be noted that whilst this provides an accurate measurement of the relative energy jitter and variations along the pulse, it cannot be used to determine the absolute energy value. For example, the mean beam position in CT.0608 is non-zero due to device misalignments, and can change depending on the setup of CTF3. The mean position offset is subtracted in all cases so that the resulting energy values are centred around zero, although

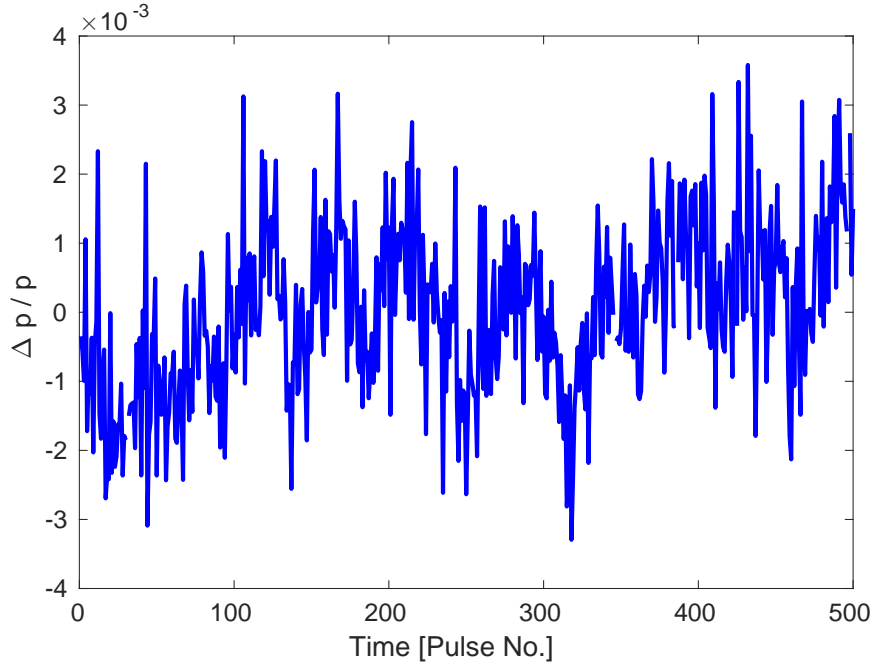


Figure 4.6: Example of variations in the mean beam energy ( $\Delta p/p$ ) across 500 pulses, with a relative jitter of  $1.2 \times 10^{-3}$ .

the actual mean energy offset may be non-zero. In certain simulations in this chapter non-zero mean energy offsets are used to improve the agreement with the data, as indicated.

### Mean Beam Energy

Figure 4.6 shows an example of variations in the mean beam energy on medium to long timescales at CTF3, in this case 500 pulses or roughly 10 minutes. Relative energy jitter on the mean is typically at the level of  $1 \times 10^{-3}$ , and varies by roughly  $\pm 50\%$  about this value. For shorter timescales, in datasets up to a couple of hundred pulses or a few minutes in length, the relative energy jitter is routinely closer to the  $0.5 \times 10^{-3}$  level (seen Figure 4.23, for example). The main sources of drifts in the mean energy at CTF3 are variations in beam current and temperature dependent effects on the klystron phase and RF power feedback loops [74]. Recent improvements have demonstrated an energy stability better than  $1 \times 10^{-3}$  energy stability on longer timescales (see Section 4.5.3), which will aid future PFF tests.

### Energy Variations Along the Pulse

The energy stability point-by-point along the pulse is at the same level as the mean energy stability, with relative jitter at, or slightly above, the  $1 \times 10^{-3}$  level, as seen in Figure 4.7. Typically the energy stability is slightly worse at the start and end of the pulse (due to transients, for example).

In addition to the jitter there are also static variations in the energy along the pulse. Figure 4.8 shows one example of this. Variations in the mean energy along the pulse are

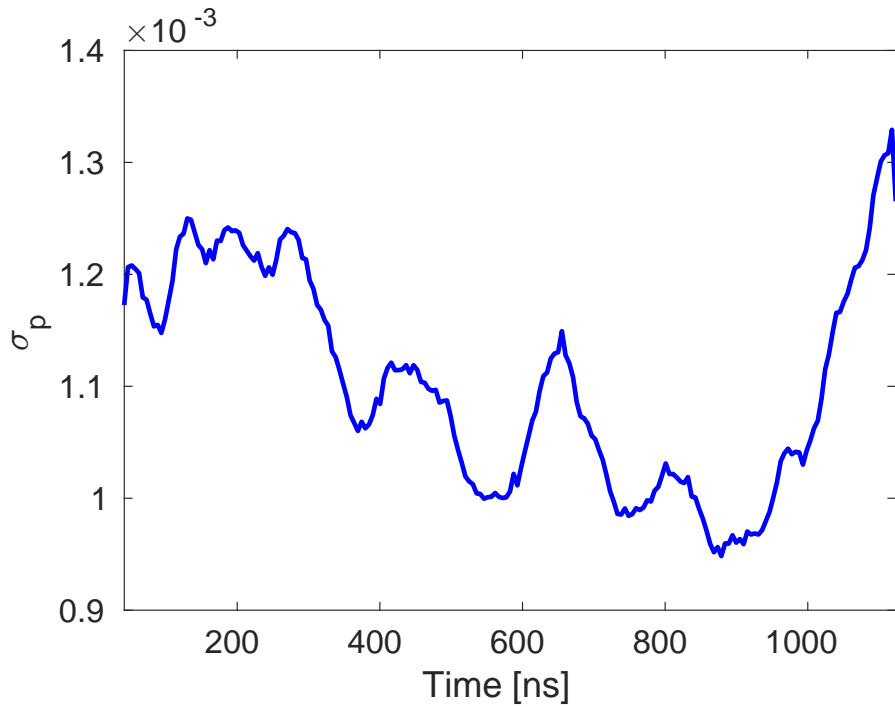


Figure 4.7: Example of relative energy jitter ( $\sigma_p$ ) along the pulse. Each point is the rms energy variation at that point along the pulse across a dataset of 213 pulses.

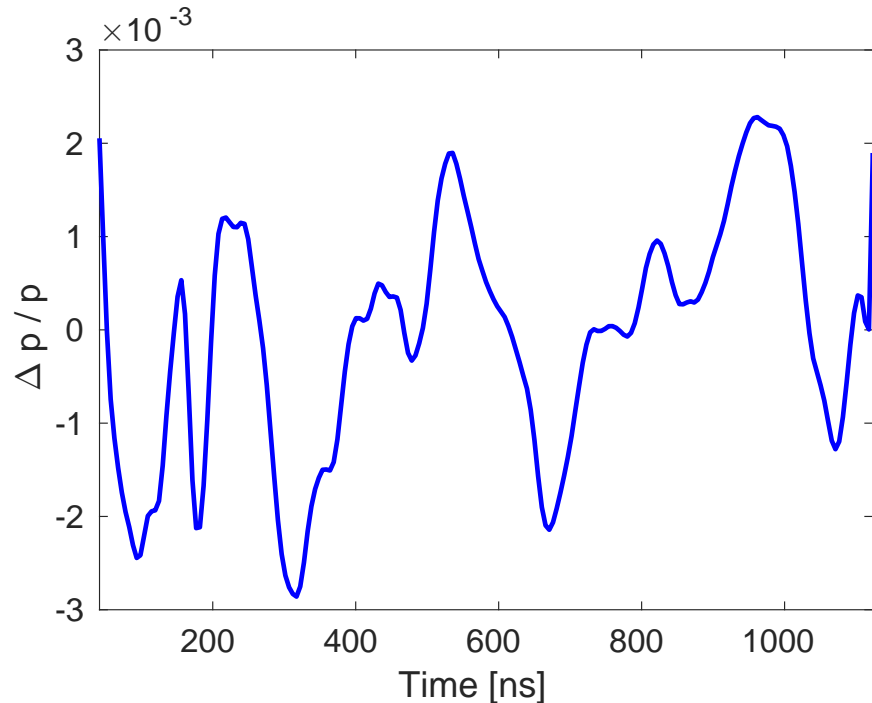


Figure 4.8: Example of variations in energy ( $\Delta p/p$ ) along the pulse, showing the mean taken across a dataset of 213 pulses.

normally several times larger than the energy jitter, at the level of  $2\text{--}5 \times 10^{-3}$  (peak-to-peak). New feedbacks have also been recently developed at CTF3 to reduce variations in energy along the pulse (Section 4.5.3).

### 4.3.2 Correlation between Phase and Energy

Figure 4.9 shows one example of the typical dependence of the mean downstream phase on the beam energy during the first PFF attempts. It's immediately clear that there is a strong relationship between the two, with a correlation in this case of  $0.82 \pm 0.03$ .

In contrast, in Figure 4.10 there is almost no dependence of the upstream phase on the energy. However, the calculated correlation coefficient of  $0.19 \pm 0.06$  is statistically significant and this has consequences for the discussions in the remainder of this chapter. Normally the small upstream phase–energy correlation typically varies between 0 and 0.4 at CTF3 depending on the conditions, in particular the energy jitter, at that time. In certain setups there can also be high correlations between the upstream phase and energy (Section 4.5.2).

By itself having a high correlation between the downstream phase and the energy is not an issue for the PFF system. The problem is the difference between the upstream phase–energy correlation and the downstream phase–energy correlation, which leads to low correlation between the upstream and downstream phase. The high downstream phase jitter is also a problem for the PFF system due to its limited correction range, as previously mentioned.

The goal of this section is to determine whether the non-zero optics  $R_{56}$  value between the upstream and downstream phase monitors is sufficient to explain both the large amplification in downstream phase jitter and the low upstream–downstream phase correlation seen here. To start with, the effect of  $R_{56}$  on the downstream phase jitter and upstream–downstream phase correlation will be more formally defined.

### 4.3.3 R<sub>56</sub>

Assuming energy is the only source of differences between the upstream and downstream phase, the downstream phase,  $\phi_d$ , can be expressed in terms of the optics transfer matrix coefficient,  $R_{56}$  (Section 2.1), as follows:

$$\phi_d = \phi_u + R_{56} \frac{\Delta p}{p} \quad (4.7)$$

Here  $\phi_u$  is the upstream phase,  $\Delta p/p$  is the relative energy offset and  $R_{56}$  is the matrix coefficient between the upstream and downstream phase monitors, defined by the machine optics. The units of  $R_{56}$  in the equation above are radians at 12 GHz per unit relative energy offset ( $\Delta p/p = 1$ ). MADX uses units of metres and this value is what will be referred to in this chapter. To obtain the  $R_{56}$  value to use in the equation above the MADX value must be multiplied by the conversion factor  $2\pi/0.025$ , where 0.025 m is the 12 GHz wavelength.

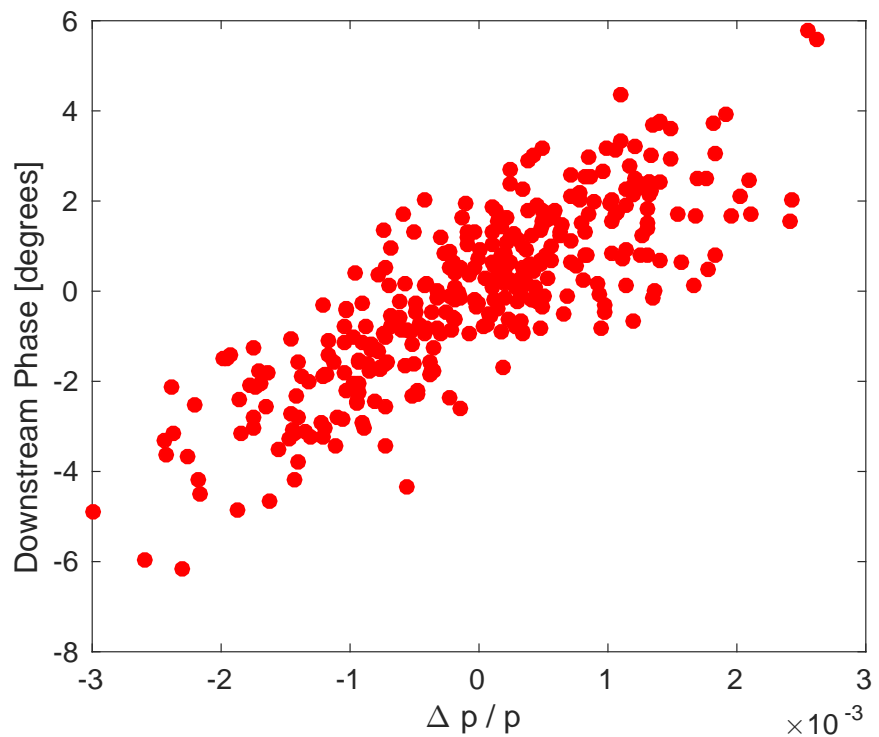


Figure 4.9: Dependence of the mean downstream phase on the beam energy ( $\Delta p / p$ ).

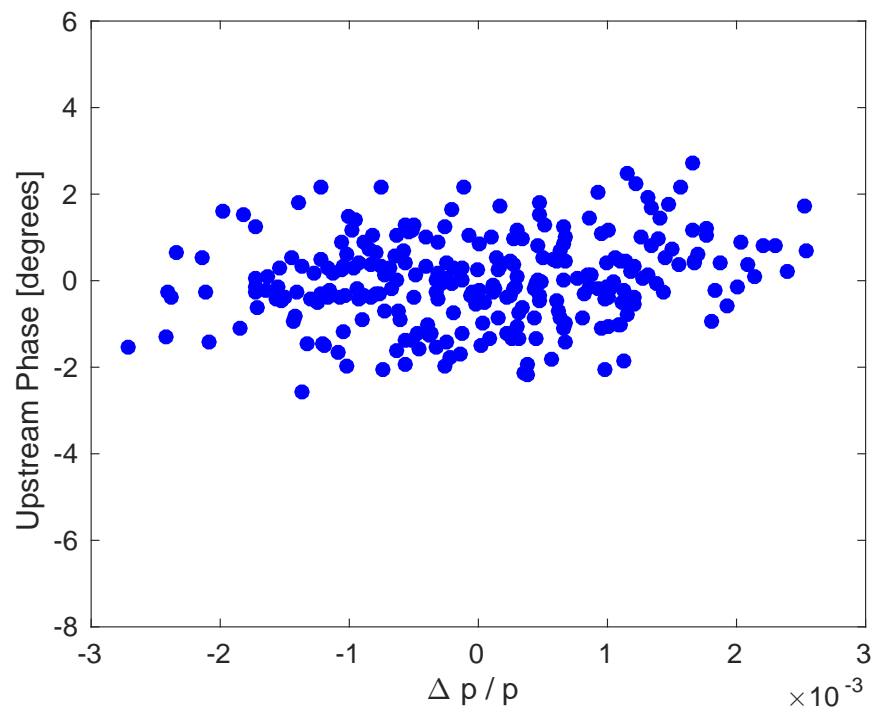


Figure 4.10: Dependence of the mean upstream phase on the beam energy ( $\Delta p / p$ ).

In terms of jitters Equation 4.7 becomes:

$$\sigma_d = \sqrt{\sigma_u^2 + R_{56}^2 \sigma_p^2 + 2R_{56}\rho_{up}\sigma_u\sigma_p} \quad (4.8)$$

Here  $\sigma_d$  is the downstream phase jitter,  $\sigma_u$  is the upstream phase jitter,  $\sigma_p$  is the relative energy jitter and  $\rho_{up}$  is the correlation between the upstream phase and the energy. This follows from the result of adding correlated variances. Clearly, any non-zero  $R_{56}$  between the upstream and downstream phase monitors introduces an additional energy component to the downstream phase that increases the downstream phase jitter.

The effect of  $R_{56}$  on the upstream-downstream phase correlation,  $\rho_{ud}$ , can also be defined starting from the definition of the Pearson product-moment correlation coefficient:

$$\rho_{ud} = \frac{\text{cov} [\phi_u, \phi_d]}{\sigma_u \sigma_d} \quad (4.9)$$

Here  $\text{cov} [\phi_u, \phi_d]$  is the covariance between the upstream and downstream phase, given by:

$$\text{cov} [\phi_u, \phi_d] = \frac{1}{N} \sum_{i=1}^N \phi_{ui} \phi_{di} \quad (4.10)$$

Here the index  $i$  refers to the pulse number out of a dataset containing  $N$  beam pulses. By inserting the definition of the downstream phase from Equation 4.7 and separating the terms in the sum this becomes:

$$\text{cov} [\phi_u, \phi_d] = \frac{1}{N} \sum_{i=1}^N \phi_{ui}^2 + R_{56} \frac{1}{N} \sum_{i=1}^N \phi_{ui} \frac{\Delta p_i}{p} \quad (4.11)$$

The first term is now the variance of the upstream phase,  $\sigma_u^2$ , and the second term is  $R_{56}$  multiplied by the covariance between the upstream phase and the energy,  $\text{cov} [\phi_u, \frac{\Delta p}{p}]$ , which can be expressed in terms of the correlation between the upstream phase and the energy,  $\rho_{up}$ :

$$\text{cov} \left[ \phi_u, \frac{\Delta p}{p} \right] = \rho_{up} \sigma_u \sigma_p \quad (4.12)$$

Therefore, Equation 4.11 becomes:

$$\text{cov} [\phi_u, \phi_d] = \sigma_u^2 + R_{56} \rho_{up} \sigma_u \sigma_p \quad (4.13)$$

Finally, substituting Equations 4.8 and 4.13 into Equation 4.9 gives:

$$\rho_{ud} = \frac{\sigma_u + R_{56} \rho_{up} \sigma_p}{\sqrt{\sigma_u^2 + R_{56}^2 \sigma_p^2 + 2R_{56} \rho_{up} \sigma_u \sigma_p}} \quad (4.14)$$

Considering that in this model the only difference between the upstream and downstream phase results from the  $R_{56}$ , it is perhaps obvious that the best conditions for the PFF correction are obtained when the  $R_{56}$  coefficient between the upstream and downstream phase monitors is zero. In these conditions  $\sigma_d = \sigma_u$  and  $\rho_{ud} = 1$ . This can be more formally

defined by using the expression for the theoretical corrected downstream phase jitter when using the optimal gain factor as derived in Section 4.1:

$$\sigma_{PFF} = \sigma_d \sqrt{1 - \rho_{ud}^2} \quad (4.15)$$

The initial downstream phase jitter and upstream-downstream phase correlation have been defined in terms of the  $R_{56}$  in Equations 4.8–4.14 above. Inserting them in to this equation gives the following expression for the corrected downstream phase jitter in terms of the  $R_{56}$ :

$$\sigma_{PFF} = |R_{56}| \sigma_p \sqrt{1 - \rho_{up}^2} \quad (4.16)$$

As expected the achievable corrected downstream phase jitter is minimised when  $R_{56} = 0$ . Note that this equation does not take in to account that the minimum achievable downstream phase jitter is limited to  $\sqrt{2}$  times the phase monitor resolution (Section 3.3).

In principle, the beam conditions for the PFF correction can also be improved by reducing the relative energy jitter ( $\sigma_p$ ) or by increasing the upstream phase-energy correlation ( $\rho_{up}$ ). Reducing the relative energy jitter decreases the additional phase jitter created by non-zero  $R_{56}$ . Increasing the upstream phase-energy correlation ( $\rho_{up}$ ) reduces the effect that non-zero  $R_{56}$  has on the upstream-downstream phase correlation ( $\rho_{ud}$ ), as the additional energy dependent downstream phase jitter is correlated with the upstream phase in this case. In practice  $\sigma_p$  and  $\rho_{up}$  are defined by the CTF3 injector and can not be varied with a great degree of flexibility, so having zero  $R_{56}$  is the only way to obtain ideal conditions for the PFF correction. However, recent improvements at CTF3 have reduced the relative energy jitter, as discussed later in Section 4.5.3. High upstream phase-energy correlations can also be created at CTF3 but not without greatly amplifying the upstream phase jitter, which causes issues for the PFF system due to its limited correction range (Section 5.3.1).

An interesting consequence of Equations 4.8 and 4.16 is that the best beam conditions for the PFF correction are not given by minimising the initial downstream phase jitter in the case where the upstream phase-energy correlation,  $\rho_{up}$ , is non-zero. As seen in Section 4.3.2 in normal conditions there is a small correlation between the upstream phase and the energy at CTF3, typically around  $\rho_{up} = 0.2$ . In these conditions the downstream phase jitter can in theory be reduced to below the level of the upstream phase jitter by using an optics with negative  $R_{56}$  between the upstream and downstream phase monitors. This then removes the energy component present upstream from the downstream phase. Differentiating Equation 4.8 gives the minimum downstream phase jitter to be obtained when  $R_{56} = -\rho_{up}\sigma_u/\sigma_p$ . However, using this  $R_{56}$  value would degrade the upstream-downstream phase correlation and increase the achievable corrected downstream jitter, which is always minimised when  $R_{56} = 0$  as in Equation 4.16. The phase propagation optimisations in this chapter must therefore be focused on zeroing the  $R_{56}$  value between the upstream and downstream phase monitors, rather than minimising the initial downstream phase jitter.

#### 4.3.4 Effect of $R_{56}$ in TL2

The PFF optics has an  $R_{56}$  value of close to  $-0.2$  m between the entrance and exit of the TL2 horizontal chicane (Section 2.6.2). All the other sections of CTF3 between the upstream

Parameter	Value
$R_{56}$	-0.2 m
$\sigma_u$	0.8°
$\rho_{up}$	0.2
$\sigma_p$	0.001

Table 4.1: Typical beam and optics conditions at CTF3 relating to the energy and upstream phase stability.

and downstream phase monitors (CT line, TL1, combiner ring and TBL, see Figure 1.5) nominally have zero  $R_{56}$  [15]. Therefore they don't introduce additional phase jitter via energy, at least to first order and to within the accuracy of the CTF3 MADX model. The overall  $R_{56}$  between the upstream phase monitors (in the CT line) and the downstream phase monitors (in the TBL line, labelled CB, after the TL2 chicane) is therefore -0.2 m also. Whether this can explain the low upstream-downstream phase correlation and high downstream phase jitter seen in Section 4.2, as well as what residual  $R_{56}$  between the two monitors can be tolerated to be able to achieve CLIC-level phase stability at CTF3, is discussed in this section.

Equations 4.8 and 4.14 can be used to estimate the downstream phase jitter and upstream-downstream phase correlation in the conditions at CTF3. Typical values for the various parameters in the equations have already been presented in previous sections, and these values are summarised in Table 4.1. The value  $R_{56} \simeq -0.2$  m was obtained in Section 2.6.2 as previously mentioned, the value  $\sigma_u \simeq 0.8^\circ$  in Section 4.2 and the values  $\rho_{up} \simeq 0.2$  and  $\sigma_p \simeq 0.001$  in Section 4.3.2.

With these parameter values Equations 4.8 and 4.14 predict that a residual  $R_{56}$  of -0.2 m between the upstream and downstream phase monitors will reduce the upstream-downstream phase correlation to below 10%. The downstream phase jitter is amplified to above 3 degrees. Therefore, the effects of  $R_{56}$  alone can explain the low upstream-downstream phase correlation and high downstream phase jitter seen in Section 4.2. In order to increase the upstream-downstream phase correlation to 97% and reduce the downstream jitter to 0.8 degrees (the conditions needed to achieve 0.2 degrees corrected downstream phase jitter at CTF3) the  $R_{56}$  between the upstream and downstream phase monitors must be removed.

Figure 4.11 and 4.12 show the expected downstream phase jitter and upstream-downstream phase correlation for residual  $R_{56}$  values from -0.2 to +0.2 m between the upstream and downstream phase monitors again using Equations 4.8 and 4.14. The theoretical corrected downstream phase jitter using the PFF correction across the range of  $R_{56}$  values is also shown. In order to obtain CLIC level phase stability at CTF3 the residual  $R_{56}$  between the upstream and downstream phase monitors must be reduced from the initial  $-0.2$  m to  $0 \pm 1.3$  cm. Also note the slight asymmetry in the phase jitter and correlation curves, which is caused by the non-zero correlation between the upstream phase and the beam energy.

To interpret the results of  $R_{56}$  optimisation attempts (Sections 4.4 and 4.5) it is useful to understand how varying the correlation between the upstream phase and the energy changes

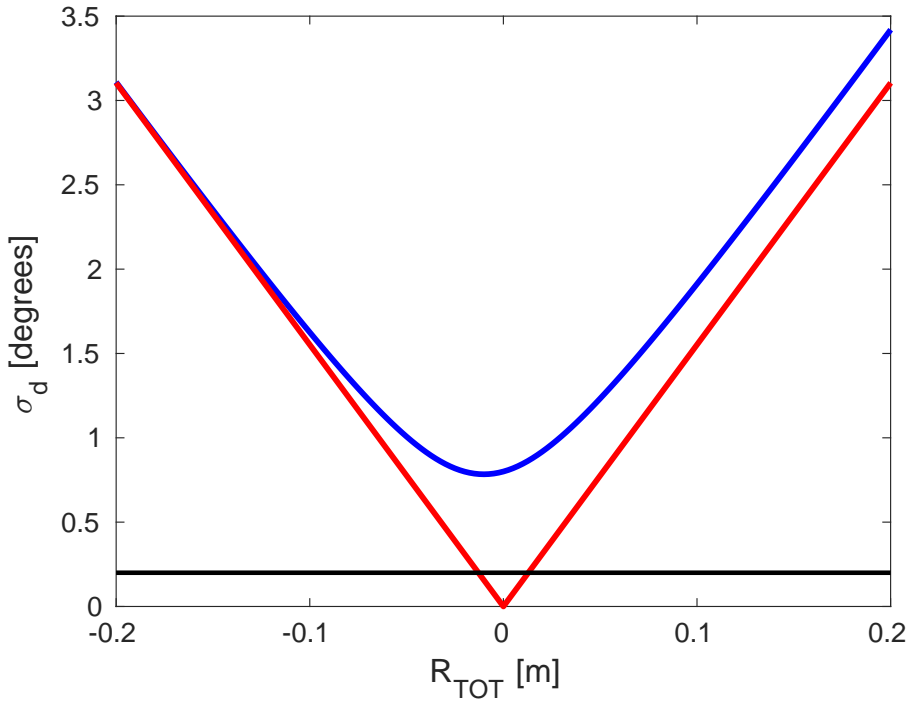


Figure 4.11: Initial (blue) and corrected (red) downstream phase jitter ( $\sigma_d$ ) vs. the  $R_{56}$  coefficient between the upstream and downstream phase monitors ( $R_{TOT}$ ). The horizontal black line shows the CLIC target of 0.2 degrees corrected downstream phase jitter.

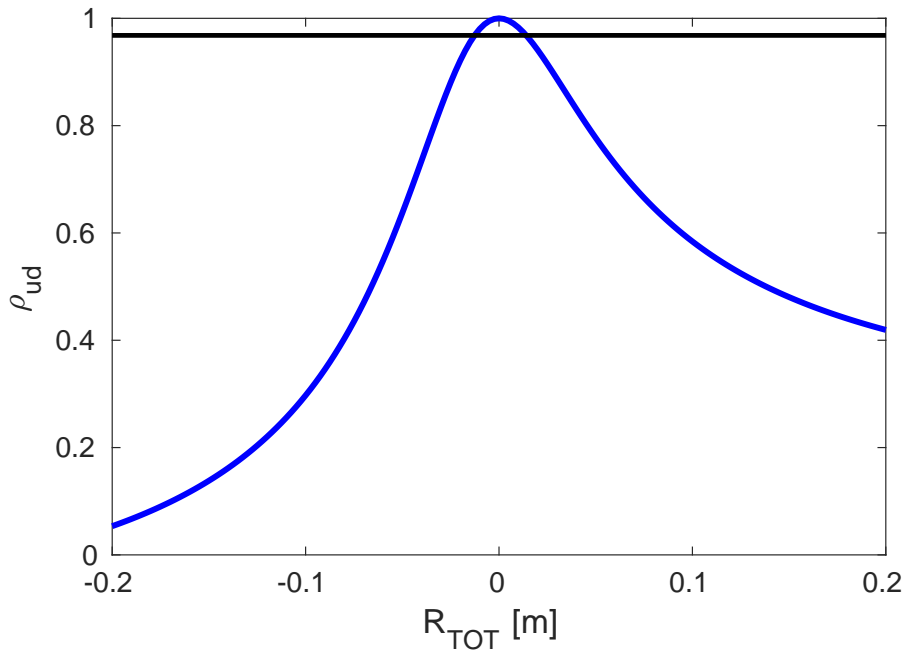


Figure 4.12: Upstream-downstream phase correlation ( $\rho_{ud}$ ) vs. the  $R_{56}$  coefficient between the upstream and downstream phase monitors ( $R_{TOT}$ ). The horizontal black line shows the 97% correlation needed to achieve 0.2 degrees corrected phase jitter at CTF3.

the dependence of the downstream phase on the  $R_{56}$  value impacts the phase propagation. In particular, in Section 4.5.2 a machine setup that increases  $\rho_{up}$  to 90% is used. Figure 4.13 shows how the upstream-downstream phase correlation varies with upstream phase-energy correlations of 0% and 40% (the range typical of normal operation), as well as with the higher correlation of 90%. With high upstream phase-energy correlations there is no longer a well defined peak in the upstream-downstream phase correlation versus the  $R_{56}$  value. Instead there is an almost constant high upstream-downstream phase correlation with positive  $R_{56}$  values, and a large anti-correlation for negative  $R_{56}$  values (as in this case the residual  $R_{56}$  acts to flip the sign of the phase jitter).

In Figure 4.14 plotting the theoretical downstream jitter with  $\rho_{up} = 0.9$  gives a clear demonstration that the best conditions for the PFF correction are always with  $R_{56} = 0$  rather than with the lowest possible initial downstream jitter, as mentioned in Section 4.3.3.

## 4.4 Mitigation of First Order Energy Dependence

The discussion in the Section 4.3.4 proves that with a residual  $R_{56}$  value of -0.2 m between the upstream and downstream phase monitors it is impossible to achieve the goals of the PFF prototype at CTF3. However, due to the highly constrained optics in TL2 it has already been seen in Chapter 2 that it was not possible to find optics for the PFF chicane that yield zero  $R_{56}$  whilst also meeting requirements for both the PFF system and transverse matching. The only way to create a total  $R_{56}$  of zero between the upstream and downstream phase monitors is therefore to add positive  $R_{56}$  to one of the other beam lines in-between the two monitors in order to compensate for the negative  $R_{56}$  in the TL2 chicane.

New optics for the transfer line TL1 with positive  $R_{56}$  values have been created to achieve this. TL1 transports the beam from the CT line (where the upstream phase monitors are installed) to the combiner ring, as seen in Figure 1.5. The layout of the TL1 transfer line is shown in Figure 4.15. It consists of: 4 dipoles (bending the beam horizontally) of 2 different types, 13 quadrupoles of 5 different types, 7 magnetic correctors, 1 sextupole (usually not used) and 8 BPMs [75] (the dispersive BPM after the first dipole in TL1, labelled CT.BPI0608, is the device that has been used to determine correlations between the phase and energy in this chapter). The total length of TL1 is approximately 30 m.

### 4.4.1 Matched Optics for TL1

Although in theory only one set of optics with  $R_{56} = +0.2$  m in TL1 is required to compensate for the  $R_{56} = -0.2$  m in TL2, in practice errors in the MADX model of CTF3 in addition to the effect of higher order energy dependences (see Section 4.5) mean it is not possible to know precisely what the optimal  $R_{56}$  in TL1 will be, and it is also possible that this value will vary with time. To determine the optimal value it is also useful to scan the  $R_{56}$  value in TL1 across a wide range of values. To allow this, MADX has been used to match optics for TL1 with  $R_{56}$  values ranging from -0.3 m to +0.6 m in steps of 0.5 cm (a total of 181 sets of optics). The optimal  $R_{56}$  value should always be guaranteed to be in this range, and the

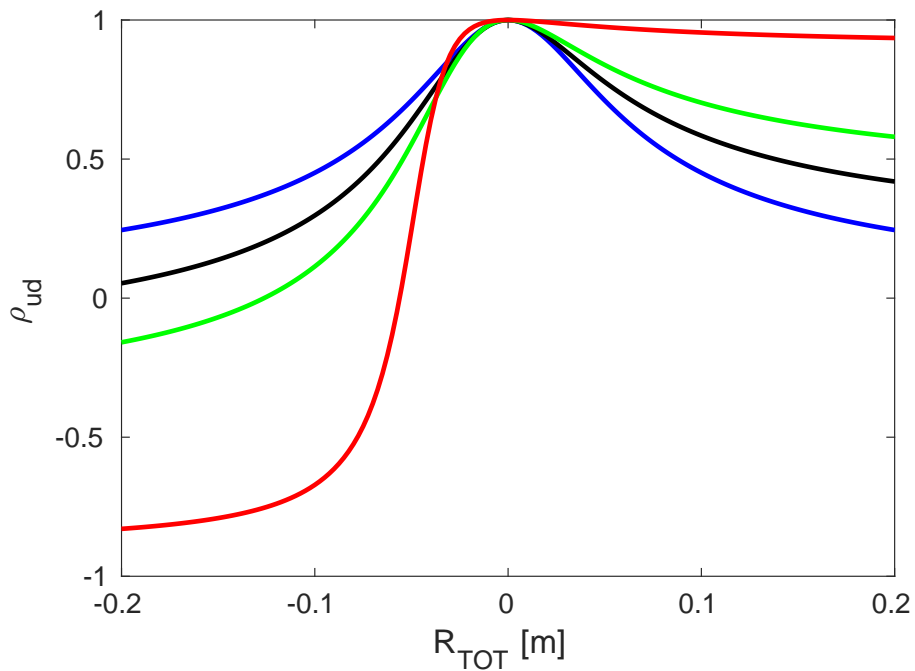


Figure 4.13: Upstream-downstream phase correlation ( $\rho_{ud}$ ) vs. the  $R_{56}$  coefficient between the upstream and downstream phase monitors ( $R_{TOT}$ ) for different upstream phase-energy correlations:  $\rho_{up} = 0.0$  (blue),  $\rho_{up} = 0.2$  (black),  $\rho_{up} = 0.4$  (green) and  $\rho_{up} = 0.9$  (red).

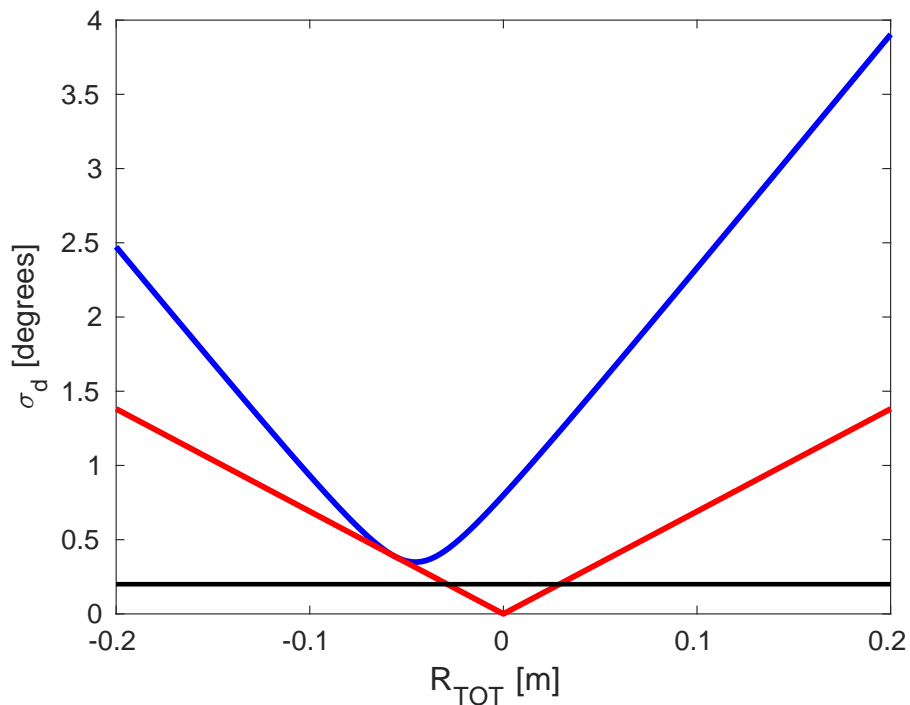


Figure 4.14: Initial (blue) and corrected (red) downstream phase jitter ( $\sigma_d$ ) vs. the  $R_{56}$  coefficient between the upstream and downstream phase monitors ( $R_{TOT}$ ) with 90% correlation between the upstream phase and the beam energy.

#### 4.4 Mitigation of First Order Energy Dependence

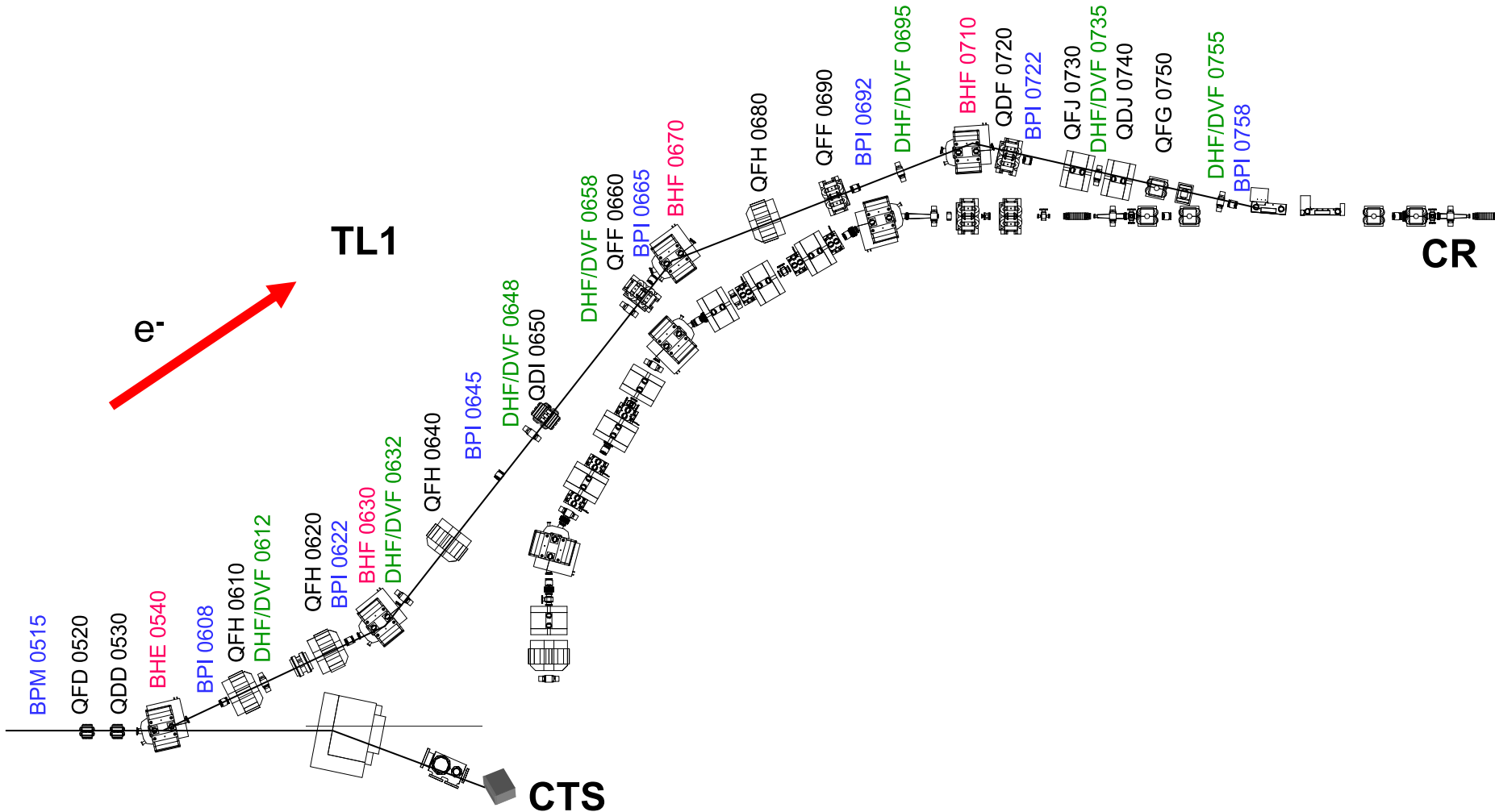


Figure 4.15: Layout of dipoles (labels starting with BH, red), quadrupoles (labels starting with QF or QD, black), BPMs (labels starting with BPM or BPI, blue), correctors (labels starting with DH or DV, green) in the TL1 transfer line [76].

Parameter	TL1 Injection	CR Injection
$\beta_x$	8.81 m	4.08 m
$\beta_y$	13.94 m	5.41 m
$\alpha_x$	-0.74	-0.31
$\alpha_y$	-0.45	-0.21
$D_x$	0 m	-0.03 m
$D_{px}$	0	0.02

Table 4.2: Initial and final conditions for optics matching in TL1.

step size of 0.5 cm allows the residual  $R_{56}$  to be zeroed to within one centimetre as derived to be necessary in Section 4.3.4.

As well as the different  $R_{56}$  values, each set of optics must maintain the same initial and final conditions, so that the injection of the beam in to the combiner ring is not affected. Values for the beta functions, alphas and dispersion at the start of TL1 and at the combiner ring injection are summarised in Table 4.2. As well as the initial and final conditions, the maximum beta functions and dispersion in TL1 are constrained to ensure a reasonable beam size throughout the line — the horizontal and vertical beta function is limited to a maximum of 35 m, and the horizontal dispersion to a maximum absolute value of 1.25 m. Around the septum used for injection in to the combiner ring the horizontal beta function is further limited to a maximum of 10 m. The strengths of the 13 quadrupoles in TL1 are varied to meet all these constraints.

Figure 4.16 shows the matched  $R_{56}$  value in TL1 across the range of targeted values. Each matched  $R_{56}$  value is within 10 microns of the desired result. Furthermore, Figure 4.17 shows an example of how the strength of one of the quadrupoles must be varied in order to achieve each  $R_{56}$  value. If the dependence of each quadrupole strength on the  $R_{56}$  value was continuous the relationship could be fitted to create a set of tuning knobs to allow  $R_{56}$  to be set to any arbitrary value in TL1. However, as seen in Figure 4.17 there are many discontinuities. The quadrupole strengths for each set of optics are therefore saved to a lookup table, with a MatLab function created to read the table and set the quadrupole currents in the machine appropriate for the specified  $R_{56}$  value. As already mentioned 0.5 cm precision in  $R_{56}$  should be adequate for the PFF requirements, but the discontinuities mean new optics would have to be matched if optics with an  $R_{56}$  value not included in the discrete set used here were required.

For reference Figures 4.18, 4.19, and 4.20 show how the horizontal and vertical beta functions and horizontal dispersion changes in TL1 for each set of optics. For all  $R_{56}$  values each parameter converges to the same value at the start and end of TL1, as needed to ensure that changing the optics does not impact injection in to the combiner ring. The maximum horizontal and vertical beta functions in TL1 roughly increase with the set  $R_{56}$  value, but in all cases are kept below the set limit of 35 m in the matching procedure. The dispersion pattern in TL1 also changes with the set  $R_{56}$  value, though in most cases the maximum absolute dispersion is around 1 m and only the location of the peak dispersion along the line changes. Again, for each set of optics the maximum absolute dispersion is limited within the

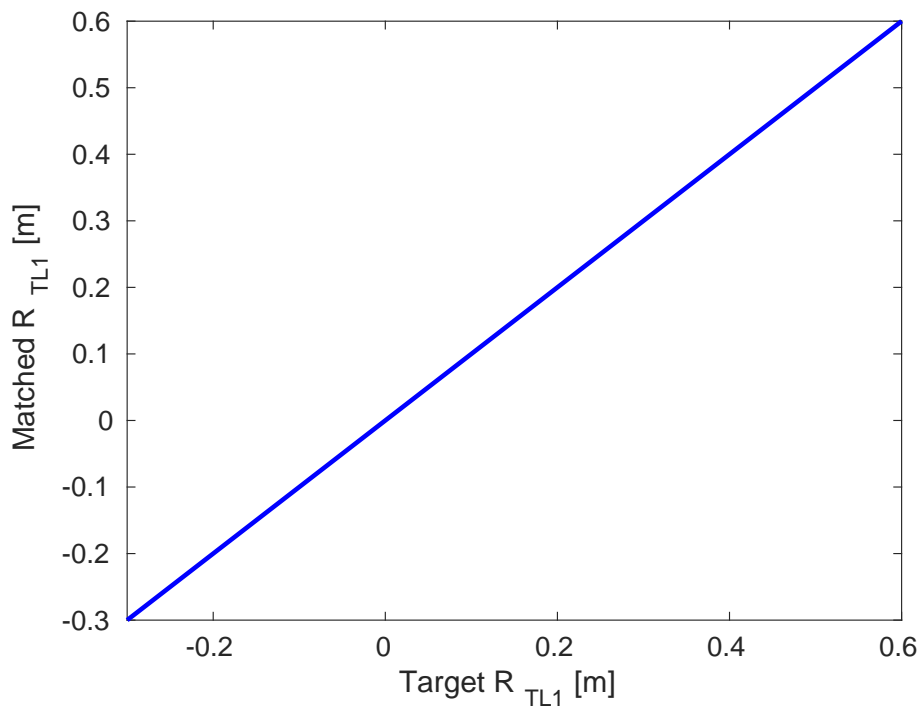


Figure 4.16: Matched  $R_{56}$  values in TL1 ( $R_{TL1}$ ) for the new sets of TL1 optics.

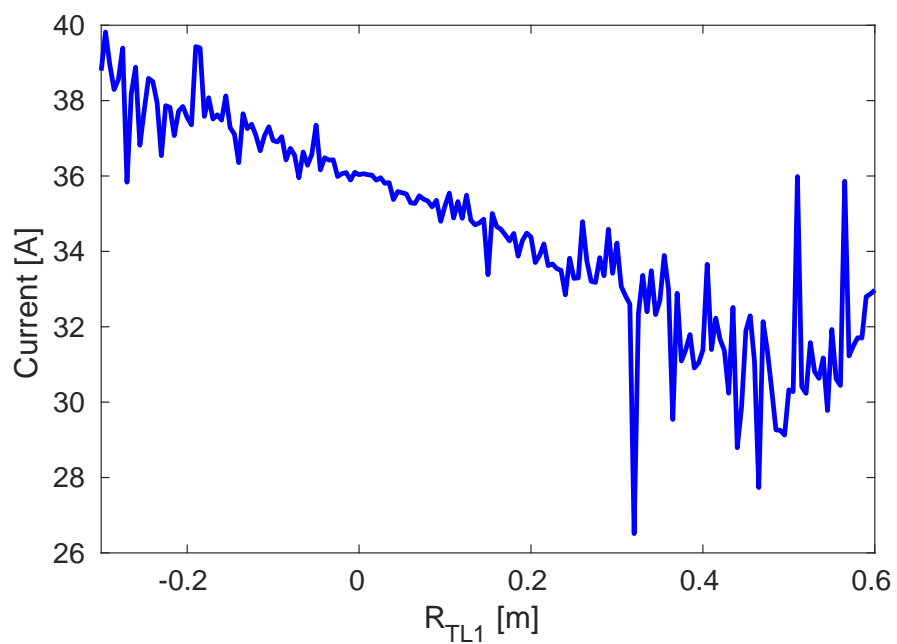


Figure 4.17: Strength (power supply current) of the CT.QFG0750 quadrupole in TL1 vs. the  $R_{56}$  value in TL1 ( $R_{TL1}$ ) for each set of matched optics.

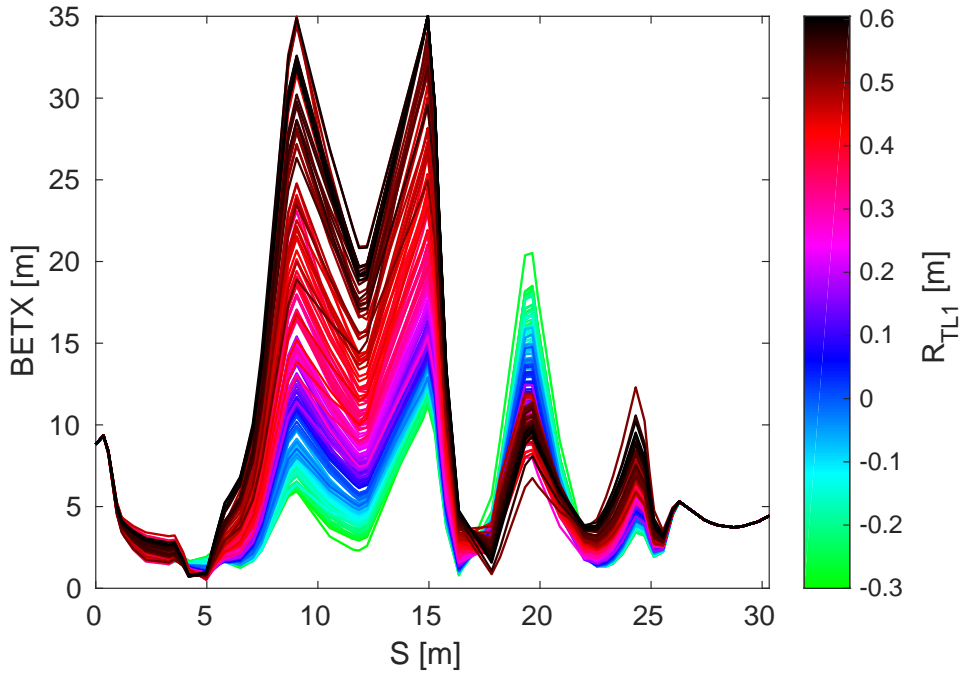


Figure 4.18: Horizontal beta function in each set of optics for TL1, with the colour scale indicating the  $R_{56}$  value in TL1 for that optics.

set constraint of 1.25 m.

Commissioning of the new TL1 optics in CTF3 was straightforward and in general they can be set with the quadrupole strengths at their nominal matched values without causing issues for the beam quality [45]. At the extremities of the range of optics (close to  $R_{56} = -0.1$  m and  $R_{56} = +0.6$  m) some slight beam losses do begin to occur, but this is not a problem for PFF operation where the required  $R_{56}$  is only 0.2 m. However, for each set of optics the magnetic correctors in TL1 may need to be changed to recover the nominal beam orbit, thus taking in to account slight misalignments in elements along the line.

#### 4.4.2 Scans of $R_{56}$ in TL1

The sets of matched optics from Section 4.4.1 can be used to perform scans of the  $R_{56}$  value in TL1 and then observe the effect on the downstream phase. Scans of this type must be performed prior to all PFF data taking periods in order to optimise the beam conditions (maximise the upstream-downstream phase correlation) for the correction. More recently scans of  $R_{56}$  in TL1 have been performed whilst varying the beam energy, which produces cleaner results and highlights additional factors that must be taken in to account during the optimisation process, as will be shown in Section 4.5.

As a starting point the simplest case, where only the TL1 optics is changed during the scan and all other parameters in the machine are left unchanged, is presented in this section. This also highlights some of the difficulties in maintaining beam conditions at CTF3, which is discussed further in Section 4.5 and in the context of the PFF correction in Section 6.2.

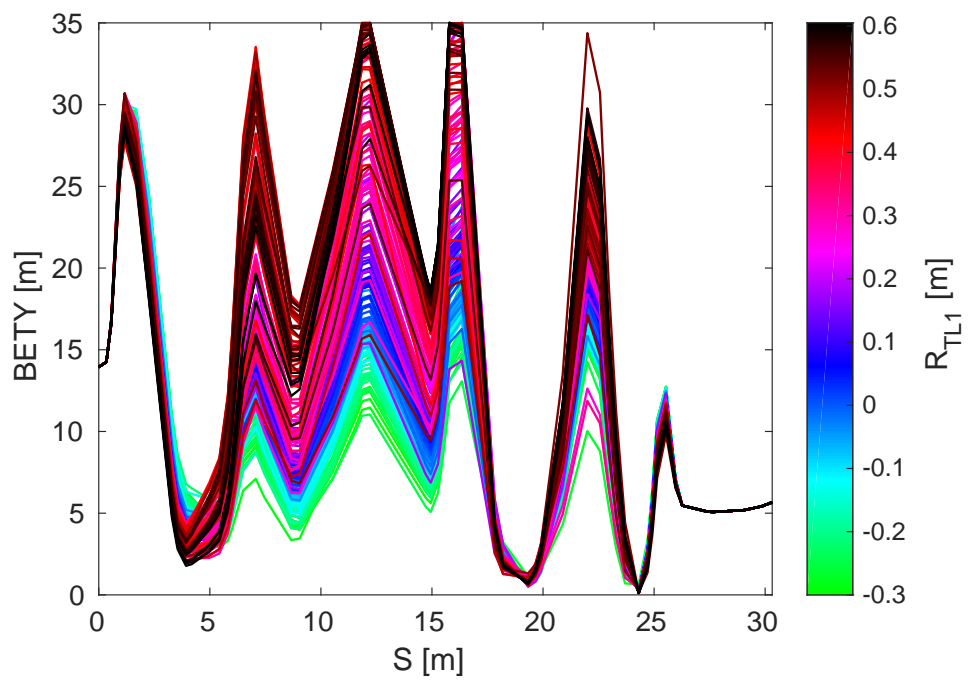


Figure 4.19: Vertical beta function in each set of optics for TL1, with the colour scale indicating the  $R_{56}$  value in TL1 for that optics.

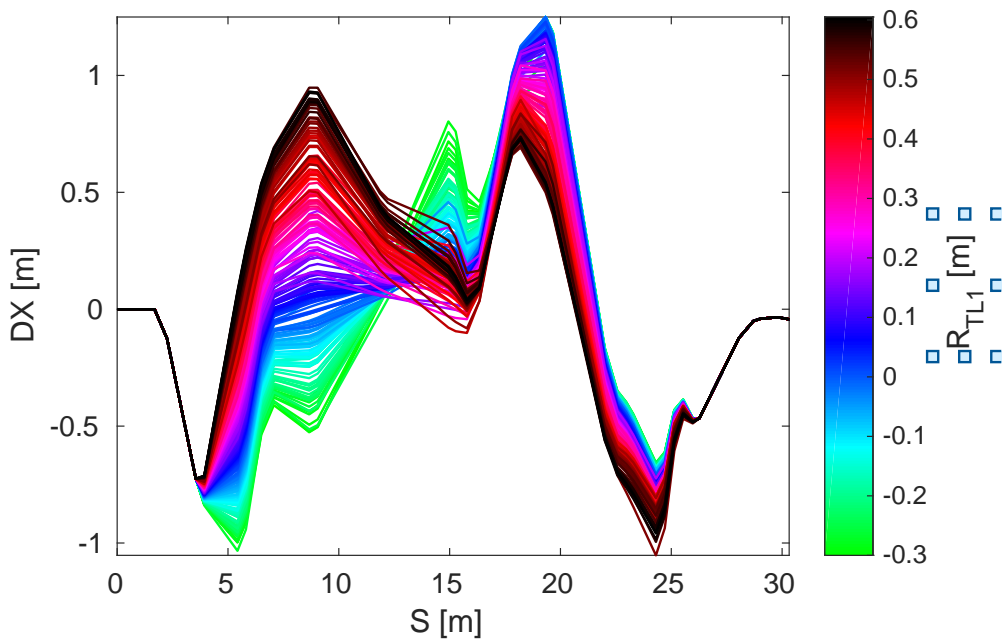


Figure 4.20: Horizontal dispersion in each set of optics for TL1, with the colour scale indicating the  $R_{56}$  value in TL1 for that optics.

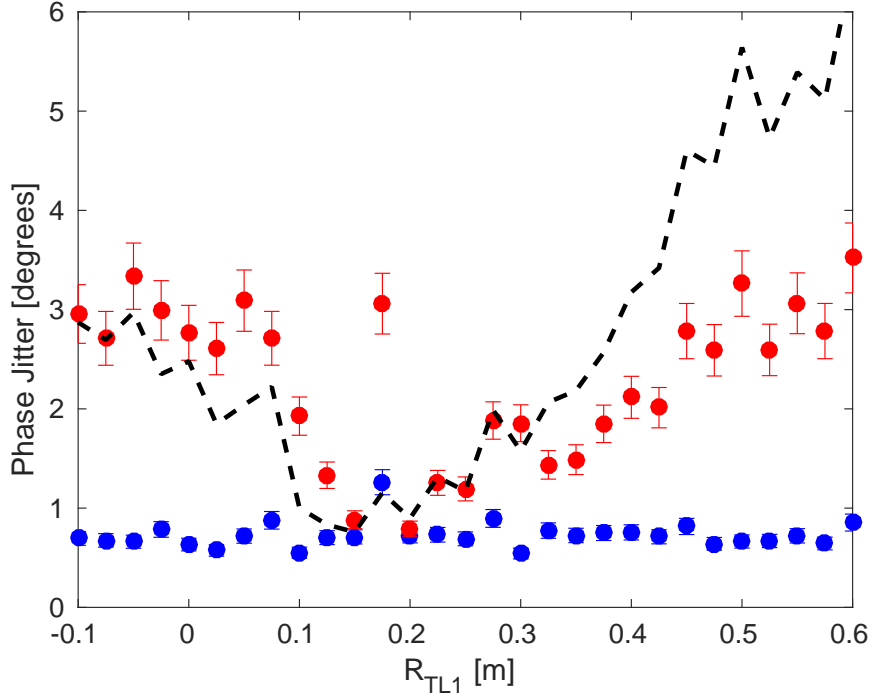


Figure 4.21: Phase jitter upstream (blue) and downstream (red) during a scan of  $R_{56}$  in TL1. The dashed line shows a simulation of the expected downstream phase jitter given the beam conditions in each dataset.

Figures 4.21 and 4.22 show one example of an  $R_{56}$  scan performed across a wide range – from  $-0.1$  m to  $+0.6$  m in TL1. The  $R_{56}$  is incremented by 2.5 cm between datasets, to give a total of 29  $R_{56}$  values in the scan, with the whole scan taking approximately one and a half hours to complete. With the knowledge gained from measurements of this type it is no longer necessary to scan the  $R_{56}$  across the full range to determine the ideal value, thus the optimisation of the phase propagation for PFF attempts can now be achieved on much shorter time scales.

### Mean Phase

Only the mean phase jitters and correlation will be considered here, features along the pulse are discussed in Section 4.5.2 for a different scan. Figure 4.21 shows the upstream and downstream mean phase jitter during the scan. The downstream phase jitter is reduced from above 2.5 degrees with zero  $R_{56}$  in TL1, to below 1 degree and close to the level of the upstream phase jitter by adding positive  $R_{56}$  in TL1. The optimal  $R_{56}$  value is approximately 0.175 m, in close agreement with expectations considering the  $-0.2$  m  $R_{56}$  in TL2. The upstream-downstream phase correlation, in Figure 4.22, is also maximised at this point, from an initial correlation of 20% with zero  $R_{56}$  to up to 80%. In terms of the PFF system, increasing the upstream-downstream phase correlation from 20% to 80% improves the theoretical correction from a 2% reduction in downstream phase jitter to a 40% decrease (Equation 4.5).

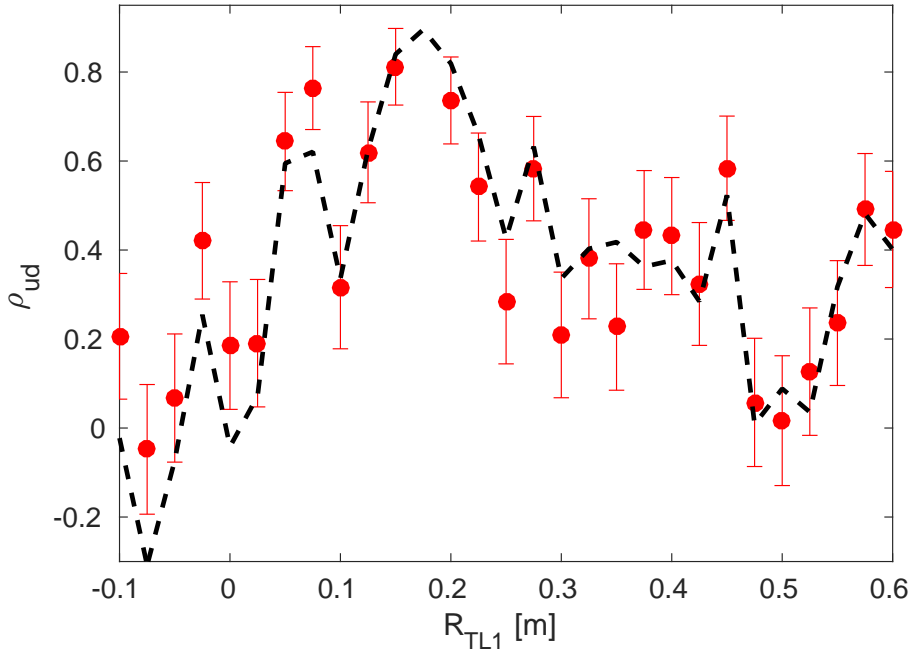


Figure 4.22: Upstream-downstream phase correlation (red) during a scan of  $R_{56}$  in TL1. The dashed line shows a simulation of the expected correlation given the beam conditions in each dataset.

As the upstream phase monitors are prior to TL1, changing the TL1 optics has no effect on the upstream phase jitter. All differences in the upstream phase jitter between datasets are caused by drifts in the CTF3 injector, typically changes in either klystron phases or beam current. Although the overall stability of the upstream phase jitter during this scan is good, it does vary between 0.5 degrees and 1.2 degrees. In addition to the upstream phase there are also differences in the relative energy jitter and upstream phase-energy correlation during the scan, as seen in Figure 4.23. The relative beam energy jitter varies between  $0.4 \times 10^{-3}$  and  $1.0 \times 10^{-3}$  and the upstream phase-energy correlation between -0.5 and +0.5. All these parameters influence the downstream phase, as per the equations in Section 4.3.3.

Differences in the phase jitter and phase-energy correlation between datasets partially explains the deviation of individual data points away from the pure dependence on  $R_{56}$  seen in Figures 4.11 and 4.12 for stable conditions. The simulated lines in Figures 4.21 and 4.22 represent the expected downstream phase jitter and upstream-downstream phase correlation taking in to account the upstream phase jitter, relative energy jitter and upstream phase-energy correlation for each point in the scan (using Equations 4.8 and 4.14). The simulated upstream-downstream phase correlation in Figure 4.22 has been scaled so that the peak value is in agreement with the data, at 0.8. The majority of the data points follow the scaled simulated distribution, with several remaining outliers. For the downstream phase jitter (which uses the simulated result directly with no scaling) the agreement with the simulation is generally good for  $R_{56}$  values below 0.3 m. However, above 0.3 m the actual phase jitter seen in the scan is smaller than the simulation. One possible explanation for this are the changes in downstream beam current between datasets, which varies by a factor 3 during the

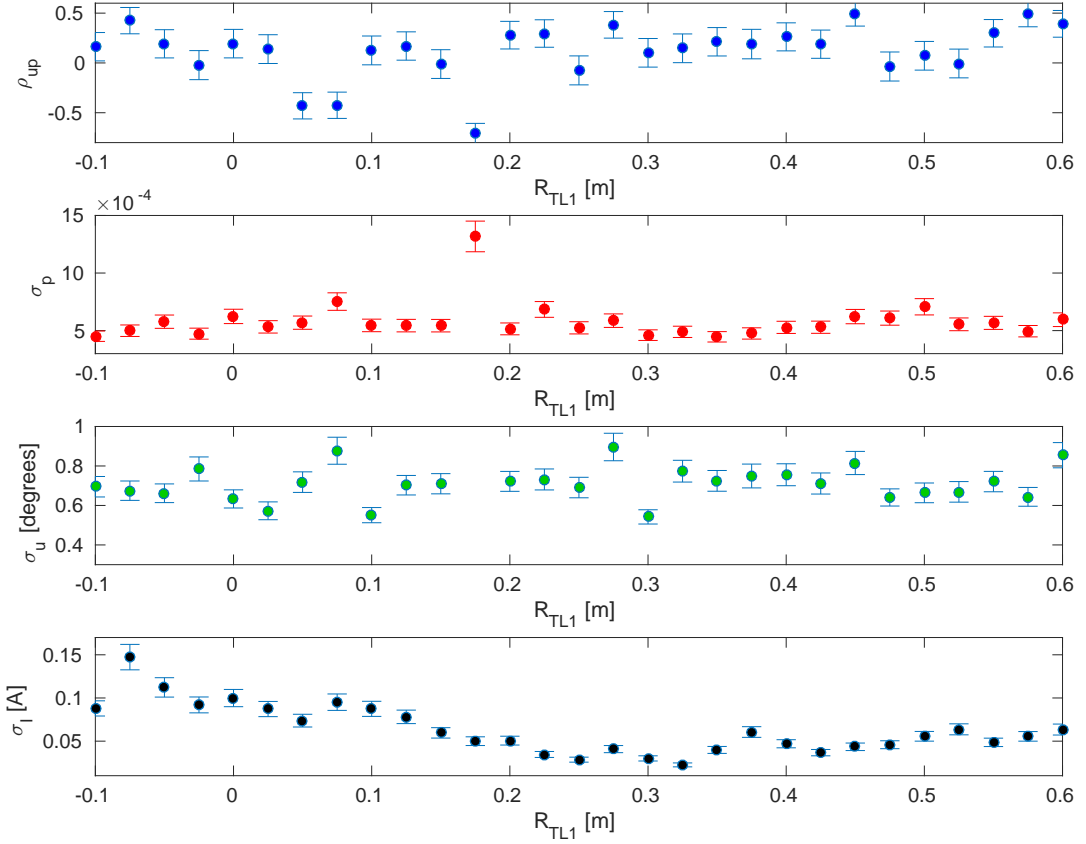


Figure 4.23: Upstream and downstream beam conditions during the  $R_{56}$  scan. From top to bottom: upstream phase-energy correlation (blue), relative energy jitter (red), upstream phase jitter (green) and beam current jitter (black).

scan (bottom plot in Figure 4.23). Small beam losses between measurements may change the phase jitter in a way that is not characterised by the  $R_{56}$ . Possible other sources are discussed in Sections 4.5 and 4.6.

### Results from Other Scans

Figures 4.24 and 4.25 show the results of two further scans of  $R_{56}$  in TL1, both taken a few days after the scan previously shown (Figures 4.21–4.23). For both scans the mean downstream phase jitter can again be decreased to the level of the upstream phase jitter by varying the  $R_{56}$  in TL1, and the upstream-downstream correlation increased to 80%. However, the optimal optics is different for each scan — the scan in Figure 4.24 has an optimal  $R_{56}$  value of around 0.1 m whereas for the scan in Figure 4.25 it is below 0.05 m. Both values are also different to the scan previously shown, which had an optimal  $R_{56}$  setting of 0.175 m.

With  $R_{56}$  alone and the model of the phase propagation used to derive the equations

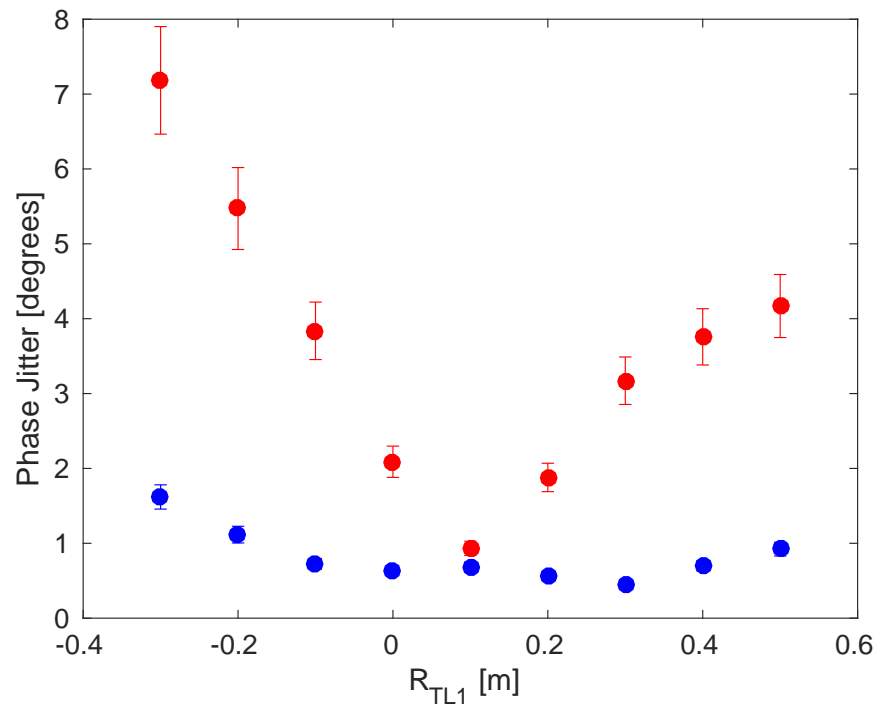


Figure 4.24: Upstream (blue) and downstream (red) phase jitter during an  $R_{56}$  scan in TL1 showing an optimal set point of around  $R_{TL1} = 0.1$  m.

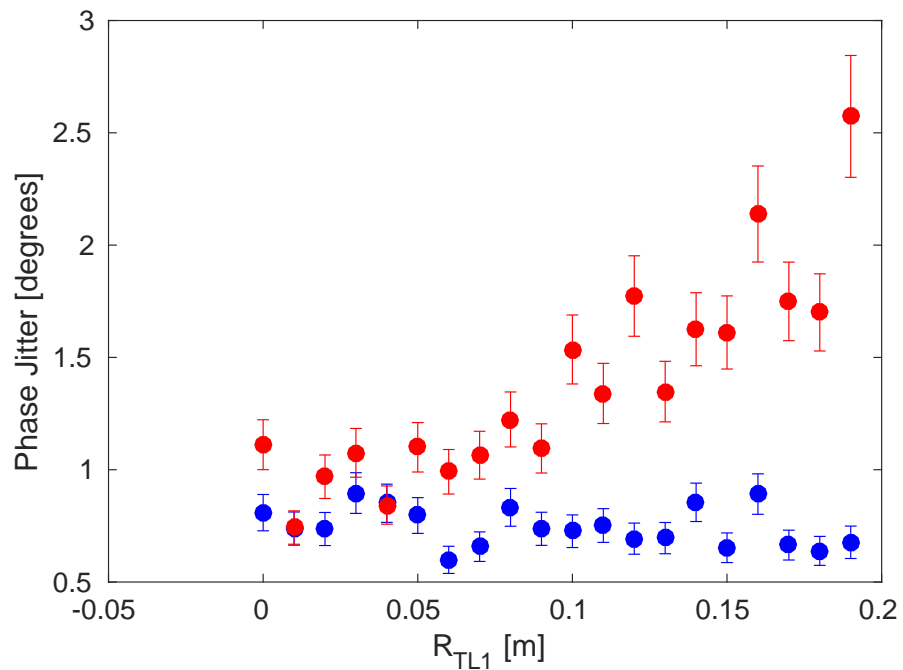


Figure 4.25: Upstream (blue) and downstream (red) phase jitter during an  $R_{56}$  scan in TL1 showing an optimal set point of  $R_{TL1} < 0.05$  m.

in Section 4.3.3 there is no mechanism for the optimal  $R_{56}$  value to vary with time. The best conditions for the phase propagation should always be provided with zero residual  $R_{56}$  between the upstream and downstream phase monitors. As the optics in all beam lines between the upstream and downstream phase monitors (apart from TL1) were unchanged between each scan, the optimal  $R_{56}$  value in TL1 should also be the same for each scan in this model, under the assumption that  $R_{56}$  explains all differences between the upstream and downstream phase. The most likely explanation is a sensitivity to higher order energy dependences, as discussed in Section 4.5.

## 4.5 Higher Order Energy Dependences

In the same way the first order optics dependences are described by the  $6 \times 6$  R-matrix, the second order effects are described using a three dimensional  $6 \times 6 \times 6$  T-matrix.  $R_{56}$  is the relevant first order transfer matrix coefficient for the energy related effects on the phase propagation, as already discussed, and the relevant T-matrix coefficient for second order energy dependences is  $T_{566}$ . By including the second order term the dependence of the downstream phase on the energy from Equation 4.7 becomes:

$$\phi_d = \phi_u + R_{56} \left( \frac{\Delta p}{p} \right) + T_{566} \left( \frac{\Delta p}{p} \right)^2 \quad (4.17)$$

$T_{566}$  introduces another source of energy dependent phase jitter which is independent from the first order  $R_{56}$  value. The ideal case for the phase propagation would be to have both zero  $R_{56}$  and zero  $T_{566}$  between the upstream and downstream phase monitors. However, constraints are not placed on the  $T_{566}$  in the optics at CTF3 and it is therefore typically non-zero. It may be possible to create optics with zero, or at least reduced,  $T_{566}$  for the TL1 and TL2 lines at CTF3 in the future by using the available sextupoles, but this has not yet been pursued, thus it will be treated as a fixed property of the optics here. Assuming constant, non-zero,  $T_{566}$  an expression for the  $R_{56}$  value that minimises the downstream phase-energy dependence can be derived:

$$R_{56} = -2T_{566} \left( \frac{\Delta p}{p} \right) \quad (4.18)$$

This is obtained by zeroing the partial differential of Equation 4.17 with respect to  $\Delta p/p$ .

The above dependence of the  $R_{56}$  value on the beam energy offset has many consequences. Firstly, it provides a mechanism by which the apparent optimal  $R_{56}$  value in TL1 can appear to vary with time (and be non-zero), as was seen comparing the results of different  $R_{56}$  scans in the previous section. CTF3 does experience drifts in beam energy (see Section 6.2.2, for example), creating small offsets between the actual beam energy and the energy that the optics has been set for (i.e. the strength of bending and focusing elements in the accelerator). In other words, it is possible for the mean of  $\Delta p/p$  to be non-zero. The optimal  $R_{56}$  value to use in TL1 is then expected to drift with the beam energy when higher order phase-energy dependences are included.

In addition, energy variations along the beam pulse and jitter in the beam energy mean that the phase propagation cannot be perfectly optimised by varying the  $R_{56}$  alone. Due

to the energy dependence in Equation 4.18, any energy variations along the pulse cause the optimal  $R_{56}$  value to set in TL1 to also vary along the beam pulse. There are static variations in the mean energy along the pulse (e.g. as seen in Section 4.3.1) at CTF3, so this means the phase propagation can never be completely optimised along the full pulse length when  $T_{566}$  is non-zero.

#### 4.5.1 Simulated Effect of $T_{566}$ on the Downstream Phase

When only the first order effect of  $R_{56}$  is considered, the dependence of the downstream phase on the energy is linear, with the gradient depending on the residual  $R_{56}$  value between the upstream and downstream phase monitors. The downstream phase versus beam energy offset with only first order  $R_{56}$  term included is shown in Figure 4.26 for each set of TL1 optics, demonstrating this effect. The optimal  $R_{56}$  value of +0.2 m in TL1 minimises the phase-energy dependence for all energy offsets.

By running varying the initial energy offset in MADX the expected effect of the higher order energy dependences on the downstream phase can be seen. This is shown in Figure 4.27, and the impact of the higher orders is immediately clear. The optimal  $R_{56}$  to use in TL1, where the phase has the minimal dependence on the energy, now depends on the energy offset. Figure 4.28 shows that the dependence of the optimal  $R_{56}$  value on the relative energy offset is linear, as expected from Equation 4.18. The plotted  $R_{56}$  value does not exceed +0.6 m or go below -0.3 m as only the available sets of optics for TL1 are considered, which are restricted to this range.

MADX does not output the optics  $T_{566}$  coefficient directly but it can be approximated using a quadratic fit to the downstream phase vs. energy curves seen in Figure 4.27. The fit coefficients then give the  $T_{566}$  and  $R_{56}$  values, as per Equation 4.17. An example of this is shown in Figure 4.29 for the nominal  $R_{56} = 0$  m optics in TL1, with fitted coefficients of  $R_{56} = -0.2$  m and  $T_{566} = -13.7$  m in this case. As the results from MADX also includes effects above second order there is a slight discrepancy between the quadratic fit and the MADX output. However, including up to the second order energy dependence is enough to characterise the true behaviour and the slight modifications induced by higher orders are beyond the scope of the discussion here.

Figure 4.30 shows the fitted  $T_{566}$  coefficient for all the sets of matched optics in TL1. The changes in  $T_{566}$  across the range of TL1 optics are much smaller than the (intentional) differences in  $R_{56}$ , varying between -13.1 m and -15.4 m. Optics around the usually optimal  $R_{56}$  value of 0.2 m in TL1 are close to where the second order effects are minimal, with  $T_{566}$  values around -13.4 m. The  $T_{566}$  coefficients are approximately two orders of magnitude larger than the  $R_{56}$  but as  $(\Delta p/p)^2 \ll (\Delta p/p) \ll 1$  the effect on the phase is smaller than for non-optimised  $R_{56}$ . For example, for a typical relative energy offset of  $1 \times 10^{-3}$  a residual  $R_{56}$  of 0.2 m between the upstream and downstream phase monitors leads to a phase shift of more than one degree. For the same energy offset the phase shift resulting from the second order  $T_{566}$  term is approximately 0.1 degrees. However, the key point for the phase propagation is that the first order dependence can be removed by zeroing  $R_{56}$  between the upstream and downstream phase monitors, whereas for all the available sets of optics the

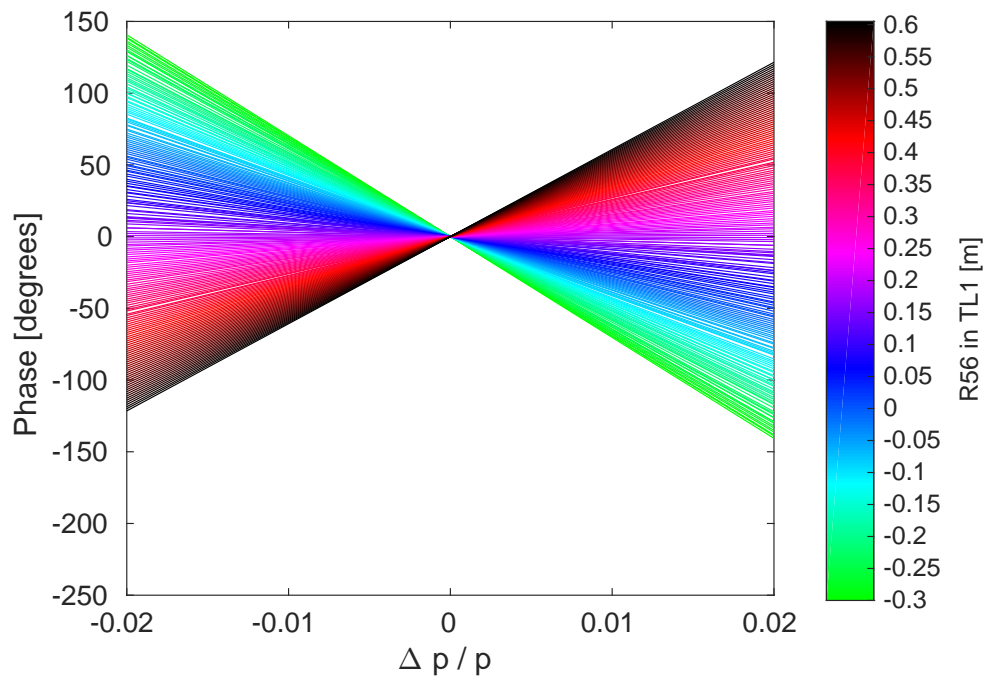


Figure 4.26: Dependence of the downstream phase on the relative energy offset for all sets of TL1 optics when only  $R_{56}$  is considered.

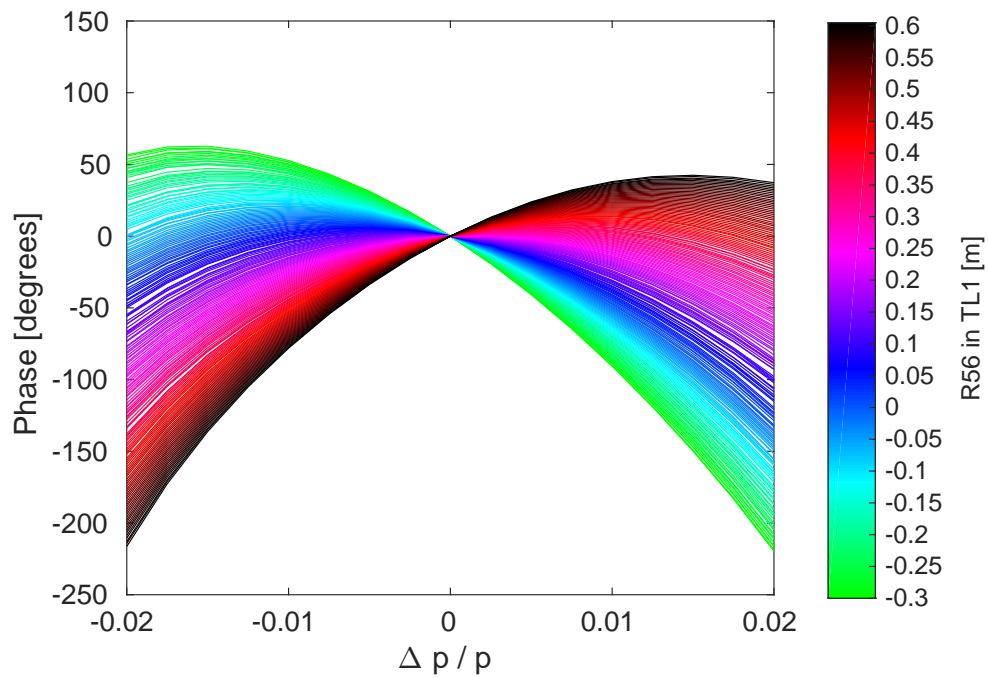


Figure 4.27: Dependence of the downstream phase on the relative energy offset for all sets of TL1 optics including higher order effects.

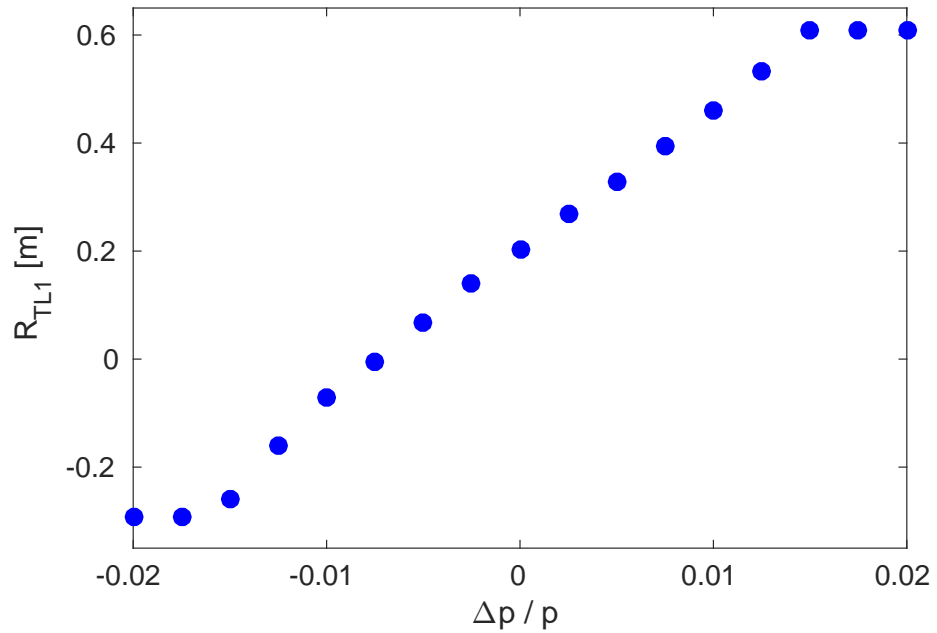


Figure 4.28: Dependence of the optimal optics to use in TL1 on the relative energy offset.

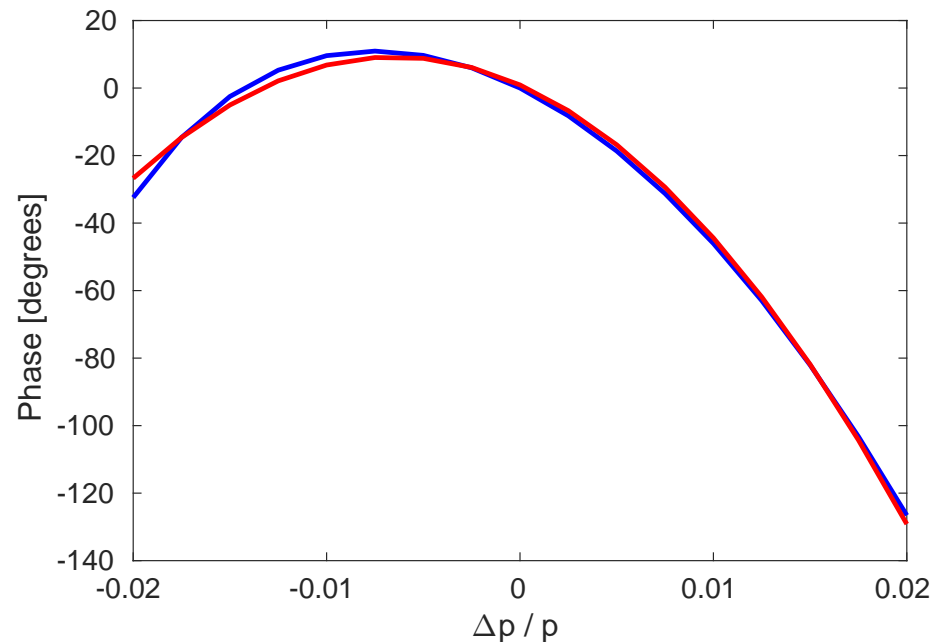


Figure 4.29: Quadratic fit (red) to the simulated downstream phase from MADX for different energy offsets (blue) for the nominal  $R_{56} = 0$  m optics in TL1.

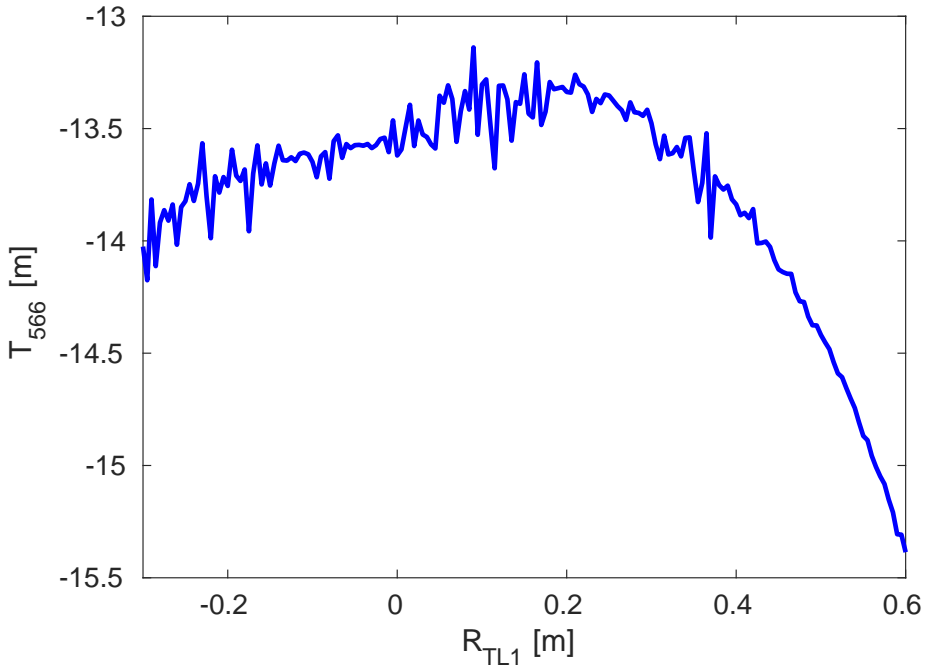


Figure 4.30:  $T_{566}$  coefficient between the upstream and downstream phase monitors for all sets of TL1 optics.

second order contribution will remain at roughly the same magnitude.

To determine the consequences of the  $T_{566}$  for the PFF system, the effect it has on the upstream-downstream phase correlation and downstream phase jitter must be calculated. This was done analytically using the equations in Section 4.3.3 for the first order  $R_{56}$ , but for the second order terms a simple Monte Carlo simulation approach has been used. Correlated random distributions are created in MatLab to match the typical CTF3 upstream phase and energy conditions — namely  $\sigma_p = 0.001$ ,  $\sigma_u = 0.8^\circ$  and  $\rho_{up} = 0.2$ . The simulated downstream phase for each set of TL1 optics is then calculated using Equation 4.17 and the known  $R_{56}$  and  $T_{566}$  values. The jitter of this simulated downstream phase and its correlation with the initial upstream phase distribution give the values shown in the following figures.

Figure 4.31 shows the downstream phase jitter versus the residual  $R_{56}$  between the upstream and downstream phase monitors in the case where only the first order  $R_{56}$  term is included and when both the  $R_{56}$  and the second order  $T_{566}$  are included. The effect of including  $T_{566}$  is very small, with the downstream phase jitter only increasing from  $0.80^\circ$  to  $0.85^\circ$  degrees at the optimal residual  $R_{56}$  of zero. The effect of including  $T_{566}$  on the upstream-downstream phase correlation is much more significant for the PFF correction. The maximum achievable correlation (excluding the effects of the phase monitor resolution) is reduced from  $\rho_{ud} = 1$  with only the first order term to  $\rho_{ud} = 0.95$  when  $T_{566}$  is included. This is shown in Figure 4.32. The achievable corrected downstream phase jitter with the PFF system is increased from zero to  $0.27^\circ$  (again excluding the phase monitor resolution).

With the initial conditions and optics used here it would therefore be impossible to achieve  $0.2^\circ$  phase stability at CTF3. However, the relative energy jitter of  $1 \times 10^{-3}$  is

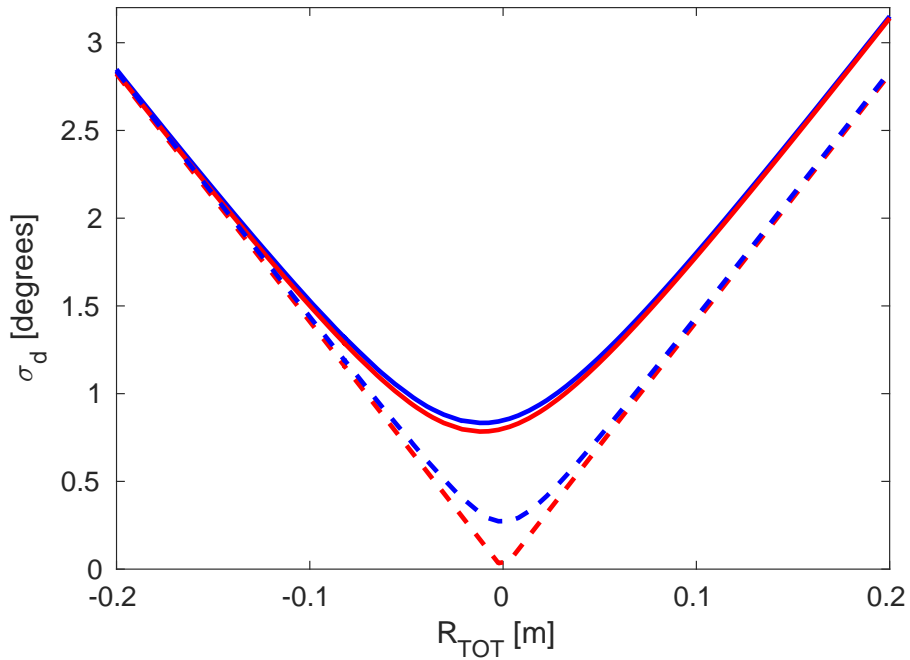


Figure 4.31: Downstream phase jitter ( $\sigma_d$ ) vs.  $R_{56}$  between the upstream and downstream phase monitors ( $R_{\text{TOT}}$ ). Blue lines include the effects of both  $R_{56}$  and  $T_{566}$ , whereas red lines include only the first order  $R_{56}$  term. Solid lines show the initial downstream jitter, and dashed lines the achievable corrected downstream phase jitter. Beam conditions of  $\sigma_u = 0.8^\circ$ ,  $\rho_{up} = 0.2$  and  $\sigma_p = 1 \times 10^{-3}$  are used for the simulation.

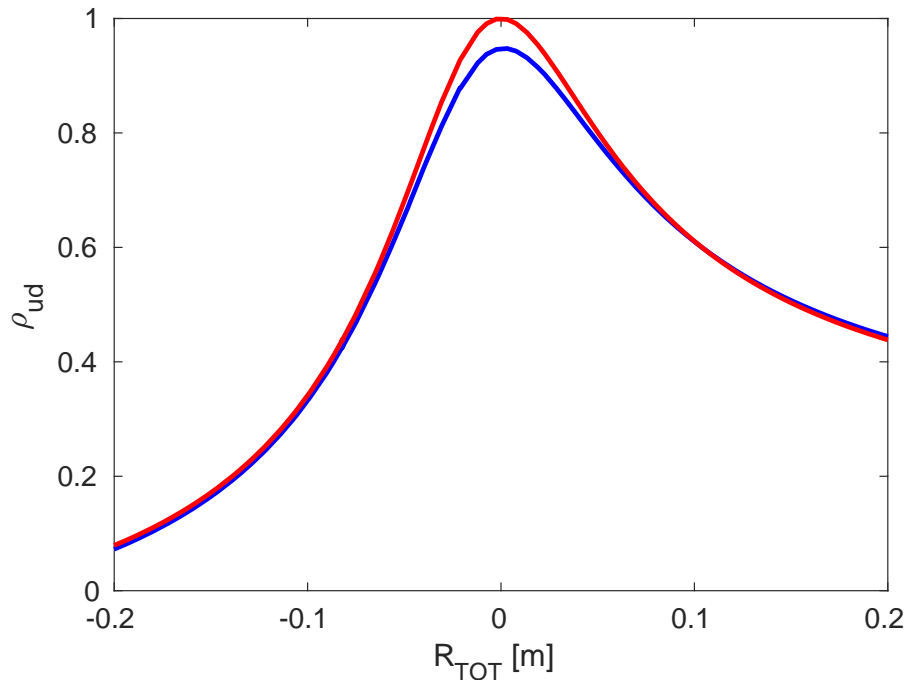


Figure 4.32: Upstream-downstream phase correlation ( $\rho_{ud}$ ) vs.  $R_{56}$  between the upstream and downstream phase monitors ( $R_{\text{TOT}}$ ). The blue line includes the effects of both  $R_{56}$  and  $T_{566}$ , whereas the red line includes only the first order  $R_{56}$  term. Beam conditions of  $\sigma_u = 0.8^\circ$ ,  $\rho_{up} = 0.2$  and  $\sigma_p = 1 \times 10^{-3}$  are used for the simulation.

in fact somewhat pessimistic for the conditions that can be achieved at CTF3, at least on short time scales. Figure 4.33 shows how the maximum achievable upstream-downstream phase correlation varies with the relative energy jitter when the effect of  $T_{566}$  is included. An upstream-downstream phase correlation of 97% is required to make achieving 0.2° downstream phase jitter at CTF3 possible. This can be achieved with a relative energy jitter of  $0.85 \times 10^{-3}$  if the  $R_{56}$  is perfectly optimised. In good conditions, especially with recent developments (Section 4.5.3), the CTF3 energy jitter can be reduced to around  $0.5 \times 10^{-3}$  on short timescales, in which case correlations up to 99.6% are theoretically achievable. With further improvements to the energy stability of CTF3 it should therefore still be possible to achieve the necessary conditions for the PFF system even after taking in to account  $T_{566}$ .

One final consequence of the non-zero  $T_{566}$  between the upstream and downstream phase monitors is the effect of energy variations along the pulse, or equivalently cases where the mean value of  $\Delta p/p$  is non-zero. All previous calculations have assumed the energy jitter to be about a mean  $\Delta p/p$  of zero, but this can not be true for all points along the CTF3 pulse due to the variations in mean beam energy along the pulse seen in Section 4.3.1. The effect of mean energy offsets on the upstream-downstream phase correlation is shown in Figure 4.34, in this case assuming a relative energy jitter of  $0.5 \times 10^{-3}$  about the offset mean value and zero  $R_{56}$ . Typically the energy variation along the CTF3 pulse is at the  $\pm 2 \times 10^{-3}$  level, and this by itself can cause the correlation to drop below 90%. As a result the achievable corrected downstream phase jitter with the PFF system will also vary along the pulse. Without reducing either the energy variations along the pulse, or changing the optics to decrease the magnitude of  $T_{566}$ , it is unlikely that 0.2° sample-by-sample jitter along the pulse can be achieved for more than very short portions of the pulse where the energy is optimal. Reducing energy variations along the pulse to below  $\pm 1 \times 10^{-3}$  would allow correlations above 96% to be achieved across the full pulse length, increasing the feasibility of achieving the 0.2° target. New feedbacks have been developed at CTF3 to try to achieve this (Section 4.5.3).

### 4.5.2 R<sub>56</sub> Scans whilst Varying Beam Energy

By intentionally varying the CTF3 beam energy to artificially increase the energy jitter during an  $R_{56}$  scan the energy dependent effects in both the upstream and the downstream phase are amplified. This has the benefit of increasing the visibility of the higher order effects, but it also improves the results of the scan in general by reducing the sensitivity to other small drifts in beam conditions. In this section the results of an  $R_{56}$  scan in which the  $R_{56}$  value in TL1 was varied between -0.1 m and +0.3 m whilst the beam energy was varied by approximately 1% peak-to-peak are discussed. The resulting relative energy jitter is  $3 \times 10^{-3}$ , or 3–6 times larger than the relative energy jitter in nominal conditions. Direct observations of the effect of higher order energy dependences during the scan will be presented first, before discussing the overall results of the scan to expand upon the conclusions from the  $R_{56}$  scans shown in Section 4.4.2.

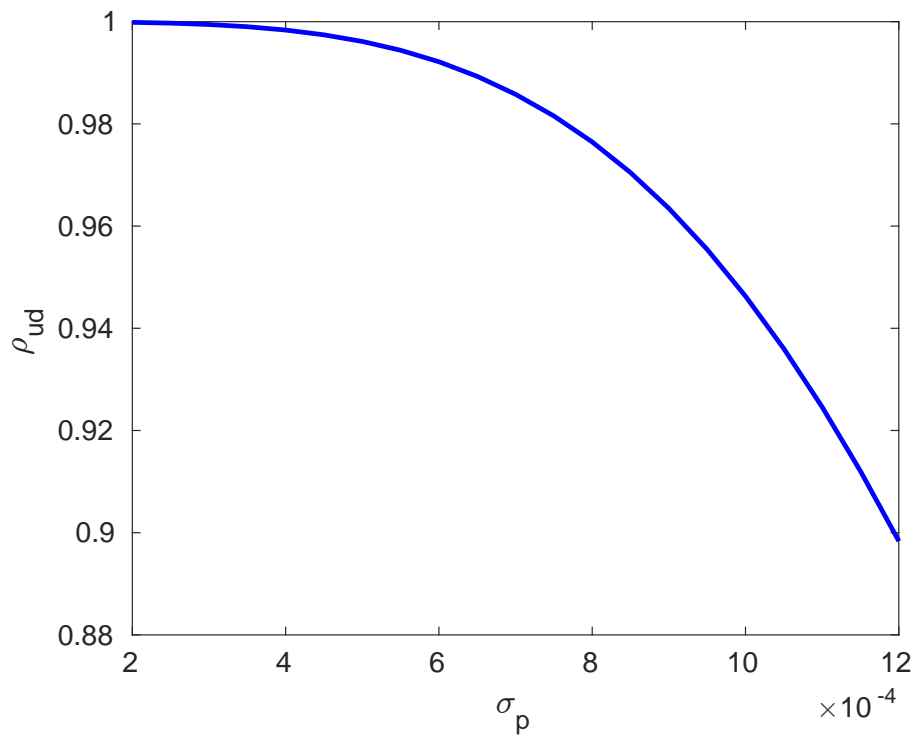


Figure 4.33: Simulated upstream-downstream phase correlation ( $\rho_{ud}$ ) vs. relative beam energy jitter ( $\sigma_d$ ) including the second order  $T_{566}$  term.

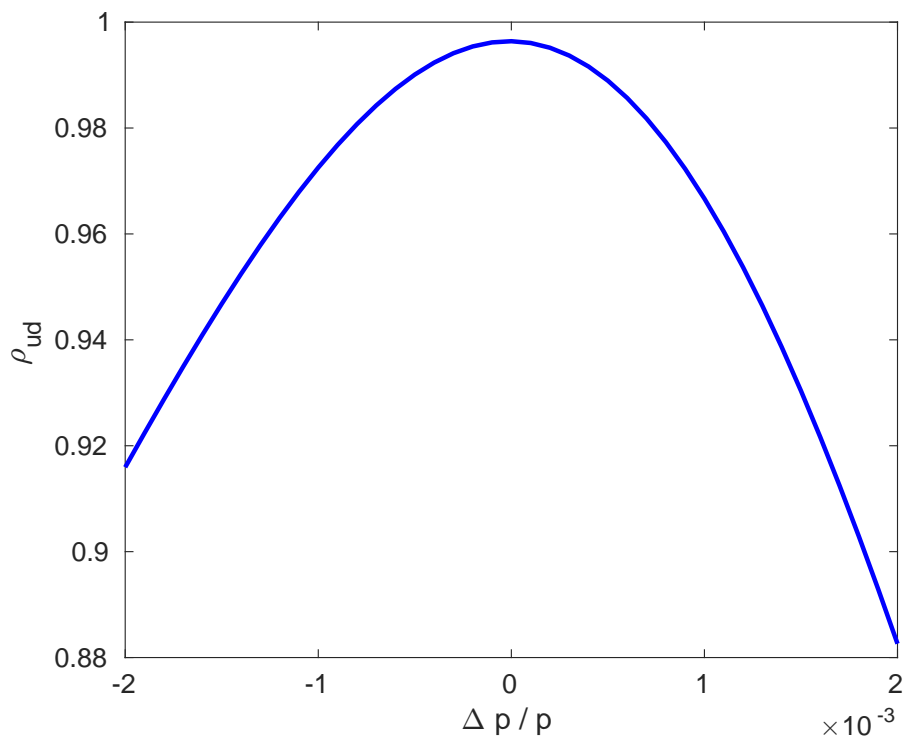


Figure 4.34: Simulated upstream-downstream phase correlation ( $\rho_{ud}$ ) vs. relative beam energy offset ( $\Delta p / p$ ) including the second order effects of  $T_{566}$ .

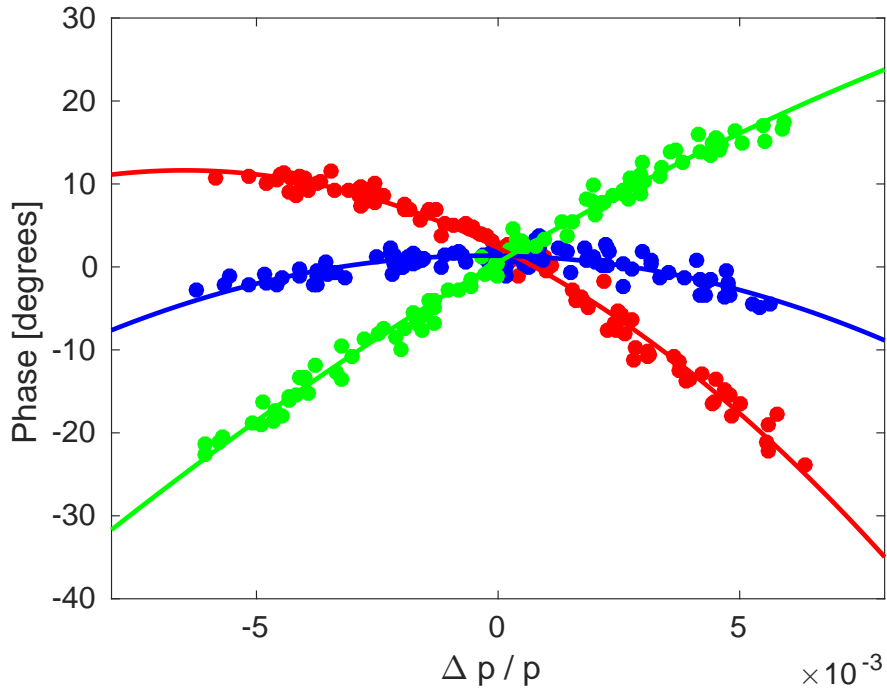


Figure 4.35: Measured downstream phase vs. beam energy ( $\Delta p/p$ ) for three different sets of  $R_{56}$  optics in TL1:  $R_{TL1} = -0.100$  m (red),  $R_{TL1} = 0.075$  m (blue), and  $R_{TL1} = 0.300$  m (green). Lines show quadratic fits to the data for each set of optics.

### Energy Dependence

Figure 4.35 shows the dependence of the mean downstream phase on the beam energy for three of the  $R_{56}$  values set in TL1 during the scan – the lowest value of  $-0.1$  m, the maximum value of  $0.3$  m and a mid-range value of  $0.075$  m, which gives the lowest downstream phase jitter during the scan as seen later in this section. This plot shows similar features to the simulated result from MADX in Figure 4.27. With the increased energy jitter the non-linear dependence of the downstream phase on the energy is clear. The first order effect means that changing the  $R_{56}$  value changes the gradient of the phase-energy dependence about the central energy. The effect of  $T_{566}$  means that there is an energy dependent  $R_{56}$  value that minimises the phase-energy dependence. For example, for an  $R_{56}$  of  $-0.1$  m in TL1, the minimum energy dependence will be observed for an energy offset of around  $-7 \times 10^{-3}$  in Figure 4.35.

The coefficients of a quadratic fit to the curves in Figure 4.35 (plus their equivalents for other points in the scan) give estimates for the residual  $R_{56}$  and  $T_{566}$  values between the upstream and downstream phase monitors. The results of doing this are shown in Figure 4.36 for the fitted  $R_{56}$  values, and Figure 4.37 for the fitted  $T_{566}$  values.

The fitted  $R_{56}$  values roughly follow a linear dependence on the set  $R_{56}$  optics in TL1, as expected. With an  $R_{56}$  value of  $-0.2$  m in TL2, varying the  $R_{56}$  between  $-0.1$  and  $+0.3$  m in TL1 would be expected to give a total residual  $R_{56}$  of between  $-0.3$  m and  $+0.1$  m. The fitted range is between  $-0.20$  m and  $+0.25$  m, so is  $+0.1$  m offset compared to expectations. The

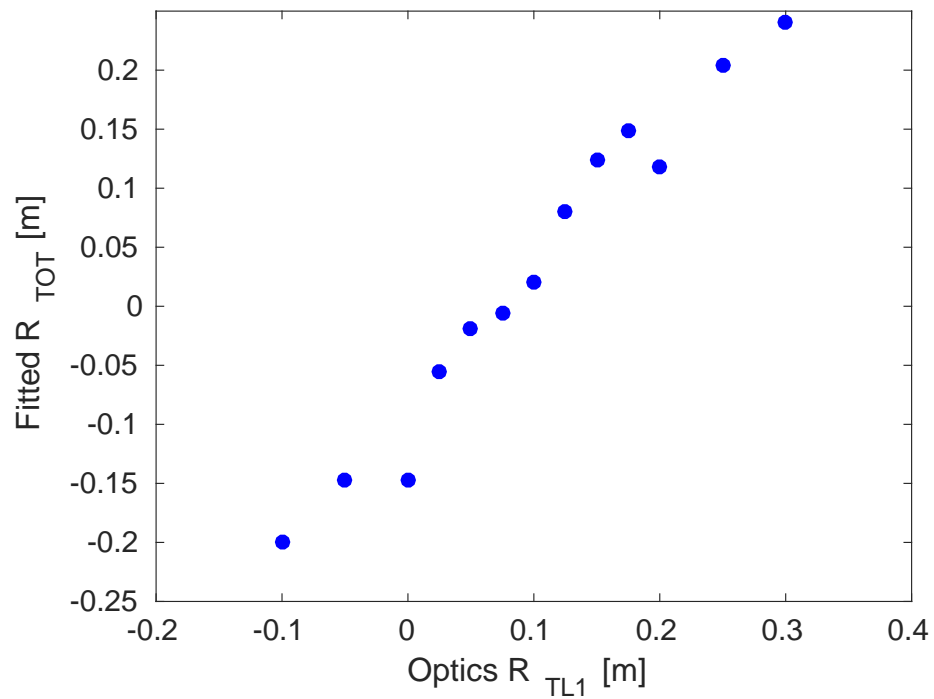


Figure 4.36: Fitted total  $R_{56}$  value between the upstream and downstream phase monitors ( $R_{TOT}$ ) for each  $R_{56}$  value applied in TL1 ( $R_{TL1}$ ) during the scan.

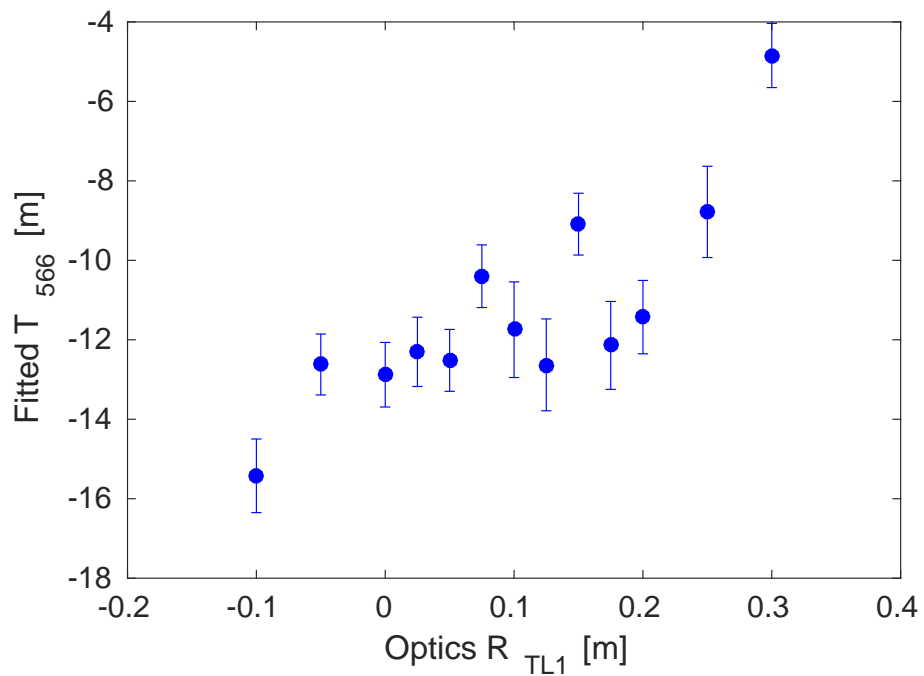


Figure 4.37: Fitted  $T_{566}$  value between the upstream and downstream phase monitors for each set of  $R_{56}$  optics applied in TL1 ( $R_{TL1}$ ) during the scan.

fitted  $R_{56}$  values depend on the absolute mean energy offset, which is not easily verifiable from the BPM measurement alone. Figure 4.36 assumes a mean energy offset of zero. Using a mean relative energy offset of  $2 \times 10^{-3}$  instead would bring the fitted  $R_{56}$  values close to the expected range.

For  $R_{56}$  values in TL1 up to 0.2 m the fitted  $T_{566}$  values in Figure 4.37 are close to the simulated values (typically around -13.5 m in Figure 4.29). For  $R_{56}$  values larger than 0.2 m in TL1 the fitted  $T_{566}$  value is smaller than expected. However, the measured first and second order energy dependent effects are overall in good agreement with expectations given the constraints of measurement and accuracy of the MADX model.

### Mean Phase

Figure 4.38 shows the mean phase jitter during this  $R_{56}$  scan both upstream and downstream. Simulations of the expected phase jitter given the beam conditions and optics are also shown, both for the case where only  $R_{56}$  is considered and when both  $R_{56}$  and  $T_{566}$  are taken in to account. Varying the beam energy during the scan has the effect of increasing the upstream phase jitter from its typical level of 0.8 degrees to 2.0 degrees. The correlation between the upstream phase and the beam energy is also increased from 20% in normal conditions to above 90% whilst varying the beam energy. An example of this is shown in Figure 4.40 for the dataset at  $R_{56} = -0.1$  m in TL1. The likely source of the upstream phase-energy dependence is the energy variation leading to differences in beam orbit through the compressor chicane in the CTF3 linac (see Figure 1.5).

The downstream phase jitter is reduced to close to the level of the upstream phase jitter for  $R_{56}$  values between 0.05 m and 0.1 m in TL1. With knowledge that the  $T_{566}$  can cause a dependence between the optimal  $R_{56}$  value in TL1 and the beam energy it is not completely unexpected that the lowest downstream phase jitter is not at the 0.2 m expected due to the optics in TL2. A mean relative energy offset of  $-2 \times 10^{-3}$  can lead to the minimum jitter being shifted to 0.075 m as seen in the scan. This offset has been used to create the simulated lines in Figures 4.38 (and 4.39). The simulation including this energy offset and the effects of  $T_{566}$  follows the actual downstream phase jitter during the scan more closely than the simulations including only  $R_{56}$ , which are also shown. There are still differences between the data and the  $T_{566}$  simulation, in particular in the range between  $R_{56} = 0.125$  m and 0.175 m in TL1. Some potential sources of additional downstream phase jitter are investigated in Section 4.6, but these can not explain the differences seen in this scan so there are remaining effects that have not yet been identified.

The upstream-downstream phase correlation during the scan is shown in Figure 4.39. As the correlation between the upstream phase and the beam energy is greatly increased by varying the beam energy during the scan as previously discussed, there is no longer a clear singular peak in the upstream-downstream phase correlation. Instead, the correlation quickly flips between a highly correlated state and a highly anti-correlated state. This effect was previously seen in Figure 4.13 as a consequence of the  $R_{56}$  equations derived in Section 4.3.3. The actual upstream-downstream phase correlation during the scan is in good agreement with the simulation including the effects of  $T_{566}$  (again with an assumed mean energy offset

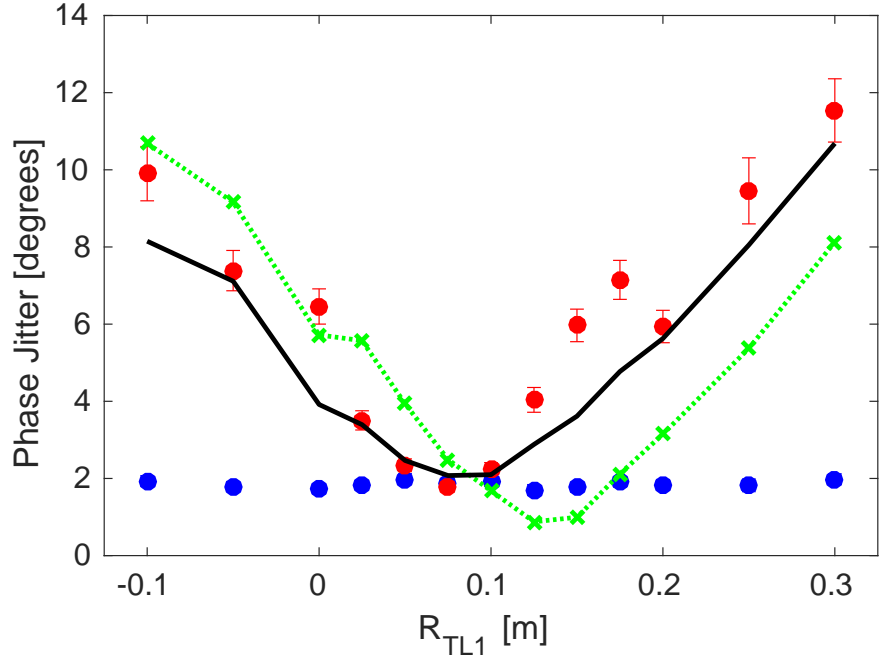


Figure 4.38: Phase jitter downstream (red markers) and upstream (blue markers) for each set of  $R_{56}$  optics used in TL1 during the scan whilst varying the beam energy. The dashed green line shows a simulation of the expected downstream jitter including only the first order  $R_{56}$  effects. The solid black line shows a simulation of the expected downstream phase jitter including the effects of both  $R_{56}$  and  $T_{566}$ .

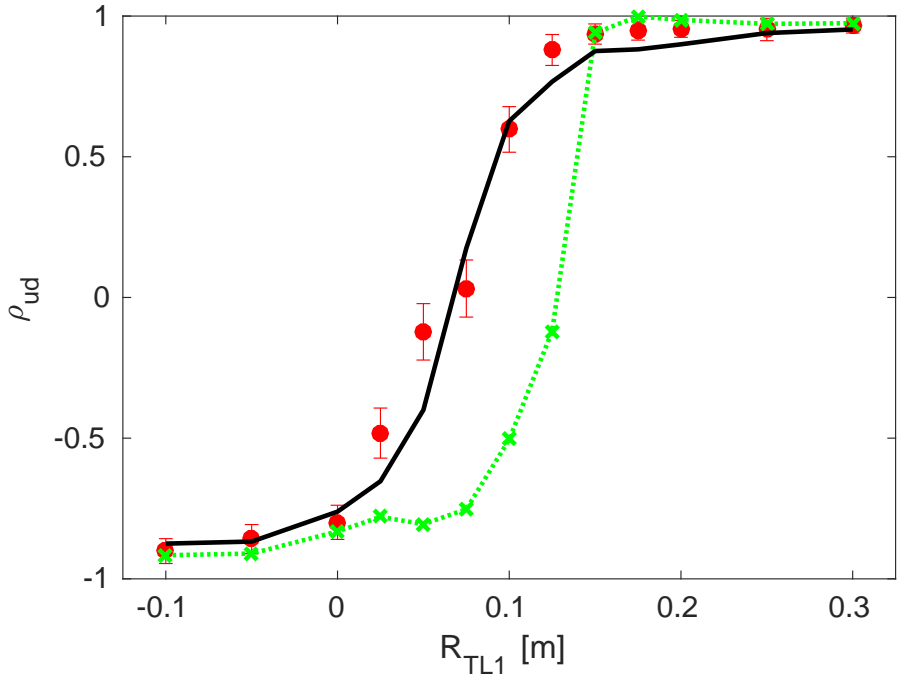


Figure 4.39: Upstream-downstream phase correlation (red markers) for each set of  $R_{56}$  optics used in TL1 during the scan whilst varying the beam energy. The dashed green line shows a simulation of the expected correlation including only the first order  $R_{56}$  effects. The solid black line shows a simulation of the expected correlation including the effects of both  $R_{56}$  and  $T_{566}$ .

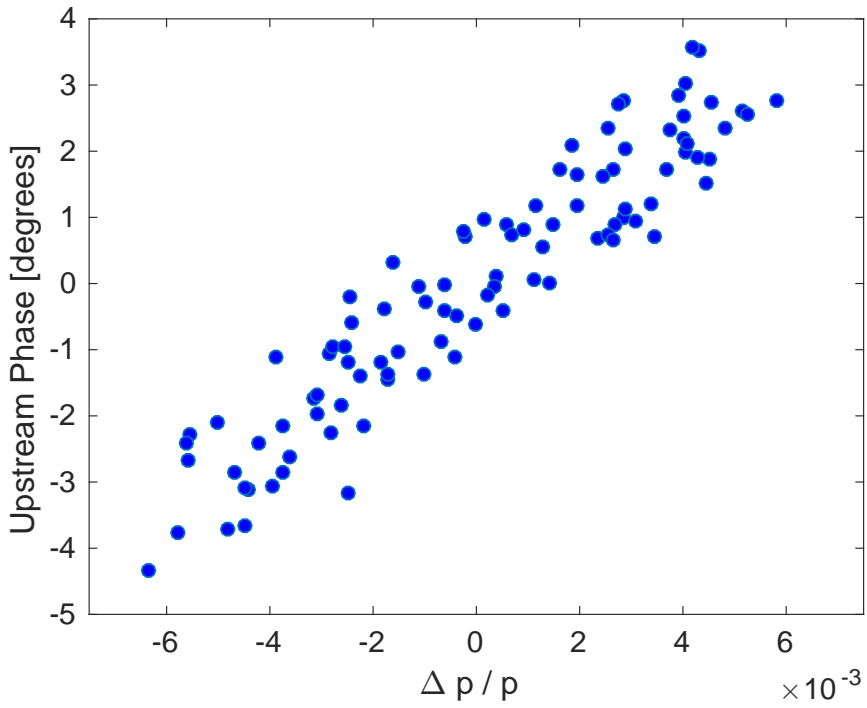


Figure 4.40: Upstream phase-energy correlation whilst varying the beam energy, and with the  $R_{56} = -0.1$  m optics in TL1.

of  $-2 \times 10^{-3}$ ). The highest upstream-downstream phase correlations are obtained for  $R_{56}$  values above 0.175 m in TL1. However, for these values the downstream phase jitter is much larger than the upstream phase jitter (see Figure 4.38) due to the effects of the upstream phase-energy correlation and  $T_{566}$  in the high energy jitter conditions during the scan. This makes it more difficult to precisely define the best  $R_{56}$  optics to use based on the results of a scan of this type alone.

### Phase Along the Pulse

As well as the mean phase it is interesting to look at the effect of varying  $R_{56}$  on the phase along the pulse. To understand differences in the downstream phase along the pulse it is important to know the properties of the beam energy along the pulse during the  $R_{56}$  scan. Figures 4.41 and 4.42 show typical examples of the mean energy and the energy jitter along the pulse. During this scan the mean beam energy was systematically varied about its initial value, as noted previously. This has no effect on the shape of energy variations along the pulse, but does increase the point-by-point energy jitter. The relative beam energy offset along the pulse (Figure 4.41) varies by  $3.5 \times 10^{-3}$  peak-to-peak. The energy jitter along the pulse varies between  $4 \times 10^{-3}$  and  $3 \times 10^{-3}$ , with better stability towards the end of the pulse.

Figure 4.43 shows the mean phase along the pulse for each  $R_{56}$  setting in TL1 during the scan. Any difference in the mean (rather than the jitter) along the pulse with the  $R_{56}$  value should originate from variations in the mean energy along the pulse. If there were no

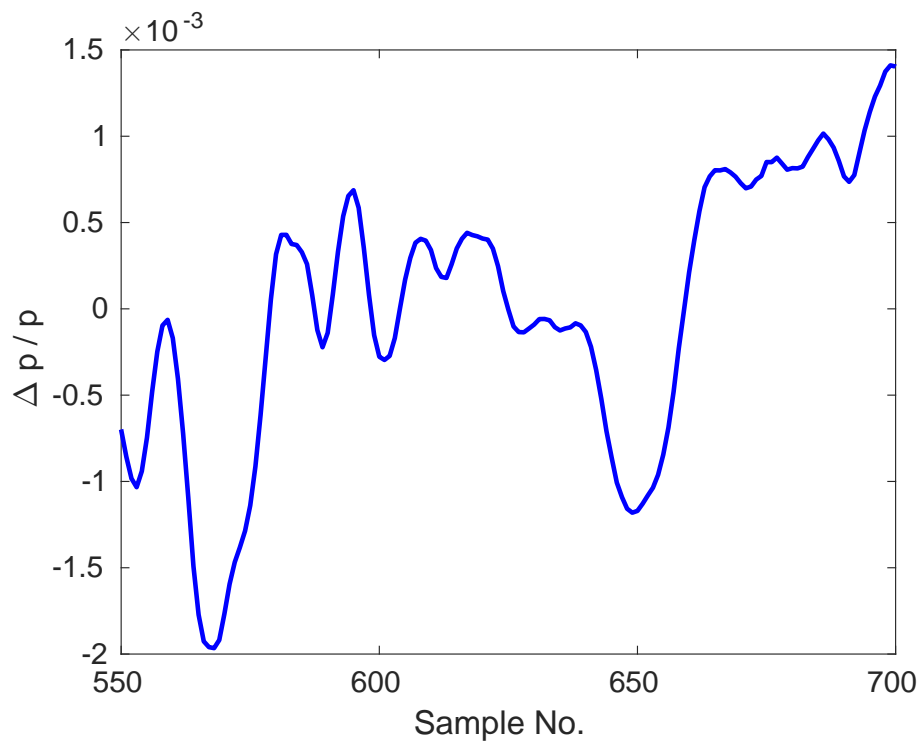


Figure 4.41: Typical example of variations in the mean energy ( $\Delta p/p$ ) along the pulse during the  $R_{56}$  scan.

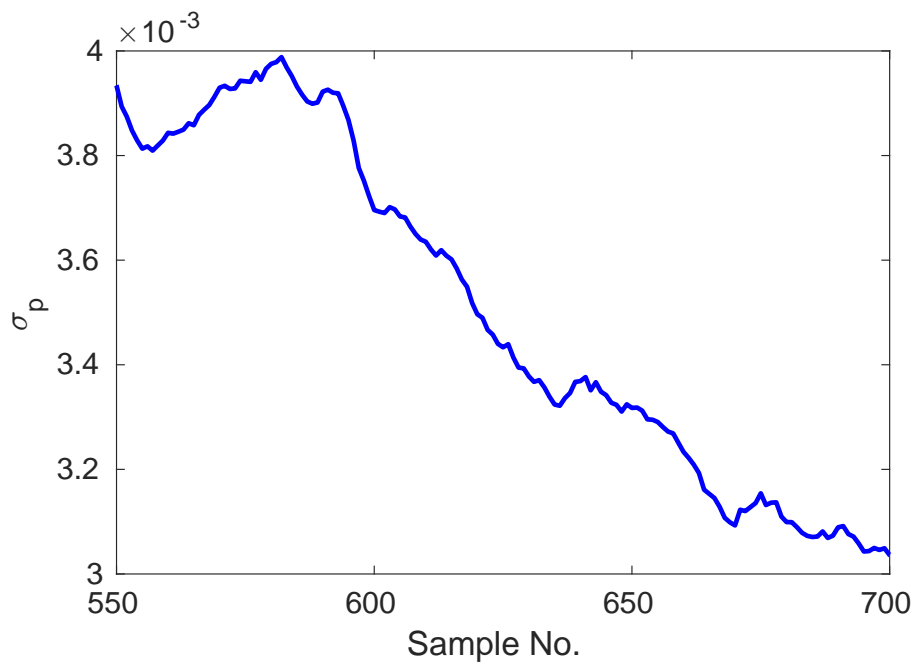


Figure 4.42: Typical energy jitter ( $\sigma_p$ ) along the pulse during the  $R_{56}$  scan, amplified by varying the mean beam energy during the scan.

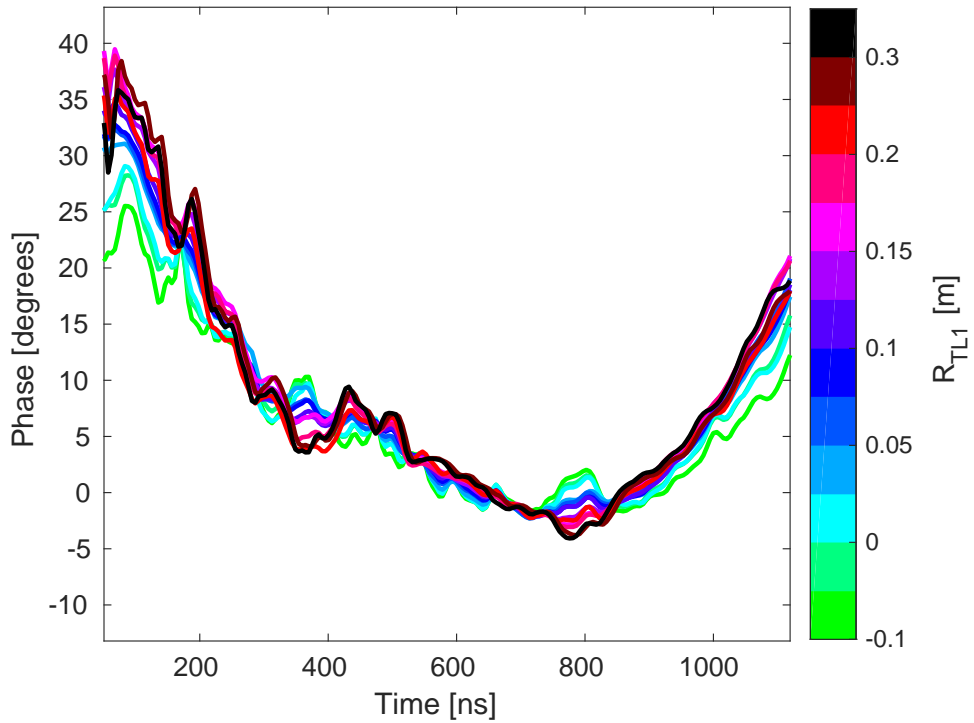


Figure 4.43: Mean downstream phase along the pulse for all sets of  $R_{56}$  optics used in TL1 during the scan whilst varying beam energy.

variations in the energy along the pulse, changing the  $R_{56}$  would only affect the phase jitter and would not change the mean pulse shape. The clear change in certain features along the pulse in the downstream phase is therefore an indication of energy variations in these regions. Perhaps the best example of this is the effect around a time of 800 ns, where the phase swings upwards when a negative  $R_{56}$  in TL1 is used or downwards for  $R_{56}$  values above 0.15 m.

The difference between the phase along the pulse for two different settings of  $R_{56}$  in TL1 should be proportional to the beam energy along the pulse. Figure 4.44 plots the difference between the  $R_{56} = +0.3$  m optics and the roughly optimal  $R_{56} = +0.075$  m optics, and compares this to the beam energy along the pulse. Both lines are mean subtracted and normalised to give equivalent amplitudes in arbitrary units. Overall, the differences in phase along the pulse resulting from using non-optimal  $R_{56}$  in TL1 are very well matched with the energy variation along the pulse, as expected.

Figure 4.45 shows the downstream phase jitter along the pulse for each  $R_{56}$  optics in TL1 used during the scan. Like the mean phase jitter, the jitter along the pulse is lowest for  $R_{56}$  values between 0.05 m and 0.1 m in TL1 (blue). Lower  $R_{56}$  values (green) and higher  $R_{56}$  values (purple, red and black) give higher jitter. Close to the optimal  $R_{56}$  value many of the variations in jitter along the pulse are reduced, although in all cases some features remain.

Differences in the phase jitter along the pulse between two different  $R_{56}$  optics in TL1 should also be related to the beam energy. One might expect the features in the downstream

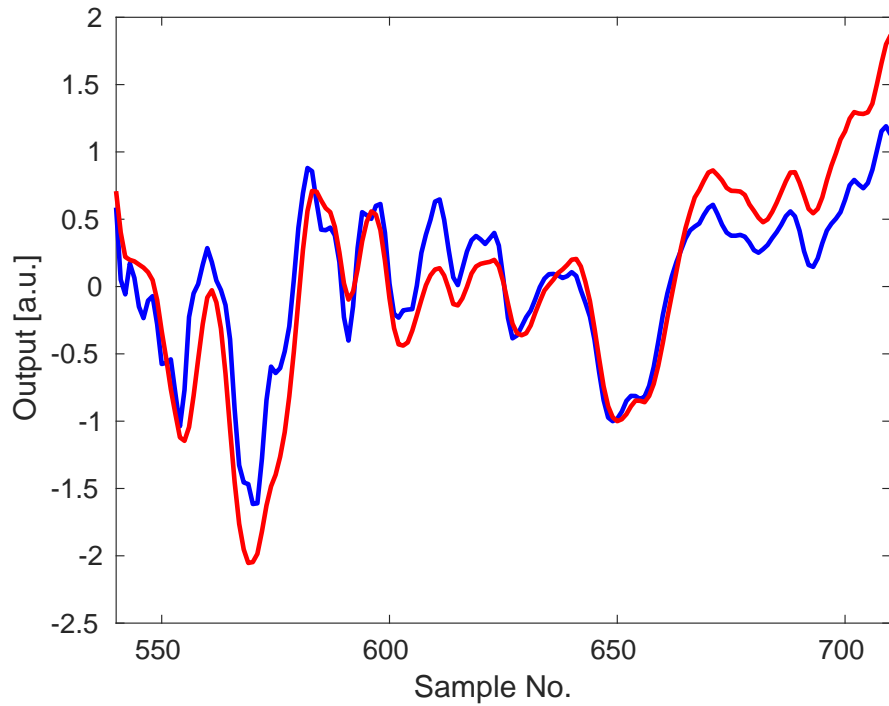


Figure 4.44: Difference between the mean downstream phase along the pulse with  $R_{56} = 0.3$  m and 0.075 m in TL1 (blue) compared to the mean beam energy along the pulse (red).

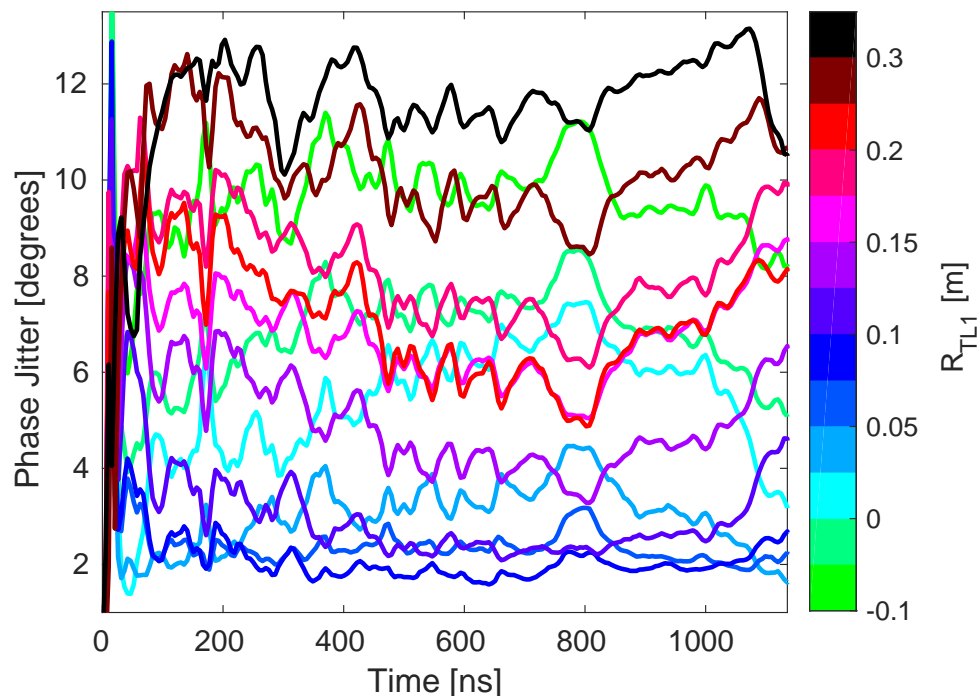


Figure 4.45: Downstream phase jitter along the pulse for each set of optics used in TL1 during the  $R_{56}$  scan whilst varying beam energy.

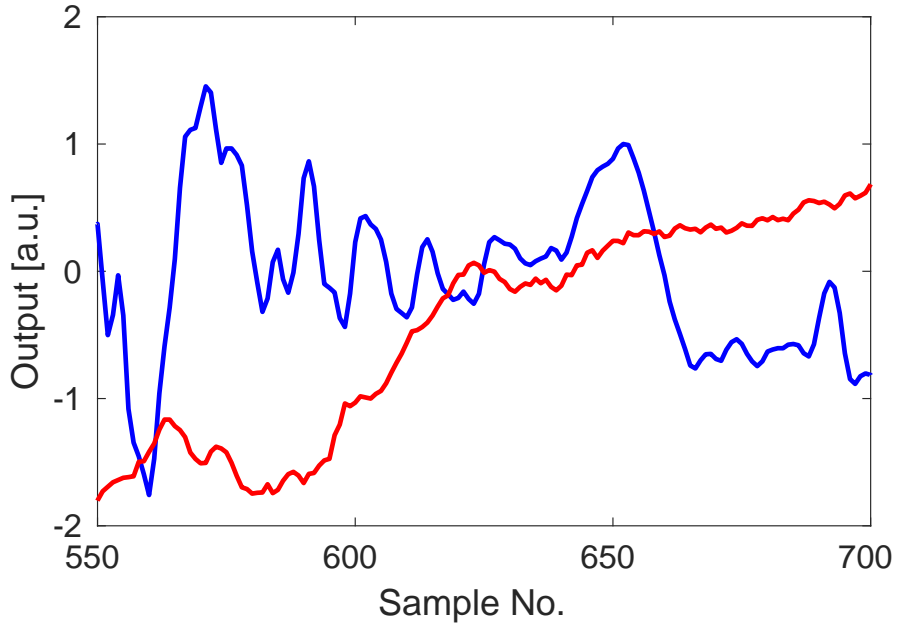


Figure 4.46: Difference between the downstream phase jitter along the pulse with  $R_{56} = 0.3$  m and  $0.175$  m in TL1 (blue) compared to the energy jitter along the pulse (red).

phase jitter along the pulse to match the shape of the variations in energy jitter along the pulse shown previously. Figure 4.46 compares the difference in phase jitter along the pulse for the  $R_{56} = 0.075$  m and  $R_{56} = -0.1$  m optics to the energy jitter along the pulse. There is no clear similarity between the two. In Figure 4.47 the phase jitter along the pulse is compared to the mean energy along the pulse instead. In this case most of the features in the downstream phase jitter are also present in the energy along the pulse. Static variations in the mean energy along the pulse therefore appear to be more critical for the phase propagation than differences in energy jitter along the pulse.

### 4.5.3 Mitigation of Higher Order Dependences

The first order energy dependent effects on the downstream phase due to the  $R_{56}$  in TL2 have largely been successfully removed by adding positive  $R_{56}$  to the TL1 line. If necessary, further improvements could be made by creating further sets of TL1 optics in smaller  $R_{56}$  steps. Although the higher order energy dependent effects due to  $T_{566}$  have been identified it has not yet been attempted to remove, or at least reduce, them in the optics. Optics including sextupole magnets (usually left off at CTF3) in TL1, the combiner ring and TL2 could be created to achieve this. However, to be completely successful this depends on the accuracy of the MADX model of CTF3 to second order, which is not guaranteed although the result in Figure 4.37 is promising in this regard.

Alternatively, the second order effects can be reduced by decreasing the energy jitter and variations along the pulse at CTF3. Many improvements have recently been made at CTF3 to achieve this via the implementation of several new feedbacks [74]. New feedbacks on the phases of each klystron in the CTF3 injector as well as on the beam energy are now

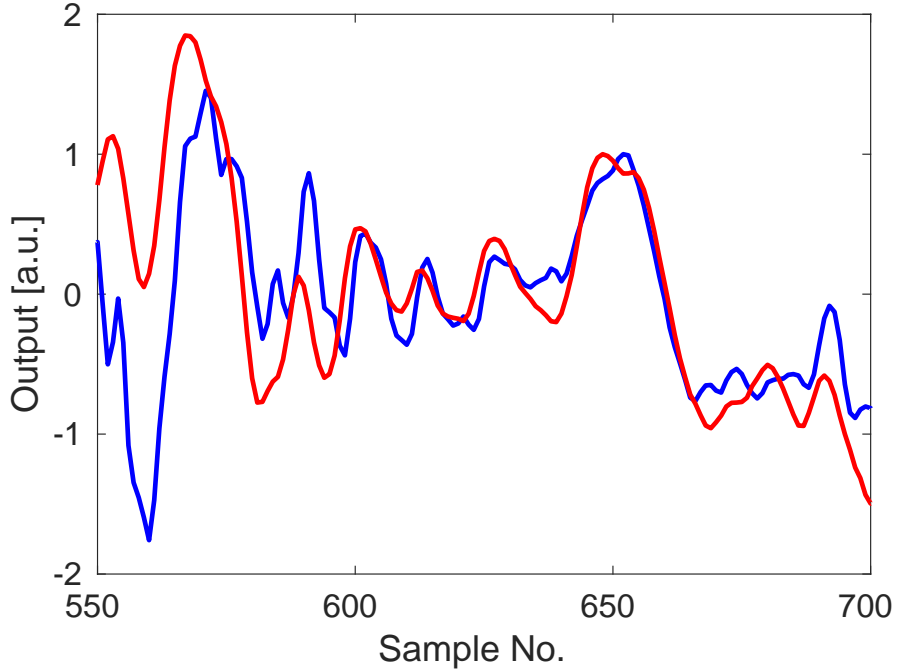


Figure 4.47: Difference between the downstream phase jitter along the pulse with  $R_{56} = 0.3$  m and  $0.175$  m in TL1 compared to the mean beam energy along the pulse (red).

routinely in operation, and these have already improved the mean energy jitter to  $0.5 \times 10^{-3}$  on short time scales of several minutes, or  $0.8 \times 10^{-3}$  on longer time scales. Hardware changes and further improvements to the implementation of these feedbacks should allow the mean energy stability to be improved further.

In addition, although they are not yet run online in normal operation, new feedback systems have also been implemented and commissioned that can smooth energy variations along the pulse, or directly smooth the upstream phase along the pulse itself. The energy flattening feedback [77] varies the waveform of the last klystron in the CTF3 linac based on the measurement of the same dispersive BPM used to measure the beam energy in this chapter — CT.0608 in TL1. This flattens the energy along the pulse by varying the energy gain along the pulse in the last accelerating structure. In addition, prior to the best phase propagation conditions currently achieved (presented in Section 4.7) a similar feedback was used to smooth features in the upstream phase along the pulse by varying the waveform of the first klystron in the CTF3 linac [44], as seen in Figure 4.48. Feedbacks of this type will be critical to be able to improve the PFF performance for future tests.

## 4.6 Possible Other Sources of Phase Jitter

The energy related effects on the downstream phase have been the main focus of attempts to improve the phase propagation for the PFF system. As shown in the Section 4.7 this by itself has allowed upstream-downstream correlations in excess of 90% to be achieved at CTF3. Further optimisations will be needed to achieve the CLIC target of 0.2 degrees phase jitter

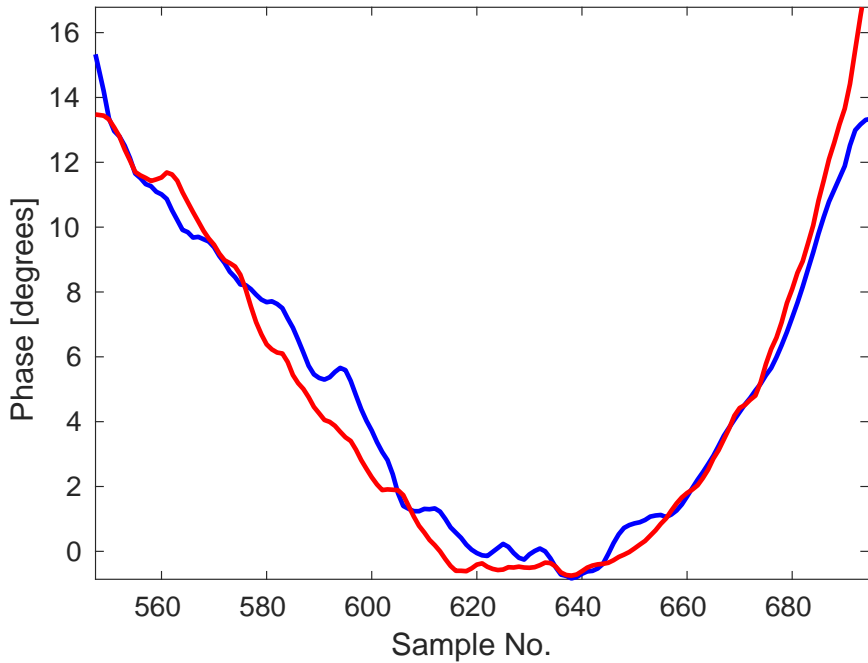


Figure 4.48: Effect of feedback used to smooth variations along the upstream phase (initial upstream phase in blue, and after applying the feedback in red).

with the PFF prototype, however. This can partly come from further improvements of the CTF3 injector setup and stability, which will help to reduce any remaining effects from  $T_{566}$  by reducing beam energy jitter, drifts and variations along the pulse. At correlations above 90% any remaining small differences in the performance of the upstream and downstream phase monitors may also become significant, but this has been addressed in Chapter 3 so will not be discussed again here.

Preliminary measurements have been performed to investigate whether there may be any other effects at CTF3, apart from energy jitter, that can change the downstream phase and reduce the upstream-downstream phase correlation. The most likely culprits are magnetic elements between the upstream and downstream phase monitors that have a strong effect on the beam orbit. Any change in beam orbit can change the path length between the upstream and downstream phase monitors, and thus shift the downstream phase with respect to the upstream phase. The main elements for which this could be significant include the dipoles in TL1 and the combiner ring, as well as the two septum magnets used at the combiner ring injection and extraction. Fluctuations in the power supplies for one of these devices could be an additional source of uncorrelated downstream phase jitter.

The current applied from the power supplies for each of these devices has been varied to determine their effect on the downstream phase. In some cases one power supply drives multiple devices, meaning these devices can not be changed independently from each other and any jitter in their strengths should be correlated (assuming the jitter source is the power supply, rather than a separate issue with the device itself). There are four power supplies that control the strength of the devices of interest in the following groups:

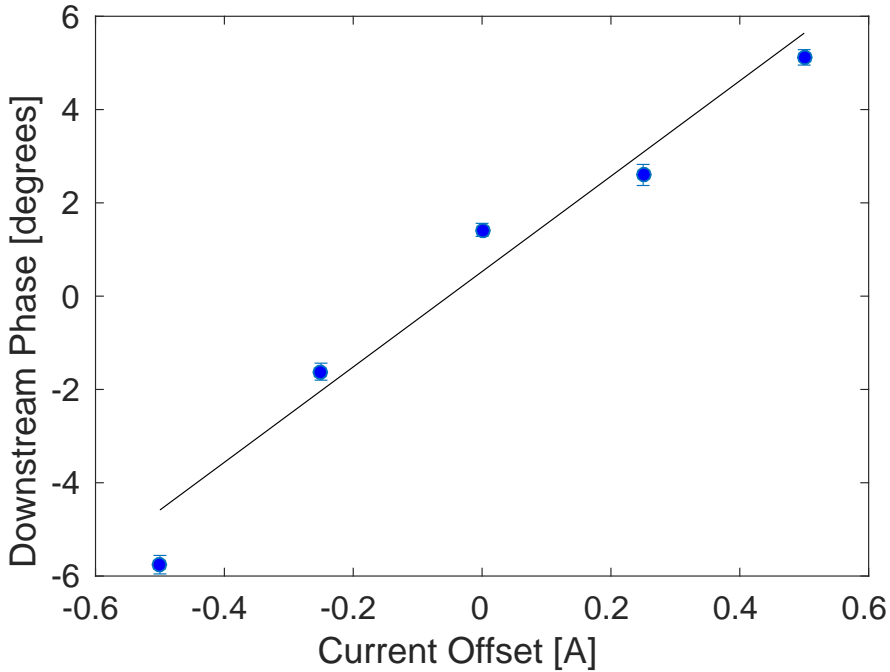


Figure 4.49: Downstream phase vs. strength (power supply current) of the first two dipoles in TL1 (CT.0670 and CT.0710).

- **Power supply 1:** The first (CT.0540) and second (CT.0630) dipole in TL1.
- **Power supply 2:** The third (CT.0670) and fourth (CT.0710) dipole in TL1.
- **Power supply 3:** The combiner ring injection and extraction septa.
- **Power supply 4:** All combiner ring dipoles.

Figure 4.49 shows the effect of changing the last two dipoles in TL1 (power supply 2 above) on the downstream phase, which is the strongest observed dependence. The fitted downstream phase shift per ampere change on this power supply is  $10 \pm 2^\circ$ . Table 4.3 summarises the phase shift per ampere for the other three power supplies.

The power supplies at CTF3 give a relative stability in the supplied current of approximately  $10^{-4}$ . Assuming this stability the effect of each device on the downstream phase jitter can be estimated by using the fitted phase shifts per ampere and the known power supply current setting for each device. These approximate phase jitters are also summarised in Table 4.3. By far the strongest potential source of phase jitter appears to be the last two dipoles in TL1 (CT.0670 and CT.0710), which by themselves could contribute  $0.17 \pm 0.03$  degrees phase jitter. The explanation for these two dipoles having a much larger effect on the phase than the first two dipoles in TL1 is not known and will need to be verified by repeated measurements and checks of the expected response in the CTF3 MADX model. The combiner ring devices contribute roughly 5 times less phase jitter than the CT.0670 and CT.0710 dipoles. Combining the estimated phase jitters resulting from all the devices in quadrature gives an overall contribution of  $0.18 \pm 0.03^\circ$  additional downstream phase jitter.

Device	Current	Fit Gradient	Estimated Phase Jitter
TL1 540/630 Dipoles	133 A	$-0.4 \pm 0.3^\circ/\text{A}$	$0.005 \pm 0.004^\circ$
TL1 670/710 Dipoles	164 A	$10 \pm 2^\circ/\text{A}$	$0.17 \pm 0.03^\circ$
CR Septa	890 A	$-0.5 \pm 0.1^\circ/\text{A}$	$0.05 \pm 0.01^\circ$
CR Dipoles	156 A	$1.8 \pm 0.7^\circ/\text{A}$	$0.03 \pm 0.01^\circ$

Table 4.3: Power supply current setting, dependence of the downstream phase on the current and estimated contribution to downstream phase jitter for the dipoles and septa in TL1 and the combiner ring.

Modelling the downstream phase as  $\phi_d = \phi_u + x$ , where  $x$  is a generic additional source of uncorrelated jitter, the downstream jitter and upstream-downstream phase correlation are given by:

$$\sigma_d = \sqrt{\sigma_u^2 + \sigma_x^2} \quad (4.19)$$

$$\rho_{ud} = \frac{\sigma_u^2}{\sigma_u^2 + \sigma_x^2} \quad (4.20)$$

These are equivalent to the equations derived for the phase monitor resolution in Section 3.3. Assuming an initial upstream phase jitter of  $0.8^\circ$  plus a  $\sigma_x = 0.18^\circ$  source of jitter resulting from the power supply stabilities previously discussed, the downstream phase jitter is increased slightly to  $0.82^\circ$  and the upstream-downstream phase correlation reduced to 95%.

The effect on the predicted upstream-downstream phase correlation is significant for the PFF system, which requires correlations above 97% to achieve CLIC level phase stability at CTF3. Therefore, jitter on the power supplies may become a limiting factor for the PFF system performance and this will be verified with repeated measurements of the power supply dependences and stabilities in the future.

## 4.7 Best Phase Propagation

This section summarises the best phase propagation conditions that have been achieved to date after the extensive work to identify and reduce the energy dependence of the downstream phase. The results shown here are taken from the same dataset with which the best PFF results were achieved, presented later in Section 6.1. At this time the  $R_{56} = +0.1$  m optics was used in TL1. The achieved conditions are a remarkable improvement compared to the original status presented in Section 4.2. The reproducibility of these conditions is discussed in the context of the PFF results in Section 6.2.

### Mean Phase

The best phase propagation conditions are achieved when the upstream phase-energy correlation and the downstream phase-energy correlation is the same. Figure 4.50 shows the correlation of the upstream and downstream phase with the beam energy. With the optimised conditions almost all correlation between the downstream phase and the beam energy

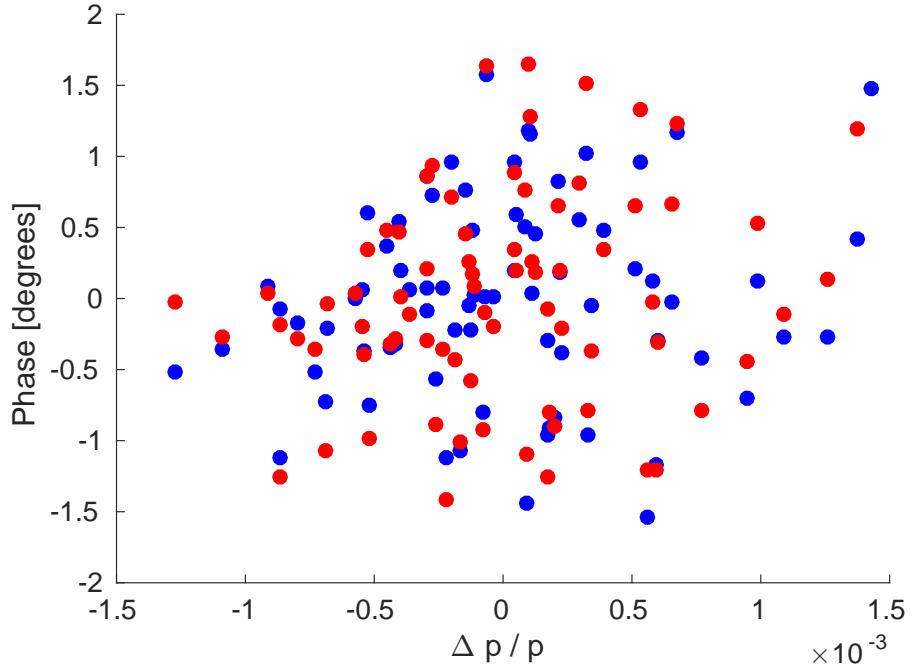


Figure 4.50: Upstream (blue) and downstream (red) phase-energy correlation with optimised phase propagation.

is removed, with a correlation of  $0.2 \pm 0.1$ . This agrees with the upstream-downstream phase correlation of  $0.1 \pm 0.1$  within error bars.

Figure 4.51 shows that all drifts in the upstream phase are also present downstream, and that the upstream and downstream mean phase jitters also agree within errors bars —  $0.69 \pm 0.06^\circ$  upstream and  $0.74 \pm 0.06^\circ$  downstream. The standard deviation of the residuals between the upstream and downstream phase is  $0.27 \pm 0.02^\circ$ . The correlation between the mean upstream and downstream phase is  $93 \pm 4\%$ , as shown in Figure 4.52. This is very close to the targeted 97% that would make a reduction in downstream jitter to  $0.2^\circ$  possible with the PFF system.

### Phase Along Pulse

Figure 4.53 compares the phase along the pulse upstream and downstream in the optimal conditions. For reference, the mean phases presented above were calculated in the region between 530 ns and 950 ns. This is the flattest central part of the pulse where the PFF system can provide the maximum reduction in phase jitter, as seen in Section 6.1. The overall agreement in shape between the upstream and downstream phase is much better than the original conditions seen in Figure 4.4, with almost all energy dependent features removed from the mean downstream phase along the pulse. There are still some remaining differences in shape, particularly at the start and end of the pulse before and after the 530–950 ns range.

By viewing the phase jitters and correlations along the pulse the remaining areas for

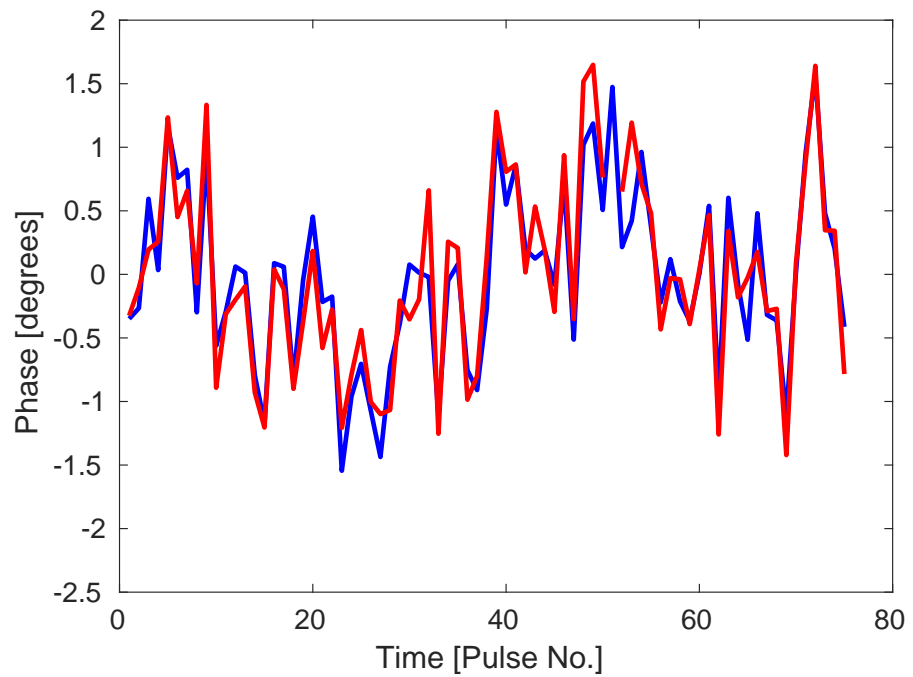


Figure 4.51: Mean phase vs. time upstream (blue) and downstream (red) with optimised phase propagation.

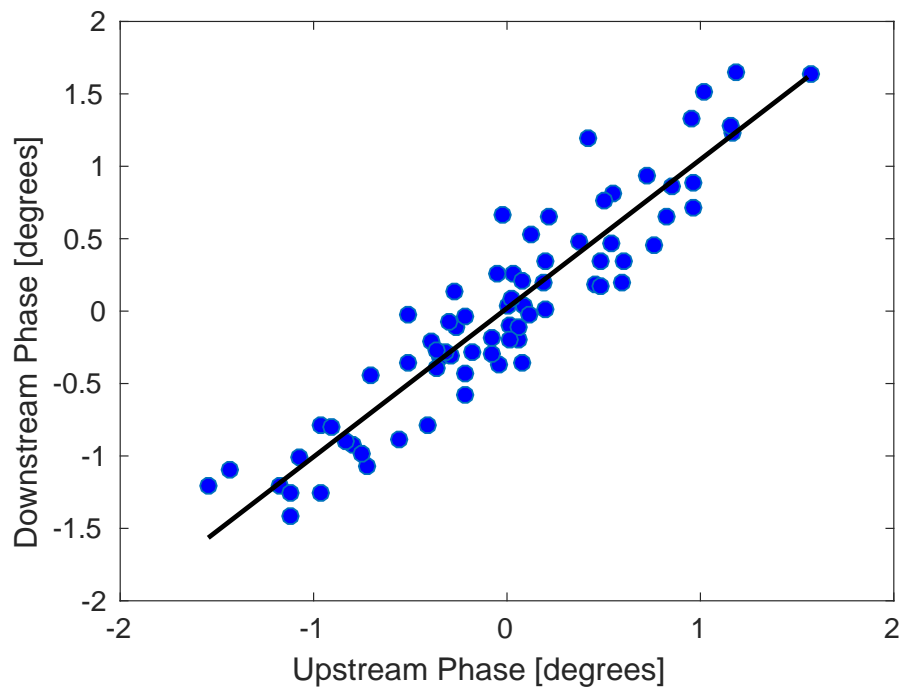


Figure 4.52: Upstream-downstream phase correlation with optimised phase propagation. The black line shows a linear fit to the data (blue markers).

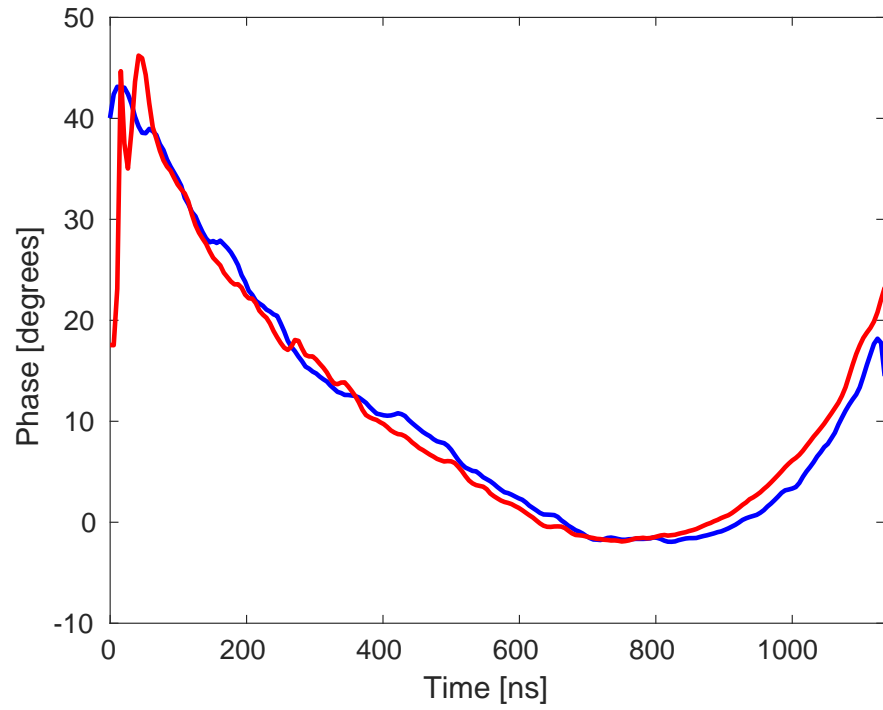


Figure 4.53: Phase along the pulse upstream (blue) and downstream (red) with optimised phase propagation.

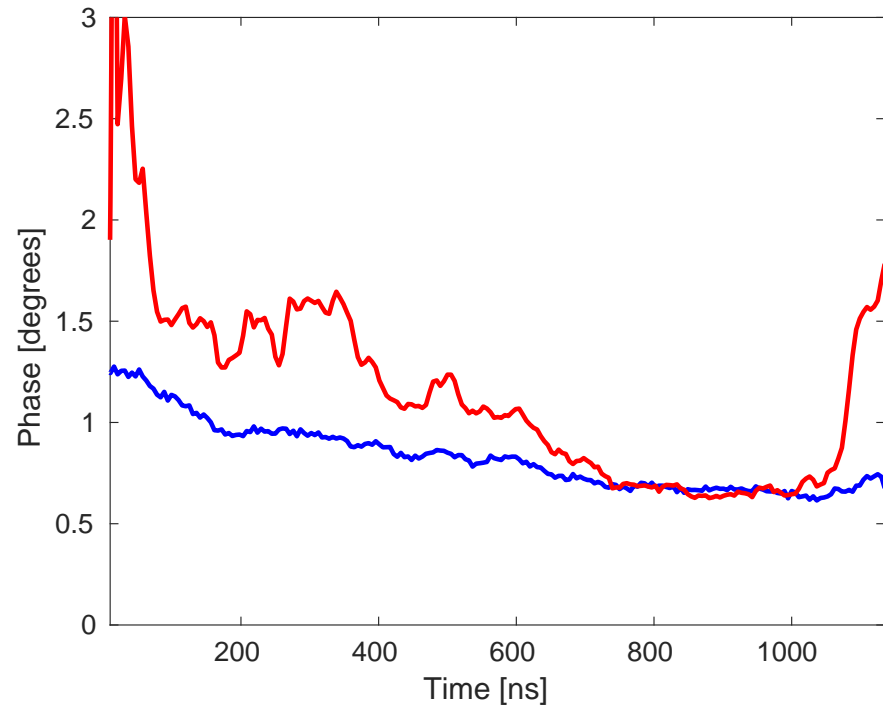


Figure 4.54: Phase jitter along the pulse upstream (blue) and downstream (red) with optimised phase propagation.

improvement start to become apparent. In Figure 4.54, showing the phase jitter along the pulse, it is clear that the start of the pulse is less stable. For times between 100 ns and 600 ns the downstream phase jitter is as much as 60% larger than the upstream phase jitter. However, there is a 400 ns portion of the pulse where the downstream phase jitter has been successfully reduced to the level of the upstream phase jitter. The best PFF results can be expected in this region.

The upstream-downstream phase correlation along the pulse (the point by point correlation between the upstream and downstream phase calculated for each individual sample along the pulse), in Figure 4.55, is at the same level as the mean phase correlation in the region between 450 ns and 650 ns. However, there are also parts of the pulse where the upstream-downstream phase correlation is greatly reduced – to 55% at 300 ns and 70% at 700 ns, for example. Differences earlier in the pulse are not critical for the PFF system, but the feature at 700 ns is in the area where the correction is attempted.

By comparing the upstream-downstream correlation along the pulse to the correlations with energy along the pulse, in Figure 4.56, the problem becomes clear. Due to energy variations along the pulse and the effect of higher order energy dependences, as previously discussed, the phase propagation can not be optimised across the full pulse length. As a result there are parts of the pulse where the downstream phase-energy correlation is still high, up to 75%. Areas where there is a large difference between the upstream phase-energy correlation and the downstream phase-energy correlation correspond to regions of degraded upstream-downstream phase correlation in Figure 4.55. This is the key area where improvements are needed to further improve the PFF performance.

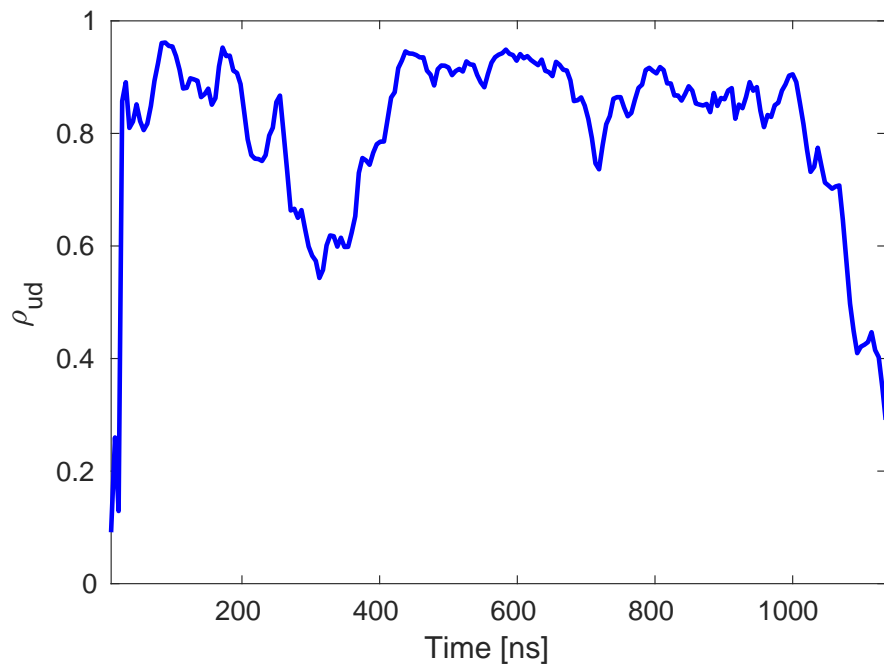


Figure 4.55: Upstream-downstream phase correlation along the pulse with optimised phase propagation.



Figure 4.56: Upstream (blue) and downstream (red) phase-energy correlation along the pulse with optimised phase propagation.

# Chapter 5

## Setup and Commissioning of the PFF System

The function of the phase monitor electronics has already been introduced in Chapter 3. This chapter discusses the design, setup and performance of the remaining PFF hardware — the FONT5a board and the kicker amplifiers. The second part of the chapter then presents remaining measurements that had to be taken to commission the PFF system, such as setting up the correction timing and verifying the ability to shift the phase in the TL2 chicane using the kickers and PFF optics.

Figure 5.1 shows the complete PFF electronics setup in the klystron gallery, consisting of three racks. The cables from the phase monitors and kickers in the accelerator hall on the floor below enter the rack from behind. They are connected to the patch panels at the lower left side of the figure, for the phase monitors, and below the amplifier in the middle rack, for the kickers. Signals are then directed from the patch panels to the relevant pieces of hardware in the PFF chain.

### 5.1 Feedforward Controller (FONT5a Board)

This section describes the design, firmware and operational aspects of the FONT5a board, which acts as the PFF controller. Its role is to digitise the signals from the upstream phase monitor (usually Mon 1), process them and calculate the appropriate voltage with which to drive the kicker amplifiers in order to correct the phase downstream. In addition it must ensure the timing of the correction output is such that the drive output from the amplifiers reaches the kickers precisely in time with the beam.

The FONT5a board is a custom built digital board designed and constructed at Oxford University (John Adams Institute) [25]. More details of the design of the board and the internal components can be found in [78]. At the heart of the FONT5a board is a Xilinx Virtex-5 field programmable gate array (FPGA) [79], an integrated circuit with customisable logic that the user can program as desired for his or her application. The same hardware can therefore be used for multiple applications, with different firmware loaded on to the FPGA

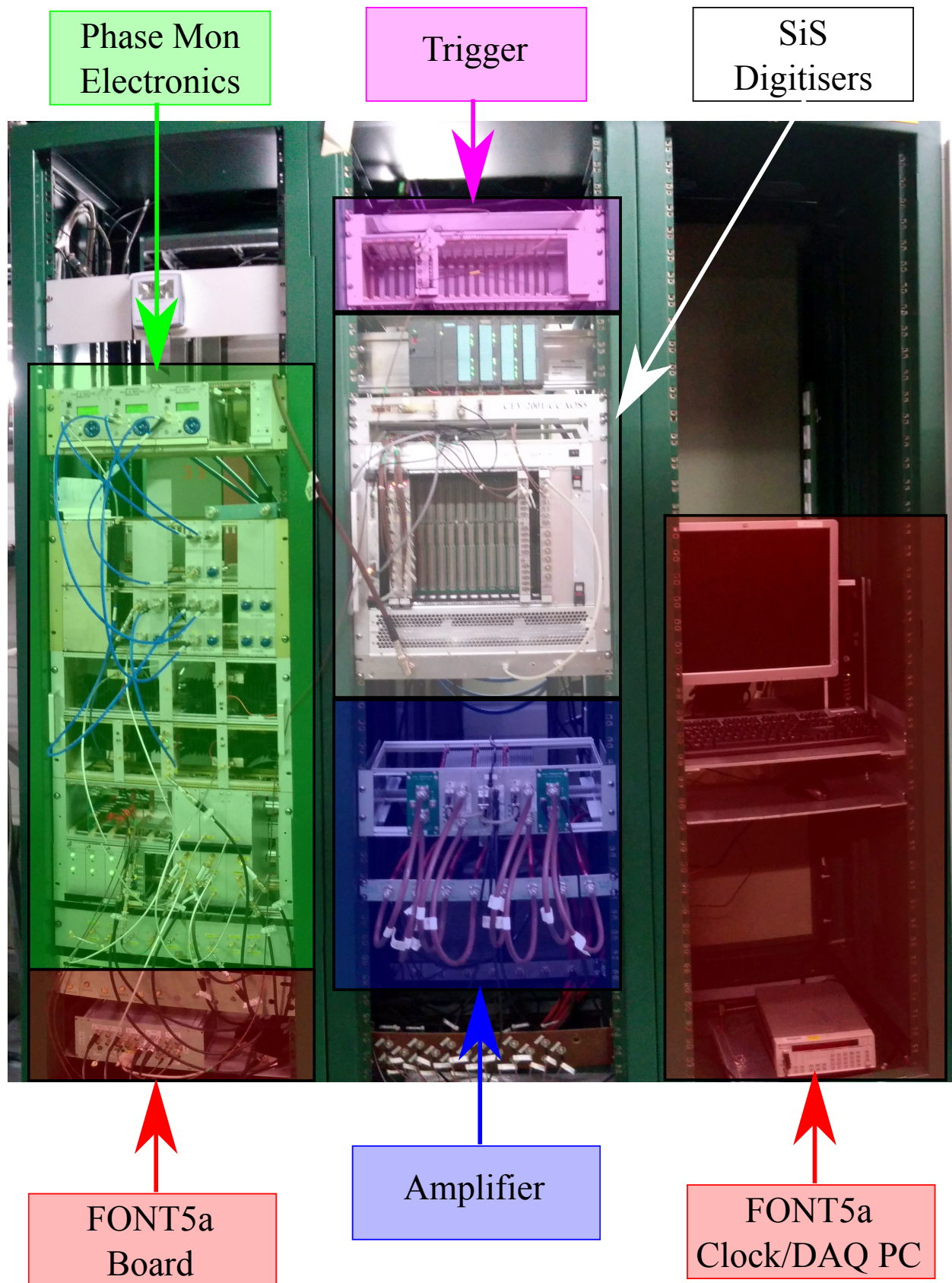


Figure 5.1: The PFF system electronics racks. Each major component of the system is labelled, including the phase monitor electronics, FONT5a board and kicker amplifier.

to take in to account the different signal processing required for the input and output signals in each case. As well as the PFF system, the FONT5a board is also used for tests of an interaction point position feedback for ILC/CLIC, for example [80].

An annotated picture of the FONT5a board front panel is shown in Figure 5.2. Apart from the FPGA (inside the board and therefore not seen in the figure) the main components of the FONT5a board are nine analogue to digital converters (ADCs) and four digital to analogue converters (DACs). In addition there is a serial RS232 port used to communicate with a LabVIEW data acquisition and control system (DAQ), a JTAG connector used to program the FPGA and its non-volatile configuration PROMs, and several other inputs and outputs mostly used for the timing and triggering of the board.

The outputs from the phase monitor electronics, mixer and diode signals, are connected to the ADC inputs on the FONT5a board. Usually only the Mon 1 outputs are connected to the FONT5a board, with the diode on ADC 1 and the mixer on ADC 2, although the signals from additional monitors can be connected if needed. The ADCs are 14-bit resolution with an input range of  $\pm 0.5$  V. Due to the expected noise on the ADCs the least significant bit is discarded and only the most significant 13 bits are processed by the FPGA [81]. The processed ADC outputs therefore have a range of 8192 values, or between  $-4096$  and  $+4095$  “counts”, with each count corresponding to 0.12 mV. More details on the digitisation of the phase monitor signals were given in Section 3.4.

Each ADC output can have a non-zero mean voltage in its baseline noise. To be able to remove these intrinsic voltage offsets each analogue input is combined with the output from a DAC, labelled “trim DACs” (separate from the DACs used as the PFF correction outputs). By varying the trim DAC voltages it can be ensured that the baseline output of each ADC is 0 V, so that its full  $\pm 0.5$  V range can be used for the signal of interest.

For the PFF system the ADCs and timing-critical logic are usually clocked at 357 MHz, generated by an external clock generator [82] and connected to the “FST CLK” input, a dedicated input with a fast comparator, on the FONT5a board. This clock can be in the range between 200 and 400 MHz, with 357 MHz chosen as a convenient frequency at the upper end of this range where the boards had previously been tested extensively for other applications. The start of the ADC sampling window is determined by an external 0.8 Hz trigger derived from the CTF3 timing and therefore locked to the beam. The trigger is connected to the “DIG IN B” input on the board, and arrives 17  $\mu$ s before the beam to take in to account the ADC warm-up time.

After being processed on the FPGA the calculated correction is applied to the DACs, which are 14-bit with an output range of  $\pm 1$  V (20 mA full swing in to  $50 \Omega$ ). The DAC outputs are then amplified so that the final DAC 1 and DAC 2 output range of the FONT5a board is  $\pm 2$  V, matching the required range for the input of the PFF kicker amplifiers. Only DAC 1 and DAC 2 are used for the PFF system, the other two DACs are unused. In addition the FONT5a board generates the trigger for the amplifier (“AUX OUT A”), which must arrive at the amplifier 1.5  $\mu$ s before the DAC signals.

The FONT5a board is controlled using a LabVIEW control and data acquisition system (DAQ) documented in [78], with communication between the board and the DAQ via the

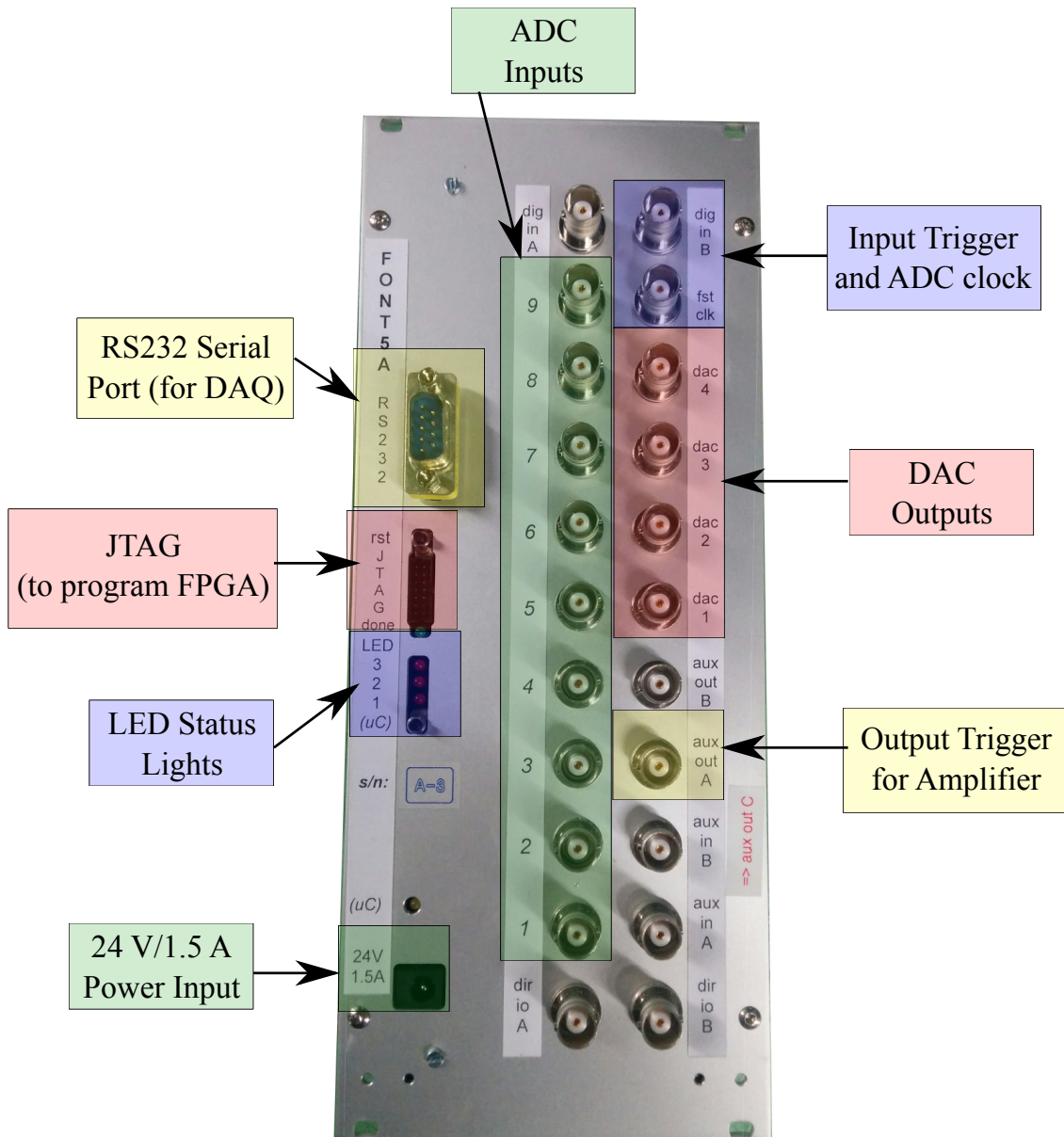


Figure 5.2: Front panel of the FONT5a board. All the connectors relevant to PFF operation are highlighted, the remaining connectors are not used at CTF3. All connectors are BNC apart from the power connector, RS232 serial port used to communicate with the LabVIEW data acquisition system (DAQ) and the JTAG connection used to program the firmware on the FPGA. The use of the ADCs, DACs and timing (trigger and clock) connections is summarised in Figure 5.4.



Figure 5.3: Screenshot of the LabVIEW DAQ used to control the FONT5a board when setting up the PFF system. The right panel shows plots of the current ADC and DAC outputs. Parameters for the correction can be changed in the left panel. The Mon 1 diode output is seen on ADC 1, and the mixer on ADC 2.

serial RS232 port. The implementation of data transfer and setting controls over the RS232 link is documented in [83]. An example screenshot from the DAQ is shown in Figure 5.3. It provides functionality to change all the setup parameters in the FONT5a firmware for the PFF system setup, view the real-time ADC and DAC data, and to save the data, control values and status readbacks to file. However, as the FONT5a board and DAQ currently run as a standalone system at CTF3, PFF data has, so far, been saved via the CERN control system and SiS digitisers where data from other devices, such as BPMs, can be saved synchronously with the phase monitor signals (Section 3.4). The DAQ runs on a Windows PC alongside the racks used for the phase monitor electronics, FONT5a board and amplifier. The PC can be connected to remotely to allow the FONT5a board to be controlled in the CTF3 control room.

### 5.1.1 Implementation of the PFF Correction in Firmware

The diagram in Figure 5.4 shows all the connections to and from the FONT5a board that were introduced in the previous section, from the phase monitor and timing inputs on the left side of the diagram to the outputs for the amplifier and DAQ on the right side of the figure. The central portion of the figure shows a simplified schematic of how the FONT5a firmware calculates and applies the PFF correction. All the parameters shown in the figure, and several others not shown in the diagram but described later in this section, must be appropriately set (via the DAQ) for correct operation of the PFF system.

The basic logic of the firmware is as follows. The ADC timing, sampling rate and start time, are determined by the input trigger and external 357 MHz clock. During the set sampling window the ADC outputs are processed, adding channel offsets and applying filters.

The processed ADC 2 (Mixer) output is then split in to two, to create the two parallel strands that become the DAC 1 and DAC 2 outputs. Note that as the Mixer is used directly (rather than  $\arcsin(\text{Mixer})$ ) this uses the small angle approximation. The effect of this is discussed in Section 5.4.2. If the diode (ADC 1) is being used in the calculation the ADC 2 output is also multiplied by  $1/\sqrt{\text{ADC 1}}$ , with values taken from a lookup table rather than being calculated directly to reduce the number of clock cycles needed for the calculation [84]. Prior to being sent to the DACs the two output strands are multiplied by set gain factors and then can be delayed by a set amount of time. The two calculated DAC outputs are connected to the amplifier drive inputs, where they are amplified and eventually output to the kickers to deflect the beam and correct the phase. The overall latency of the FONT5a board, from the arrival of the signal at the ADCs to the output of the calculated correction at the DACs, is around 22 clock cycles (at 357 MHz) or 60 ns [26].

All the parameters and controls that must be adjusted during the PFF system setup, and their respective values where relevant, are listed below for reference. These are only introduced in brief here, but parameters that are either non-trivial to derive or are critical for the PFF performance are described in more detail in later sections and chapters as indicated. The values given are in the units as they are set in the DAQ and firmware, with each parameter expressed by up to a 14 bit number, and the size of each control chosen to give a reasonable degree of flexibility around the expected set point.

## Input Timing

The following parameters must be adjusted in order to set the properties of the ADC sampling as desired:

**Trig in delay:** The Trig in delay allows the start of the ADC sampling window to be delayed with respect to the arrival of the external trigger. The timing of the trigger and DAC outputs to the amplifier (Trig out delay and K1/K2 delay) are relative to this delay, therefore changing the Trig in delay value does not effect the synchronisation of the correction output with the beam. The only requirement is to ensure that the full acquired upstream phase monitor signals arrive within the sampling window, and that the trigger arrives early enough to account for the  $10\ \mu\text{s}$  warm-up time of the ADCs [68]. The trigger is set to arrive  $17\ \mu\text{s}$  before the beam, so a trig in delay of around 2500 clock cycles of 357 MHz, or  $7\ \mu\text{s}$ , is used to define the time at which the ADCs are turned on (with them then ready  $10\ \mu\text{s}$  later when the beam arrives).

**Enabled channels:** The FONT5a board has 9 ADCs but only two are usually needed for the PFF system (for the mixer and diode of Mon 1 connected to ADC1 and ADC2, with the other two monitors normally connected to the SiS digitisers, see Section 3.4). The FONT5a board can transmit a full data payload (including all 9 ADC channels) over the RS232 port at a rate of up to 460.8 kbps [68]. However, the serial port on the PC is limited to 115.2 kbps and extra hardware would therefore be needed to process this data stream. The unused ADC channels can be disabled instead, so that their data is not transmitted and the data transfer rate is within the limitations of the PC.

## 5.1 Feedforward Controller (FONT5a Board)

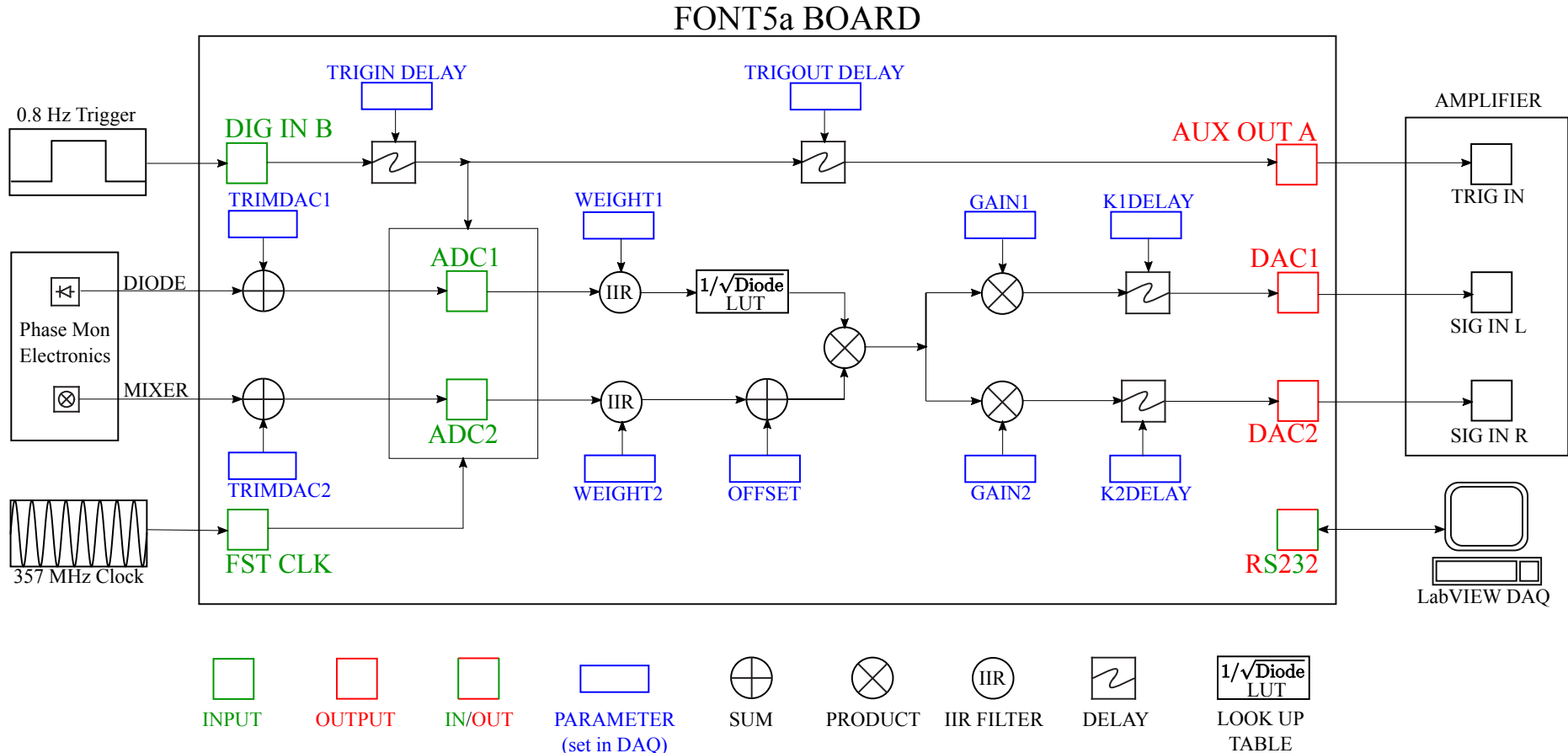


Figure 5.4: Schematic of connections to and outputs from the FONT5a board, as well as the PFF calculation in firmware in the case where the diode is used. If the diode is not used the ADC1 input is not required.

**No. samples:** The length of the ADC sampling window, in number of samples, can also be varied up to 1024. Typically 900 samples are used, covering a time window of  $2.5 \mu\text{s}$  with the 357 MHz clock. If the signal from more than two ADCs is needed the number of samples can be reduced to avoid hitting the baud rate limit of the RS232 port on the PC, the only requirement is that the time window is long enough to encompass the full  $1.1 \mu\text{s}$  beam pulse length.

### ADC Signal Processing

The following parameters must be correctly set in order to remove offsets and droop in the ADC outputs:

**Trim DACs:** As mentioned in Section 5.1 the FONT5a board includes trim DACs in order to remove intrinsic voltage offsets in the output of each ADC. The trim DAC output is added to the ADC inputs, and each trim DAC value must be set correctly in the DAQ. For ADC1 (Diode) and ADC2 (Mixer) the Trim DAC values are typically around 1650 and 1400 counts, corresponding to 8 mV and 7 mV [78], respectively.

**Filter Weights:** Infinite Impulse Response (IIR) filters are implemented in the FONT5a firmware in order to remove droop in the ADC response caused by AC-coupling from their input transformers (see Section 5.1.2). The filter weights for each ADC can be adjusted in the DAQ. Representative values are 50 for ADC1 (Diode) and 56 for ADC2 (Mixer).

**Channel Offset:** To maximise the effect of the PFF system it is necessary to zero the mean upstream mixer (ADC 2) output in the region of the pulse where the correction is desired. This can be achieved by varying the ADC 2 channel offset, as discussed in Section 5.4.3.

### Output Mode

The following parameters control the nature of the DAC output signals:

**Feedforward enable:** The DAC output can be enabled or disabled, as required.

**Interleaved mode:** With interleaved mode enabled the DAC outputs from the FONT5a board are only sent for every second beam pulse. This is useful for interpreting the PFF results, as well as being used for many of the other tests presented in this thesis, as it allows a comparison between beam conditions with and without an applied kick at the same time. In this case the effects of any slow drifts should be equivalent in both the corrected and non-corrected data, thus any differences between the two should be a real effect of the PFF system. Data with the DAC output disabled can also be used to simulate the expected effect of the PFF system in those conditions. All the PFF results in Chapter 6 use interleaved data.

**DAC Output Mode:** The DAC output to the amplifier can be sent in two modes — Sample-by-sample or Constant DAC. In Sample-by-sample mode the DAC output is as needed for the PFF system, being shaped along the pulse by the measured phase multiplied

by the set gain as shown in Figure 5.4. In constant DAC output mode a fixed DAC output between  $-4096 / +4095$  counts is applied, with 4095 counts corresponding to 2 V. This can either be applied across the full length of the ADC sampling window or for a shorter time with an applied gate (see Output Timing). The majority of the results presented in the remainder of this chapter use constant DAC outputs for verification of the amplifier, optics, correction range and correction timing.

**Gain:** In sample-by-sample mode the PFF gain can also be set independently for each correction output, with each being a 14-bit value (between  $-8192$  and  $+8191$ ). The conversion between the gain in the units set in the DAQ and the actual applied gain is derived in Section 5.4.1. A gain of approximately 624 set in the DAQ represents a physical system gain of unity, for which an upstream phase offset of +1 degree results in a downstream phase correction of -1 degrees.

**Diode Mode:** The FONT5a firmware provides three modes for the treatment of the diode signal on ADC1 — normalisation, gating and unused. With diode normalisation enabled the PFF system reconstructs the phase as originally envisaged using Mixer/sqrt(Diode). Due to the issues with the phase monitor diodes as discussed in Chapter 3 the option to not include the diode in the PFF calculation and only include the mixer was later added, which is now the nominal setup. Rather than leaving the diode completely unused, it is usually used to gate the correction output (see below).

**Overflow Mode:** The PFF correction output can behave in three ways in the case where the calculated output is outside the maximum range of  $-4096 / +4095$  DAC counts. In the first iteration of the PFF firmware the calculated correction output would overflow, causing sign flips in the output in the regions where the correction range was exceeded [68]. This behaviour can still be applied in the current firmware if desired. However, in normal operation the output is set to saturate, so that the maximum DAC value of  $-4096 / +4095$  counts, or  $\pm 2V$  at the amplifier, is given when the calculated output is out of range. A final option to provide no output at samples where the calculated output is outside  $-4096 / +4095$  DAC counts, is also provided for test and setup purposes.

## Output Timing

The following parameters control the timing of the DAC output signals:

**Trig out enable:** The trigger sent to the amplifier can be enabled or disabled as required. Clearly the trigger must be enabled for any correction output to have an effect on the beam (the PFF correction output can be turned on with the amplifier trigger disabled for testing purposes).

**Trig out delay:** The timing of the trigger sent to the amplifier can be delayed with respect to the start of the ADC sampling window. This must be adjusted so that the arrival of the  $1.1 \mu s$  beam pulse at the kickers is aligned with the  $1.4 \mu s$  time during which the amplifier is powered and the correction output can be applied [85]. The trig out delay can be varied between 0 and 127, where each unit corresponds to 26 clock cycles or around 70 ns [68]. With a trig out delay of zero the trigger is output when the ADCs turn on, or around

$10 \mu\text{s}$  before the beam (see Input Timing above). The trigger to the amplifier must arrive around  $1.5 \mu\text{s}$  before the beam, so a trig out delay of 110 is typically used. The precise timing of the phase correction output with respect to the beam is set by the K1 and K2 delays below.

**K1, K2 delay:** The K1 and K2 delay are used to fine tune the timing of the two correction outputs (DAC1/K1 for the first kicker and DAC2/K2 for the second kicker), and can be varied by up to 32 ADC clock cycles, or 86 ns with a 357 MHz clock. The optimal delays are 7 clock cycles for K1 and 7–8 clock cycles for K2. The importance of the correction timing and derivation of these values is presented in Section 5.5.

**Gate enable:** The correction output can be restricted to a certain sample range by applying a “gate”. The gate can be defined either as a custom sample range picked by the user or by the presence of the diode signal (ADC1) above a pre-determined threshold (set to 500 ADC counts). Diode gating is typically used so that no output is sent to the amplifier outside the time of the beam pulse. Using a custom sample range has been useful for early PFF tests and to apply a constant kick along only part of the beam pulse (this is used in Section 5.5.4, for example).

### 5.1.2 ADC Droop Correction

The FONT5a (and previous FONT5) boards were originally designed and operated extensively on very short (delta-function like) pulsed signals. During the first tests of the FONT5 board at CTF3, where the beam pulse length is up to  $1.2 \mu\text{s}$ , it was immediately apparent that there was a large droop in the measured phase monitor diode outputs using the FONT ADCs. An example of this, taken from the FONT5a board, is shown in Figure 5.5, remembering that as the diodes are highly saturated the response should be close to a perfect square wave. The measured diode output droops by 200 counts (approximately 15%) across the pulse length, with this difference also visible as an offset in the baseline after the pulse.

The droop emerges as a result of the use of AC coupling on the ADC input transformers for electrical isolation. This results in the low frequency (or DC like) components, with  $dV/dt \sim 0$  ( $V$  being voltage and  $t$  time), of the input signal being blocked [86]. In particular for the diode channel the output is increasingly well described by a DC signal on the flat top as you move away from the leading edge of the pulse, with the capacitor causing droop in the response as a result. There is also a small effect on the mixer output, as will be seen later.

In the simplest case the droop should be well described by an exponential decay of the form  $A \exp(-t/\tau)$ , where  $t$  is the time or sample number along the pulse and  $\tau$  is the decay time constant. For the FONT5 board this only gave a rough approximation of the true droop characteristics due to non-linear properties of the input transformers. On the updated FONT5a board the transformers were changed to both reduce the magnitude of the droop and give closer to the expected exponential decay [85]. Figure 5.6 shows an exponential fit to the Mon1 diode output as seen on the FONT5a board (ADC1). Apart from a small deviation at the beginning of the pulse the agreement is excellent, with residuals to the fit

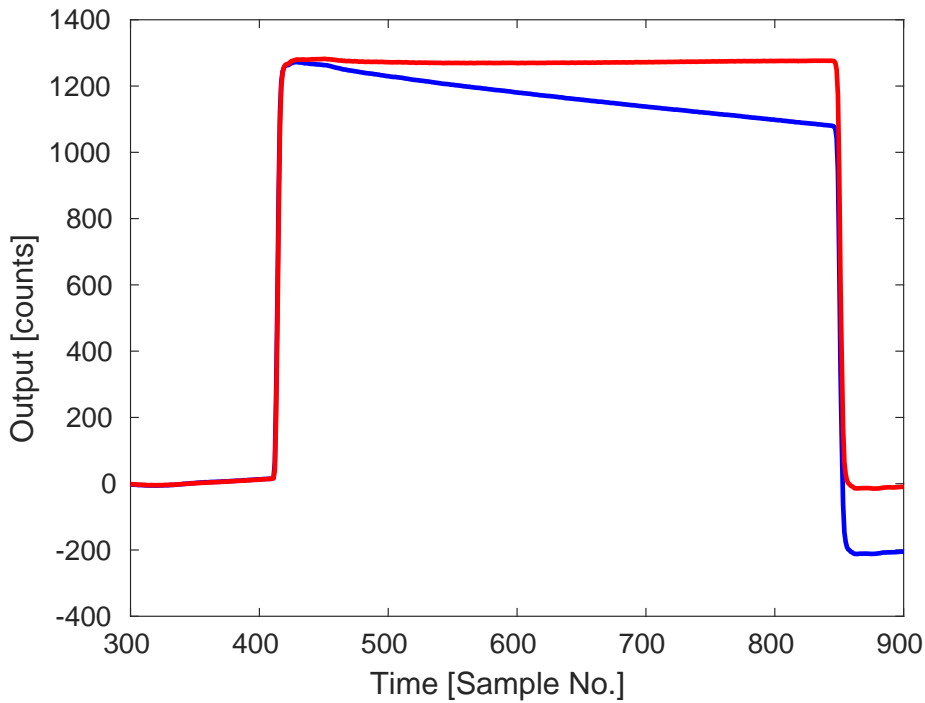


Figure 5.5: Diode output on the FONT5a board with the IIR filter off (blue) and on (red).

of only up to 2 counts compared to a signal magnitude of 1250 counts. For ADC1 the fitted decay time constant is  $\tau = 838 \pm 16$  samples, or  $2.35 \pm 0.05 \mu\text{s}$ . Each ADC on the FONT5a board has slightly different droop characteristics, with the decay time constant for ADC2 being  $938 \pm 18$  samples, or  $2.62 \pm 0.05 \mu\text{s}$ , for example (calculated with the diode moved on to ADC2).

In the case where the diode is used in the phase reconstruction as originally envisaged the ADC droop would propagate in to the applied correction and create an output to the amplifier that increases with time with respect to the ideal value (as the Mixer is divided by  $\text{sqrt}(\text{Diode})$ ). The effect on the correction is much smaller without diode normalisation but it still slightly distorts the measured Mixer input to ADC2. Therefore, a digital Infinite Impulse Response (IIR) filter has been implemented in the FONT5a board firmware to remove the exponential droop in the ADC outputs [26]. This works by recursively adding the expected droop to the ADC output based on the known decay constants, so that:

$$y(t) = x(t) + \frac{1}{\tau} \sum_{i=1}^t x(i-1) \quad (5.1)$$

Here  $y(t)$  is the filtered ADC output at sample  $t$ ,  $x(t)$  is the original unfiltered output at sample  $t$ , and  $\tau$  is the decay time constant. Rather than being hard-coded in the firmware the applied decay constant in the filter for each ADC is calculated using a 7-bit  $-64/+63$  filter weight (set in the DAQ), which is then divided by a common division factor to get the real applied value of  $1/\tau$  [68]. The optimal filter weights for each ADC in the FONT5a board currently used for PFF operation are shown in Table 5.1, these can be converted in to the true decay constant values using the fitted values for ADC1 and ADC2 quoted above.

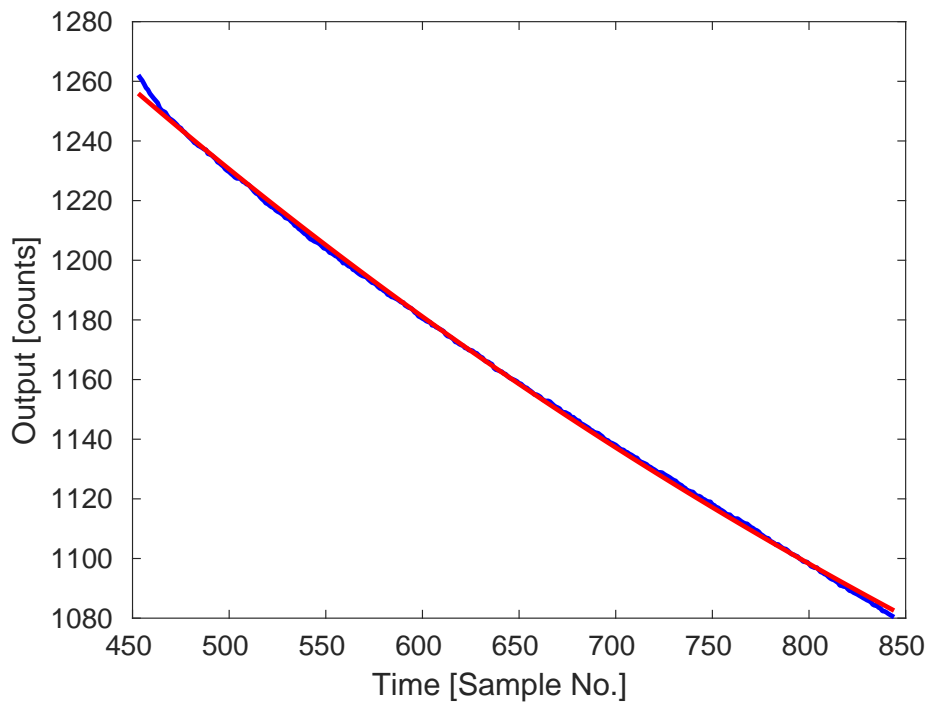


Figure 5.6: Exponential fit (red) to droop on the measured diode output (blue).

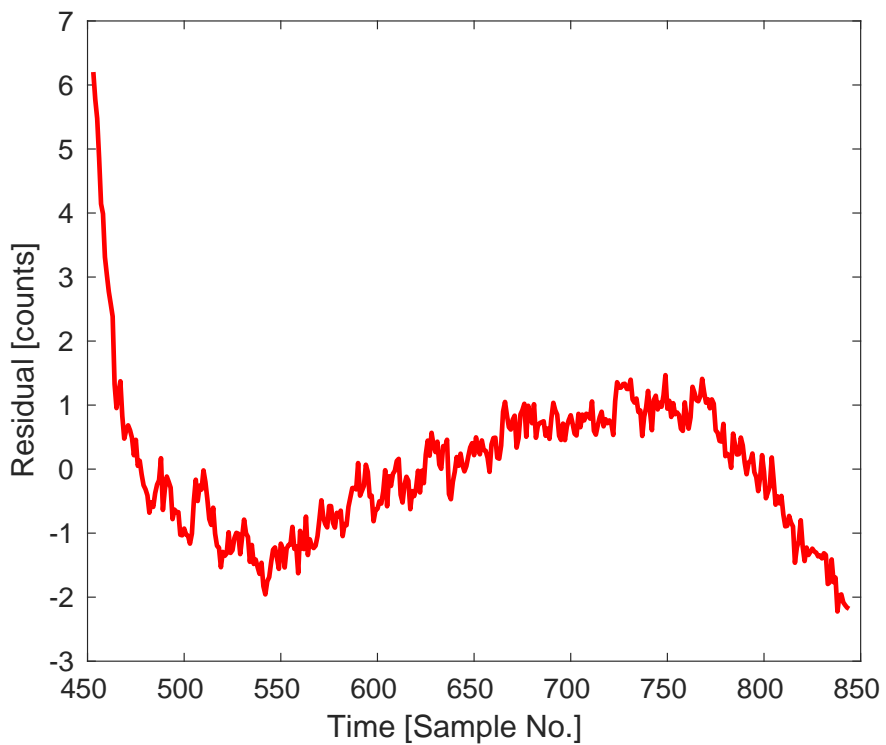


Figure 5.7: Residuals between the measured diode output and the exponential fit to the droop shown in Figure 5.6.

ADC	Decay Constant	Filter Weight
1 (Mon 1 Diode)	$2.35 \pm 0.05 \mu\text{s}$	50
2 (Mon 1 Mixer)	$2.62 \pm 0.05 \mu\text{s}$	56
3	$2.36 \pm 0.05 \mu\text{s}$	50
4	$2.50 \pm 0.05 \mu\text{s}$	53
5	$2.11 \pm 0.04 \mu\text{s}$	45
6	$2.40 \pm 0.05 \mu\text{s}$	51
7	$2.24 \pm 0.05 \mu\text{s}$	48
8	$2.59 \pm 0.06 \mu\text{s}$	55
9	$2.30 \pm 0.04 \mu\text{s}$	49

Table 5.1: Fitted decay constants for the FONT5a board ADCs and the appropriate IIR filter weights to apply in the DAQ.

With the IIR filters enabled on the FONT5a board the droop on the diode (ADC1) is almost perfectly removed as shown in Figures 5.5 and 5.8, although in the zoomed-in Figure 5.8 some slight deviation from flat is visible due to the residuals around the exponential fit seen previously. The effect on the reconstructed phase using only the mixer (ADC2) is shown in Figure 5.9, with a modest adjustment to the overall shape that is most visible at the start and end of the pulse.

## 5.2 Amplifier

The amplifier takes the two DAC signals from the FONT5a board and uses them to produce four high voltage outputs. These are connected to the downstream ends of the kicker strips (two kickers and two strips per kicker gives four connections at the downstream ends in total), creating the potential difference between the strips that deflects the beam in order to correct the phase. The returning signals from the upstream ends of the kicker strips are then terminated back at the amplifier. As the amplifier is installed together with the phase monitor electronics and FONT5a board in the klystron gallery the cables between the amplifier and kickers are long and represent the single largest contribution to the overall system latency, as discussed in Section 5.5.1. This section discusses the design and performance aspects of the amplifier that are relevant to PFF operation.

### 5.2.1 Design

The amplifier is purpose built for the PFF prototype, also at Oxford University, with further details of its design available in [27]. An annotated picture of its front panel is shown in Figure 5.10 and a simplified diagram showing the flow of signals between the FONT5a board, amplifier and kickers is shown in Figure 5.11. The amplifier is installed in a standard 3U rack and has a modular design. It consists of five individual modules split between two sides, labelled left and right. The left side of the amplifier, which uses the DAC 1 output, powers the first kicker in the chicane, and the right side of the amplifier, which uses the DAC 2 output,

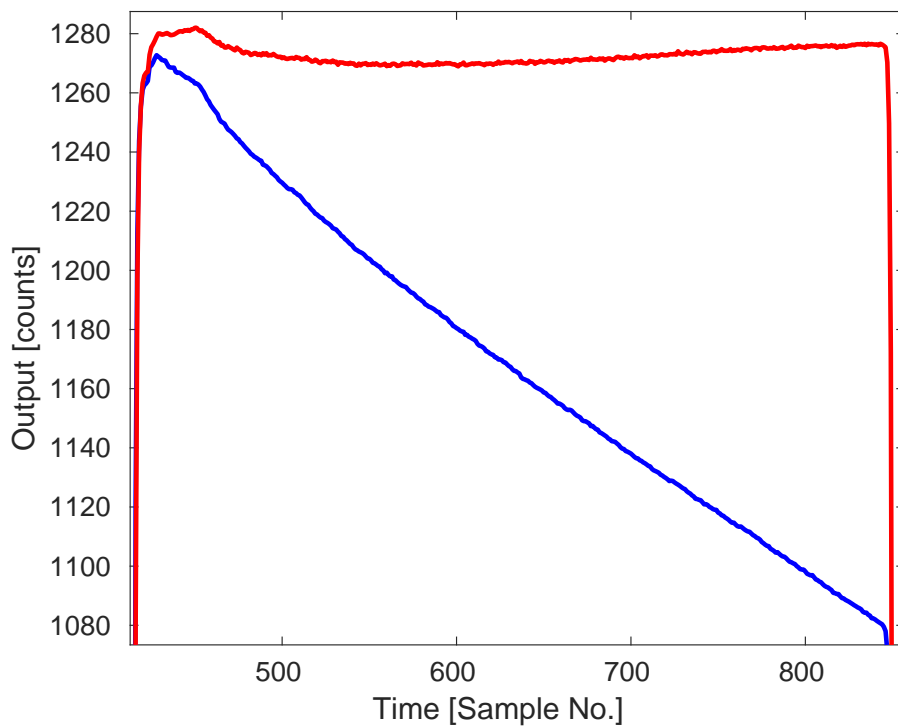


Figure 5.8: Measured diode output on the FONT5a board with the IIR filter off (blue) and on (red). Zoomed in to show deviations from the ideal square wave that are not visible in Figure 5.5.

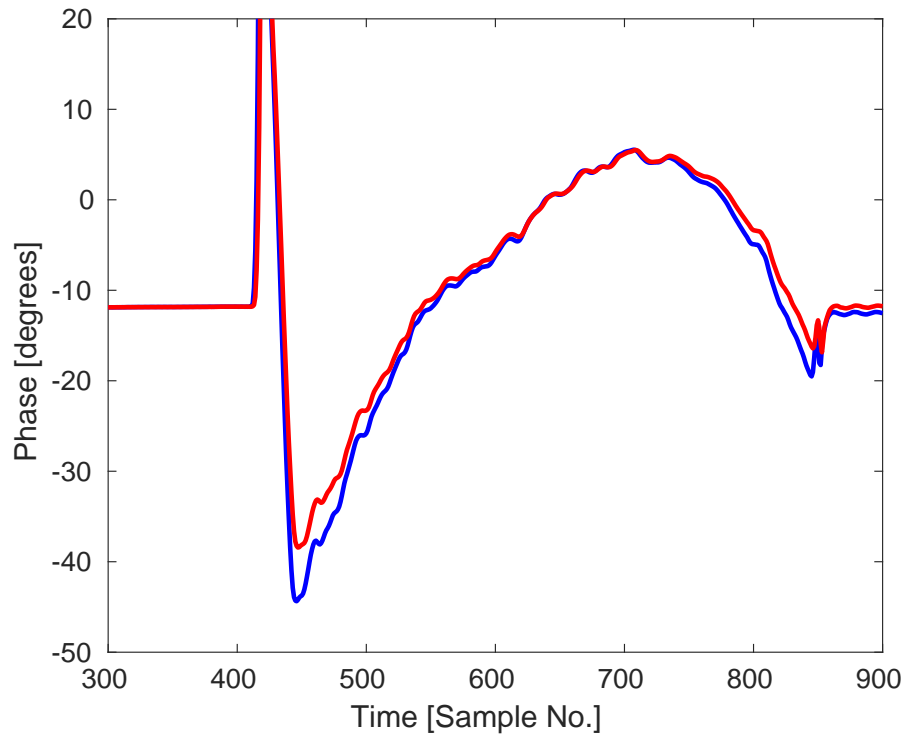


Figure 5.9: Measured phase on the FONT5a board with the IIR filter off (blue) and on (red).

powers the second kicker. Each side of the amplifier contains its own “drive module” and “terminator module”. Finally there is a central “control module” that is common to both sides of the amplifier.

The control module takes the amplifier trigger and drive signals from the FONT5a board, as well as 24 V, 1.1 A power from the mains. It then deals with the distribution of power and input signals (derived from the DAC inputs) to the two drive modules, including signal processing designed to protect the drive modules. For example, it ensures the maximum signal level sent to the drive modules is at a safe level and limits the rate of large changes in the input drive signal (limits the slew-rate), as well as disabling the trigger for the drive modules if a problem is detected.

The amplification of the signals to create the high voltage outputs occurs in the drive modules. Each drive module takes one input signal but creates two high voltage outputs (A and B) which have equal magnitude but opposite polarity. These are connected to the downstream end of the left and right strips of one of the kickers, to create a potential difference across the kicker strips that is double the voltage of each individual drive output. The signal amplification consists of low voltage Si FETs (Ixys DE150-201N09A [87]) driving high voltage SiC FETs (Wolfspeed C2M0160120D [88]) and a final output transformer, giving a peak output of around  $\pm 700$  V (seen in more detail in Section 5.2.2). The output has a bandwidth of 47 MHz for small signal variations up to 20% of maximum output (around 140 V). The bandwidth for larger variations is slew rate limited, and around 25 MHz for variations up to 50% of the maximum output, for example [27].

Each drive module requires a ramp up time of  $1\ \mu s$ , which defines when the trigger must arrive from the FONT5a board. After this period the drive modules are powered for  $1.6\ \mu s$  with full output across  $1.3\ \mu s$  (slightly longer than needed to correct the full  $1.1\ \mu s$  CTF3 beam pulse length). The control module includes a monitoring output (labelled “ON”) that can be used as a reference to observe the time period within which the drive modules are on and ready to receive input.

The high voltage signals leaving the upstream ends of the kicker strips are terminated back at the amplifier on the terminator modules. Each module consists of two  $50\ \Omega$  terminators designed to be able to withstand the maximum 20 kW output from the drive modules [27]. Each terminator also provides a monitoring signal, which gives output at around -40 dB or approximately  $1/115$  of the input voltage [85]. These can be used to verify that the applied output from the drive modules is as expected, and form the basis of most of the measurements in the remainder of this section as well as for the timing checks in Section 5.5.3, for example.

The description of the amplifier here represents the version of the amplifier that was used for the latest PFF tests, and for almost all results in this thesis. A first version of the amplifier, which delivered half the output voltage (up to  $\pm 350$  V), was used for early PFF tests. Additional FETs were added in the second version described above to boost the output voltage to  $\pm 700$  V. It was also originally planned to combine four drive modules on each side of the amplifier to give a voltage of up to  $\pm 1400$  V [84], but this would require additional hardware and is being considered as a future option.

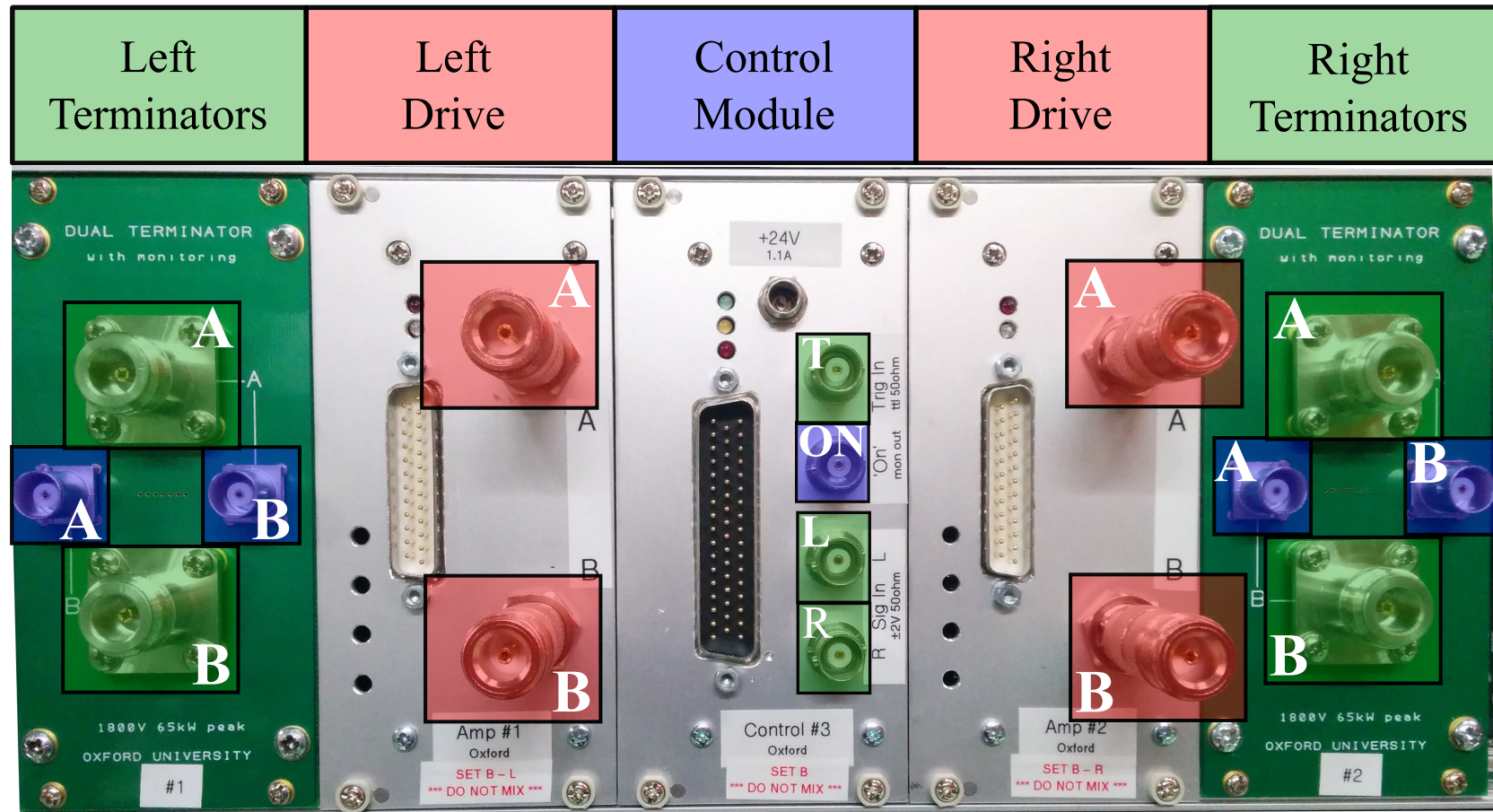


Figure 5.10: Front panel of the amplifier. Inputs to the amplifier are highlighted in green, drive outputs in red and monitoring outputs in blue. Inputs to the control module are the trigger (T) and the two DAC outputs from the FONT5a board used to determine the drive to the left (L) and right (R) sides. Each side of the amplifier has two pairs of drive outputs and terminators, A and B. The signal returning to each of the terminators can be observed on their corresponding monitoring outputs. The monitoring output on the control module (ON) shows the  $1.4 \mu\text{s}$  time during which the amplifiers are able to provide their output. Not highlighted in the figure are the 24 V, 1.1 A power connector at the top of the control module, and also the three custom connectors used to communicate between the control module and drive modules.

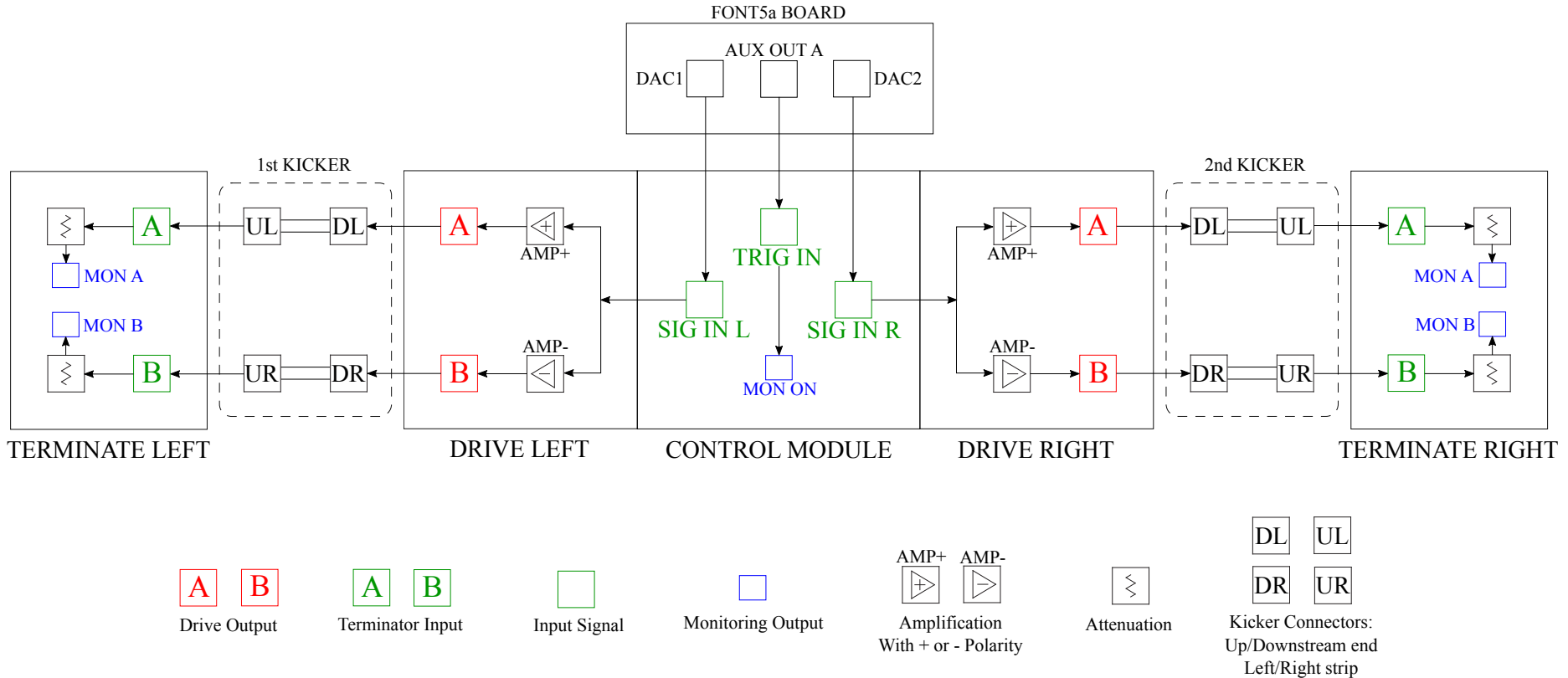


Figure 5.11: Simplified flow diagram showing the connections between the FONT5a board, the amplifier and the kickers. The kickers are inserted between the drive and terminator modules for the purposes of the diagram, but in reality the terminator modules neighbour the drive modules in the same unit as seen in Figure 5.10. Note that the A and B outputs on each side always have opposite polarity, as needed to create a large potential difference between the kicker strips.

### 5.2.2 Linearity

Figure 5.12 shows the amplifier output, measured using the monitoring signals, at different constant input voltages sent from the FONT5a board between the minimum of -2V (-4095 DAC counts) and maximum of 2V (+4095 DAC counts). The amplitude of the monitoring signals is converted in to the amplifier output Voltage using the approximate conversion factor of 115 [85]. All four amplifier outputs are shown (one for each strip of the two kickers). The values plotted are the mean of the 480 ns central region of the whole 1400 ns output pulse.

The relative polarity of the four outputs used is equivalent to what would be applied to the kickers during PFF operation, with opposite polarity of the L and R amplifier outputs (powering the first and second kicker respectively), so that the beam is kicked in opposite directions by each kicker. The second kicker should then act to close the orbit bump created by the first kicker. Within each side of the amplifier the A and B outputs (applied to the left and right strip of each kicker respectively) also have opposite polarity. This is necessary to create the potential difference between the kicker strips that produces the deflecting field for the beam. The relative polarity of the A and B outputs is fixed in the amplifier design and cannot be controlled via the FONT5a board.

The response of the amplifier is linear up to  $\pm 1.2$  V input voltage. Outside this range the amplifier clearly begins to enter saturation, in particular above input voltages of  $\pm 1.7$  V. The linear fits shown include only the points up to  $\pm 1.2$  V, in order to not be biased by the effects of saturation. Figure 5.13 shows the difference between the linear fit and the real amplifier output across the full range of input voltages. A slight deviation from linearity in the  $\pm 1.2$  V range is also visible, although the maximum difference is only 10 V or a 3% relative error. At the maximum input voltage of  $\pm 2$  V the deviation from linearity rises above 150 V, a relative error of more than 25%. For example, the RB output at an input voltage of +2 V is 605 V but the fitted response gives 769 V, a difference of 164 V or 27%.

The effects of amplifier saturation are not taken in to account in the PFF algorithm on the FONT5a board, in which the DAC output is linearly dependent on the input phase (voltage from the phase monitor mixer signal) across the full range. The correction applied to the downstream phase will therefore be non-optimal when the output calculated by the PFF algorithm is above an absolute value of 2500 DAC counts (1.2 V amplifier input). To date the non-linearity of the amplifier as it begins to enter saturation has also not been included in the PFF simulations presented in the following chapters. This may partially explain the small discrepancies seen between the simulated and measured results in some datasets, so including the effect will be pursued in the future.

Discrepancies between the four amplifier outputs are seen in Figure 5.13 and Table 5.2, both in terms of gradient and peak output. These differences can be partially but not completely explained by errors of up to a few percent in the precise calibration of the four monitoring outputs, which do not output exactly 1/115 of the real input voltage [85]. Differences between the A and B outputs for each kicker are not an issue for the PFF performance as both are linear (in the  $\pm 1.2$  V range) and the kick experienced by the beam in each kicker is proportional to the difference of the two. Therefore, only the calibration between

Amplifier Port	Input Voltage	Output Voltage
LA	+1 V	+416 $\pm$ 3 V
LB	+1 V	-453 $\pm$ 3 V
RA	-1 V	-426 $\pm$ 3 V
RB	-1 V	+409 $\pm$ 3 V

Table 5.2: Fitted output voltage for each amplifier channel with an applied input voltage of +1 V or -1 V, as indicated.

the output from the FONT5a (the amplifier input) and the resulting phase shift in the TL2 chicane is affected. However, disparity between the potential difference across each kicker (LA-LB and RA-RB), so that the deflection of the beam in each kicker is different, leads to the orbit bump created by the PFF system not being closed in the chicane, degrading the horizontal beam stability downstream. The fitted potential difference at 1 V input is 869 V for the left amplifier (LA-LB, applied to the first kicker) and 835 V for the right amplifier (RA-RB, applied to the second kicker), a difference of 4%. This could be compensated in the PFF setup on the FONT5a board by using a different gain for each correction output, so that the DAC output to the right amplifier is higher but the resulting voltage applied to both kickers is the same. Orbit closure is discussed further in Section 5.3.2.

### 5.2.3 Amplifier Pulse Shape Characteristics

In the previous section the linearity of the mean output was considered but the performance of the PFF correction is clearly also sensitive to any variations in output voltage along the amplifier output pulse. Figures 5.14 and 5.15 show the full 1.4  $\mu$ s amplifier output with a constant input of +1 V (-1 V) applied to the left (right) amplifier respectively. Spikes in the signal just prior to 2000 ns and after 3000 ns on the time axis as seen in the plots are pickup on the kicker strips induced by the beam. These are therefore not a property of the amplifier performance and are excluded from the analysis in this section. However, the beam pickup is used later in Section 5.5.3 for the purposes of optimising the correction timing.

For each side of the amplifier both the A and B outputs are plotted as well as the difference of the two, which is the relevant quantity in terms of the kick received by the beam. In the ideal case the potential difference should be flat along the full pulse length. However, for both the left and right side variations are visible, with an initial increase in output across the first 500 ns of the pulse followed by a droop in response across the second half of the pulse. Figure 5.16 shows the peak-to-peak and mean deviation of the output voltage along the pulse across the full range of input voltages. The peak-to-peak deviation refers to the difference between the minimum and maximum output along the pulse, whilst the mean deviation is the average absolute difference between the mean output and the output at each sample point. For a constant input voltage the output voltage along the pulse varies by up to 88 V peak-to-peak (mean 12 V) for the left amplifier or 93 V peak-to-peak (mean 14 V) for the right amplifier. As a relative difference, this corresponds to approximately a 6 % peak-to-peak, or 1 % mean, variation along the pulse.

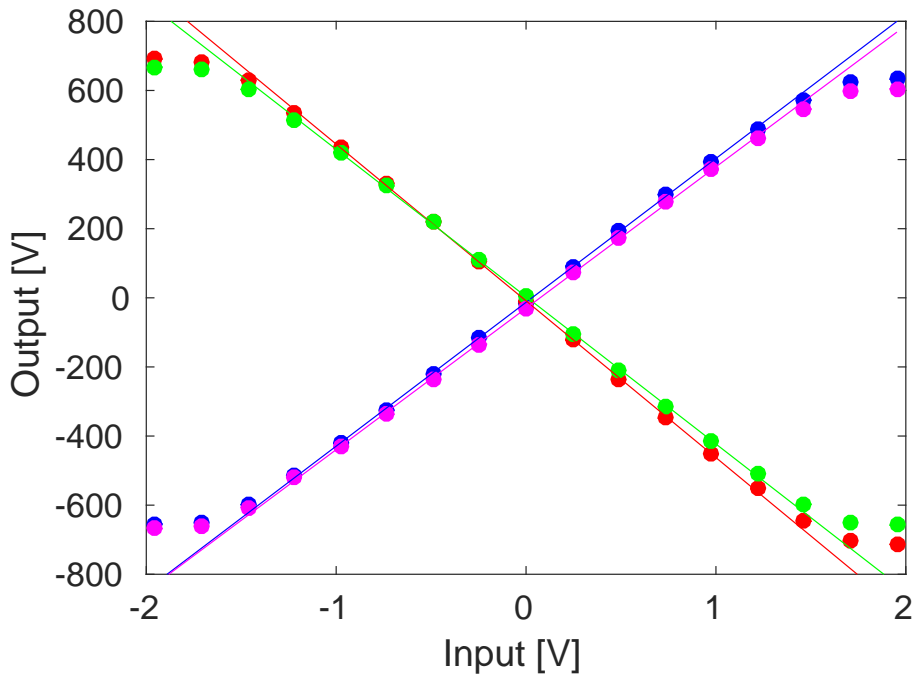


Figure 5.12: Mean output of each amplifier channel vs. the input voltage. The four amplifier channels are: LA (blue), LB (red), RA (green) and RB (magenta). Markers show the measured output, and lines a linear fit to the output in the  $\pm 1.2$  V input range.

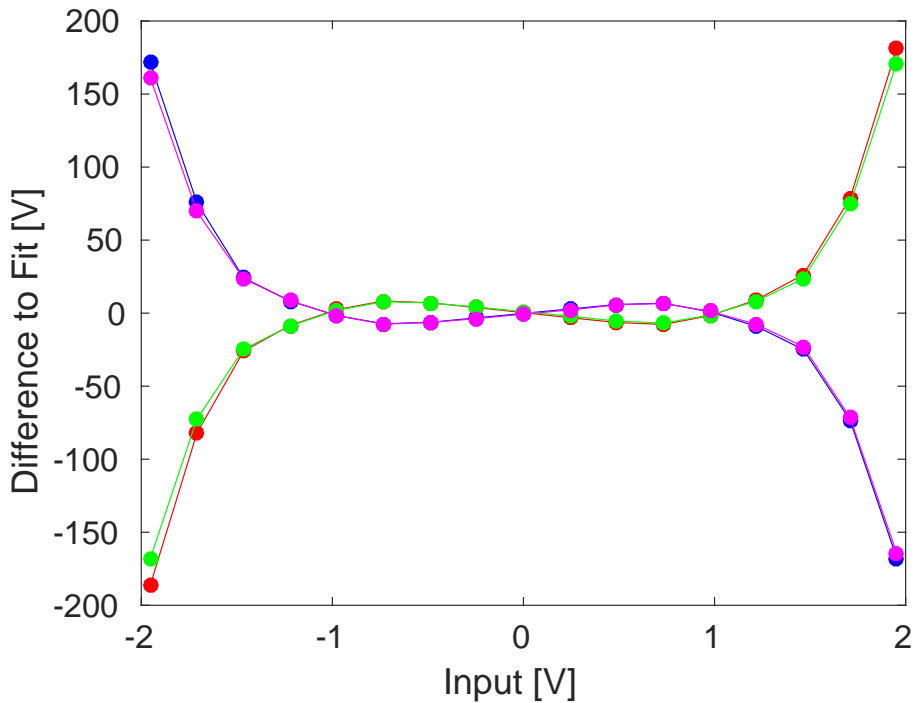


Figure 5.13: Residuals between the amplifier output voltage and the linear fits seen in Figure 5.12. The four amplifier channels are: LA (blue), LB (red), RA (green) and RB (magenta).

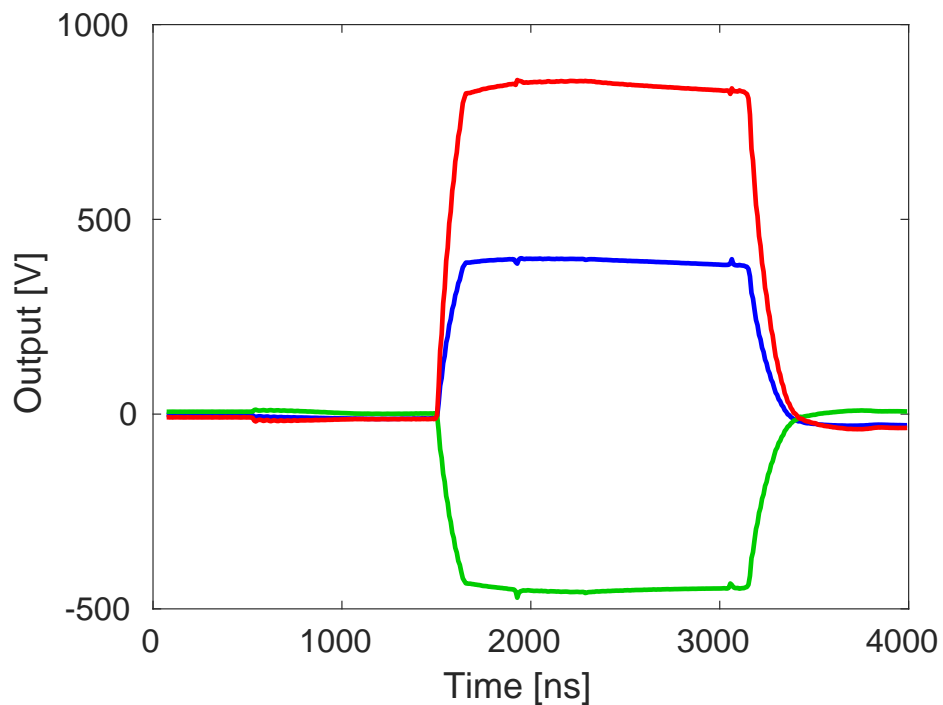


Figure 5.14: The full output pulse of the A (blue) and B (green) channels for the left side of the amplifier, at an input voltage of +1 V. The difference between the A and B output is shown in red.

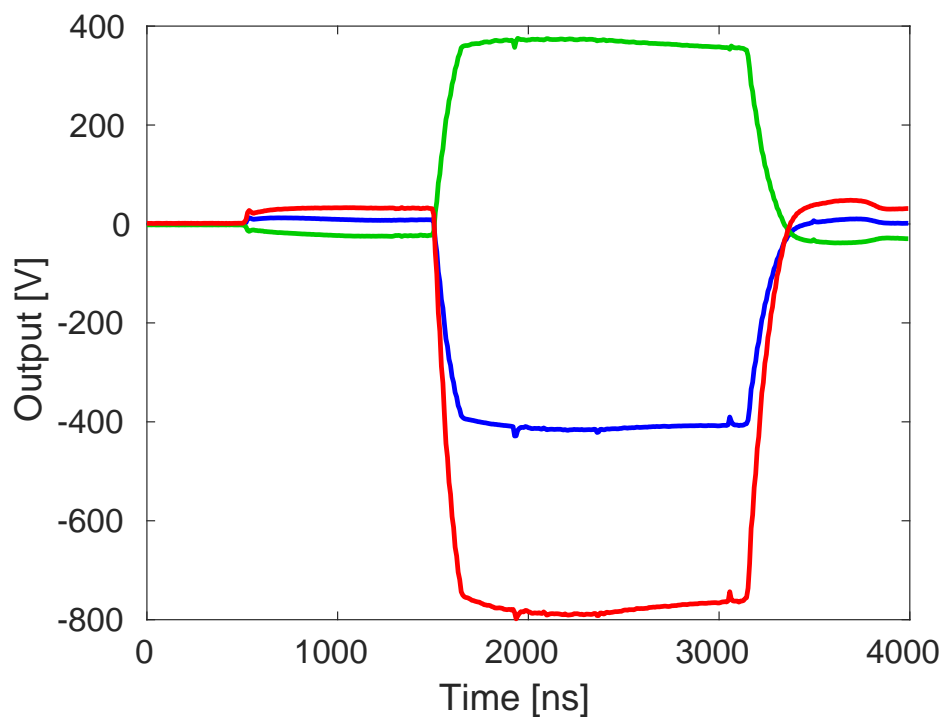


Figure 5.15: The full output pulse of the A (blue) and B (green) channels for the right side of the amplifier, at an input voltage of -1 V. The difference between the A and B output is shown in red.

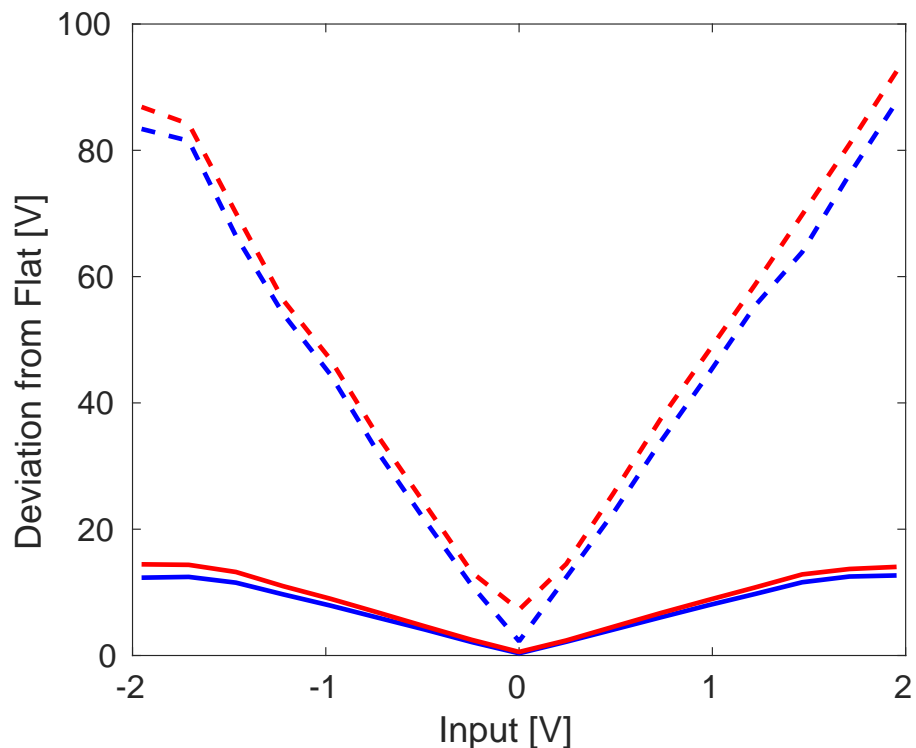


Figure 5.16: Peak-to-peak (dashed lines) and mean (solid lines) deviation from a flat output along the full amplifier output pulses for the left (blue) and right (red) side of the amplifier. The values are calculated using the difference between the A and B outputs of each side, the quantity relevant for kick experienced by the beam.

The PFF algorithm on the FONT5a board uses a single gain value across the whole pulse length for each correction output, thus making the approximation that the amplifier response is flat along the pulse. The variations along the amplifier pulse therefore directly translate in to discrepancies between the intended phase shift as calculated and the real phase shift experienced by the beam. As the region of interest for the correction is a few hundred nanoseconds about the central part of the pulse, as opposed to the full pulse length, the 1 % mean variation is more indicative of the resulting error than the 6 % peak-to-peak variation. With a correction range (Section 5.3.1) of  $\pm 5.5^\circ$ , the effects of the non-flat amplifier output should be below  $0.06^\circ$  and not measurable considering the phase monitor resolution of  $0.13^\circ$ .

Variations in the amplifier output along the pulse can also lead to imperfect orbit closure in the chicane, as discussed in Section 5.2.2 for differences in the mean output. However, this would also be a small effect and in any case orbit closure has not yet been strictly enforced during operation of the PFF system (Section 5.3.2). Nevertheless, it could be foreseen to implement a droop correction in the PFF algorithm on the FONT5a board, taking the variations in the amplifier output along the pulse in to account and providing a modest improvement to both the phase correction and orbit closure. A first attempt could use IIR filters on the FONT5a DAC outputs in the same way as implemented to correct the ADC droop (Section 5.1.2), so that the DAC output to the amplifier towards the end of the pulse is boosted slightly to compensate for droop in the amplifier output.

## 5.3 Kicker and Optics Performance Verification

### 5.3.1 Correction Range

Knowledge of the correction range of the PFF system, or more specifically the relationship between the DAC output voltage from the FONT5a board and the resulting phase shift in the chicane, is critical for the PFF setup. In particular, it is needed to derive the optimal correction gain, as seen in Section 5.4.1.

Figure 5.17 shows the measured mean phase shift in the downstream phase monitor across the full  $\pm 2$  V input range of the amplifier. Constant DAC outputs in 17 steps between -4095 counts (-2 V) and +4095 counts (+2 V) were used to drive the amplifier. For each amplifier input voltage 100 beam pulses were acquired in interleaved mode (Section 5.1.1) in order to reduce the sensitivity to any drifts in beam phase between data points. The phase plotted in Figure 5.17 is the difference between the 50 beam pulses with the DAC output enabled (non-zero amplifier input) and the 50 beam pulses with the DAC output disabled (0 V amplifier input).

At the maximum amplifier input voltage of 2 V the phase is shifted by  $5.5 \pm 0.3^\circ$ . The fitted phase shift per Volt input is  $3.5 \pm 0.1^\circ$  in the  $\pm 1.2$  V linear range of the amplifier. This fitted gradient is required for the conversion between the PFF gain in the units on the FONT5a board and the effective system gain in Section 5.4.1.

Given knowledge of the amplifier output characteristics (Section 5.2.2), the kicker speci-

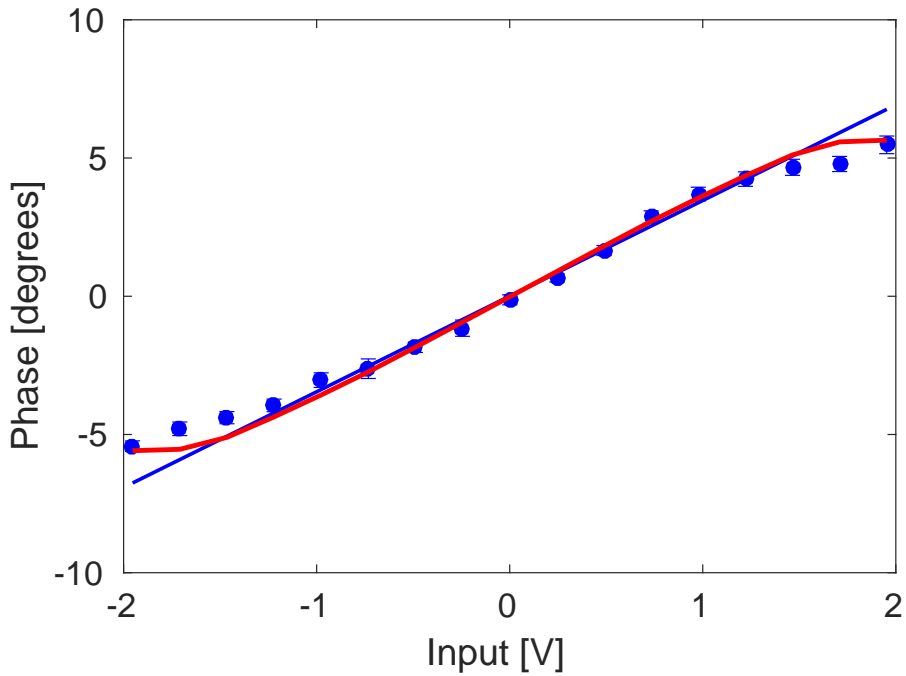


Figure 5.17: Measured downstream phase shift versus amplifier input voltage (blue markers). The blue line shows a linear fit to the measured phase shift for inputs between  $\pm 1.2$  V. The red line shows the expected phase shift taking in to account the TL2 chicane optics, amplifier output voltage and kicker design (using Equation 5.2).

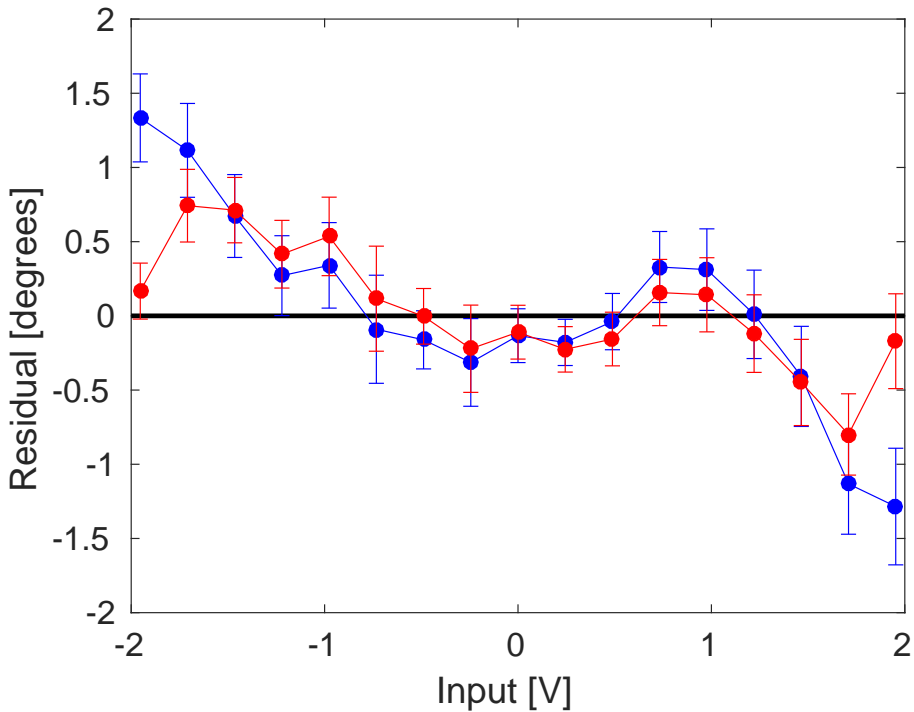


Figure 5.18: Residuals between the measured phase shift and the expected (red) and fitted (blue) phase shifts from Figure 5.17.

	Phase Shift at +1 V Input	Max Phase Shift
Data	$3.5 \pm 0.1^\circ$	$5.5 \pm 0.3^\circ$
Model	$3.6^\circ$	$5.6^\circ$

Table 5.3: Downstream phase shift resulting from an amplifier input of 1 V (+1 V for the left amplifier/first kicker, and -1 V for the right amplifier/second kicker). The “Data” row shows the fitted gradient from the actual measured phase shift. The “Model” row shows the expected result given the known hardware and optics parameters.

fications (Section 2.2) and the chicane optics (Section 2.6) the measured phase shift in the scan can be compared to the expected phase shift based on the system parameters. The predicted phase shift,  $\Delta\phi$ , in degrees is given by:

$$\Delta\phi = V_{amp}[V_{font}].K.R_{52} \cdot \frac{360}{\lambda_{12\text{GHz}}} \quad (5.2)$$

Here  $V_{amp}[V_{font}]$  is the amplifier output Voltage at an input voltage of  $V_{font}$  (the FONT5a board DAC output),  $K$  is the angular deflection of the beam per Volt applied to each kicker strip,  $R_{52}$  is the transfer matrix coefficient between the kickers in the PFF optics and  $360/\lambda_{12\text{GHz}}$  converts the calculated orbit length difference in to an equivalent 12 GHz phase using the 12 GHz wavelength  $\lambda_{12\text{GHz}}$ . The value of most of these parameters has already been derived, in Sections 2.2, 2.6 and 5.2.2. They are:

$$\begin{aligned} V_{amp}[1 \text{ V}] &= 435 \text{ V} \\ K &= 0.8 \text{ } \mu\text{rad/V} \\ R_{52} &= -0.7 \text{ m} \\ \lambda_{12\text{GHz}} &= 2.5 \text{ cm} \end{aligned}$$

The value of  $V_{amp}[1 \text{ V}]$  is given as a representative value in the linear range of the amplifier but the actual amplifier output at all input voltages is used in the predictions to include the effects of saturation in the calculated phase shift values. Also, the first kicker is used as this is most relevant for the phase shift in the chicane (the orbit should be closed after the second kicker with no further phase shift in the chicane after that point). The value of  $K$  is derived from the kicker design, in which 1.4 kV applied to each strip gives a 1 mrad kick for a 150 MeV beam [28]. The actual CTF3 beam energy is approximately 135 MeV (calculated based on the dipole currents used in the machine setup and segmented dump measurements), so the value of  $K$  above is scaled by a factor 150/135.

In Figure 5.17 the predicted phase shifts using Equation 5.2 are also shown. Table 5.3 compares the fitted gradients and maximum phase shift for the model and the measurement. The overall agreement between the two is good, with the residuals between the model and the data generally consistent with zero within error bars in the  $\pm 1.2$  V linear range of the amplifier as shown in Figure 5.18. The residuals between the data and the linear fit to the data are also consistent with zero in this range.

Outside the linear range some discrepancies appear, with the difference being largest where the amplifier has started to enter saturation but before it has reached peak output.

The actual amplifier output voltage at all inputs (from Section 5.2) is used to calculate the expected phase shift shown in the figure. This means any differences between the measured and expected results are unlikely to be related to the amplifier. Possible explanations could be remaining higher order errors in the TL2 chicane optics, or unexpected behaviour from the kickers or amplifier. Although subtracting alternating pulses should remove the sensitivity to drifts in the machine it is possible that some residual effect remains. To determine whether the discrepancies are reproducible further scans of this type will need to be performed in the future. The residuals between the data and the linear fit between  $\pm 1.2$  V would also be of significance for the PFF correction should they not converge to zero with additional measurements, as they are of similar magnitude to the  $0.2^\circ$  downstream jitter target.

However, the overall conclusion is as expected — the phase shift in the chicane linearly depends on the amplifier input in the  $\pm 1.2$  V ( $\pm 2500$  DAC counts) region thus a close to optimal correction can be applied in this range, corresponding to a  $\pm 4.2 \pm 0.1^\circ$  phase shift within the total range of  $\pm 5.5 \pm 0.3^\circ$ . When the calculated optimal correction is between an absolute input voltage of 1.2 V and 2.0 V, 2500 to 4096 DAC counts, or  $\pm 4.2 \pm 0.1^\circ$  to  $\pm 7.0 \pm 0.2^\circ$ , the actual phase shift in the chicane is lower, only up to  $\pm 5.5 \pm 0.3^\circ$ , due to the amplifier entering saturation (and possibly other effects to be determined). Any calculated correction outside  $\pm 5.5 \pm 0.3^\circ$  receives a static phase shift of  $\pm 5.5 \pm 0.3^\circ$  in the chicane. In the limit where all pulses are outside this range the PFF system can only induce a static shift in the mean phase and makes no improvement to the phase jitter. The effect of limited correction range on the most recent PFF results is seen in Section 6.3.

Aside from its use for the PFF setup demonstrating the ability to shift the phase in the TL2 chicane is already a significant accomplishment. In particular a phase shift is only possible if  $R_{52}$  is non-zero between the kickers in the optics for the chicane (Section 2.4.2). The agreement between the modelled and measured correction range verifies the optics is performing as expected, which would not have been possible without the improvements made to the MADX model of the line in Section 2.5. It also shows the kickers are performing as per their design, imparting the expected angular deflection to the beam for the applied voltage from the amplifier.

### 5.3.2 Orbit Closure

At CLIC the PFF system must not degrade the transverse beam stability. This means for any voltage sent to the kickers the horizontal beam orbit after the PFF chicane must be unchanged, or closed, despite the different orbits inside the chicane. As such, the PFF optics for the TL2 chicane at CTF3 is also designed to give a closed kick, as presented in Section 2.6. However, up until now the main focus during PFF operation has been the primary goal of reducing the downstream phase jitter and ensuring good beam transmission to the downstream phase monitor. As a result orbit closure after the TL2 chicane has not yet been strictly enforced during PFF operation as will be seen in this section, but the current status is shown here as an additional cross-check of the PFF optics and to highlight where improvements are needed for future tests.

Using the same constant kick data as Section 5.3.1, Figure 5.19 shows mean the horizontal

orbit before, inside and after the TL2 chicane across the full  $\pm 2$  V range of amplifier input voltages. Two BPMs before and after the chicane, as well as the four inside the chicane, are included. The positions plotted are the difference between the kicked and nominal (non-kicked) orbit at each BPM, thus removing any misalignment in the BPM centres. Before the chicane and the first kicker there is no significant effect on the orbit as expected. Inside the chicane the PFF system induces an orbit offset of up to  $1.4 \pm 0.1$  mm. After the chicane, in BPMs CC.845 and CC.930, the orbit should return to zero in the ideal case. However, a clear residual offset can be seen, up to  $0.5 \pm 0.1$  mm in CC.930.

Although every effort has been made to keep the TL2 optics as close to nominal as possible, particularly inside the chicane, it is an extremely sensitive area for the setup of CTF3 and beam transport in to the CLEX area downstream of TL2 (including the location of the downstream phase monitor in the TBL line) is always difficult [45]. Minor modifications have therefore been necessary in order to achieve full beam transmission to the downstream area, both for PFF and other experiments at CTF3. The largest changes have been made to the four quadrupoles following the chicane but one quadrupole inside the chicane, CC.IQFL0730 (just prior to the 2nd kicker) has a set value 10% lower than the nominal optics, as well as differences up to 2% in the other quadrupoles.

Figure 5.20 compares the measured beam orbit in the BPMs to the expected response in the PFF optics with the nominal quadrupole strengths, and the expected response taking in to account the actual quadrupole strengths used in this dataset. The full MADX orbit propagated through all elements is shown, with the eight measured BPM offsets included at their respective positions. Each BPM point represents the gradient of a linear fit using the variation with input voltage seen previously in Figure 5.19. Before and inside the chicane the agreement between the BPM data and both models is excellent. After the chicane the orbit is closed in the nominal optics but the measured position offset in the BPMs is non-zero, as seen previously. However, there is excellent agreement between the measured positions and the expected response in the MADX model taking in to account the actual quadrupole strengths applied in TL2 during this dataset.

This gives confidence that if a completely nominal optics could be used in TL2 orbit closure would be obtained. For future tests attempts will be made to further optimise the setup of CTF3 and allow a completely nominal optics to be used in TL2. It should also be noted that for these tests both sides of the amplifier were driven with the same magnitude input voltage. This has also been the case for all the PFF correction attempts presented in Chapter 6. However, in Section 5.2.2 it was seen that the right side of the amplifier (powering the second kicker) gave 4% lower output than the left side (powering the first kicker). To strictly enforce orbit closure with a nominal optics it would therefore be necessary to drive the right side of the amplifier with a 4% higher input voltage (by using a 4% higher gain for the DAC2 output compared to the DAC1 output on the FONT5a board).



Figure 5.19: Horizontal orbit offset in and around the TL2 chicane at different amplifier input voltages (as indicated by the colour scale). The approximate positions of the chicane entrance and exit are indicated by vertical black lines. The two PFF kickers are located at index CC.480 and CC.780 (before the first and last dipoles in the chicane).

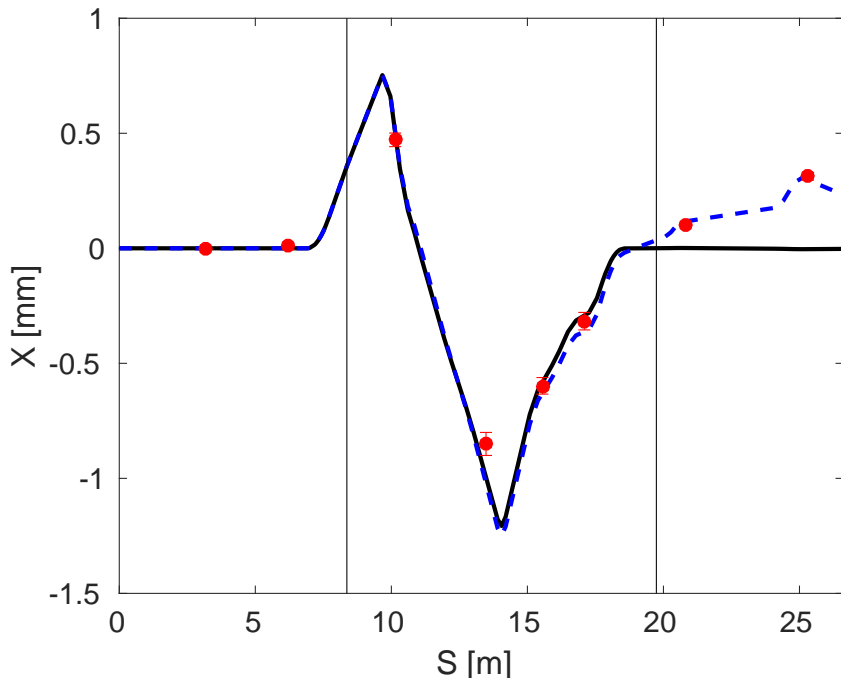


Figure 5.20: Orbit in the TL2 chicane at 1 V amplifier input for the BPM data (red markers), nominal model (black line) and the model taking in to account the actual quadrupole currents used in TL2 at this time (dashed blue line). Vertical black lines mark the entrance and exit of the chicane.

## 5.4 Calculation and Application of the PFF Correction Output

### 5.4.1 Gain Calculation

As shown in Section 4.1 the effect of the PFF system can be modelled by simply subtracting the measured upstream phase,  $\phi_u$ , from the downstream phase,  $\phi_d$  with a gain factor,  $g$ :

$$\phi_{PFF} = \phi_d - g\phi_u \quad (5.3)$$

Here  $\phi_{PFF}$  is the corrected downstream phase. The gain set in the FONT5a DAQ is not directly a multiplication factor in terms of the phase, but rather a multiplication in terms of DAC counts and other constants. How the set gain on the FONT5a board relates to the true gain  $g$  is derived in this section.

In the case where diode normalisation is not used, which is the nominal setup, the DAC outputs when the PFF system is enabled are given by:

$$\begin{aligned} \text{DAC1} &= \frac{F1}{64} \text{ADC2} \\ \text{DAC2} &= \frac{F2}{64} \text{ADC2} \end{aligned} \quad (5.4)$$

Here DAC1 and DAC2 are the two DAC outputs, in DAC counts, F1 and F2 are the respective gains for each DAC output set in the DAQ, and ADC2 is the Mon1 mixer signal level in ADC counts, which is connected to ADC2 for normal PFF operation. The whole calculation uses 16-bit architecture, with the 3 sub-integer bits discarded when sent to the 13-bit DACs [68]. The FONT gains F1 and F2 are 14-bit (-8192 to +8191) and the common division factor of 1/64 is set by several parameters fixed in the FONT5a firmware [68]. Typically  $F2 = -F1$ , so that the beam is deflected in opposite directions in each kicker to achieve orbit closure in the chicane. With a maximum gain of 8192 an ADC2 input of 1 ADC count gives an output of 128 DAC counts. If diode normalisation is enabled the expressions above are multiplied by  $1/\sqrt{\text{ADC1}}$  (with the Mon1 diode signal connected to ADC1 in normal operation) and different scale factors are used [68].

To determine the optimal values for F1 and F2 given the current beam conditions it is important to know how they translate in to the real applied gain  $g$  from Equation 5.3. The real gain  $g$  is related to the DAC outputs derived above by:

$$g\phi_u = k\text{DAC} \quad (5.5)$$

Here  $k$  is the phase shift, in radians, in the chicane resulting from a DAC output of 1 count. The indices 1 and 2 are dropped from DAC1, DAC2, F1 and F2 from this point for simplicity. The upstream phase, also in radians, can then be related to the ADC2 input by:

$$\phi_u \simeq \frac{\text{ADC2}}{A} \quad (5.6)$$

Here  $A$  is the calibrated maximum Mon1 mixer amplitude, in ADC counts, determined in the same way as Section 3.7. Note that both this and the direct proportionality with ADC2 in

Equations 5.4 assume the small angle approximation  $\text{ADC2} = A \sin \phi_u \simeq A\phi_u$  for small  $\phi_u$ . This is done for latency reasons [68] and its effect on the accuracy of the applied correction is discussed in Section 5.4.2.

Combining Equations 5.4, 5.5 and 5.6 gives:

$$\begin{aligned} \frac{g}{A} \text{ADC2} &= \frac{kF}{64} \text{ADC2} \\ g &= \frac{kA}{64} F \end{aligned} \quad (5.7)$$

In Section 5.3.1 a phase shift of  $3.5^\circ$  per volt amplifier input is determined. As 4095 DAC counts corresponds to 2 V output to the amplifier this value can be converted into  $k = 29.8 \mu\text{rad}/\text{DAC count}$ . Typical calibrations for Mon1 on the FONT5a board give  $A \simeq 3440$  ADC counts (Section 3.7.2). Overall, the actual effective gain therefore relates to the gain as set in the DAQ via:

$$g \simeq \frac{F}{624} \quad (5.8)$$

The optimal gain to apply (Section 4.1) is given by the upstream-downstream phase correlation,  $\rho_{ud}$ , multiplied by the downstream-upstream jitter ratio,  $\sigma_d/\sigma_u$ :

$$g_{\text{opt}} = \frac{\sigma_d}{\sigma_u} \rho_{ud} \quad (5.9)$$

Therefore the optimal gain to set in the units used in the DAQ, dependent on the current beam conditions, is:

$$F_{\text{opt}} \simeq 624 \frac{\sigma_d}{\sigma_u} \rho \quad (5.10)$$

In good conditions the correlation and jitter ratio are close to one, although the downstream phase jitter can be up to a factor two larger than the upstream jitter at CTF3 thus the applied gains in the DAQ are typically in the range between 625 and 1250.

## 5.4.2 Effect of Using Small Angle Approximation

As mentioned previously the phase calculation in the PFF algorithm in the FONT5a firmware uses the small-angle approximation, and thus differs from the correct full phase reconstruction method used in Chapter 3 as follows:

$$\phi_{\text{SA}} = \frac{\text{Mixer}}{A} \quad (5.11)$$

$$\phi_{\text{FULL}} = \arcsin \left( \frac{\text{Mixer} - d}{A} \right) \quad (5.12)$$

Here  $\phi_{\text{SA}}$  and  $\phi_{\text{FULL}}$  are the upstream phase calculated using the small angle approximation as implemented on the FONT5a board, and with the full phase reconstruction method (derived in Section 3.6.5), respectively. Mixer is the phase monitor mixer output, and  $A$  and  $d$  are the phase monitor calibration constants, amplitude and offset, respectively (calculated as in Section 3.7). The PFF correction output is  $\phi_{\text{SA}}$ , using the upstream phase monitor Mon 1, multiplied by a gain factor.

Any differences between the calculated phase with the small angle approximation and the actual phase using the full phase reconstruction method will lead to imperfections in the applied PFF correction. The calculated phase with each approach is plotted in Figure 5.21 for offsets between the beam phase and the electronics LO phase between  $\pm 90^\circ$ . For small incoming phases (close to zero Mixer output) the only difference between the two methods is a static offset of  $-d/A$  in the measured phase, and this holds up to  $\pm 10^\circ$  (and is a good approximation up to  $\pm 20^\circ$ ). In this case the applied correction will also contain this constant offset, but the corrected downstream phase jitter, which has been the only focus of the PFF prototype to date, will still be optimal.

With larger offsets between the beam phase and the LO (i.e. for large Mixer output) the small angle approximation is no longer valid and the difference between the two methods rises to up to  $35^\circ$ . Most importantly the measured phase, and therefore the correction output, is no longer linearly dependent on the incoming beam phase when there is a large offset between the beam and LO phases. In the most extreme case, the measured phase difference between two pulses with a beam-LO phase offset of  $80^\circ$  and  $90^\circ$  would only be  $1^\circ$  when using the small angle approximation, instead of the expected  $10^\circ$ . In turn, the difference in the correction applied to the two pulses would only be  $1^\circ$  instead of  $10^\circ$ , degrading the achievable corrected phase jitter.

Figure 5.22 shows a simulation of the theoretical downstream jitter that can be achieved with both phase reconstruction methods with  $0.8^\circ$  initial upstream and downstream phase jitter and an upstream-downstream phase correlation of 97%. These values are chosen to represent the beam conditions that will need to be achieved in order to demonstrate  $0.2^\circ$  phase stability at CTF3. In the  $\pm 10^\circ$  region where the small angle approximation holds there is no degradation in the achievable corrected phase jitter using the simplified method in the PFF algorithm. Outside this region the jitter is degraded, increasing from below  $0.2^\circ$  to  $0.3^\circ$  for a beam-LO phase offset of  $50^\circ$ .

As the correction range of the PFF system is less than  $\pm 10^\circ$  (Section 5.3.1) there should be no degradation in the PFF performance resulting from the use of the small angle approximation in the PFF algorithm, providing the LO phase shifter in the phase monitor electronics has been set correctly. This highlights the importance to adjust the phase shifters to zero the Mixer output not only in order to maximise the phase monitor resolution (Section 3.9.3) but also to ensure the correction calculation itself is valid. However, it is perhaps interesting to note that it would not be possible to correct the full CTF3 pulse length to  $0.2^\circ$  jitter with this implementation of the PFF algorithm even if the correction range were large enough to encompass the  $40^\circ$  phase sag.

### 5.4.3 Channel Offset

The channel offset for ADC 2 (to which the PFF input, the Mon 1 mixer, is connected) allows the zero point for the correction to be adjusted. In other words it allows the user to decide which phase the PFF system should correct to.

In the PFF algorithm on the FONT5a board the DAC output is proportional to the



Figure 5.21: Difference (green) between a phase reconstruction method using the small angle approximation (blue), and the full reconstruction method taking in to account non-linearities in the mixer output for large phase offsets (red).



Figure 5.22: Achievable PFF jitter versus phase offset for the full phase reconstruction method (red), and the phase reconstruction using the small angle approximation (blue).

ADC 2 input, multiplied by the set gain and other constants (Equation 5.4). However, the ADC 2 input used in the algorithm is not only dependent on the Mon 1 mixer, but rather the sum of the mixer and the channel offset:

$$\text{ADC2}(t) = M(t) + \delta \quad (5.13)$$

Here  $M(t)$  is the Mon 1 mixer input, in ADC counts, which varies with time  $t$  along the pulse, and  $\delta$  is the channel offset, which is a constant offset applied to the full pulse length.

Adjusting the channel offset is important as the  $\pm 5.5^\circ$  correction range of the PFF prototype is much smaller than the  $\sim 40^\circ$  phase sag along the pulse. The PFF correction output is therefore saturated for most of the pulse length, apart from the region of the pulse that gives close to zero ADC 2 input. Using an effective system gain of unity, or 624 in the units used in the DAQ as derived in Section 5.4.1, an ADC 2 input of 420 counts gives the maximum DAC output of 4095 counts (Equation 5.4). Parts of the pulse where the ADC 2 input is above 420 counts therefore receive a constant kick resulting from the maximum 4095 counts (2 V) output to the amplifier, but the PFF system can no longer correct variations in phase along the pulse or reduce the phase jitter in these regions. In practice the limit is less than 420 counts, as the optimal gain values are typically larger than unity and the amplifier begins to enter saturation for DAC outputs below 4095 counts (Section 5.2.2).

Figure 5.23 shows an example of the measured ADC 2 input with the channel offset optimised to give zero output at the mid-point of the pulse. The phase sag results in ADC 2 inputs of above 2500 counts at the start and end of the pulse. Figure 5.24 shows a simulation of what the DAC output would be in the PFF system (with unit gain), with this ADC 2 input. The DAC output matches the shape of the input between samples 346 and 506 (a 450 ns period), but is saturated for the rest of the pulse length. Figures 5.23 and 5.24 also show the effect of using a non-optimal channel offset giving an ADC 2 input of 200 counts at the mid-point of the pulse. In this case the region of the pulse where the DAC output is not saturated is reduced to between sample 367 and 486 (a 330 ns period).

With the non-optimal channel offset the central point of the pulse receives a constant kick of -1950 DAC counts. This reduces the range of the PFF system for correcting jitter about the mean phase at the mid-point of the pulse. With the optimal channel offset, giving a mean ADC 2 input of zero at sample 421, the PFF system can correct jitter of  $\pm 420$  ADC counts about the mean (to give  $\pm 4095$  counts DAC output). With the non-optimal offset, giving a mean ADC 2 input of 200 ADC counts at sample 421, this is changed to a correctable range of  $+220 / -620$  ADC counts about the mean. The range of the system is therefore almost halved for phase jitter giving positive offsets in the ADC 2 input.

The adjustment of the channel offset and its effect for the PFF system is discussed further in Section 6.2.3. It is important to note that the the mixer output can also be zeroed in the region of the pulse where the correction is desired by varying the phase shifters in the phase monitor electronics, as is done after calibrations (Section 3.7.4). As the phase monitor resolution is degraded for large phase offsets (Section 3.9.3) the channel offset should only be used to make small adjustments remotely. For large mixer outputs (corresponding to phase offsets above  $20^\circ$ ) the phase shifters should be adjusted in the klystron gallery to reset the

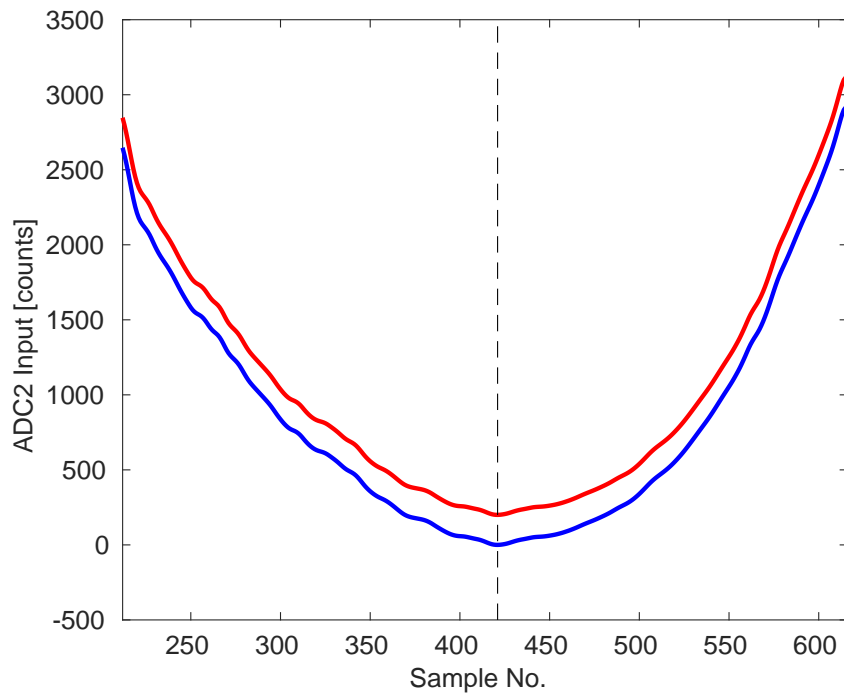


Figure 5.23: ADC 2 input (connected to the Mon 1 mixer) with the channel offset optimised to give zero output at sample 421 (blue), and with a non-optimal channel offset giving 200 counts output at sample 421 (red). The location of sample 421 is marked by the vertical dashed line.

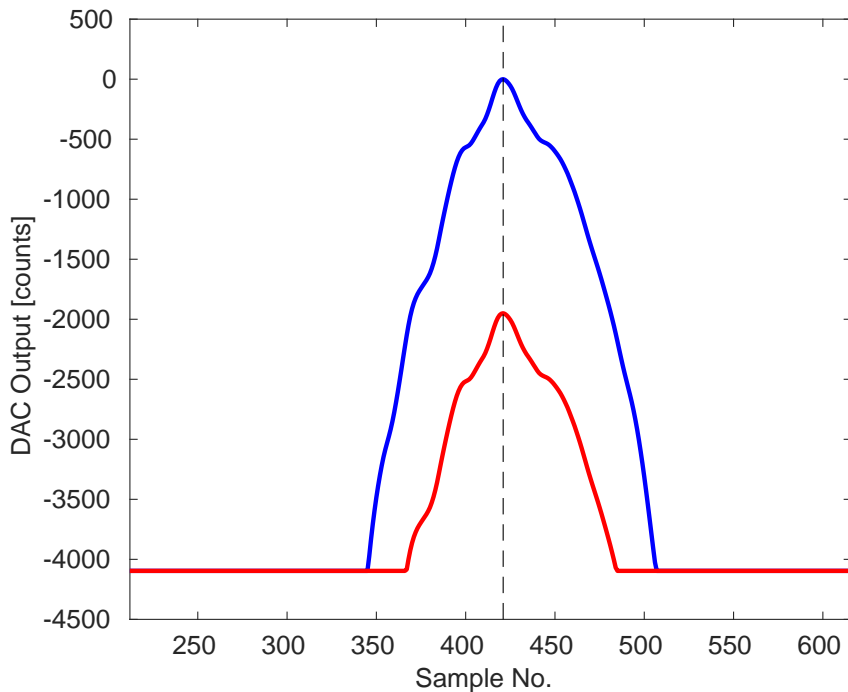


Figure 5.24: Simulated DAC output resulting from the ADC 2 inputs in Figure 5.23 and using a set correction gain of 624 units in the DAQ. Blue: Channel offset optimised to give zero output at sample 421. Red: Non-optimal channel offset giving 200 counts output at sample 421. The location of sample 421 is marked by the vertical dashed line.

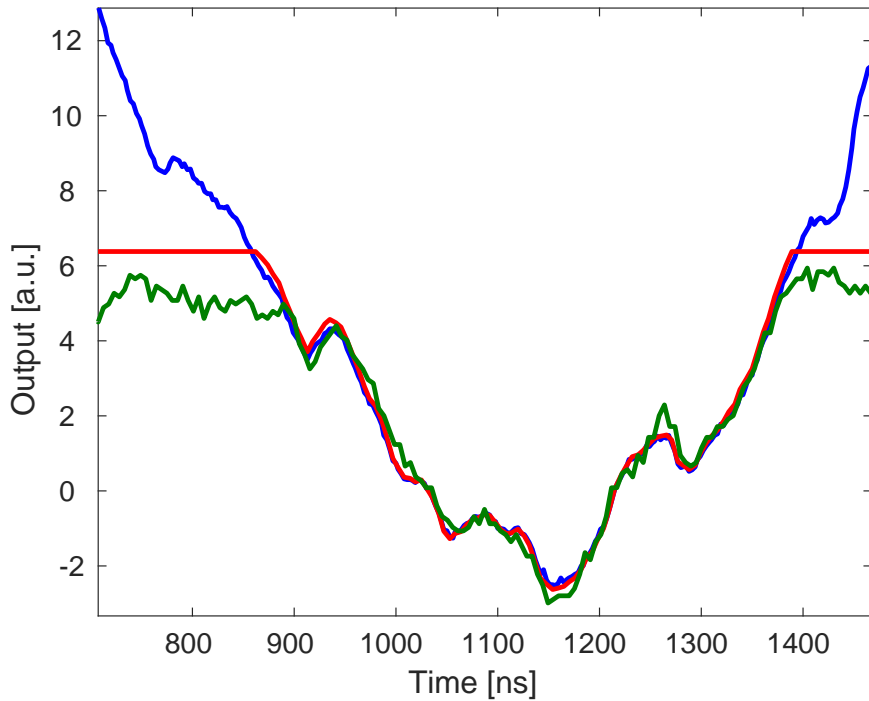


Figure 5.25: Comparison between the upstream phase (blue), used as the PFF input, the resulting DAC output from the FONT5a board (red) and the measured downstream phase shift as a result of the applied kick (green).

zero crossing instead.

#### 5.4.4 Verification of Correction Shape

The previous result in Section 5.3.1 demonstrated that the kickers in the chicane can be used to shift the mean beam phase. However, the PFF correction also aims to remove variations in the phase point by point along the beam pulse. In the PFF algorithm the DAC output is varied along the pulse based on the measured upstream phase in order to achieve this, rather than being constant as has been the case in the tests presented up until this point. The amplifier and kickers must then have sufficient bandwidth to respond to fast changes in input voltage, in order to ultimately remove these features from the corrected downstream phase.

To verify that the FONT5a board, amplifiers and kickers respond as expected Figure 5.25 shows the first example in the thesis of results with the complete PFF system turned on. The input upstream phase, calculated DAC output and the observed difference in the downstream phase resulting from the applied kick are all shown. The downstream phase trace shows the difference between subsequent pulses with the correction on and off (using the interleaved correction mode).

In the ideal case the shape of all three lines should be identical, apart from the DAC output and downstream phase shift having opposite sign to the input upstream phase (in

order to remove the upstream phase variations from the corrected downstream phase). Each trace is scaled, aligned in time and sign flipped where appropriate to make a comparison between the shapes easier. When operating the PFF system to reduce the downstream jitter as intended these scale factors and times must be applied in the PFF setup rather than in offline data analysis. The scale factor is analogous to the system gain, for which the optimal value is derived in Section 5.4.1, and the correction output timing is discussed in Section 5.5.

In the central region of the pulse all three traces have the same shape as expected. The upstream phase and DAC output should be close to identical by definition, as the calculated correction output is only dependent on the input phase, but this verifies the functionality of the FONT5a board correction algorithm and firmware. The agreement in shape of the downstream phase shift is a significant achievement, and verifies the linearity of the amplifier output, kicker response and optics for a varying input voltage. This result demonstrates that everything is in place for the PFF prototype to flatten variations in the downstream phase and to reduce the downstream phase jitter.

The agreement in shape holds for times between around 900 ns and 1375 ns as indicated on the figure, and this defines a 475 ns portion of the pulse within which the applied correction should be close to optimal. Outside this range the large phase sag along the pulse leads to the correction being saturated – the maximum possible DAC output (2 V) is applied and the shape can no longer be corrected. It can also be seen that the measured downstream phase shift saturates earlier than the applied DAC output. This is because the amplifier begins to saturate at input voltages below 2 V, as seen in Figure 5.12.

## 5.5 Derivation of Optimal Timing for the Correction Outputs

Most the results based on the amplifier outputs and kicked beam presented so far have used a constant voltage across the full  $1.4 \mu\text{s}$  time window that the amplifier is powered for. As the  $1.4 \mu\text{s}$  amplifier output to the kickers is longer than the  $1.1 \mu\text{s}$  CTF3 beam pulse it is relatively straightforward to ensure that the full length of the pulse experiences the constant kick with this setup. However, for operation of the PFF system precise control of the correction output timing becomes critical.

In order to remove phase variations along the pulse with the PFF system the output correction signal, shaped by the upstream phase, must arrive at the kickers exactly synchronised with the beam. Timing misalignments between the beam and correction signal arrival will result in residual offsets in the corrected downstream phase, which in the ideal case should be zero across the full pulse length. Figure 5.26 shows a simulated example of this for a correction applied 78 ns later than the beam. The resulting corrected downstream phase (the sum of the initial phase and the correction output) is clearly non-zero, with different behaviour for slow and fast variations in the initial phase. Considering the phase sag along the CTF3 beam pulse (a low frequency effect), applying the correction late (early) results in an approximately linear increase (decrease) in the corrected downstream phase

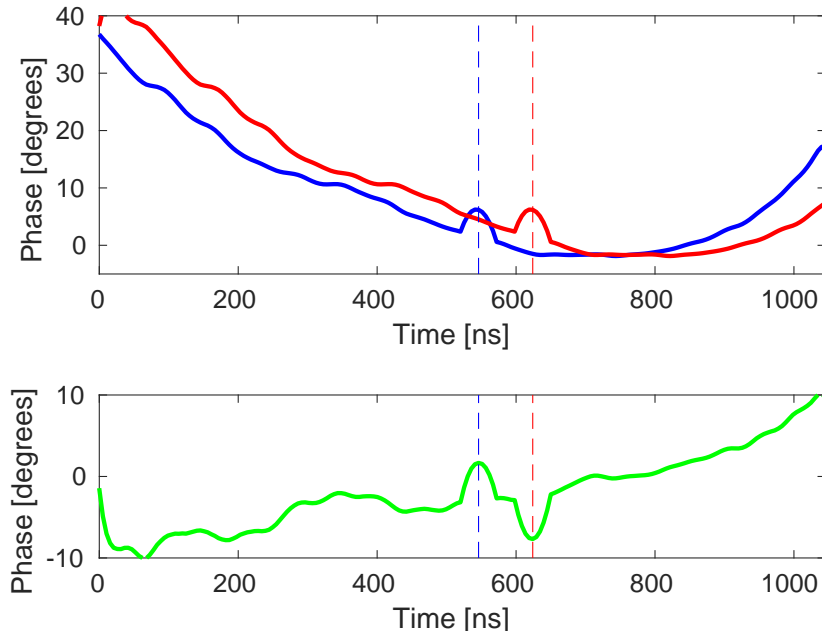


Figure 5.26: Simulated effect of a 78 ns timing misalignment between the beam and the applied correction. Top: The initial downstream phase (blue) and the correction signal (red), sign flipped for easier comparison. Bottom: The resulting corrected downstream phase (green). A 57 ns width feature is added at time 546 ns in the initial phase, as marked by vertical dashed lines.

along the pulse. Alternatively, faster features, with similar or smaller width than the timing mis-alignment, are introduced with opposite sign in the corrected downstream phase rather than being removed (also shown in Figure 5.26).

Although the effects are most visible along the pulse, any mis-timing of the correction will also degrade the achievable mean phase jitter. This section gives an overview of the methods that have been used to ensure that the correction output to the two kickers arrives in time with the beam. The “absolute timing”, in Section 5.5.3, refers to the timing that ensures the correction signal arrives to the first kicker synchronous to the beam. The “relative timing”, in Section 5.5.4, then derives whether the output from the FONT5a board for the second kicker must be delayed with respect to the first to ensure the timing is synchronised for both kickers.

### 5.5.1 Kicker Cable Lengths

The cables carrying the correction signal between the PFF amplifier and the kickers in the TL2 chicane are the single largest contributor to the overall system latency (see Section 5.5.2). They must be routed from the PFF electronics racks (in the klystron gallery, directly above the location of the upstream phase monitors), down in to the combiner ring hall and across the width of the CTF3 facility to the TL2 chicane (see Figure 1.6). To be able to meet the system latency requirements the kicker cables are routed on dedicated paths, rather than using pre-existing cable trays and pathways for other devices. Precise

measurements of the cable lengths are presented in this section, as well as their significance beyond ensuring the system is within the latency requirements.

With two kickers, two strips per kicker and two ends of each strip a total of eight cables are needed. The drive from the amplifier is applied to the downstream end of each kicker strip, traverses the kicker, and is then terminated back at the amplifier after leaving the upstream end. Drive is applied to the downstream end of each kicker (meaning it propagates through the kicker in the opposite direction to the beam) so that the electric and magnetic fields between the strips are in the same direction, as discussed in Section 2.2. Rather than being connected directly to the amplifier, the eight kicker cables are connected to a patch panel below the amplifier in the PFF electronics racks. Eight additional cables, around 70 cm in length, are used to connect the amplifier outputs to the patch panel. This is in order to ease configuration changes and provide mechanical strain relief to the amplifier connectors. The patch panel also deals with the conversion between HN-type connectors (used on the kickers and kicker cables) and N-type connectors (used on the patch panel cables and to connect to the amplifier after a further transition to TNC connectors [27]). All of the cable connections between the amplifier, patch panel and kickers are shown in Figure 5.27.

The length of the eight kicker cables and eight patch panel cables has been measured using time domain reflectometry (TDR) on a network analyser. The network analyser is used to transmit a short pulse down the cable, with one end of the cable connected to the network analyser and the other end disconnected from the kicker. As the signal reaches the non-terminated end of the cable the discontinuity in impedance creates a reflected signal that propagates back to the network analyser. The time difference between when the signal was output and when the reflected signal arrives back at the network analyser therefore corresponds to double the one-way signal transit time in the cable.

The patch panel cable lengths measured with this method are all 3 ns within the measurement error of 0.05 ns, estimated based on the sampling rate of the measurement. Table 5.4 shows the precise lengths of the long kicker cables. The cables connected to the first kicker have a length of around 170 ns, whilst the cables for the second kicker are longer at around 205 ns. With a signal speed of two thirds the speed of light in the cable, these times correspond to cable lengths of approximately 34 m and 41 m for the first and second kicker respectively.

For the second kicker the latency requirements are slightly relaxed due to the additional 36 ns beam time of flight between the kickers. Rather than also shortening the cables for the second kicker as much as possible some additional slack was left so that the difference in lengths is similar to the difference in the beam time of flight between the two. This means the two correction outputs (one for each kicker) can be sent from the FONT5a board at, or close to, the same time as discussed in Section 5.5.4.

The pairs of cables connected to the downstream ends of the strips for each kicker have lengths matched within the measurement error. However, for the pairs connected to the upstream ends there are some differences, with cable 2907741A more than 1 ns shorter than cable 2907740A, for example. If there is a difference between the lengths of the cables connected to the downstream left and downstream right strips of a kicker (the driven end)

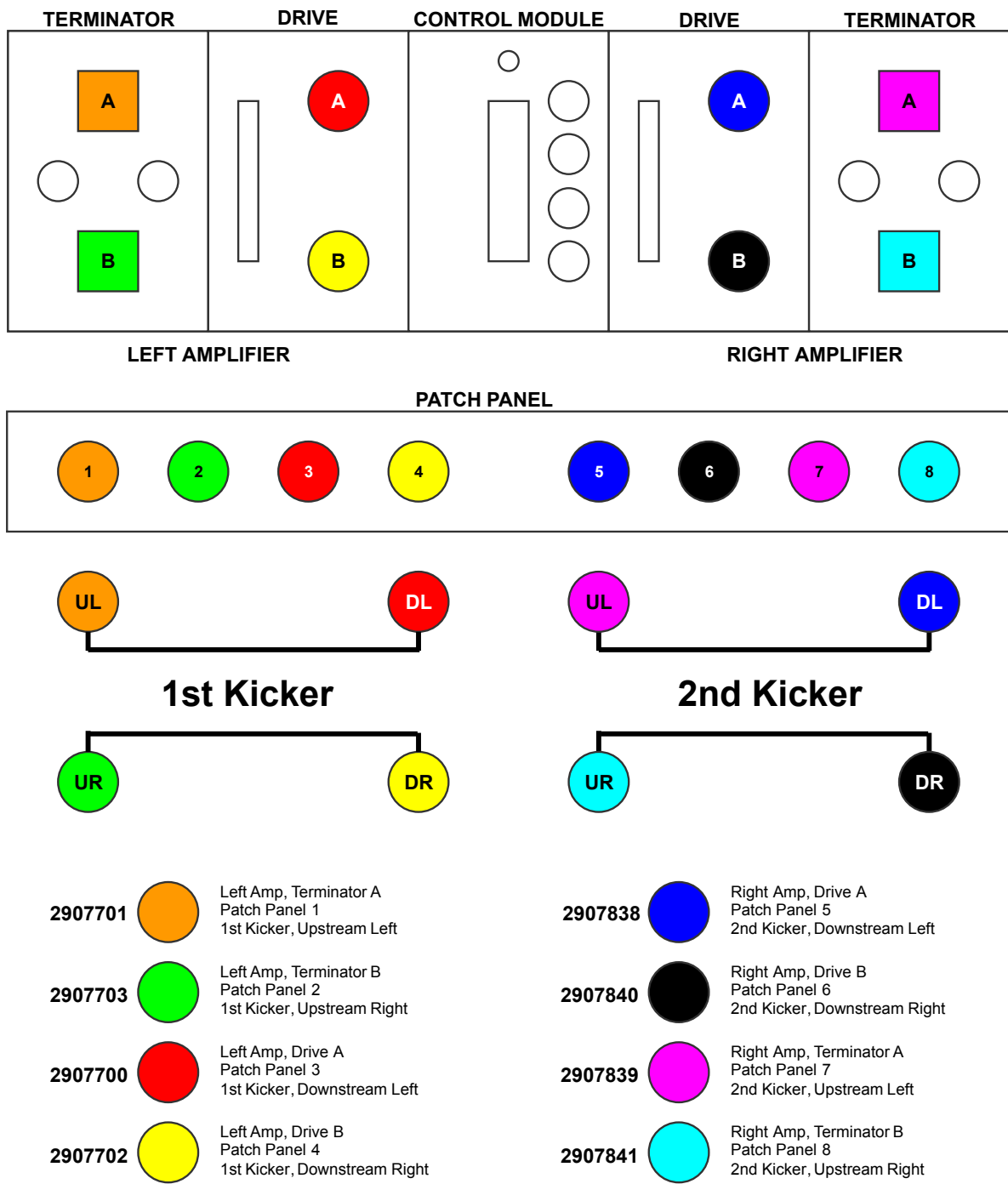


Figure 5.27: Cable connections between the amplifier, patch panel and kickers.

Label	Length	Amplifier			Kicker		
		Module	Channel	D/T	No.	Strip End	Strip Side
2907701A	171.28 ± 0.05 ns	L	A	T	1	U	L
2907703A	171.30 ± 0.05 ns	L	B	T	1	U	R
2907700A	171.29 ± 0.05 ns	L	A	D	1	D	L
2907702A	171.30 ± 0.05 ns	L	B	D	1	D	R
2907838A	205.45 ± 0.05 ns	R	A	D	2	D	L
2907740A	205.62 ± 0.05 ns	R	B	D	2	D	R
2907739A	205.15 ± 0.05 ns	R	A	T	2	U	L
2907741A	204.49 ± 0.05 ns	R	B	T	2	U	R

Table 5.4: Lengths of the cables between the amplifier and kickers (excluding the patch panel cable lengths), and where they are connected (see Figure 5.27). For the amplifier: L/R denotes whether the cable is connected to the left or right amplifier module, A/B denotes whether the cable is connected to the A or B channel on that module, and D/T denotes whether the cable carries the Drive output to the kicker, or the returning signal that is Terminated back at the amplifier. For the kickers: 1/2 denotes whether the cable is connected to the first (1) or second (2) kicker, U/D denotes whether the cable is connected to the Upstream or Downstream end of that kicker, and L/R denotes whether the cable is connected to the Left or Right strip in that kicker.

there will be a time offset in the voltage applied to each side of the kicker, which would degrade the quality of the PFF correction. However, there is no need for the cables connected to the upstream ends of the kickers to be of matched lengths, the only requirement is that they are terminated correctly at the amplifier. The shorter 2907741A cable is therefore connected to the upstream end of the second kicker, and the cables 2907838A and 2907740A, with lengths matched to within 200 ps, are used to carry the amplifier output to the downstream end of the strips.

### 5.5.2 System Latency

The PFF system aims to apply the correction in the TL2 chicane to the same beam pulse initially measured by the upstream phase monitors in the CT line (see Figure 1.5). For this to be possible the total system latency must be less than the 380 ns time of flight of the beam between the upstream phase monitors and the first kicker in the TL2 chicane (approximately 114 m of beam line). The system latency includes the latencies of each hardware component, namely the phase monitor electronics, FONT5a board and amplifier, as well as the signal transit time in all the associated cabling. As mentioned previously the cabling is the largest contribution, and includes cables from the phase monitors to the electronics in the klystron gallery, to and from the FONT5a board, and from the amplifier in the klystron gallery to the kickers in TL2.

Table 5.5 shows approximate latencies for each part of the PFF system. The length of the kicker cables was introduced in Section 5.5.1, with the 175 ns value in the table including the 3 ns added by the patch panel cable lengths. 2 m coaxial cables from the phase monitor

Component	Latency
Phase Monitors (inc. cables & electronics)	50 ns
Cables: Phase monitor electronics to FONT5a board	10 ns
FONT5a Board	60 ns
Cables: FONT5a board to amplifier	10 ns
Amplifier	30 ns
Cables: Amplifier to First Kicker	175 ns
Total System Latency	335 ns
Beam Time of Flight (Mon 1 to first kicker)	380 ns

Table 5.5: Approximate latency of each hardware component and cabling in the PFF system.

electronics to the FONT5a board, and from the FONT5a board to the amplifier, both add 10 ns to the system latency. The total latency of the phase monitors and their electronics, including approximately 10 m of cabling between the monitors and the electronics in the klystron gallery, was measured to be 50 ns [56]. The latency of the FONT5a board, including the time to process the input signals and calculate and apply the appropriate output, is 60 ns as mentioned in Section 5.1.1. Finally, the estimated amplifier latency is around 30 ns, although precise measurements of this have not been made [85].

Overall the latency of the complete PFF system is therefore expected to be 335 ns, meeting the latency requirements and meaning that the correction signal should arrive at the first kicker 45 ns before the beam in the case where the correction is output is soon as possible. The outputs of the FONT5a board are delayed in order to synchronise the arrival time of the correction with the beam, as discussed in Sections 5.5.3 and 5.5.4.

### 5.5.3 Absolute Timing

#### Using Beam Pickup

When the beam traverses the kickers image currents induce a voltage at the upstream and downstream ports of the kicker, which is visible on the amplifier monitoring outputs for the transients at the beginning and end of the pulse [37]. This is referred to as beam pickup on the kicker strips. Figure 5.28 shows an example of beam pickup as seen on one of the amplifier monitoring outputs (with each amplifier monitoring output giving a similar response). The separation of the peaks in the beam pickup is equal to the CTF3 beam pulse length of  $1.1 \mu\text{s}$ . By comparing the timing of these peaks with respect to the start and end of the amplifier output pulse, using the same amplifier monitoring signal, it is possible to ensure that the correction output arrives synchronous to the beam.

An example of this is shown in Figure 5.29. A small constant voltage output of 0.1 V (200 DAC counts) is used to drive the amplifier and both the resulting amplifier output pulse and the beam pickup, at samples 275 and 493, are visible in the figure. A small output voltage is used so that the beam pickup can still be seen clearly in the presence of the amplifier output pulse. Importantly, the DAC output is gated using the upstream phase

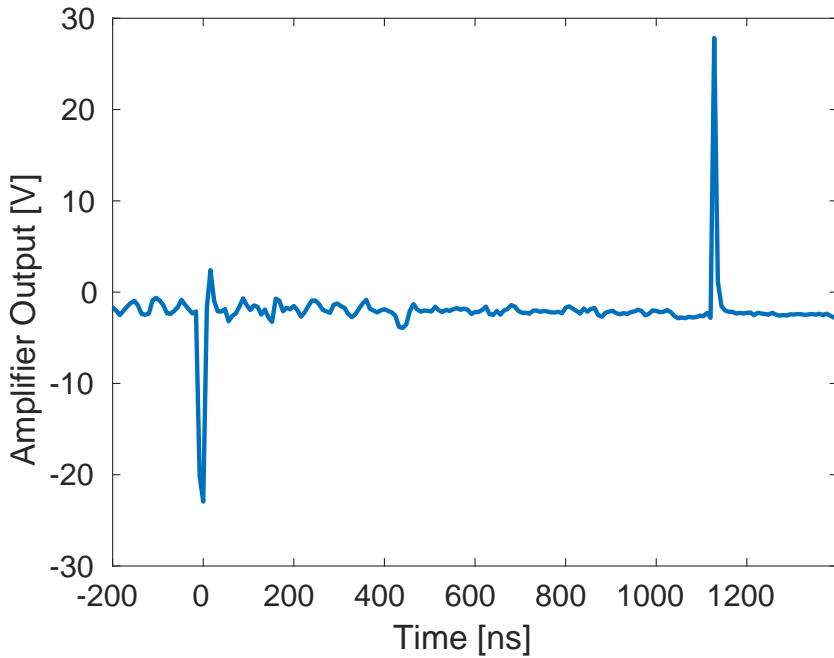


Figure 5.28: Beam pickup on the kicker strips as seen on amplifier monitoring signals.

monitor diode signal (in other words, the constant DAC output is only enabled during the time when the diode is non-zero) and this has two consequences. Firstly, the amplifier output pulse has the same length as the beam pulse in the upstream phase monitor. Secondly, the timing of the output is identical to what it would be in normal PFF operation. In the case of Figure 5.29 the drive to the amplifier is output with minimal delay after the arrival of the upstream diode signal at the FONT5a board. It can be seen that the amplifier pulse arrives before the beam pickup, thus with the PFF system setup this way the correction would be applied early.

This result therefore proves that the PFF system just meets the latency requirements, with the overall time needed to transmit and process all the relevant signals being a few tens of nanoseconds less than the 380 ns time of flight of the beam between the upstream phase monitor and the first kicker. However, what is also clear in the figure is that the time offset between the start of the amplifier pulse and the first beam pickup spike is much larger than the time difference between the end of the amplifier pulse and the second beam pickup spike. This is due to the energy transient across the first 100 ns of the CTF3 beam pulse which is present in the upstream phase monitor but is then lost prior to the TL2 chicane, predominantly in TL1. As a result the downstream beam pulse is shorter than the upstream beam pulse which defines the length of the correction output. Therefore, in order to align the correction output with the beam the signals from the end of the amplifier and beam pulses must be used, not the start.

The firmware for the FONT5a board includes an output delay parameter that is used to fine-tune the timing of the correction output sent to the amplifier (Section 5.1.1). This can be done independently for each of the two correction outputs so that it can be ensured the correction arrives in time with the beam in each kicker individually (the relative timing

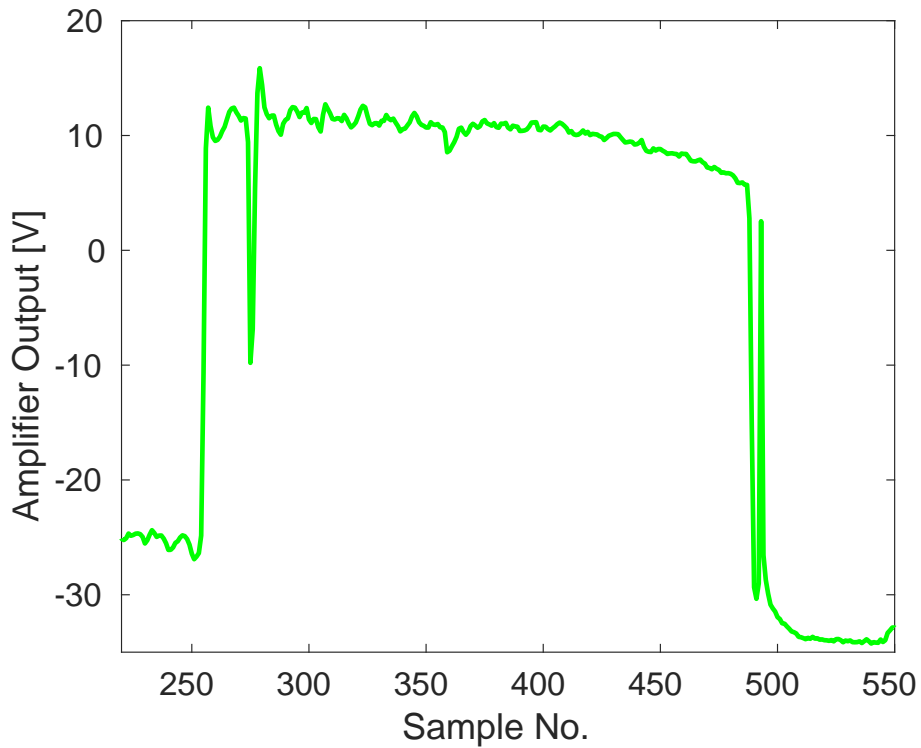


Figure 5.29: Alignment between the amplifier output (square pulse) and the beam pickup on the kickers strips (spikes) for an applied output delay of 0 ns (0 clock cycles).

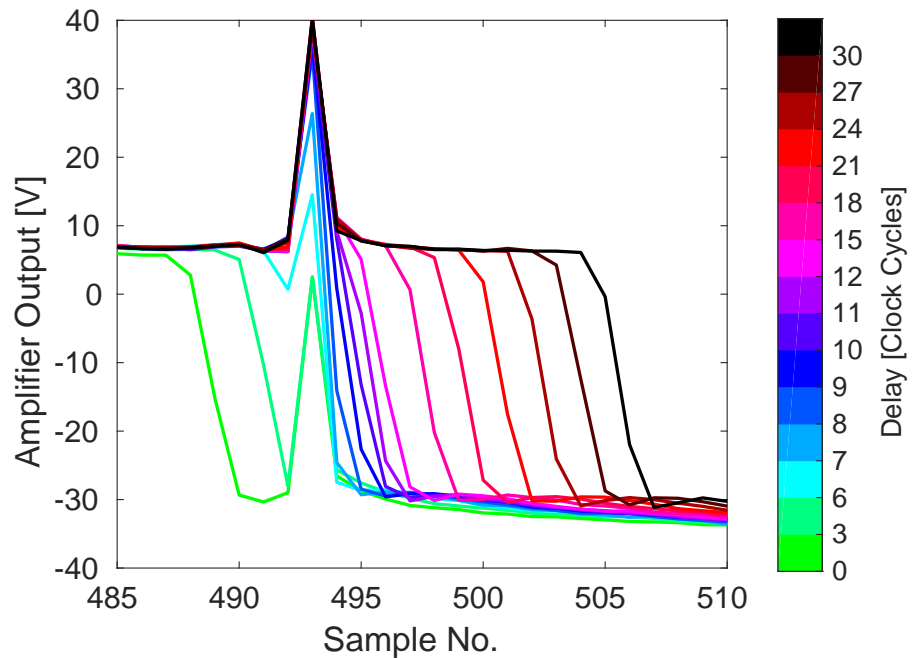


Figure 5.30: Alignment between the amplifier output (square pulse) and the beam pickup on the kickers strips (spikes) across the full range of possible output delays (as indicated by the colour scale).

of the two kickers is discussed in the Section 5.5.4). The delay can be varied in integer steps between 0 and 31 cycles of the system clock, so up to 86.8 ns, in steps of 2.8 ns, for a 357 MHz clock. Figure 5.30 shows the effect of varying the output delay across the full range of possible values, zoomed in on the end of the pulse. For all output delays the beam pickup remains at sample 493, as expected. Meanwhile, the end of the amplifier pulse is moved from before the beam pickup (output too early) to after the beam pickup (output too late). To achieve the optimal correction timing the end of the amplifier pulse must be aligned with the beam pickup and this is achieved with a delay of 7 clock cycles, or 19.6 ns, as shown in Figures 5.31 and 5.32. This delay has been used for the latest PFF runs presented in Chapter 6. Due to ambiguity in which point along the falling edge of the amplifier pulse the beam pickup should be aligned to there may be a remaining error of up 3 clock cycles (8.4 ns) in the exact alignment, and this can only be verified by beam based measurements (not using the amplifier monitoring outputs).

## Using BPMs

This section presents one way in which the correction output timing can be determined using a combination of the phase monitor measurements and a BPM signal downstream of the TL2 chicane.

The FONT5 (and FONT5a) board firmware provides the functionality to be able to change the gain of each PFF correction output independently. This means it is possible to apply the correction to only one kicker, or to kick the beam in the same direction in each kicker (i.e. to use the same sign for the gain in each kicker, rather than gains with equal magnitude but opposite sign). In both of these cases the kicked PFF orbit in the chicane is not closed, thus the horizontal position along the beam pulse in a BPM after the chicane depends on the shape and timing of the applied correction.<sup>1</sup>

Figure 5.33 compares the upstream phase, downstream phase and horizontal position (in a BPM after the TL2 chicane) along the pulse in the case where the PFF correction is applied with gains set to kick the beam in the same direction in each kicker, and with no output delay applied in the FONT5 board. The data is taken in interleaved mode, with the plotted phases shown using the PFF off data and the BPM trace being the difference between the PFF on and PFF off data. Each signal is scaled and sign flipped where necessary to give variations along the pulse with the same magnitude and sign, in arbitrary units. The BPM and phase monitor signals are acquired with the same sampling frequency of 192 MHz, with each aligned so that the end of the pulse is at the same sample number.

By taking the difference of the PFF off and PFF on data in the BPM any residual orbit variations along the pulse not related to the PFF system are removed, thus the remaining shape should match that of the PFF correction output, which in turn depends upon the upstream phase. The downstream phase should also have the same shape as the upstream phase with the PFF system off, within the limits of the upstream-downstream phase corre-

---

<sup>1</sup>In Section 5.3.2 it was shown that the corrected orbit is not perfectly closed in normal PFF operation either. However, in this case no attempt at orbit closure is made so the measured effect seen in the BPMs is much larger.

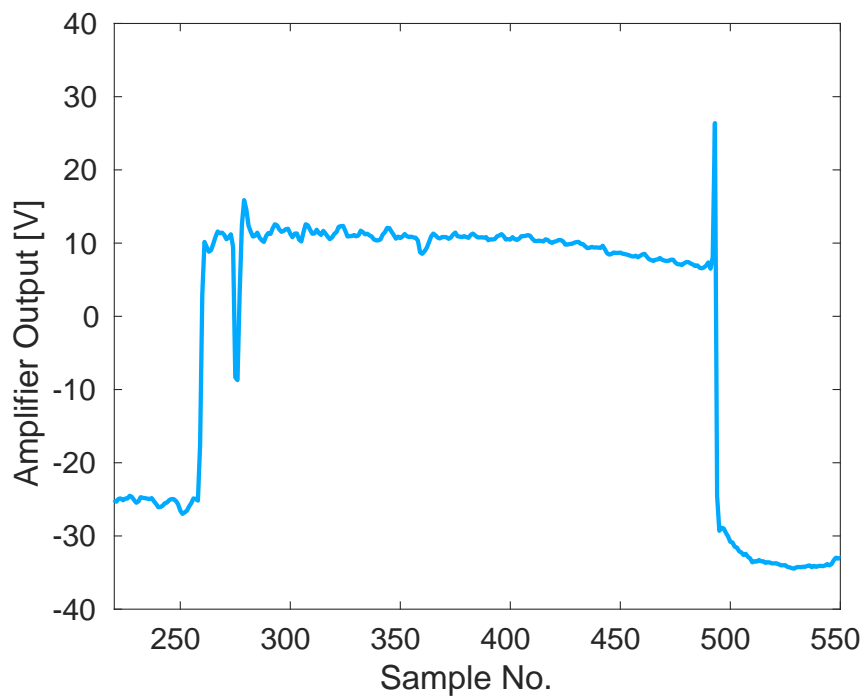


Figure 5.31: Alignment between the amplifier output (square pulse) and the beam pickup on the kickers strips (spikes) for an applied output delay of 19.6 ns (7 clock cycles).

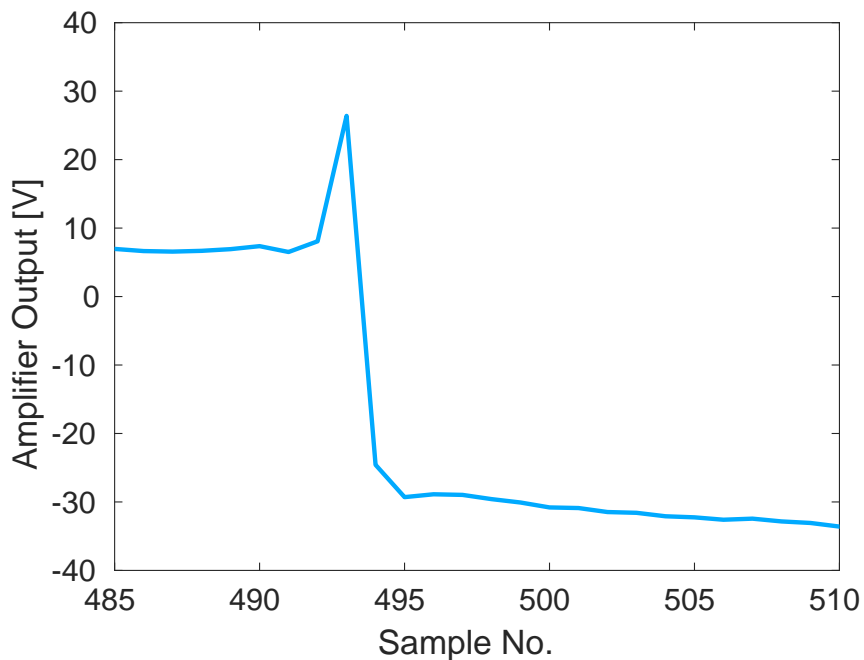


Figure 5.32: Alignment between the amplifier output (square pulse) and the beam pickup on the kickers strips (spikes) for an applied output delay of 19.6 ns (7 clock cycles), zoomed in to the end of the pulse.

lation achieved at this time. During this measurement many oscillations along the upstream phase were present, which usually are not desired but for this measurement are perfect points of reference to check the time alignment of the signals. As expected the overall shape of the residual horizontal position in the BPM along the pulse and the two phase signals is very similar. The largest feature in the upstream phase that is present in all three signals occurs at sample 671 in the upstream phase, with the location of the peak of this oscillation in the phase signals and the BPM marked by vertical black lines in the figure. The peak as seen in the BPM signal is clearly before the peak in the phase monitor signals thus in this case the correction was applied early, with a measured offset of -36 ns between the peaks.

This measurement was repeated with four different correction output delays applied in the FONT5 board, at delays of 0, 10, 20 and 30 clock cycles (0 to 84 ns), which includes points where the correction is applied both early and late. Fitting the measured time offset between the peaks in the BPM and the phase in the same way as before yields an optimal correction output delay to apply of  $39 \pm 7$  ns (Figure 5.34), or 14  $\pm$  3 clock cycles. Applying this delay in data analysis offline gives the result shown in Figure 5.35, in which the similarity of the three signals becomes clear.

The optimal output delay of  $39 \pm 7$  ns derived with this method does not agree with the value of  $19.6 \pm 8.4$  ns from the beam pickup based measurement discussed previously. The result from the BPM measurement is closer to the estimated difference of 45 ns between the beam time of flight and total system latency shown in Table 5.5. However, the results shown for the BPM method were performed with the first, lower power version of the amplifier and the FONT5 rather than the later FONT5a board. Although the updated hardware components are expected to have similar latencies there were associated cabling changes which may explain the difference between the two measurements. As a result the optimal delay of 19.6 ns from the beam pickup measurement has been used in the PFF setup for the results presented in Chapter 6. The BPM measurement will be repeated in the future to verify that both methods give consistent results when the same hardware and cabling setup is used.

#### 5.5.4 Relative Kicker Timing

For the phase correction the absolute output timing sent to the first kicker, as derived above, is the most critical as this defines the alignment of the applied phase shift in the chicane with the beam. The second kicker's main purpose is then to close the kick created by the first, ensuring the orbit after the chicane is closed (with the caveats already mentioned in Section 5.3.2). For the purposes of orbit closure it is also important to ensure that the correction arrives at the second kicker in time with the beam. As mentioned in Section 5.5.1 the beam time of flight between the kickers is about 36 ns, thus the correction must arrive at the second kicker 36 ns later than the first kicker. Most of this difference should be accounted for by the longer cable lengths for the second kicker, but the precise relative timing is checked here. In this context the relative timing means the additional output delay that must be applied to the FONT5a correction output for the second kicker with respect to the first in order to ensure the correction is aligned in time with the beam in both kickers.

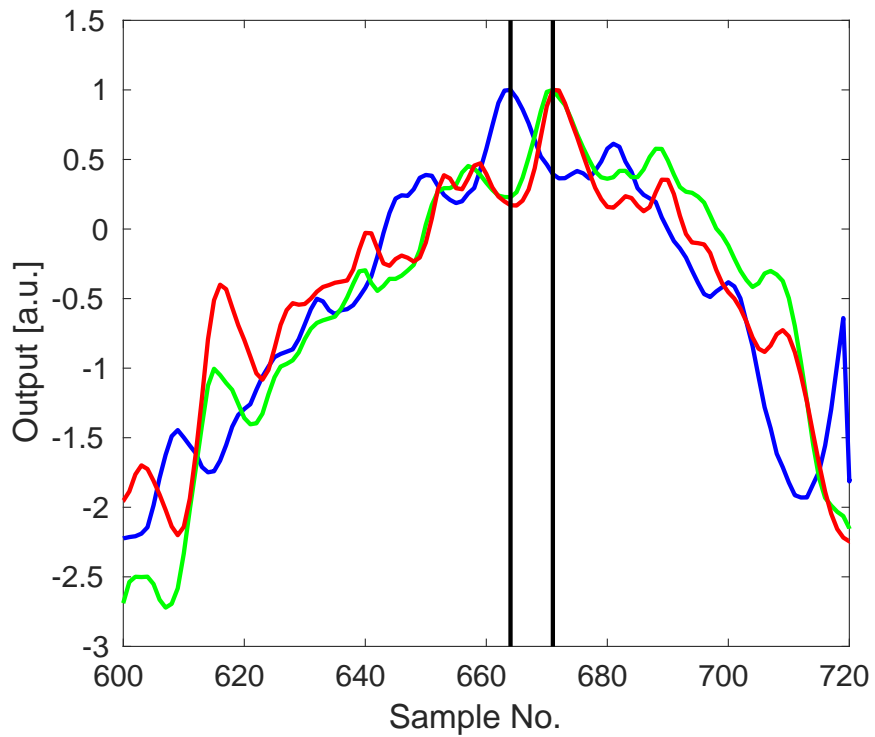


Figure 5.33: Alignment of the upstream (green) and downstream (red) phase compared to the applied kick as measured in a BPM after the TL2 chicane (blue) for an output delay of 0 ns. Vertical black lines indicate the time shift between the phase and the kick for the clearest feature visible in all three signals.

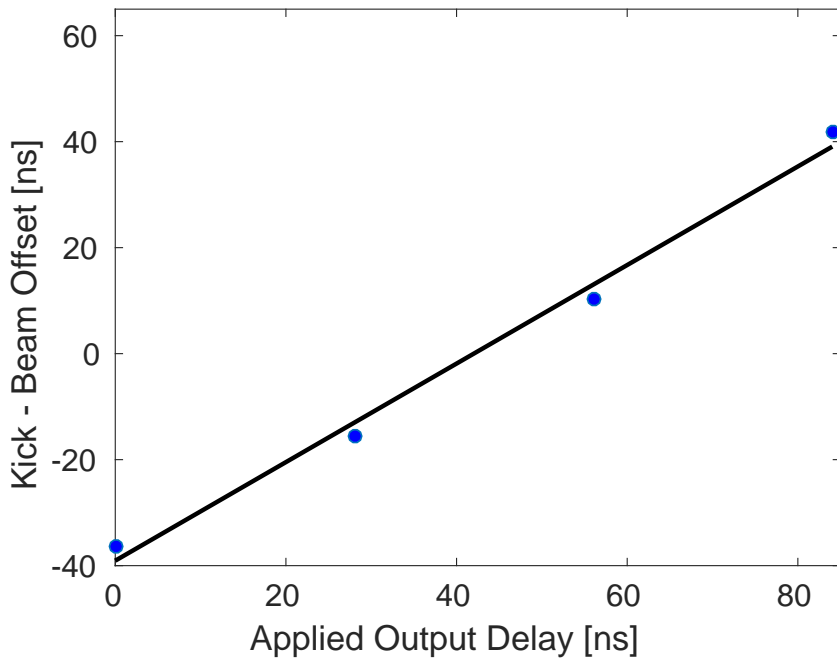


Figure 5.34: Fitted time offset between the applied kick and the beam at different output delays.



Figure 5.35: Alignment between the applied kick as measured by a BPM after the chicane (blue) and the phase signals (red downstream and green upstream) after applying the optimal output delay in data analysis.

Figure 5.36 shows a simulated example of the expected effect of kicking the beam with a relative time offset in each kicker, in this case with the output to the second kicker arriving later than the first kicker (with respect to the beam pulse). The kickers are driven with opposite polarity in the same way as the PFF system, and the first kicker is shown with a larger output than the second. The total kick received in the chicane is given by the sum of the two, as shown in the figure. In the ideal case the total/residual kick in the chicane should be zero so that the orbit is closed after the chicane. However, with a timing offset between the two kickers there are excursions in the orbit at the start and end of the pulse, where only one of the two kickers receives its full drive. Due to the different amplitude of the two kickers the residual kick is also non-zero in the central part of the pulse. With well-aligned timing the residual kick would be constant along the full pulse length, or zero across the full pulse length if the kicks had matched amplitudes.

By varying the relative timing of the two correction outputs on the FONT5a board (K1 and K2 delay, see Section 5.1.1) and using a BPM after the TL2 chicane to measure the size of the peaks at the start and end of the pulse resulting from the offset kicks (in the same way as Figure 5.36) the optimal relative delay can be determined. The optimal relative delay is the point that minimises the size of the peaks on the rising/falling edge of the pulse, with the peak magnitude approximately linearly dependent on the delay. Figure 5.37 shows the result of doing this, using a constant DAC output from the FONT5a board applied across a 168 ns portion of the pulse. The horizontal position in a BPM after the TL2 chicane is plotted for relative K2 delays ranging between -28 ns (K1 output delayed with respect to K2) and +28 ns (K2 output delayed with respect to K1) (-10 to +10 clock cycles). Aside

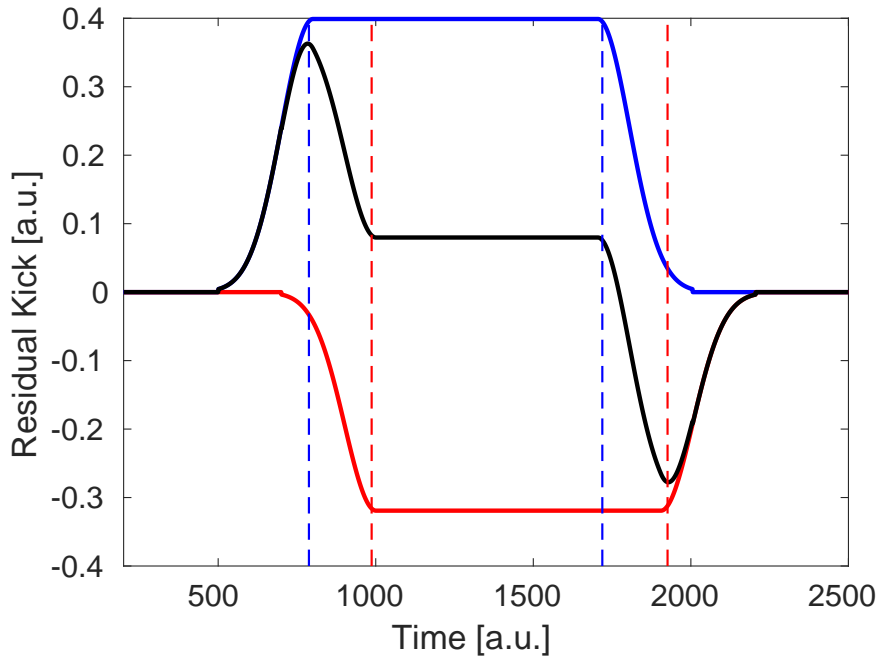


Figure 5.36: Example of the residual kick (black) experienced by a beam traversing through two kickers. A relative delay between the applied output to each kicker is applied, as well as a different magnitude kick from each kicker (shown in blue and red). Dashed blue and red lines show the kick start and end time for each kicker.

from the asymmetry between the size of the peaks at the start and end of the pulse the result is as expected from the example previously discussed. Note the non-zero position offset in the central part of the pulse. Based on the orbit closure results in Section 5.3.2 this is predominantly due to optics differences leading to a non-closed orbit, rather than the small difference in amplifier output voltage to each kicker.

Figure 5.38 shows the peak beam offset in the BPM versus the relative K2 delay. The peak beam offset is defined as the difference between the maximum and minimum beam position after the chicane between sample 425 and 447 for the rising edge, or sample 458 and 477 for the falling edge of the pulse (as seen in Figure 5.37). As the K2 delay approaches the optimal value the variation in beam position in this range converges to the 0.3 mm offset in the flat central part of the kicked pulse. The point of intersection between the two linear fits shown (one for the points with a positive peak height and the other for points with a negative peak) gives the optimal relative K2 offset to be  $0.3 \pm 1.4$  ns ( $0.1 \pm 0.5$  clock cycles) for the falling edge of the pulse. Repeating the procedure for the peaks at the rising edge of the pulse gives a result of  $5.3 \pm 5.6$  ns ( $1.9 \pm 2.0$  clock cycles), and the two results combine to give an optimal value of  $1.4 \pm 1.7$  ns ( $0.5 \pm 0.6$  clock cycles).

Relative K2 delays of both 0 and 2.8 ns (0 and 1 clock cycles have been used during PFF operation, with no measurable difference between the two as this is outside the correction bandwidth. Adding the absolute delay of 19.6 ns (7 clock cycles) derived in Section 5.5.3, the final delays to apply in the FONT5a board are:

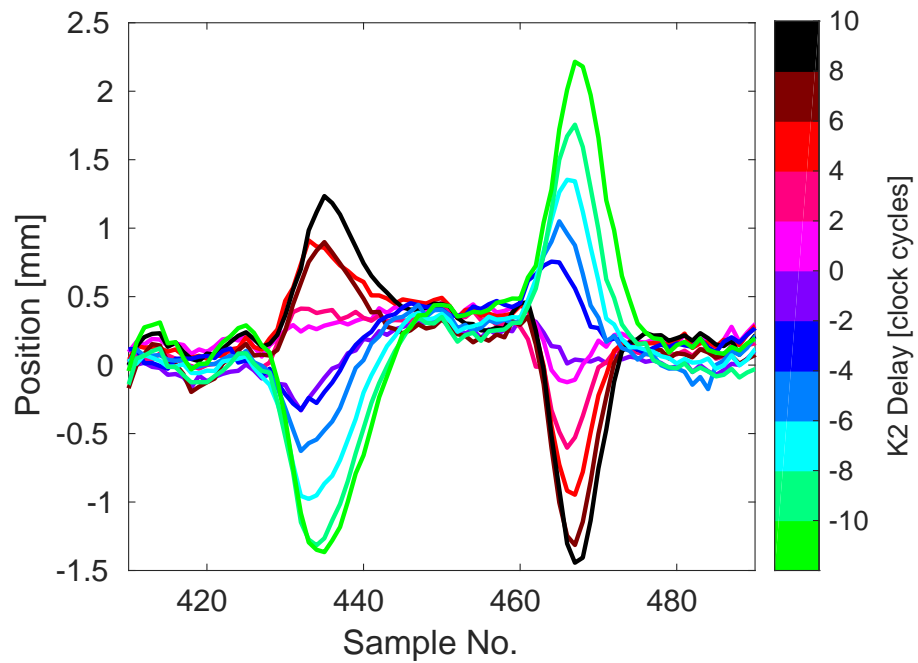


Figure 5.37: Measured position offset in a BPM after the chicane for different relative kick delays (as indicated by the colour scale).

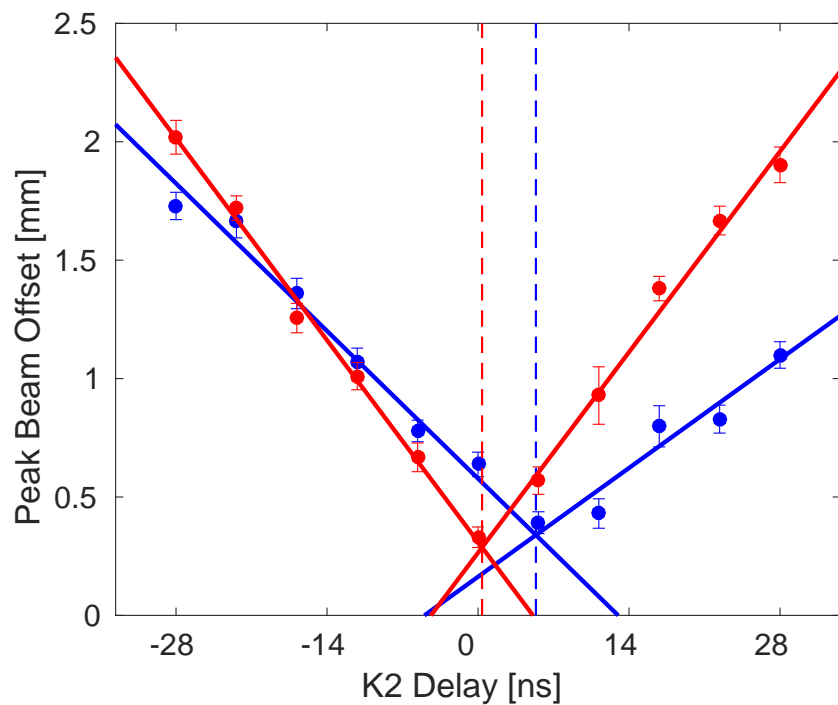


Figure 5.38: Fitted peak position offset after the chicane vs. the applied relative kick delay. Fits to the peaks at both the rising edge (blue) and falling edge (red) of the pulse are shown. Dashed vertical lines show the fitted optimal delay in each case.

- **K1 delay:** 7 clock cycles (19.6 ns).
- **K2 delay:** 7 or 8 clock cycles (19.6 or 22.4 ns).

# Chapter 6

## PFF System Performance

Over the course of 2014 and 2015 much experience has been gained with the PFF system and vast improvements have been made to the system setup, hardware performance and beam conditions as discussed in previous chapters. In all cases a reduction in downstream phase jitter has been achieved. This chapter presents and discusses the performance of the PFF system in the context of the results achieved under the best overall conditions achieved to date at CTF3 <sup>1</sup>.

### 6.1 Stabilisation of Phase Jitter

The results presented here show the best corrected downstream phase jitter obtained to date at CTF3 with the PFF system. Naturally, this was only possible after the vast improvements and optimisations presented throughout the rest of the thesis. The data was taken during the best beam conditions currently achieved at CTF3 in terms of phase propagation, following a series of R56 and beam energy optimisations using the same methods discussed in Chapter 4. At the same time the phase monitor resolution was improved to below  $0.13^\circ$  after switching to mechanical phase shifters (Section 3.8). Finally, updates to the kicker amplifiers (Section 5.2), which doubled the correction range compared to earlier tests, were an important improvement.

The data was taken as one of a sequence of short measurements, with small changes to the gain made between datasets in an attempt to empirically determine the optimal gain. Results from the other datasets in this sequence are discussed in the following section to demonstrate the phase stability achieved on longer time scales and to discuss the current limitations of the correction. The individual dataset shown here comprises 150 pulses taken in interleaved mode, with the correction applied to alternating pulses as described in Section 5.1.1. The gain was set to 800 units, corresponding to an actual applied correction of 1.3 times the upstream phase using the conversion factor calculated in Section 5.4.1.

---

<sup>1</sup>The datasets shown in this chapter were taken on 20th November 2015

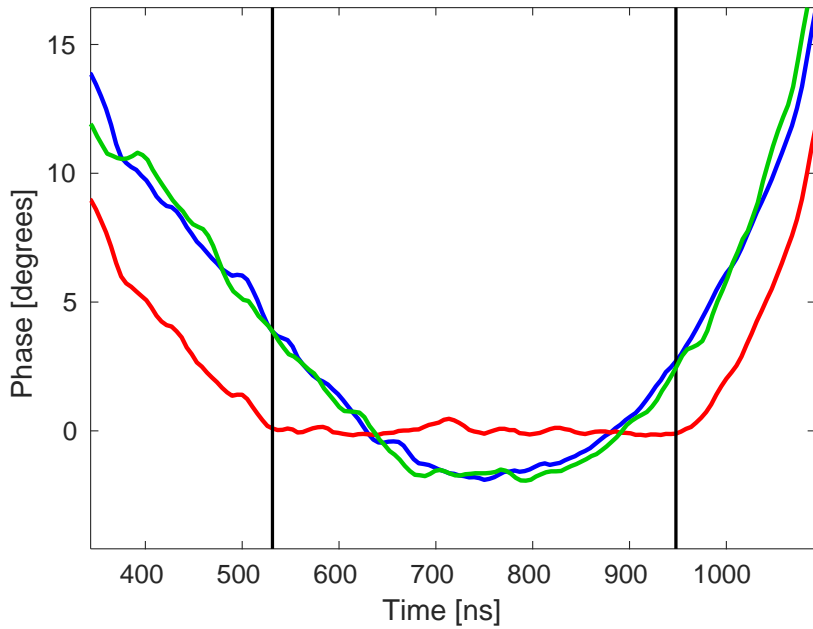


Figure 6.1: Phase along the pulse upstream (green) and downstream with the PFF system off (blue) and on (red). Vertical black lines mark the region within which the correction is not saturated.

### 6.1.1 Correction of Pulse Shape

Figure 6.1 shows the phase point by point along the pulse upstream, downstream with the PFF system off and downstream with the PFF system on. The value at each point is its mean taken across the 75 PFF on or 75 PFF off pulses in the dataset. The region of the pulse that is used to calculate the mean and other statistics throughout this chapter is also indicated, and will be referred to as the sample range. This range is chosen to cover the maximal proportion of the pulse within which the the correction is not being saturated as a result of the phase sag (plus jitter) exceeding the  $\pm 5.5^\circ$  correction range. It covers a total of 81 samples at 5.2 ns per sample, giving a total time span of 422 ns.

Following the optimisation of the phase propagation, described in Chapter 4, the overall shape of the upstream and (uncorrected) downstream phase along the pulse are very similar, although small uncorrelated variations are still visible. These uncorrelated differences are then visible in the corrected downstream phase, although the overall ability of the PFF system to flatten the CTF phase sag within the sample range is strikingly clear. The original peak-to-peak variation in the mean downstream phase along the pulse within the indicated range is  $5.76 \pm 0.14^\circ$  with the correction off. With the correction applied this is reduced to  $0.65 \pm 0.07^\circ$ . Outside the central region of the pulse, where the amplifier is saturated, the PFF system can no longer correct the shape of the phase along the pulse. The only effect is to shift the phase by the maximum possible correction of  $5.5^\circ$ .

Figure 6.2 expresses the effect of the PFF system on the phase along the pulse within the central region in terms of the distribution of ‘flatness’ values for each pulse in the data set with PFF system off and on. For each pulse the flatness value is defined as the standard

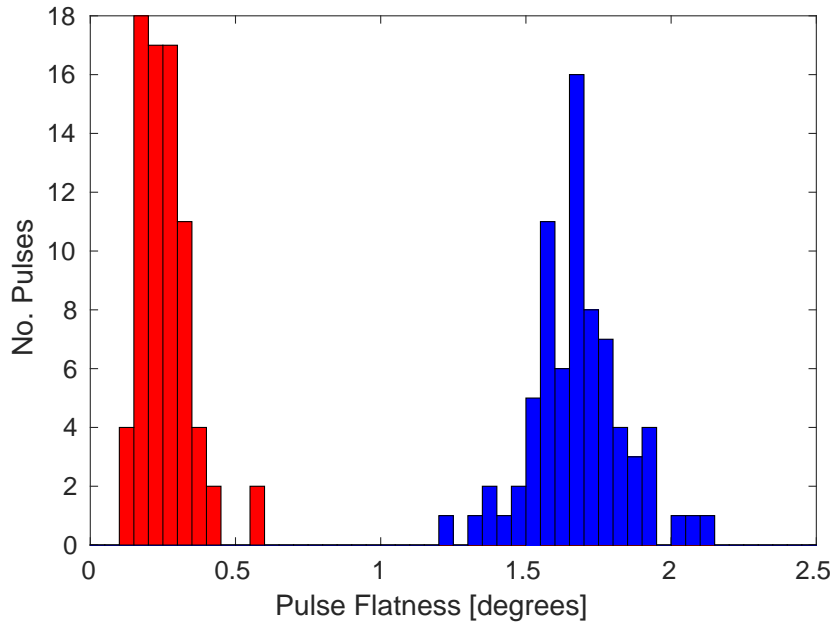


Figure 6.2: Flatness of the initial (blue) and corrected (red) downstream phase along the pulse.

deviation of phase values about the mean across the sample range. In this case the flatness value of each pulse therefore corresponds to the standard deviation of 81 values (the length of the sample range). A pulse with a flatness value of zero would have constant phase across the whole sample range, with no small variations such as those seen in Figure 6.1. The value is also insensitive to the jitter on the overall mean pulse phase seen later in Section 6.1.2. In Figure 6.2, the initial uncorrected downstream pulse flatness of  $1.68 \pm 0.02^\circ$ , dominated by the phase sag at CTF3, is reduced to  $0.26 \pm 0.01^\circ$  with the correction applied. On average, the corrected pulses are  $6.5 \pm 0.3$  times ‘flatter’ than the uncorrected pulses.

### 6.1.2 Correction of Mean Phase

This section considers the mean phase, which is calculated as the average phase of each pulse across the sample range shown in Figure 6.1. The initial correlation between the upstream and downstream phase in this dataset, as shown by the distribution in Figure 6.3, is  $0.93 \pm 0.04$ . This gives a theoretical limit of a factor  $2.7 \pm 0.4$  reduction in the downstream jitter using Equation 4.5. The uncorrected downstream jitter of  $0.74 \pm 0.06^\circ$ , and consequently the downstream-upstream jitter ratio of  $1.1 \pm 0.1$  are the lowest achieved at CTF3 to date. With this initial jitter and the theoretical reduction factor of  $2.7 \pm 0.4$  the lowest corrected downstream jitter that could be achieved is then  $0.27 \pm 0.05^\circ$ . The aforementioned correlation and jitter ratio combine to give an optimal gain of  $1.0 \pm 0.1$  (Equation 4.4). The actual system gain of 1.3 is therefore slightly larger than should be optimal.

The second distribution of points in Figure 6.3 shows the effect of the PFF correction on the phase distribution. The downstream phase jitter is reduced from  $0.74 \pm 0.06^\circ$  to  $0.28 \pm 0.02^\circ$ , a reduction of a factor  $2.6 \pm 0.3$ . Within the errors this agrees with the theoretical

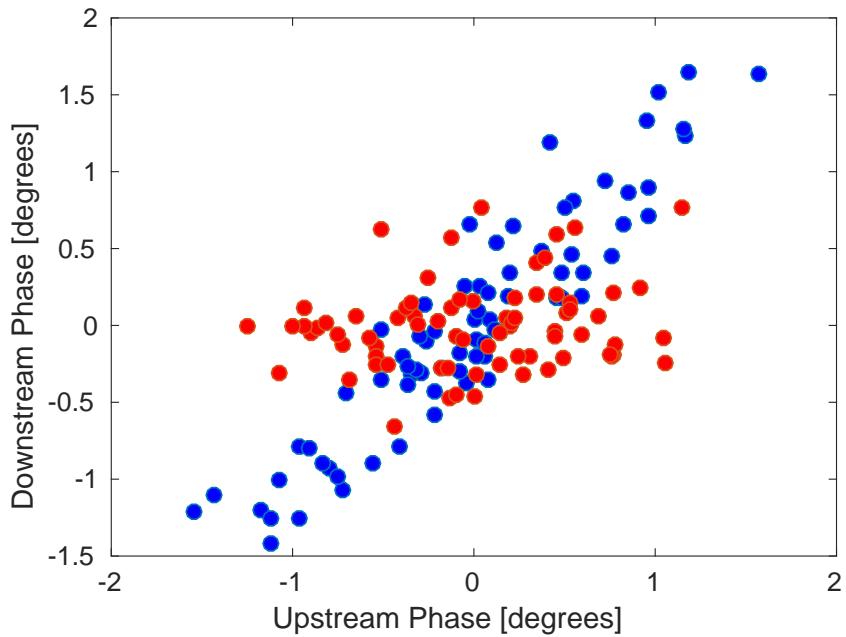


Figure 6.3: Mean downstream phase plotted versus the upstream phase with the PFF system off (blue) and on (red).

limit derived previously given the beam conditions in this dataset. The correction acts to remove almost all correlation between the upstream and downstream phase, rotating the distribution as seen in the plot. The correlation is reduced from  $0.93 \pm 0.04$  to  $0.19 \pm 0.12$ .

In terms of the achieved downstream phase jitter it should be noted, however, that the measured upstream jitter of  $0.57 \pm 0.05^\circ$  across the pulses with the PFF correction in this dataset is lower than the  $0.69 \pm 0.06^\circ$  measured without the PFF system (Table 6.1). This is assumed to be a statistical fluctuation rather than being a systematic difference between the odd and even pulses at CTF3 or an effect of the correction (which can only influence the downstream phase). Assuming the upstream jitter propagated downstream with the same ratio in each case, the true ‘natural’ downstream jitter for the pulses without the correction applied would have been  $0.61 \pm 0.09^\circ$  and the true factor reduction in the corrected jitter achieved with the PFF system would be decreased to  $2.2 \pm 0.4$ . Assuming the upstream-downstream phase correlation was also not affected by this statistical fluctuation (so that the theoretical jitter reduction of a factor  $2.7 \pm 0.4$  still holds), a corrected jitter of  $0.23 \pm 0.05^\circ$  would have been theoretically possible in this dataset.

With interleaved data it is also possible to simulate the expected effect of the correction empirically, as an additional point of comparison between the achieved and expected results, as well as verifying that the complete behaviour of the system is understood. The distribution of simulated corrected phases is shown in green on Figure 6.4. It is derived by taking the initial distribution with the PFF system off and subtracting the upstream phase, multiplied by the gain factor, from the downstream phase. This exactly mimics what the feedforward system would have done if it had been applied to the even pulses in this dataset, and can be directly compared to the odd pulses taken at the same time with the actual correction

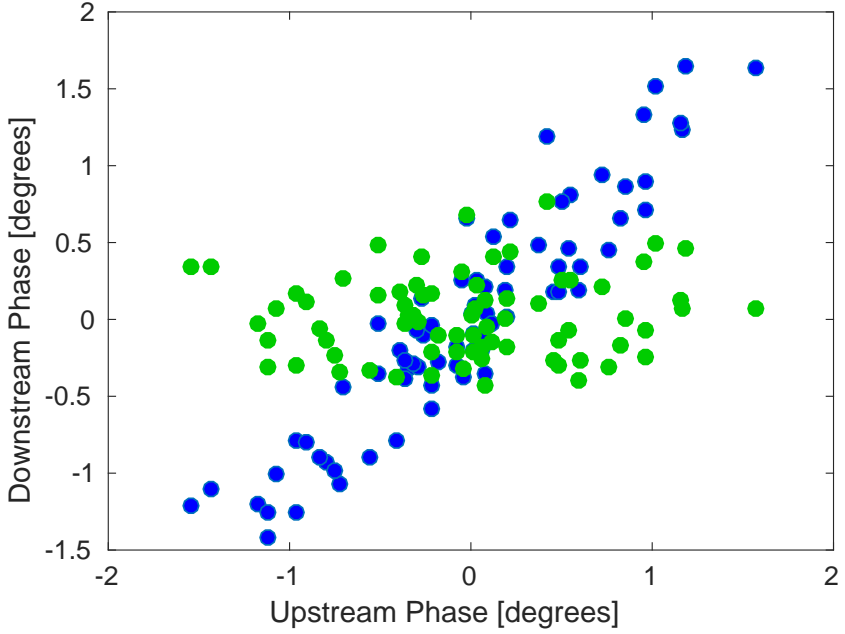


Figure 6.4: Simulated corrected downstream phase using optimal gain and unlimited correction range plotted against the upstream phase (green). The initial downstream phase (blue) is also shown.

Correction Status	$\sigma_u$	$\sigma_d$	Correlation
FF Off	$0.69 \pm 0.06^\circ$	$0.74 \pm 0.06^\circ$	$0.93 \pm 0.04$
FF On	$0.57 \pm 0.05^\circ$	$0.28 \pm 0.02^\circ$	$0.19 \pm 0.12$
FF Simulated	$0.69 \pm 0.06^\circ$	$0.27 \pm 0.02^\circ$	$0.06 \pm 0.12$

Table 6.1: Summary of results for the dataset in which the lowest downstream phase jitter has been achieved. Statistics are calculated using the mean phase.

applied. In this example the simulation shown is the ideal case, considering a correction with infinite range and bandwidth applied with the optimal gain. The simulated corrected downstream jitter of  $0.27 \pm 0.02^\circ$  agrees with the theoretical limit of  $0.27 \pm 0.05^\circ$  previously derived. The achieved jitter of  $0.28 \pm 0.02^\circ$  matches both the theoretical and simulated jitter predictions within the error, giving confidence that the overall PFF setup in this dataset (after all the commissioning steps discussed in Chapter 5) was close to optimal. There is perhaps some room for improvement due to the difference between the upstream jitter in the PFF on and off data as well as the larger than ideal gain, as mentioned previously, and this will be elaborated on in Section 6.2. Nevertheless, this result clearly demonstrates stability on the mean phase approaching the CLIC target of 0.2 degrees at 12 GHz and demonstrates that achieving this stability with a PFF system is feasible.

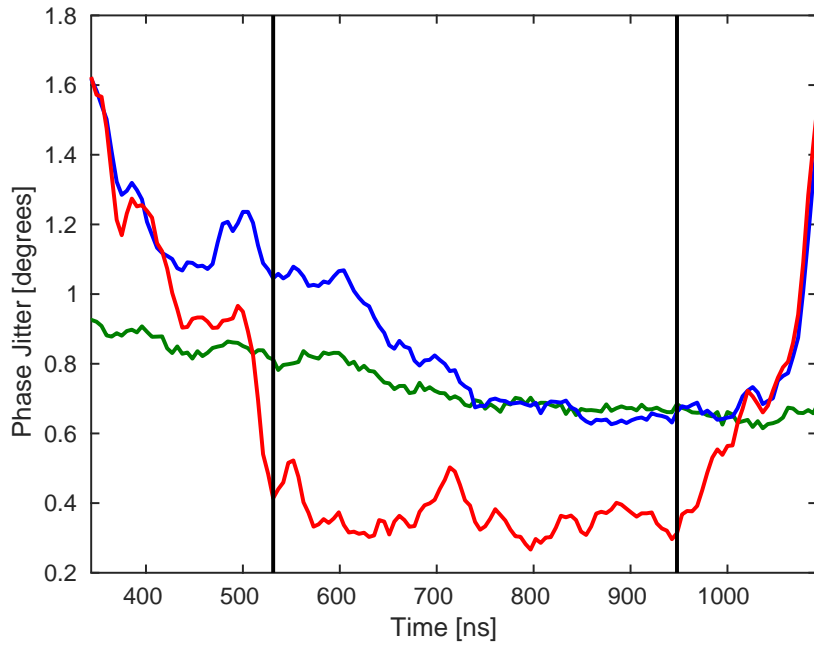


Figure 6.5: Phase jitter along the pulse upstream (green) and with the PFF system off (blue) and on (red).

### 6.1.3 Phase Jitter Along the Pulse

Figure 6.5 shows the overall phase jitter at each sample along the pulse upstream and downstream with the PFF system off and on. These jitter values contain components coming from both the jitter on the overall mean pulse phase discussed initially and from the variations along the pulse (the non-zero flatness of each pulse). These jitter values are therefore larger and taking the mean sample jitter within the sample range an initial downstream jitter of  $0.79 \pm 0.02^\circ$  is reduced to  $0.36 \pm 0.01^\circ$  by the correction in this case, a reduction by more than a factor two. There are also variations of up to a factor two in the jitter that was measured at each sample point, the lowest jitter being  $0.27 \pm 0.02^\circ$  at time 802 ns and the worst  $0.52 \pm 0.04^\circ$  at time 552 ns. The corrected jitter along the pulse within the central sample range also agrees with the simulated result of  $0.38 \pm 0.01^\circ$  using the interleaved pulses without the correction applied, as shown in Figure 6.6. Outside the sample range the PFF performance is degraded as the phase sag along the pulse exceeds the  $\pm 5.5^\circ$  correction range. The simulation assumes infinite correction range in this case, and therefore yields lower phase jitters than the actual system at the start and end of the pulse.

Although the largest component of phase jitter at CTF3 is on the pulse mean, effects such as energy variations along the pulse cause differences in the jitter and upstream-downstream phase correlation at each sample point (as seen in Section 4.7, for example). This leads to the variations in the achievable corrected downstream jitter along the pulse seen here, which can only be improved by further fine-tuning of the CTF3 injector stability and optics.

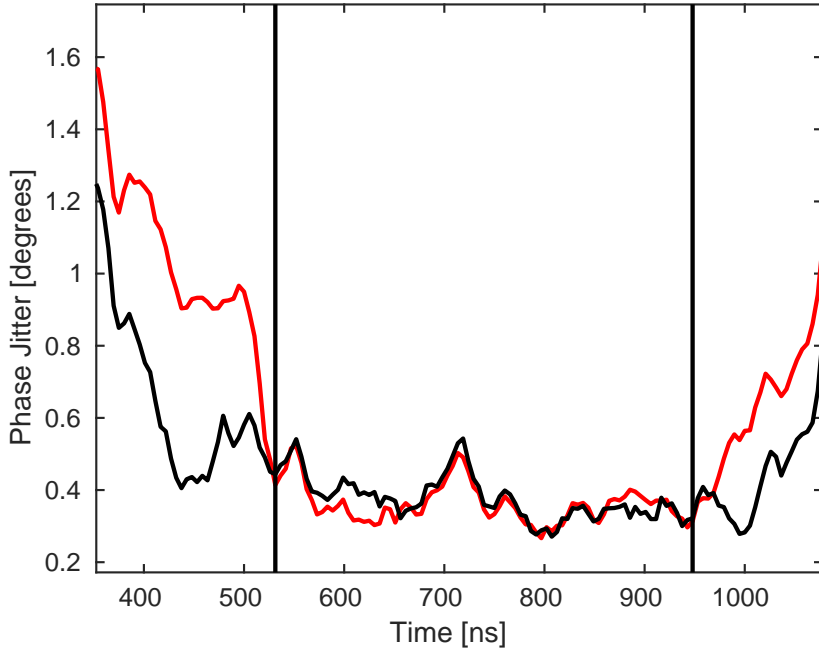


Figure 6.6: Comparison between the achieved downstream phase jitter along the pulse (red) and a simulation of the corrected jitter using optimal gain and unlimited correction range (black).

#### 6.1.4 CLIC Pulse Length

The phase stability requirements as needed for CLIC lie somewhere in-between the results presented on the mean phase and the phase point by point along the pulse so far. This section aims to express the achieved phase jitter in a way that is more relevant to CLIC.

At CLIC high frequency variations are well filtered by the drive beam recombination scheme and the filling time of the accelerating structures [14]. The scheme is therefore insensitive to features faster than around 30 ns. As the signals at CTF3 are acquired at 192 MHz (on the SiS digitisers, Section 3.4), or 5.2 ns per sample, five samples can be averaged to remove any high frequency components to which CLIC would not be sensitive. The effect of doing this on the downstream phase jitter is shown in Figure 6.7. Although there is a consistent reduction in jitter along the pulse the overall effect is small, up to a maximum of 0.06°. Some small peaks in jitter are removed by the averaging, although in most cases the reduction is predominantly due to reducing digitiser noise in the measurement, as opposed to actual high frequency features in the beam phase.

Also, the results up until this point have been calculated across the longest possible portion of the CTF3 pulse within which the correction is not saturated – a time span of 422 ns. At CLIC the combined pulse length is only 240 ns, and thus a further small improvement in the quoted achieved phase jitter can be achieved by using a sample range of this length. A 240 ns sample range is shown and compared to the original 422 ns range in Figure 6.7.

The final achieved downstream phase jitter at CTF3, across the CLIC pulse length and

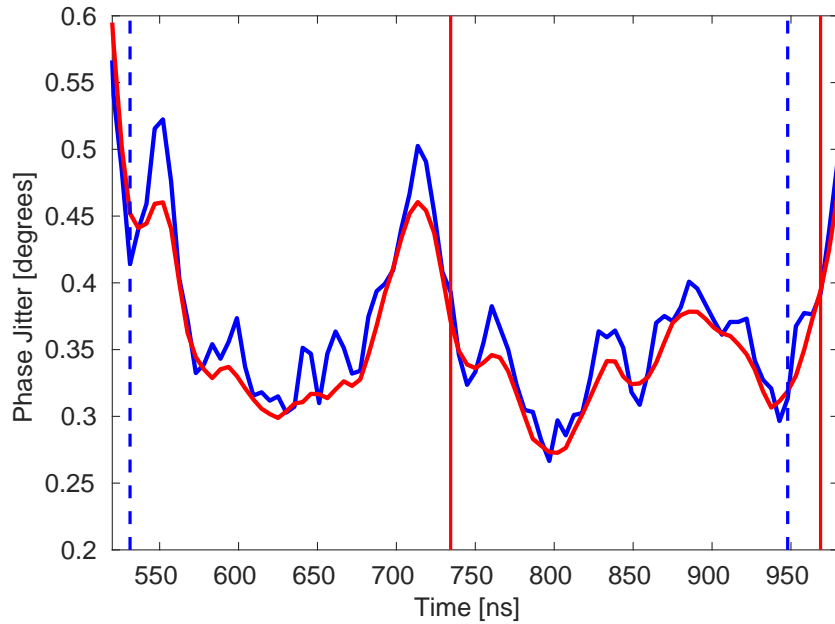


Figure 6.7: Original downstream phase jitter along the pulse sampled at 192 MHz (blue) compared to the phase jitter along the pulse using the average of 5 samples (red). Dashed vertical blue lines mark the sample range used for Sections 6.1.2–6.1.3. Vertical red lines show a 240 ns sample range relevant for CLIC.

with high frequency features removed, is  $0.33 \pm 0.01^\circ$ . This is the figure of merit which must be reduced to  $0.2^\circ$  at CLIC.

## 6.2 Limitations of the PFF System Performance

The remainder of this chapter discusses remaining operational issues for the PFF system largely resulting from drifts in the CTF3 beam conditions. This section therefore discusses the status of the correction across longer time scales, presenting both the level of corrected phase jitter that can currently be achieved routinely and to highlight areas where improvements are still needed both in the PFF setup itself and the beam conditions. Being able to regularly demonstrate and maintain corrected downstream phase jitters at the level achieved in the best dataset shown previously on the mean phase (below  $0.3^\circ$ ), is one of the key remaining goals for the PFF prototype. To be concise this section focuses on the mean phase jitter, though exactly the same arguments can be applied to the correction of the jitter along the pulse and the pulse shape.

### 6.2.1 Phase Monitor Resolution

The quoted initial and corrected phase jitters throughout this chapter and the thesis as a whole are the measured phase jitters including the contribution of the phase monitor resolution. The true achieved corrected downstream beam phase jitter is therefore slightly less

than these measured values. The actual beam jitter can be given by (using Equation 3.15):

$$\sigma_b^2 = \sqrt{\sigma_m^2 - \sigma_n^2} \quad (6.1)$$

Where  $\sigma_b$  is the actual phase jitter of the beam,  $\sigma_m$  is the usually quoted measured phase jitter, and  $\sigma_n$  is the phase monitor resolution.

For the mean phase the phase monitor resolution is around  $0.11^\circ$ , whereas it is  $0.13^\circ$  for the measured phase point by point along the pulse for which the electronics noise makes a slightly larger contribution (Section 3.9). As these are much lower than the achieved corrected phase jitters to date they only have a small contribution to the total measured jitter. Excluding the effects of the phase monitor resolution the actual mean downstream phase jitter achieved in Section 6.1 is reduced from  $0.28 \pm 0.02^\circ$  to  $0.26 \pm 0.02^\circ$ . The point by point jitter along the pulse is reduced from  $0.36 \pm 0.01^\circ$  to  $0.34 \pm 0.01^\circ$ . Finally, for the results across a CLIC pulse length in Section 6.1.4, the jitter is reduced from  $0.33 \pm 0.01^\circ$  to  $0.31 \pm 0.01^\circ$ .

The minimum achievable corrected phase jitter is a factor  $\sqrt{2}$  larger than the phase monitor resolution (Equation 3.26). This effect is included in the theoretical predictions and simulations presented in this chapter via the measured upstream-downstream phase correlation, which also has a dependence on the phase monitor resolution (Equation 3.25). Again, with the corrected phase jitter currently achieved this is only a small effect, with the main limitations coming from the beam conditions and phase propagation.

### 6.2.2 Beam Conditions

Figure 6.8 shows the history of the mean phases upstream and downstream with the correction on and off during one afternoon of data taking. The PFF system was not operated continuously throughout this two and a half hour period but 15 individual datasets of a few hundred pulses each were taken and these results have been combined to create a large sample of 3083 interleaved pulses (1541 with the correction on and 1542 with the correction off). The time span of each individual dataset during the overall data taking period is indicated on the figure. The data presented in Section 6.1, showing the lowest downstream phase jitter achieved to date, was taken from the 15:38 dataset on this afternoon. Note that the large jump in the downstream phase between the 16:00 and 16:04 datasets was caused by changes made to magnetic correctors in the TL2 chicane in order to re-optimise the beam orbit and transmission to the downstream phase monitors at this time. In Figure 6.20 the mean phase is subtracted (separately for the upstream, downstream PFF off and downstream PFF on phase) from each dataset to remove this effect, making a comparison between datasets easier. It is important to emphasise that, apart from this jump in the downstream phase, the overall picture is a fair reflection of the (uncorrected) phase stability at CTF3 in optimal conditions.

Figure 6.10 shows how the mean beam energy and the beam energy jitter varied during the afternoon. The mean relative beam energy offset varies between  $1.8 \pm 0.1 \times 10^{-3}$  and  $-1.9 \pm 0.1 \times 10^{-3}$ , with an overall trend of decreasing energy with time. Meanwhile the relative

## 6.2 Limitations of the PFF System Performance

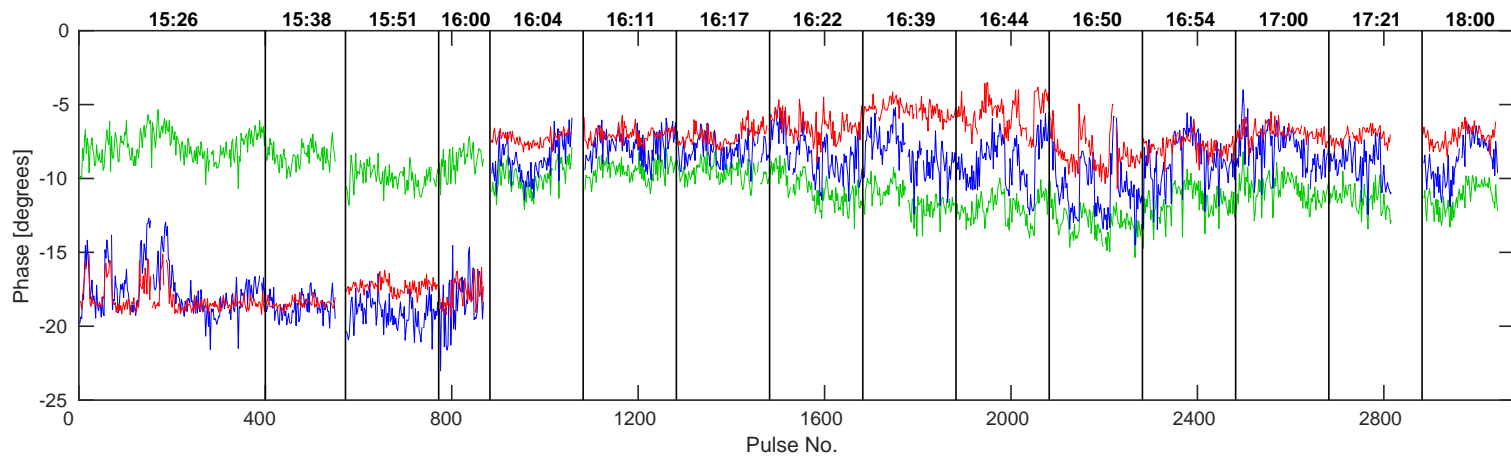


Figure 6.8: History of the mean phase upstream (green) and downstream with the PFF system off (blue) and on (red) across several hours. Vertical black lines mark the start time and span of each individual dataset. The start time of each dataset is also indicated at the top of the plot.

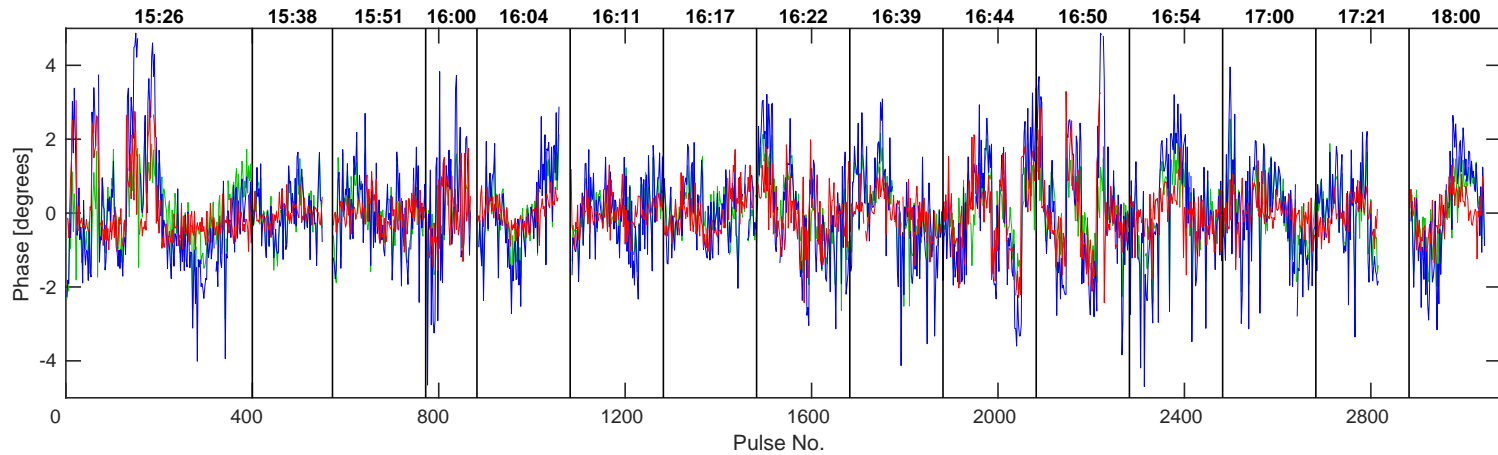


Figure 6.9: Mean phase history from Figure 6.8 with the mean phase offsets of each individual dataset subtracted.

energy jitter varies by up to a factor 3 between datasets, between  $0.56 \pm 0.05 \times 10^{-3}$  (in the record 15:38 dataset) and  $1.6 \pm 0.1 \times 10^{-3}$  (in the 16:44 dataset). In Section 4.5.1 it is shown that mean energy offsets and energy jitters at this level are by themselves expected to reduce the upstream-downstream phase correlation to below 90% due to the effects of  $T_{566}$  (second order phase-energy dependences). The remainder of this section and Section 6.3 focuses on how various drifts and changes during this afternoon effect the performance of the PFF system, largely in terms of the system setup. However, like the phase monitor resolution it will be seen that deviations from the optimal PFF system setup have only a small effect compared to the limitations placed by the phase propagation (initial upstream-downstream phase correlation and jitters). The phase propagation has been discussed extensively in Chapter 4, thus is only mentioned in brief here.

Figure 6.11 shows that these energy variations and drifts do indeed change the energy dependence of the downstream phase. The horizontal axis shows the difference between the phase-energy correlation upstream and downstream, which should be zero in the ideal case. For large differences between  $\rho_{dp}$  (downstream phase-energy correlation) and  $\rho_{up}$  (upstream phase-energy correlation) the upstream-downstream phase correlation ( $\rho_{ud}$ ) is degraded. Section 4.5.3 discussed new feedbacks being implemented at CTF3 in order to improve the energy stability, which is likely to be the most significant area of improvement for future PFF tests.

### 6.2.3 Upstream Phase Drifts

Over the course of the data taking period the mean upstream phase, in green, varies by ten degrees peak-to-peak or  $1.75 \pm 0.02^\circ$  in terms of root-mean-square variation (Figure 6.8). The main sources of drifts are temperature related effects and instabilities of the klystrons at CTF3 [74]. Small drifts of up to a few degrees in the upstream phase are not an issue for the performance of the PFF correction providing the correlation between the upstream and downstream phase is not degraded. However, larger drifts may lead to a loss in correlation, for example if the source of the drift is a variation in beam energy due to the issues discussed in Chapter 4. The variation of the correlation between datasets is discussed in Section 6.2.4.

Larger changes in the upstream phase such as the ten degree drift seen here may also impact the PFF performance purely via the limited correction range of  $\pm 5.5^\circ$  combined with the phase sag along the CTF pulse. Indeed the PFF prototype's main purpose is not to remove any large, slow phase drifts but rather the faster pulse-to-pulse jitter and high frequency variations along the pulse. The phase shift applied by the PFF correction at each sample along the downstream phase,  $\Delta\phi_d(t)$ , is given by:

$$\Delta\phi_d(t) = \begin{cases} -5.5^\circ, & \text{if } g\phi_u(t) \geq +5.5^\circ. \\ +5.5^\circ, & \text{if } g\phi_u(t) \leq -5.5^\circ. \\ -g\phi_u(t), & \text{otherwise.} \end{cases} \quad (6.2)$$

Here  $\phi_u(t)$  is the upstream phase at each sample point and  $g$  is the gain factor used. As the optimal gain (Section 4.1) for the correction is typically larger than unity due to the slight amplification in the downstream phase jitter with respect to the upstream jitter, the range of the PFF system in terms of the upstream phase is less than  $\pm 5.5^\circ$  (for example

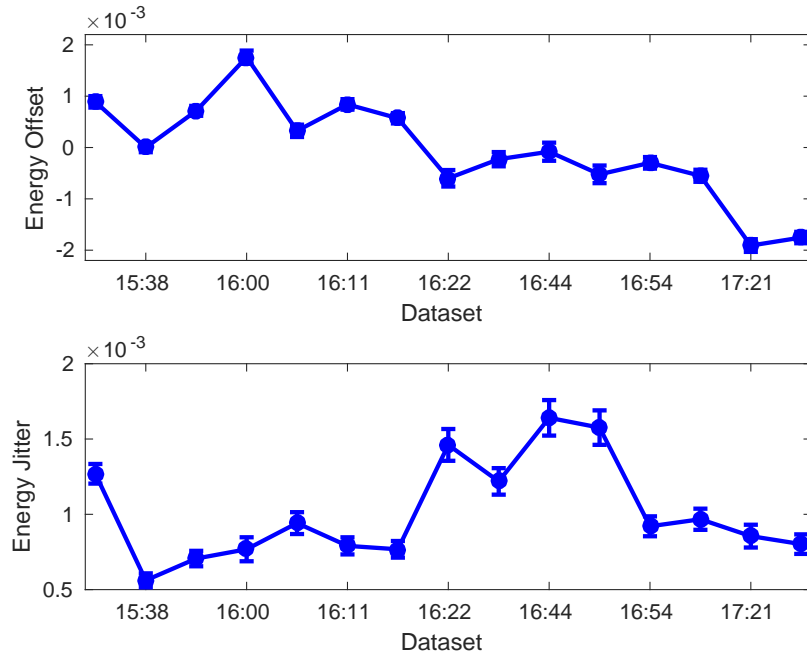


Figure 6.10: Mean relative energy offset (top) and energy jitter (bottom) in each dataset during the data taking period.

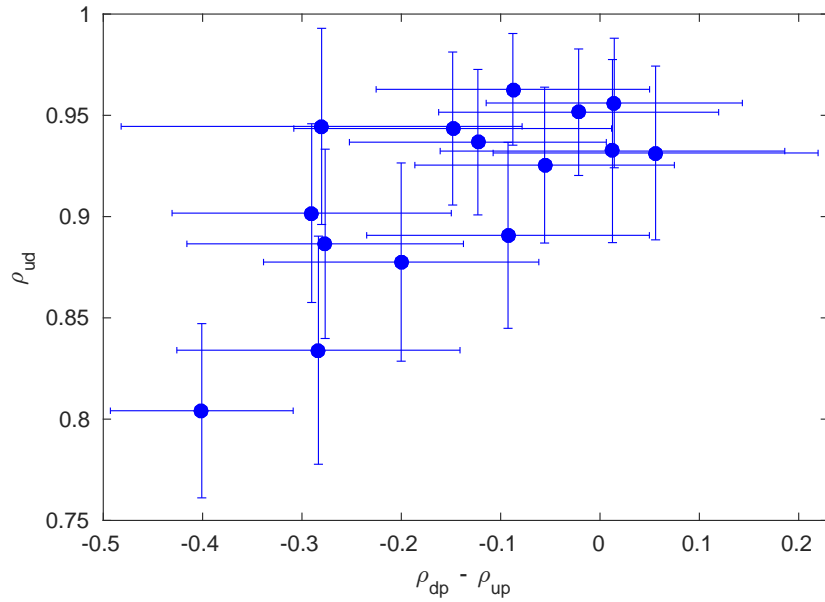


Figure 6.11: Upstream-downstream phase correlation ( $\rho_{ud}$ ) plotted against the difference between the upstream phase-energy and downstream phase-energy correlation ( $\rho_{dp} - \rho_{up}$ ).

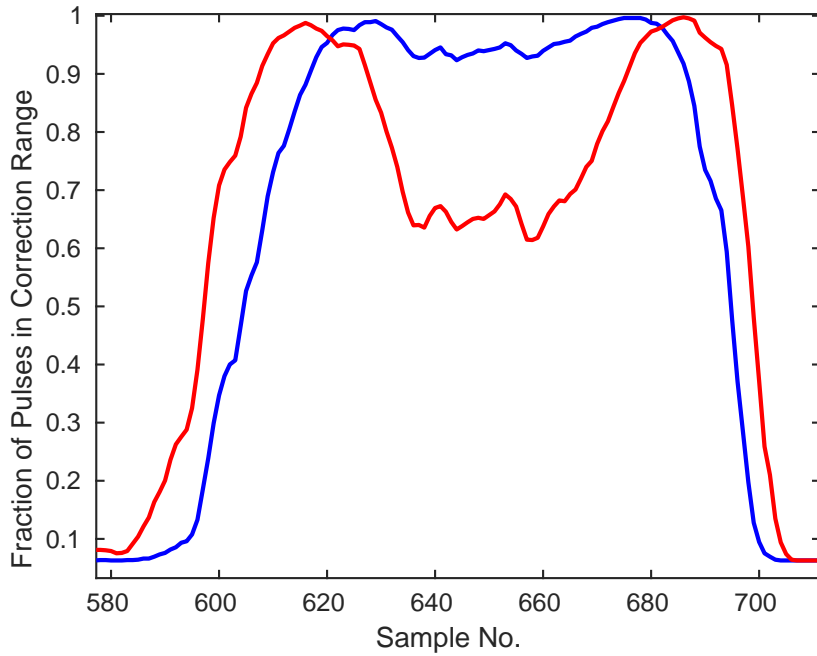


Figure 6.12: Fraction of pulses within the correction range of  $\pm 5.5^\circ$  at each sample point. The blue line shows the ideal case with a mean phase of zero across the central part of the pulse. The red line shows the effect of operating the PFF system with a static 2 degree offset in this region.

$\pm 4.6^\circ$  for the 15:38 jitter record dataset with a gain of 1.3). Any point along the upstream phase with  $|g\phi_u(t)| > 5.5^\circ$  receives the maximum  $5.5^\circ$  phase shift downstream but can not be corrected to zero, with this remaining residual degrading the corrected phase jitter that can be achieved. Samples with  $|g\phi_u(t)| > 5^\circ$  will also receive a slightly non-optimal correction due to the effects of the amplifier entering saturation, shown in Section 5.2.2, although this effect is not yet considered in the discussion here.

Figure 6.12 shows the fraction of pulses for which the optimal correction is within the correction range in the combined dataset. During the setup of the PFF system it is necessary to choose the zero point for the correction, i.e. the incoming upstream phase at which the correction output to the kickers is 0 V. This is done in the PFF firmware on the FONT5a board by varying the channel offset (Section 5.4.3). The optimal channel offset zeroes the mean phase taken across the part of the pulse where the best correction is desired (usually the flatter central part of the pulse at CTF3). In this case the effects of limited correction range are minimised, as the full  $\pm 5.5^\circ$  range can be used to remove variations about the mean phase, rather than also having to remove a static phase offset in the overall mean. When the channel offset is optimal the ideal correction across a 310 ns portion of the pulse is within the  $\pm 5.5^\circ$  range 96% of the time.

However, as to date the channel offset has been set manually small deviations from the ideal case are possible. Figure 6.12 also shows the fraction of pulses within the correction range if there is a static two degree offset in the upstream phase. In this case as many as 39% of pulses are outside the correction range within the normally correctable central region of the

pulse. To mitigate these effects and to get the largest reduction in jitter possible within each individual dataset the channel offset is normally adjusted on the FONT5a board between datasets. As a consequence of this, differences in the upstream phase between datasets are not removed in the corrected downstream phase, as the zero point for the PFF correction is effectively moving with the phase drifts during the data taking period.

The accuracy to which the channel offset for the upstream phase has been set can be inferred by comparing the mean downstream phase in each dataset with the correction on and off in Figure 6.8. In the ideal case the mean phase should be identical with the PFF system on and off, so that the full correction range is being used to correct jitter about the mean as mentioned previously. Although this is the case for some datasets, such as the 15:38 dataset, a clear difference between the two is often present, most visible in the datasets between 16:39 and 16:50 in which the corrected phase is clearly shifted several degrees with respect to the uncorrected phase. The absolute offset in each dataset is plotted in Figure 6.13. In the region between 16:22 and 16:50 the offset rises above  $2^\circ$ . The mean offset across the combined dataset is  $1.5 \pm 0.2^\circ$ .

In the following sections it will be shown that the effect of the non-optimal set point for the offset is small overall, although there is a noticeable degradation in the jitter that can be achieved in the datasets with the largest offsets. In any case, implementing an automatic procedure to set the zero point for the correction optimally in the FONT5a DAQ would be a useful improvement to the PFF setup procedure. This would involve adding a new module to the LabVIEW DAQ that keeps a history of the mean upstream phase (ADC2 output), and then slowly updates the ADC2 channel offset at regular intervals in order to zero the measured phase. For example, if the mean ADC2 output across the previous time period was +300 counts, the new LabVIEW module would change the ADC2 channel offset by -300 counts so that the mean is brought to zero. The full range of the PFF system can then be used to correct jitter about the mean, rather than removing static phase offsets. However, if the zero point for the correction was regularly updated in this way slow drifts in the phase would not be removed by the PFF system. To remove these drifts a complimentary slow phase feedback, utilising magnetic correctors in the TL2 chicane, would have to be run in parallel with the PFF system [43].

#### 6.2.4 Gain Stability

Another PFF parameter that has been mostly set up empirically to date is the feedforward gain. Historically, the gain set point for the PFF prototype has been determined by a combination of viewing the results of gain scans and by observing the flatness of the corrected downstream phase in online displays of the phase monitor signals. If, for example, the applied gain is too large this can be quickly seen in the online monitors as the PFF system will act to invert the original phase sag along the pulse. In this way it is relatively simple to find the approximate gain set point and to further fine-tune it by varying the gain in small steps between datasets. In later PFF attempts this approach was complimented by implementing an online display of the optimal gain, given the latest values for the upstream and downstream phase jitters and correlation. However, in this section it will be shown that

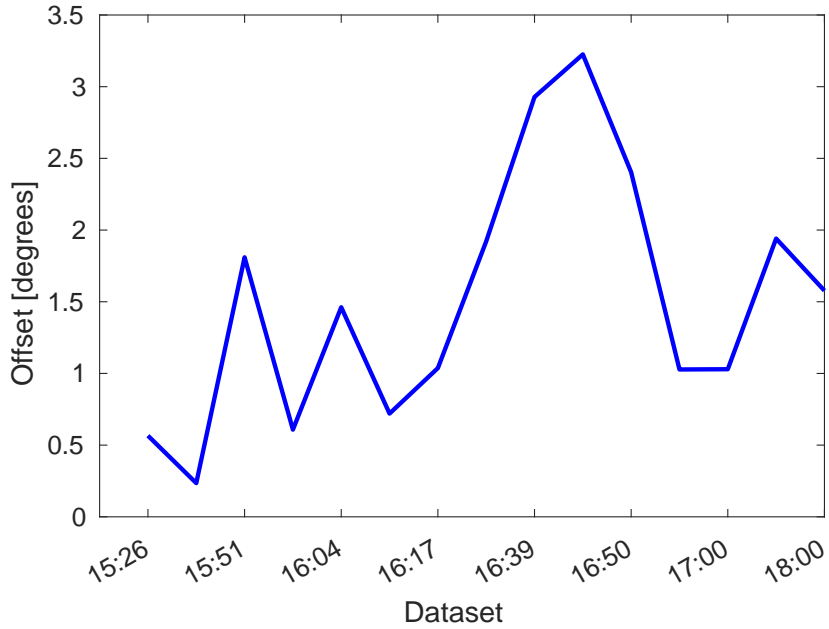


Figure 6.13: Mean offset between the initial and corrected downstream phase in each dataset.

due to drifts in the beam conditions at CTF3 there are large variations in the optimal gain between datasets, and these variations are rarely accurately followed in the PFF setup when using this empirical approach.

The optimal gain depends on the downstream-upstream phase jitter ratio and the correlation (Section 4.1). In Figures 6.8 and 6.9 large differences in the phase stability in each dataset are clearly visible, comparing for example the large phase jumps in the 15:26 and 16:50 datasets to the comparatively calm periods at 15:38 and 16:17. This is summarised in Figure 6.14, which shows the upstream and downstream (PFF off) phase jitter across the 5–10 minute time period of each dataset. Over the course of the data taking period the mean upstream and downstream phase jitter both vary by around a factor two — the upstream jitter between  $0.61 \pm 0.04^\circ$  in the 16:17 dataset and  $1.08 \pm 0.08^\circ$  at 16:22, and the downstream jitter between  $0.74 \pm 0.06^\circ$  at 15:38 and  $1.89 \pm 0.13^\circ$  at 16:50. Given the same correlation, a factor two increase in the uncorrected downstream jitter also doubles the corrected downstream phase jitter that can be achieved with the PFF system (Equation 4.5).

Also of key importance for the PFF correction is that not only are there large variations in jitter between datasets but additionally in the downstream-upstream jitter ratio (dashed line in Figure 6.14). In fact, the only dataset in which the upstream and downstream jitter are comparable is the record 15:38 dataset (with a ratio of  $1.1 \pm 0.1$ ). In all other datasets the downstream jitter is more than 1.3 times larger than the upstream jitter, reaching a maximum amplification of  $2.2 \pm 0.2$  in the 16:50 dataset. The mean ratio across the 15 datasets is  $1.48 \pm 0.04$ .

As well as the jitter ratio, the upstream-downstream phase correlation also varies between datasets, as shown in Figure 6.15. The worst correlation is  $0.80 \pm 0.04$  in the 15:26 dataset and the best  $0.96 \pm 0.03$  in the 16:54 dataset. Although this has a much smaller (20%)

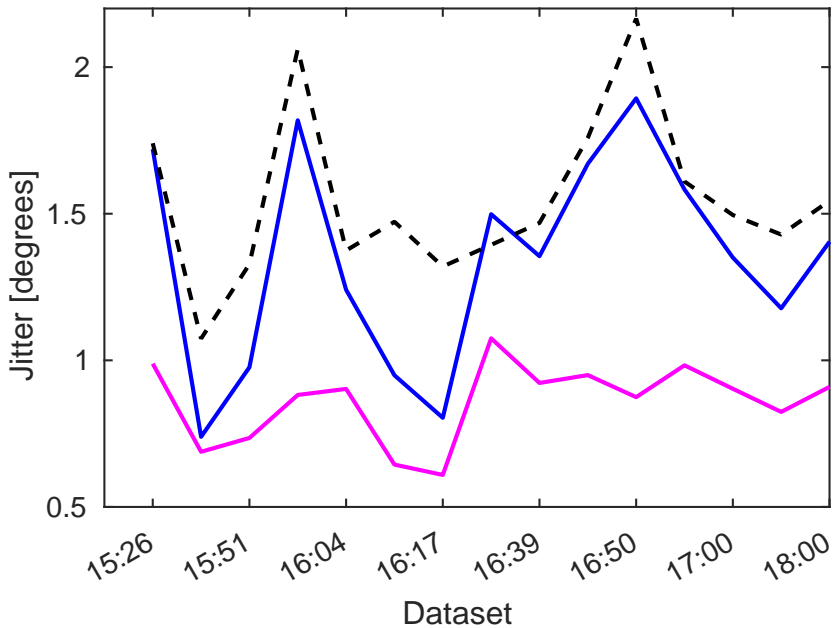


Figure 6.14: Upstream (pink) and downstream (blue) phase jitter in each dataset, as well as the ratio between the two (dashed black).

effect on the optimal gain than the factor 2 variation in jitter ratio, it has a large effect on the theoretical jitter improvement that can be achieved with the PFF system due to the dependence on the correlation in Equation 4.5. With 80% phase correlation only a theoretical factor 1.7 reduction in the downstream phase jitter can be achieved, whereas with 96% correlation this is increased to a factor 3.6.

There is no observed dependence of the phase jitter ratio on the phase correlation, as shown in Figure 6.16, so the effects of varying correlation and jitter ratio on the optimal gain are independent. They combine to give the optimal gain plotted in Figure 6.17. As it is dominated by the differences in jitter ratio, the gain also varies by close to a factor two, varying from  $1.0 \pm 0.1$  in the 15:38 dataset to  $2.0 \pm 0.3$  in the 16:00 dataset. The actual gain factor used in the dataset is also shown. The PFF system was designed under the assumption that the correct system gain would be approximately constant with time. As a result, although in places the empirically derived gain that was used follows the trend of the optimal gain, the changes are much smaller and it is clear that the real gain was systematically non-optimal. The smallest gain actually used was 1.2 (at 15:51) and the largest 1.5 (15:26 and 16:00). However, the overall mean of the used gain across the data taking period of  $1.3 \pm 0.1$  agrees with the mean of the optimal values ( $1.4 \pm 0.3$ ).

The impact of the real system using non-optimal gain is discussed in Section 6.3. Of course, in the ideal case the stability of beam conditions at CTF3 would be improved so that the variations in optimal gain over the course of a few hours are much smaller than those shown here. Nevertheless, an automatic gain optimisation procedure could be another area of interest for future PFF attempts. Particularly if the gain were automatically updated in real time during long datasets a significant reduction in jitter could be achieved. Like

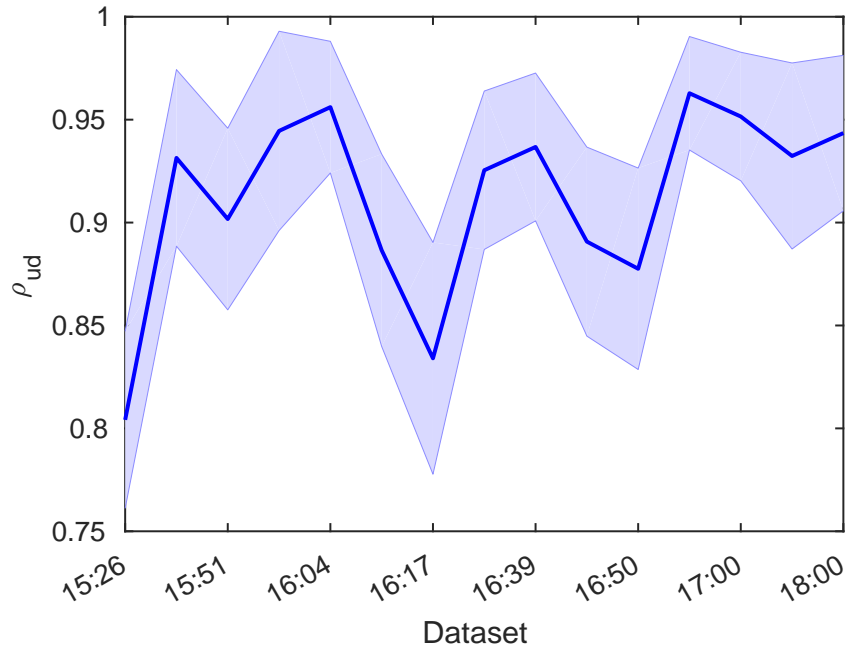


Figure 6.15: Upstream-downstream phase correlation ( $\rho_{ud}$ ) in each dataset with PFF off. The shaded region shows the approximate error on the correlation measurement.

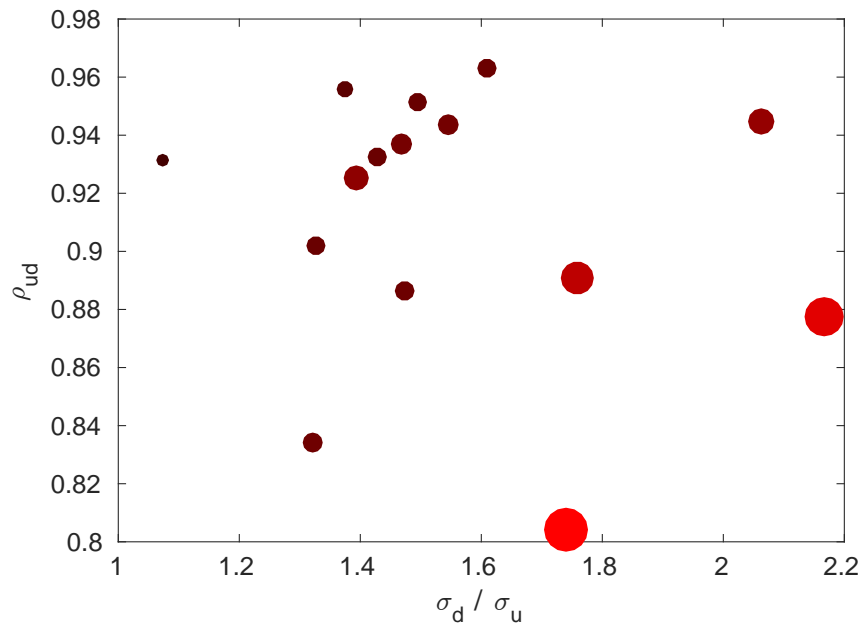


Figure 6.16: Upstream-downstream phase correlation ( $\rho_{ud}$ ) vs. jitter ratio ( $\sigma_d / \sigma_u$ ). The marker size and colour indicate the theoretical limit on the corrected downstream jitter in each dataset (small, black markers represent the lowest jitters).

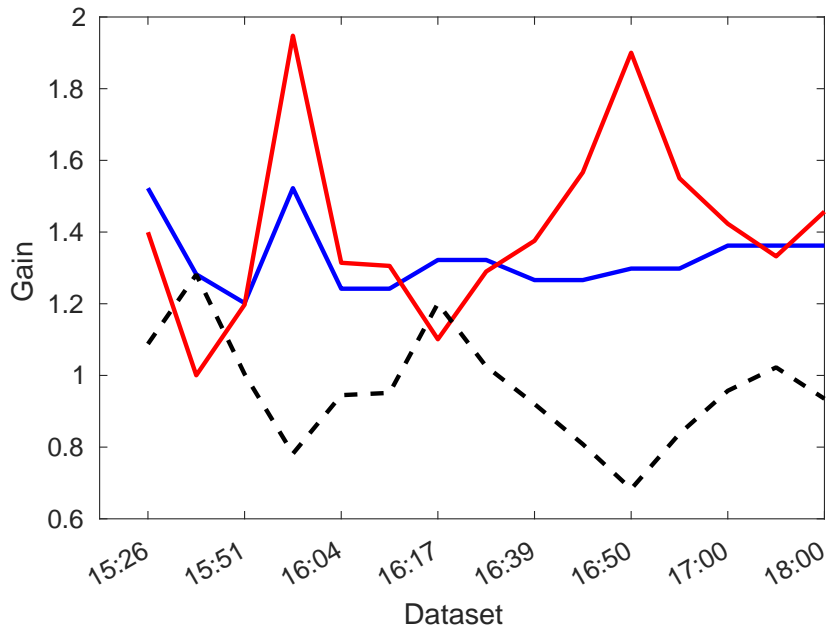


Figure 6.17: Actual gain used in each dataset (blue) compared to the optimal gain (red) and the ratio between the two (dashed black).

the offset this could be achieved by adding a new module to the LabVIEW DAQ. In this case the module would measure the current beam conditions (upstream-downstream phase correlation, upstream jitter and downstream jitter) and then use Equation 5.10 to calculate, and set, the optimal gain. This process would only work for interleaved data, in which the initial correlations and jitters can be calculated using the alternating pulses for which the PFF correction is not applied. With the PFF system turned on permanently a different gain optimisation technique would be required, such as an iterative procedure aiming to zero the correlation between the upstream and corrected downstream phase.

### 6.3 Achieved and Simulated Corrected Phase Jitter

It has been shown that the frequent drifts in both phase and downstream-upstream phase jitter ratio have not been optimally taken in to account in the PFF setup in terms of the actual offset and used gain. Nevertheless, even with a sub-optimal setup a large reduction in the downstream phase jitter can be achieved in all datasets. In the remainder of this section it will be shown that considering these constraints the PFF system is achieving close to peak performance, as well as highlighting the benefit that more accurate gain and offset control would have.

Firstly referring back to Figure 6.16, the size (area) and colour of the markers in the plot depend on the corrected downstream jitter that could be achieved in that dataset using the optimal gain. This is to emphasise again that it is a compromise between high correlation and low initial downstream jitter (and by extension low downstream-upstream jitter ratio) that gives the best conditions for the PFF correction. For example, there are seven datasets

showing correlation above 93% (as seen in the 15:38 record result), but they yield worse theoretical corrections, as 15:38 remains the only dataset in which a high correlation and low upstream-downstream jitter ratio have been achieved at the same time.

Figure 6.18 and Table 6.2 show the simulated corrected downstream jitter chronologically for each dataset with five different simulation setups:

- **Unlimited:** With unlimited correction range and the optimal gain (theoretical limit).
- **Range:** With  $\pm 5.5^\circ$  correction range, the optimal gain and zero offset.
- **Gain:** With  $\pm 5.5^\circ$  correction range, the actual gain used in the PFF system setup, and zero offset.
- **Offset:** With  $\pm 5.5^\circ$  correction range, the optimal gain, and the actual offset in the PFF setup.
- **All effects:** With  $\pm 5.5^\circ$  correction range, and the actual gain and offset used in the PFF setup.

By comparing the results of these five simulations it is possible to identify which PFF parameters are most critical for the correction performance. Later, by comparing the most restricted simulation, including the real offset and gain, to the phase jitter actually achieved it can be determined whether the PFF system is behaving as expected or whether there are remaining effects that need to be understood.

With the ideal PFF setup the  $\pm 5.5^\circ$  range set by the amplifier power is sufficient to be able to optimally correct almost all the natural phase jitter, thus the difference between the “Unlimited” and “Range” simulation is small. Depending on the dataset, the effects of using non-optimal gain and non-optimal offset are much larger.

In the 15:26, 15:51, 16:11 and 16:17 datasets the gain and offset are close enough to optimal so that all five simulations give close to the same result, with no further reduction in jitter possible by improving the PFF setup. For the other datasets a noticeable degradation in phase jitter can be seen either as a result of the non-optimal gain or offset. For the gain the largest effect on the achievable corrected jitter is seen at 16:00, with an increase of  $0.16 \pm 0.10^\circ$  due to the gain being around 20% smaller than optimal in this dataset. Alternatively, in the period between 16:22 and 16:50 the offset in the PFF setup was above  $2^\circ$  and this gives an effect on the correction of the same magnitude as using non-optimal gain. The maximal degradation in the achievable downstream jitter as a result of the offset is  $0.16 \pm 0.10^\circ$  in the 16:50 dataset. With the effects of limited correction range, non-optimal offset and non-optimal gain combined the achieved corrected jitter is expected to be up to  $0.25 \pm 0.11^\circ$  worse than the theoretical limit (16:50).

The achieved downstream jitters with the actual PFF system are presented in Figure 6.19 and Table 6.3, along with the uncorrected downstream and upstream jitter and the most realistic ”All Effects” simulation of the expected performance. Overall the agreement between the downstream jitter achieved with the actual PFF system and the simulation is very

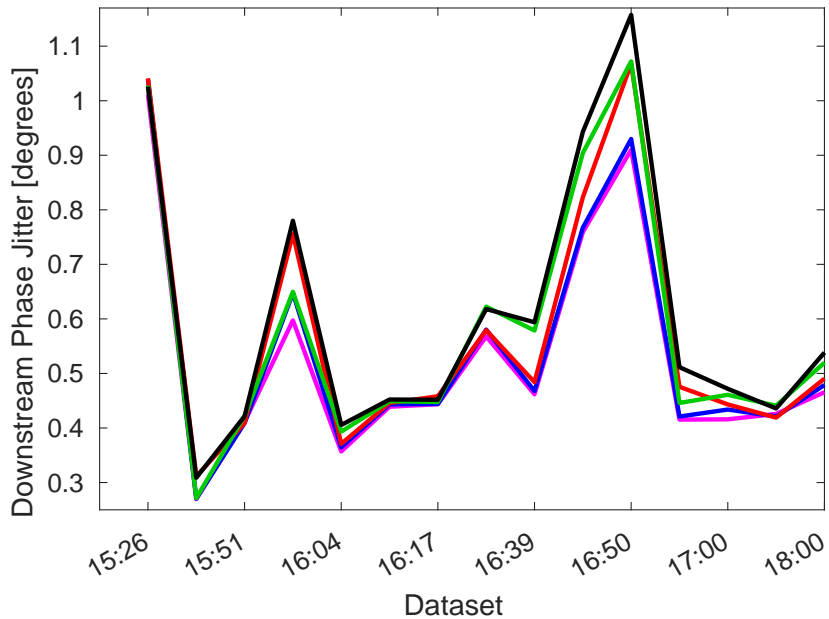


Figure 6.18: Simulated downstream jitter in each simulation setup: Unlimited (pink), Range (blue), Gain (red), Offset (green) and All Effects (black).

good. This gives confidence that the PFF system is behaving as expected and all the effects limiting the current performance are understood and in principle can be improved to yield lower jitter in future PFF attempts. However, there is a region between 16:17 and 16:44 where differences between the simulation and actual system can be seen. In particular, the  $0.58 \pm 0.04^\circ$  and  $0.82 \pm 0.06^\circ$  downstream jitter in the 16:17 and 16:22 datasets, respectively, are noticeably worse than the simulated results of  $0.45 \pm 0.03$  and  $0.62 \pm 0.04$ . The source of this is not yet understood and possibly hints at additional areas for improvement in the PFF setup.

Only the 15:38 dataset has a theoretical (and in all simulation scenarios) corrected downstream jitter of below  $0.3^\circ$  but in 10 out of 15 datasets below  $0.5^\circ$  jitter could have been achieved with an optimal PFF setup (or in 6 out of 15 with the actual setup). Nevertheless, the overall benefit of the PFF system is clear - the downstream phase jitter is reduced in every dataset, with a maximum reduction factor of 3.2 in the 16:05 dataset (in which the highest correlation of 96% was achieved).

Alternatively, rather than showing each individual dataset Figures 6.20—6.24 and Table 6.4 present the upstream-downstream phase distribution and overall jitter improvement with all the datasets combined. In order to yield meaningful results the mean upstream and downstream phase (both with FF on and FF off) are subtracted separately for each dataset. The effect of this can be seen by comparing Figure 6.8 (with no mean subtraction) and Figure 6.9. Without this subtraction any calculated jitter and correlation values across the combined dataset would be dominated by changes in the downstream phase resulting from changing the zero point (offset) for the correction between datasets, plus the large step in the downstream phase between the 16:00 and 16:04 datasets due to a beam setup change.

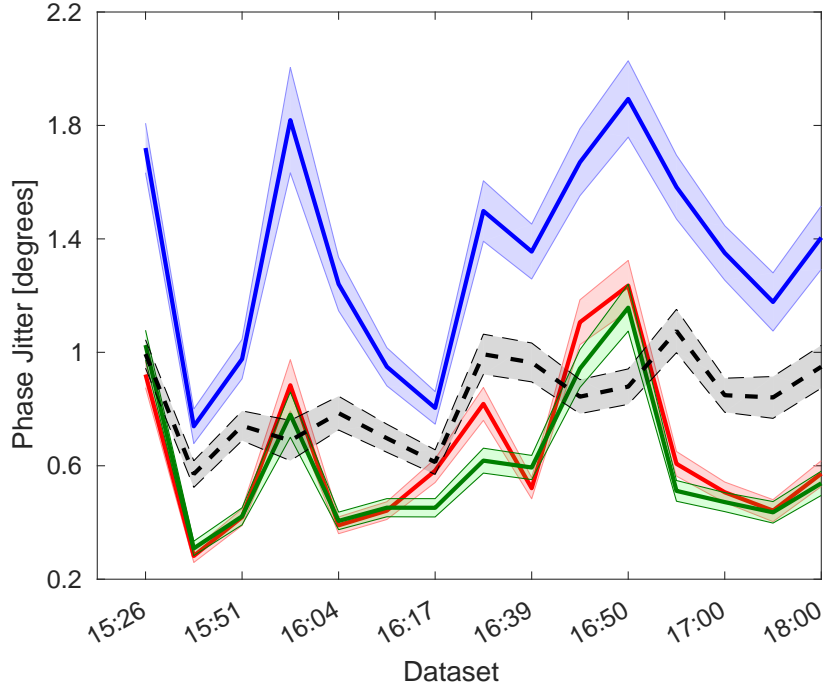


Figure 6.19: Downstream phase jitter with the PFF system off (blue) and on (red) in each dataset compared to the expected corrected jitter using the All Effects simulation (green). The upstream phase jitter is also shown for reference (dashed black).

Time	Unlimited	Range	Gain	Offset	All Effects
15:26	$1.01 \pm 0.05^\circ$	$1.04 \pm 0.05^\circ$	$1.04 \pm 0.05$	$1.03 \pm 0.05^\circ$	$1.03 \pm 0.05^\circ$
15:38	$0.27 \pm 0.02^\circ$	$0.27 \pm 0.02^\circ$	$0.31 \pm 0.03$	$0.27 \pm 0.02^\circ$	$0.31 \pm 0.03^\circ$
15:51	$0.41 \pm 0.03^\circ$	$0.41 \pm 0.03^\circ$	$0.41 \pm 0.03$	$0.42 \pm 0.03^\circ$	$0.42 \pm 0.03^\circ$
16:00	$0.60 \pm 0.06^\circ$	$0.65 \pm 0.07^\circ$	$0.76 \pm 0.08$	$0.65 \pm 0.07^\circ$	$0.78 \pm 0.08^\circ$
16:04	$0.36 \pm 0.03^\circ$	$0.36 \pm 0.03^\circ$	$0.37 \pm 0.03$	$0.39 \pm 0.03^\circ$	$0.41 \pm 0.03^\circ$
16:11	$0.44 \pm 0.03^\circ$	$0.44 \pm 0.03^\circ$	$0.45 \pm 0.03$	$0.45 \pm 0.03^\circ$	$0.45 \pm 0.03^\circ$
16:17	$0.44 \pm 0.03^\circ$	$0.44 \pm 0.03^\circ$	$0.46 \pm 0.03$	$0.45 \pm 0.03^\circ$	$0.45 \pm 0.03^\circ$
16:22	$0.57 \pm 0.04^\circ$	$0.58 \pm 0.04^\circ$	$0.58 \pm 0.04$	$0.62 \pm 0.04^\circ$	$0.62 \pm 0.04^\circ$
16:39	$0.46 \pm 0.03^\circ$	$0.47 \pm 0.03^\circ$	$0.48 \pm 0.03$	$0.58 \pm 0.04^\circ$	$0.59 \pm 0.04^\circ$
16:44	$0.76 \pm 0.05^\circ$	$0.77 \pm 0.05^\circ$	$0.82 \pm 0.06$	$0.90 \pm 0.06^\circ$	$0.94 \pm 0.07^\circ$
16:50	$0.91 \pm 0.07^\circ$	$0.93 \pm 0.07^\circ$	$1.07 \pm 0.08$	$1.07 \pm 0.08^\circ$	$1.16 \pm 0.08^\circ$
16:54	$0.42 \pm 0.03^\circ$	$0.42 \pm 0.03^\circ$	$0.48 \pm 0.03$	$0.45 \pm 0.03^\circ$	$0.51 \pm 0.04^\circ$
17:00	$0.42 \pm 0.03^\circ$	$0.43 \pm 0.03^\circ$	$0.44 \pm 0.03$	$0.46 \pm 0.03^\circ$	$0.47 \pm 0.03^\circ$
17:21	$0.43 \pm 0.04^\circ$	$0.42 \pm 0.04^\circ$	$0.42 \pm 0.04$	$0.44 \pm 0.04^\circ$	$0.44 \pm 0.04^\circ$
18:00	$0.47 \pm 0.04^\circ$	$0.48 \pm 0.04^\circ$	$0.49 \pm 0.04$	$0.52 \pm 0.04^\circ$	$0.54 \pm 0.04^\circ$

Table 6.2: Downstream phase jitter for each simulation setup and dataset.

Time	$\sigma_u$	$\sigma_d$ PFF Off	$\rho_{ud}$ PFF Off	$\sigma_d$ PFF On	$\sigma_d$ Sim
15:26	$0.99 \pm 0.05^\circ$	$1.72 \pm 0.09^\circ$	$0.80 \pm 0.04$	$0.92 \pm 0.05^\circ$	$1.03 \pm 0.05^\circ$
15:38	$0.57 \pm 0.05^\circ$	$0.74 \pm 0.06^\circ$	$0.93 \pm 0.04$	$0.28 \pm 0.02^\circ$	$0.31 \pm 0.03^\circ$
15:51	$0.74 \pm 0.05^\circ$	$0.98 \pm 0.07^\circ$	$0.90 \pm 0.04$	$0.42 \pm 0.03^\circ$	$0.42 \pm 0.03^\circ$
16:00	$0.69 \pm 0.07^\circ$	$1.82 \pm 0.19^\circ$	$0.94 \pm 0.05$	$0.88 \pm 0.09^\circ$	$0.78 \pm 0.08^\circ$
16:04	$0.79 \pm 0.06^\circ$	$1.24 \pm 0.09^\circ$	$0.96 \pm 0.03$	$0.39 \pm 0.03^\circ$	$0.41 \pm 0.03^\circ$
16:11	$0.70 \pm 0.05^\circ$	$0.95 \pm 0.07^\circ$	$0.89 \pm 0.05$	$0.44 \pm 0.03^\circ$	$0.45 \pm 0.03^\circ$
16:17	$0.61 \pm 0.04^\circ$	$0.80 \pm 0.06^\circ$	$0.83 \pm 0.06$	$0.58 \pm 0.04^\circ$	$0.45 \pm 0.03^\circ$
16:22	$0.99 \pm 0.07^\circ$	$1.50 \pm 0.11^\circ$	$0.93 \pm 0.04$	$0.82 \pm 0.06^\circ$	$0.62 \pm 0.04^\circ$
16:39	$0.96 \pm 0.07^\circ$	$1.36 \pm 0.10^\circ$	$0.94 \pm 0.04$	$0.52 \pm 0.04^\circ$	$0.59 \pm 0.04^\circ$
16:44	$0.84 \pm 0.06^\circ$	$1.67 \pm 0.12^\circ$	$0.89 \pm 0.05$	$1.11 \pm 0.08^\circ$	$0.94 \pm 0.07^\circ$
16:50	$0.88 \pm 0.06^\circ$	$1.89 \pm 0.13^\circ$	$0.88 \pm 0.05$	$1.24 \pm 0.09^\circ$	$1.16 \pm 0.08^\circ$
16:54	$1.08 \pm 0.08^\circ$	$1.58 \pm 0.11^\circ$	$0.96 \pm 0.03$	$0.61 \pm 0.04^\circ$	$0.51 \pm 0.04^\circ$
17:00	$0.85 \pm 0.06^\circ$	$1.35 \pm 0.10^\circ$	$0.95 \pm 0.03$	$0.51 \pm 0.04^\circ$	$0.47 \pm 0.03^\circ$
17:21	$0.84 \pm 0.07^\circ$	$1.18 \pm 0.10^\circ$	$0.93 \pm 0.05$	$0.44 \pm 0.04^\circ$	$0.44 \pm 0.04^\circ$
18:00	$0.95 \pm 0.08^\circ$	$1.40 \pm 0.11^\circ$	$0.94 \pm 0.04$	$0.57 \pm 0.05^\circ$	$0.54 \pm 0.04^\circ$

Table 6.3: Summary of PFF system results for each individual dataset. The simulated results are from the “All Effects” simulation in Table 6.2

Correction Status	$\sigma_u$	$\sigma_d$	$\rho_{ud}$
FF Off	$0.88 \pm 0.02^\circ$	$1.40 \pm 0.03^\circ$	$0.89 \pm 0.01$
FF On	$0.86 \pm 0.02^\circ$	$0.72 \pm 0.01^\circ$	$0.48 \pm 0.02$
FF Sim Unlimited	$0.88 \pm 0.02^\circ$	$0.61 \pm 0.01^\circ$	$-0.01 \pm 0.03$
FF Sim All Effects	$0.88 \pm 0.02^\circ$	$0.69 \pm 0.01^\circ$	$0.31 \pm 0.03$

Table 6.4: Summary of achieved and simulated results across the whole data taking period.

Overall, the actual system is able to reduce an initial downstream jitter of  $1.40 \pm 0.03^\circ$  by a factor of two, down to  $0.72 \pm 0.01^\circ$  (Figures 6.20, 6.21 and 6.22). Due to the non-optimal setup in some datasets as shown the PFF system does not remove all correlation between the upstream and corrected downstream phase, with the initial correlation of  $0.89 \pm 0.01$  reduced only to  $0.48 \pm 0.02$ . With a completely optimal setup and unlimited correction range all the correlation would be removed and the jitter could have been reduced further to  $0.61 \pm 0.01^\circ$  (Figure 6.23). However, considering the constraints of the actual system and non-optimal setup, the achieved downstream jitter and residual correlation are as expected (Figure 6.24).

Optimisations to the PFF system setup can therefore yield around a 15% reduction in corrected downstream phase jitter in a typical dataset. To demonstrate a larger reduction and achieve CLIC level phase stability both on short and long time scales at CTF3 the beam conditions are more critical. Further improvements not only to the best phase propagation (downstream phase jitter and upstream-downstream phase correlation) achieved so far but also clearly to the stability of these conditions are required.

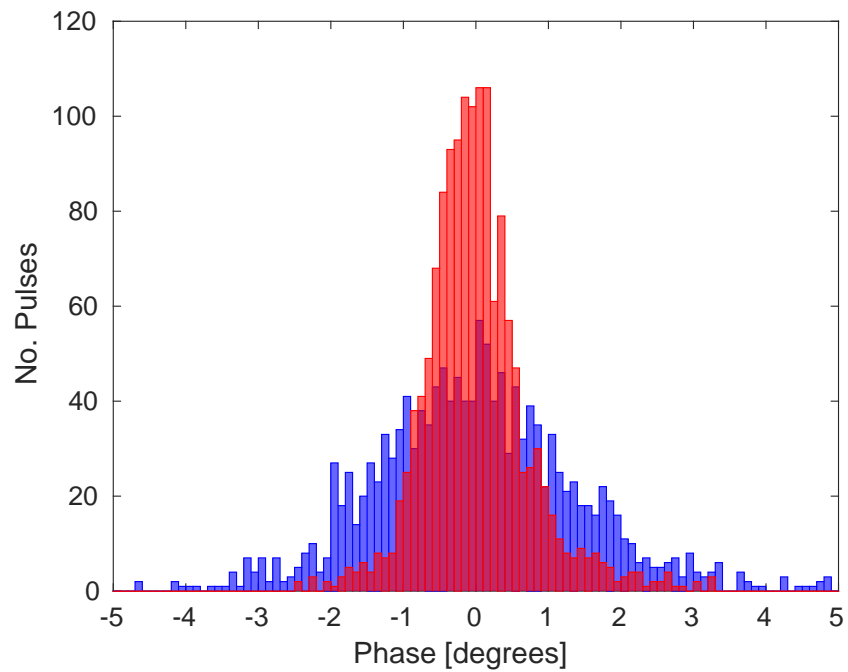


Figure 6.20: Histogram showing the downstream phase distribution with the PFF system off (blue) and on (red) across the whole data taking period.

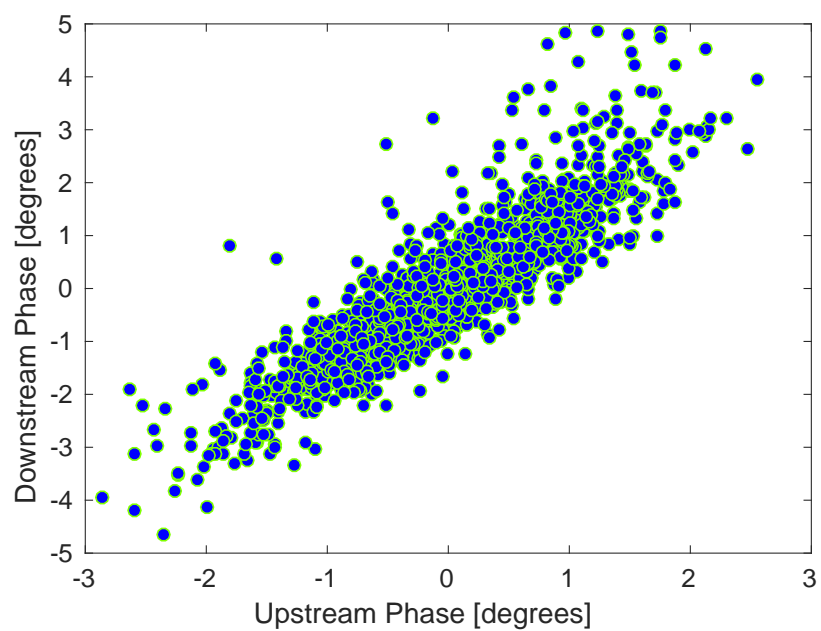


Figure 6.21: Downstream phase vs. upstream phase with the PFF system off across the whole data taking period.

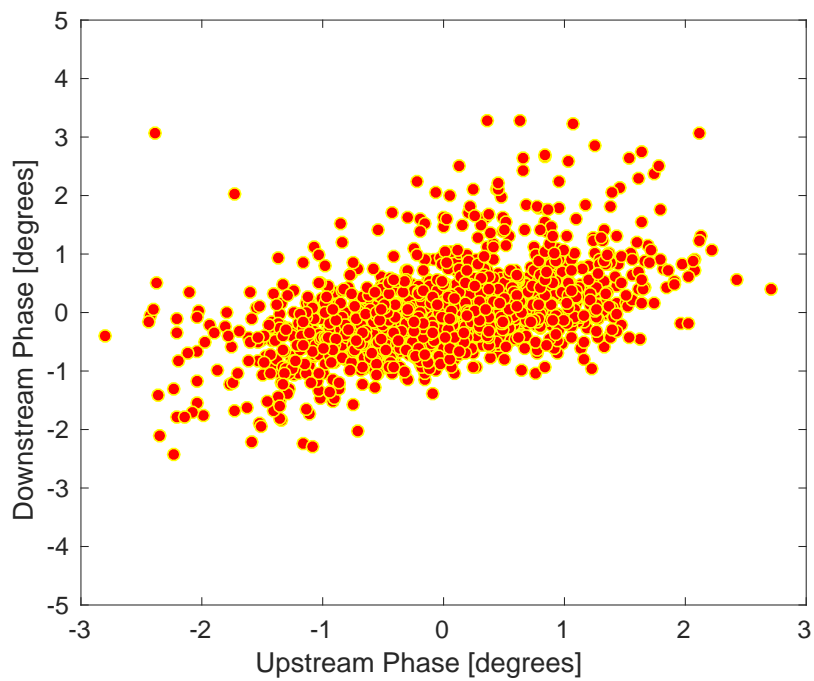


Figure 6.22: Downstream phase vs. upstream phase with the PFF system on across the whole data taking period.

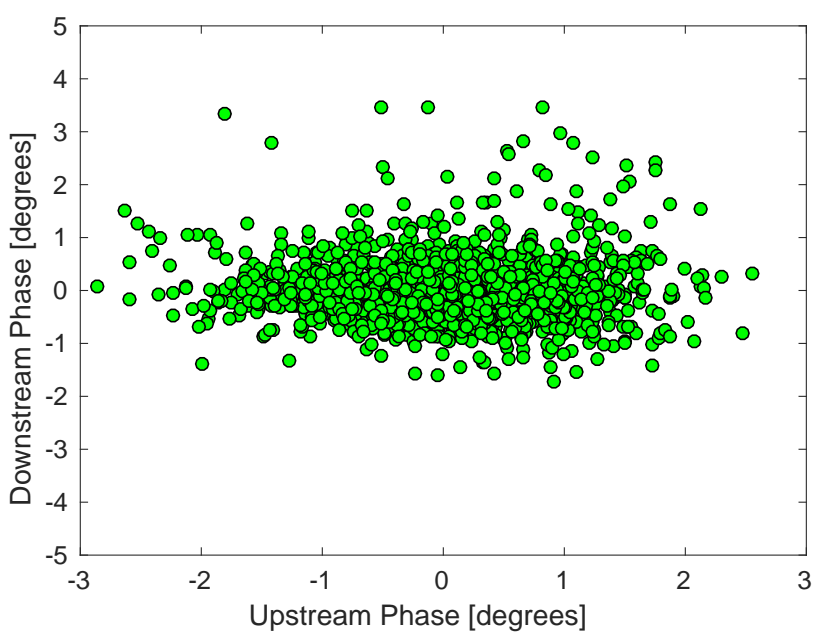


Figure 6.23: Unlimited simulation of the downstream phase vs. upstream phase distribution across the whole data taking period

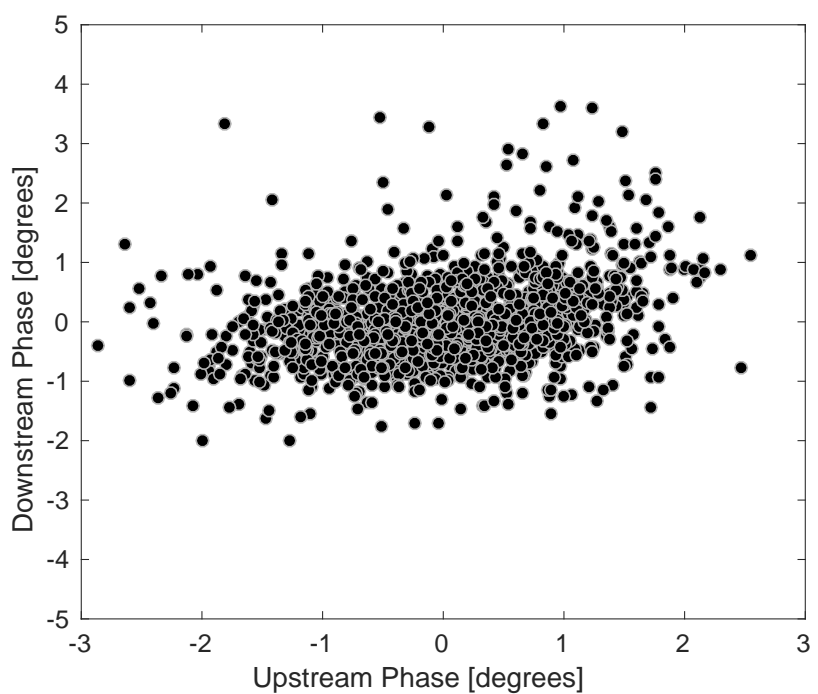


Figure 6.24: All Effects simulation of the downstream phase vs. upstream phase distribution across the whole data taking period.

# Chapter 7

## Conclusions

### 7.1 Summary

CLIC is a proposal for a future linear electron–positron collider in which 12 GHz, normal conducting accelerating cavities with an accelerating gradient of 100 MV/m are used to achieve collision energies of up to 3 TeV. The RF power for these cavities is extracted from a second, high intensity, drive beam. This two beam acceleration concept is a unique feature of CLIC and the generation of and power extraction from the drive beam presents many challenges. In particular, as the energy of the main beam is determined by the properties of the drive beam there are strict tolerances on the drive beam stability. One such constraint is on the phase stability, which must be  $0.2^\circ$  at 12 GHz or better to limit luminosity loss at the collision point resulting from energy errors to below 1%.

As the expected drive beam phase stability is  $2^\circ$  at 12 GHz CLIC requires the use of a “phase feedforward” (PFF) system, which will improve the phase stability by an order of magnitude. In the PFF system kickers are used to deflect the drive beam on to longer or shorter paths in a chicane. Based on the phase measured in a monitor upstream of the chicane the kicker voltage is varied so that the bunches arriving early at the monitor are deflected on to longer paths, and vice versa, so that the phase is on reference at the exit of the chicane. By placing the monitor before a turnaround in the beam line the correction signals can travel a shorter distance between the monitor and the kickers than the beam, thus the correction can be applied to exactly the same beam pulse that was initially measured. This thesis has documented the design, commissioning and operation of a prototype PFF system at the CLIC test facility CTF3.

Changes were made to the TL2 line at CTF3 in order to accommodate the PFF kickers. In Chapter 2 new optics were developed for TL2, in order to take these changes in to account and to create the desired phase shifting behaviour in the chicane. Optics measurements were first taken to identify and remove errors in the MADX model of the line. Adjusting the focusing strength of quadrupoles and dipoles along the line reduced the discrepancy between the measurements and the model by an order of magnitude. With the corrections in place the new PFF optics were matched to give the largest possible value of the transfer matrix coefficient  $R_{52}$ , which defines the correction range, whilst maintaining constraints on the

dispersion, twiss parameters and  $R_{56}$ . An optics was found with an  $R_{52}$  value of 0.74 m and dispersion below 1 m, but a non-zero  $R_{56}$  value of -0.18 m had to be accepted.

With non-zero  $R_{56}$  in TL2 the downstream phase jitter (following the correction chicane) is expected to contain an energy dependent component that is not present in the upstream phase (used as the PFF input). This reduces the correlation between the upstream and downstream phase, which must be 97% to reduce an initial phase jitter of  $0.8^\circ$  to the targeted  $0.2^\circ$  with the PFF system. In Chapter 4 the first measurements of the upstream-downstream phase correlation were below 40%. To compensate for the negative  $R_{56}$  in TL2 new optics with positive  $R_{56}$  values have been used in the transfer line TL1 so that the overall  $R_{56}$  between the monitors is zero. By fine-tuning the  $R_{56}$  in TL1 upstream-downstream phase correlations of up to 93% have been achieved. However, a strong second order ( $T_{566}$ ) effect has also been identified, which causes apparent optimal  $R_{56}$  value to vary with energy. Relative beam energy jitter and variations along the pulse must therefore be kept below the  $10^{-3}$  level to be able to maintain high correlations.

Another requirement to be able to theoretically achieve  $0.2^\circ$  corrected phase jitter with the PFF system is for the phase monitor resolution to be better than  $0.14^\circ$ . Achieving this target required extensive measurements of the phase monitor electronics, as well as several changes as described in Chapter 3. Tests of the electronics with a signal generator determined that the power dependent diode outputs saturated at a much lower power level than the phase dependent mixer outputs. The diodes were therefore excluded from the phase reconstruction process to be able to use higher input powers and increase signal to noise on the mixer outputs. Digital phase shifters initially used in the reference phase (LO) were found to be introducing noise to the system and were limiting the resolution to  $0.4^\circ$ . Replacing these with mechanical phase shifters then yeilded an immediate resolution improvement. This combined with several other improvements, such as reducing digitiser noise, finally yielded  $0.13^\circ$  resolution, better than required.

Chapter 5 dealt with the setup and commissioning of the remaining pieces of hardware for the PFF system – the PFF controller (FONT5a board) and the kicker amplifiers. On the FONT5a board droop in the response of the ADCs was removed with the implementation of IIR filters, the conversion factor between the 14-bit gain set in the firmware and the true applied gain was derived and the correction output timing was setup. An optimal output delay of around 20 ns was determined in order to synchronise the voltage sent to the kickers with the arrival of the beam. The output voltage versus input voltage of the amplifier was characteried, with the output found to be linear in the range between  $\pm 1.2$  V input and a voltage gain of between  $409 \pm 3$  and  $453 \pm 3$  in this range, depending on the amplifier channel. Variations in the output along the pulse were identified, which may cause imperfections in the phase correction, but these are small and at a level similar to or below the phase monitor resolution. When applied to the kickers the maximum amplifier output voltage yields a phase correction range of  $5.5 \pm 0.3^\circ$ .

Finally, with the hardware and optics setup optimised Chapter 6 presents the best results achieved with the PFF system to date. An initial mean phase jitter of  $0.74 \pm 0.06^\circ$  has been corrected to  $0.28 \pm 0.02^\circ$  using the PFF prototype, thereby achieving close to the CLIC target of  $0.2^\circ$  phase stability. The achieved jitter is in agreement with the theoretical prediction of

$0.27 \pm 0.02^\circ$  given the beam conditions at that time. The current limitations of the system were also discussed. In a longer dataset corresponding to several hours of operation the jitter was reduced from  $1.40 \pm 0.03^\circ$  to  $0.72 \pm 0.01^\circ$ . The larger corrected jitter on these timescales is dominated by drifts in beam conditions, leading to a theoretical best possible corrected jitter of  $0.61 \pm 0.01^\circ$ . The difference between the achieved and theoretical jitter could be reduced by automatically adjusting the PFF setup based on the current beam conditions. However, to be able to achieve much lower corrected phase jitters on longer timescales new feedbacks are being implemented at CTF3 to improve the reproducibility of the beam conditions.

## 7.2 Future Work

In terms of proving the feasibility of the PFF concept the prototype at CTF3 has fulfilled its goal. The most important remaining task in the context of CLIC is to use the experience gained with the prototype to make recommendations for the design of the CLIC PFF system. Probably the most critical area here is the strict optics constraints needed to achieve 99.5% upstream–downstream phase correlation, as required to reduce the initial jitter by an order of magnitude. The optics must be such that the chicane and turnaround introduce no additional first order ( $R_{56} = 0$ ) or higher order ( $T_{566} = 0$ ) energy dependent phase jitter. Using an energy measurement as a secondary input to the PFF system could also be considered, which would ensure that any uncorrelated energy component in the downstream phase jitter can be removed. There are also areas where hardware development is needed. Conceptual design of the higher power, 500 kW, amplifiers needed for CLIC has already begun [27]. Modifications to the phase monitor electronics will also be necessary, in particular to address the issues at CTF3 that prevented the use of the diodes to create a power independent measurement. The resolution of the phase measurement should ideally be  $0.1^\circ$  so that the correction is not resolution limited very close to the  $0.2^\circ$  target. Based on the sensitivity of these devices to small changes in the environment at CTF3 it would also be useful to have the possibility of an in-situ resolution measurement, in the ideal case by installing pairs of monitors together in the beam line.

In each chapter areas where improvements could be made to the prototype at CTF3 have been identified, and future tests will attempt to address some of these issues. Although it will be difficult to achieve significantly better than the  $0.27^\circ$  jitter result it is targeted to demonstrate close to this stability on much longer timescales, closer to the timescale of an hour rather than minutes. To date a reduction in downstream jitter by around a factor 2–3 has been achieved, whereas CLIC will have a larger initial jitter and require a factor 10 reduction. Tests at CTF3 will also be performed in which the initial phase jitter is artificially increased closer to the expected CLIC conditions, which will yield higher correlations and allow a larger relative reduction in phase jitter with the PFF system. As mentioned previously, the largest source of improvement will come from work to increase the stability of CTF3, in particular feedbacks to reduce energy jitter and drifts, with an additional small improvement possible by developing automatic procedures to determine the optimal PFF gain and other settings.

There are several new PFF setups that could also be attempted, each of which would require new logic and firmware for the correction. One example is attempting to run the PFF system with combined beam – measuring the uncombined upstream phase and correcting the downstream, combined beam pulse. If shown to be feasible CLIC could then consider using one PFF system per drive beam (2 systems total), rather than one per drive beam decelerator sector (48 systems total). In addition, there are several small hardware effects that in principle could be removed with adjustments to the PFF algorithm. The simplest example of this would be using a non-linear DAC output from the FONT5a board to compensate for droop and other small variations in the amplifier response along the pulse. A first iteration of this could be achieved by using IIR filters on the DACs, similar to what has already been implemented for the ADCs. The current PFF firmware also provides the functionality to be able to use a secondary correction input [68]. This was implemented to allow either the position dependence of the phase measurement (Section 3.13) or the energy dependence of the downstream phase to be taken in to account in the correction. However, the position dependence only makes a small contribution to the overall phase monitor resolution and the energy dependence of the downstream phase has been greatly reduced with the  $R_{56}$  optimisations. A two input correction is therefore unlikely to provide a significant improvement, but would still be useful as a proof of principle.

In terms of the optics and phase propagation, an attempt to create optics with lower  $T_{566}$  between the upstream and downstream phase monitors could be worthwhile, requiring the use of sextupoles. This would loosen the constraints on the energy stability required to achieve high upstream–downstream phase correlation. Alternatively, it may also be interesting to attempt to create an optics with larger  $R_{52}$  in the TL2 chicane (to give a larger correction range) whilst tolerating larger  $R_{56}$  values. The larger  $R_{56}$  value could then be compensated by varying the TL1 optics, in the same way as before. However, it is likely that larger dispersion in TL2 would also have to be accepted to be able to achieve this. Demonstrating that the prototype can be operated whilst maintaining orbit closure would also be a useful demonstration for CLIC, requiring further work to achieve beam transport with a completely nominal optics in TL2 and also using a different correction gain for each kicker to take in to account differences between the amplifier outputs.

# Bibliography

- [1] M. Herrero. The standard model. *NATO Sci. Ser. C*, 534:1–59, 1999.
- [2] P. W. Higgs. Broken symmetries and the masses of gauge bosons. *Phys. Rev. Lett.*, 13:508–509, 1964.
- [3] G. Aad et al. Observation of a new particle in the search for the standard model Higgs boson with the ATLAS detector at the LHC. *Phys. Rev. Lett. B*, 716 (1):1–29, 2012.
- [4] S. Chatrchyan et al. Observation of a new boson at a mass of 125 GeV with the CMS experiment at the LHC. *Phys. Rev. Lett. B*, 716 (1):30–61, 2012.
- [5] P. J. E. Peebles and B. Ratra. The cosmological constant and dark energy. *Rev. Mod. Phys.*, 75:559–606, 2003.
- [6] A. S. Gilmour. Klystrons traveling wave tubes, magnetrons, cross-field amplifiers, and Gyrotrons. Artech House, 2011.
- [7] O. S. Brüning et al. LHC design report. CERN-2004-003, 1, 2004.
- [8] E. Wilson. An Introduction to Particle Accelerators. Oxford University Press, 2001.
- [9] CERN. LEP design report. CERN-LEP-84-01, 2, 1984.
- [10] A. Abada et al. ILC technical design report, 2013. <https://www.linearcollider.org/ILC/Publications/Technical-Design-Report>.
- [11] M. Aicheler et al. A multi-TeV linear collider based on CLIC technology: CLIC conceptual design report. CERN-2012-007, 2012. <https://cds.cern.ch/record/1500095>.
- [12] A. Wolski. Introduction to the ILC damping rings. Fourth International Accelerator School for Linear Colliders, Beijing, 2009.
- [13] D. Schulte and R. Tomas. Dynamic effects in the new CLIC main linac. Proceedings of PAC09, TH6PFP046, 2009.
- [14] A. Gerbershagen. CLIC Drive Beam Phase Stabilisation. PhD thesis, University of Oxford, 2013.
- [15] G. Geschonke and A. Ghigo. CTF3 design report. CERN-PS-2002-008-RF, 2002. <http://cds.cern.ch/record/559331/>.

- [16] P. Skowronski. CTF3 operations. CLIC Workshop, CERN, 2016. <https://indico.cern.ch/event/449801/>.
- [17] P. Skowronski et al. Status and plane for completion of the experimental program of the CLIC test facility CTF3. Proceedings of IPAC2016, THPMB046, 2016.
- [18] D. H. Dowell. Electron emission and cathode emittance. U.S. Particle Accelerator School, MIT, Lecture 2, 2010.
- [19] R. Bossart et al. High-power microwave pulse compression of klystrons by phase-modulation of high-q storage cavities. CERN-OPEN-2004-015, 2004.
- [20] H. H. Braun et al. Efficient long-pulse fully-loaded CTF3 linac operation. Proceedings of LINAC06, MOP002, 2006.
- [21] A. Gallo et al. Studies on the RF deflectors for CTF3. Proceedings of EPAC, Vienna, THP6B09, 2000.
- [22] R. L. Lillestol et al. Electron beam deceleration measurements using the decelerator test beam line at the Compact Linear Collider test facility. Phys. Rev. ST Accel. Beams 17, 031003, 2014.
- [23] J. L. Navarro Quirante et al. A multi-purpose electron beam for accelerator technology tests. Proceedings of LINAC2014, MOPP030, 2014.
- [24] F. Marcellini and A. Andersson. Rf phase monitor final report. EuCARD-REP-2013-023, 2013. <http://cds.cern.ch/record/1710307>.
- [25] P. Burrows et al. FONT project. John Adams Institute, University of Oxford. <http://www-pnp.physics.ox.ac.uk/~font/people.html>.
- [26] G. Christian. CTF3 phase feed-forward control, electronics and amplifiers. CLIC Workshop, CERN, 2014. <https://indico.cern.ch/event/275412>.
- [27] C. Perry. Drive beam phase feed-forward hardware – experience in CTF3 and CLIC outlook. CLIC Workshop, CERN, 2016. <https://indico.cern.ch/event/449801>.
- [28] A. Ghigo et al. Kicker and monitor for CTF3 phase feed forward. Proceedings of IPAC2011, TUPC007, 2011.
- [29] A. L. Edwards. An Introduction to Linear Regression and Correlation. W. H. Freeman & Co., 1976.
- [30] H. Wiedemann. Particle Accelerator Physics. Springer, third edition, 2007.
- [31] H. Grote et al. MAD – Methodical Accelerator Design. CERN, Version 5.02.10 User's Reference Manual, 2016. <http://madx.web.cern.ch/madx/>.
- [32] S. Lee. Accelerator Physics. World Scientific Publishing Co., 2004.
- [33] A. Wolski. Beam dynamics in High Energy Particle Accelerators. Imperial College Press, 2014.

- [34] E. D. Courant. Theory of the alternating gradient synchrotron. *Annals Phys.*, 3:1–48, 1958.
- [35] INFN – Istituto Nazionale di Fisica Nucleare. Frascati, Italy. <http://w3.lng.infn.it/?lang=en>.
- [36] F. Marcellini et al. Tests and operational experience with the DAFNE stripilne injection kicker. *PAC'09*, TU6RFP082:1739, 2009.
- [37] J. Byrd. Stripline pickups and kickers. U.S. Particle Accelerator School, Lawrence Berkeley National Laboratroy, 2009.
- [38] A. S. Abdurrahim et al. Design of the transfer line-2 for the CTF-3 at CERN. APAC, Indore, India, TUC2MA02, 2007.
- [39] L. Soby. CTF3 BPMs. International Workshop on Linear Colliders, CERN, 2010.
- [40] L. Rinolfi. Layout of TL2 line for magnets, instrumentation and vacuum. EDMS, CERN, 836624, 2009. <https://edms.cern.ch/document/836624/20>.
- [41] P. Skowronski et al. Phase feed-forward system in ctf3 and performance of fast beam phase monitors. IPAC13, Shanghai, China, 2013. [http://accelconf.web.cern.ch/accelconf/ipac2013/talks/weobb203\\_talk.pdf](http://accelconf.web.cern.ch/accelconf/ipac2013/talks/weobb203_talk.pdf).
- [42] L. Rinolfi. Magnets for TL2 & TL2' & CALIFES & TBTS & TBL. EDMS, CERN, 848911, 2008. <https://edms.cern.ch/document/848911/6>.
- [43] J. Roberts. Status of the CLIC phase feedforward prototype at CTF3. LCWS14, Belgrade, Serbia, 2014.
- [44] D. Gamba. Online optimisation of the CLIC drive beam bunch train recombination at CTF3. PhD thesis, University of Oxford, 2016.
- [45] P. Skowronski. private communication.
- [46] B. Constance. Review of CTF3 optics. EPAC, Nice, France, 1990.
- [47] D. Reistad. Status of the CELSIUS project. CLIC Workshop, CERN, 2013. <https://indico.cern.ch/event/204269/>.
- [48] B. Holzer. Introduction to transverse beam optics. CERN Accelerator School Lecture. <http://cas.web.cern.ch/cas/Baden/PDF/Holzer-1.pdf>.
- [49] A. Andersson. Phase monitor connections and signals. CLIC Collaboration Working Meeting, Phase Feed Forward WP, 2012. <http://indico.cern.ch/event/178209/>.
- [50] F. Marcellini et al. The CLIC drive beam phase monitor. Proceedings of IPAC'10, WEPEB035, 2010.
- [51] A. Zolla. Phase monitor technical drawing. EDMS, CERN, 1215687, 2012. <https://edms.cern.ch/document/1215687/1>.

- [52] R. E. Collins. Field Theory of Guided Waves. IEEE Press, New York, 1991.
- [53] E. Kreyszig. Advanced Engineering Mathematics. Wiley, 8th edition, 1999.
- [54] D. Lipka. Cavity bpm designs, related electronics and measured performances. Proceedings of DIPAC09, TUOC02, 2009.
- [55] A. Andersson. D. B. phase monitor performance. CLIC Workshop, CERN, 2013. <https://indico.cern.ch/event/204269>.
- [56] A. Andersson. private communication.
- [57] A. Andersson and J. Sladen. High precision phase monitoring. CTF3 Collaboration Technical Meeting, CERN, 2008. <http://indico.cern.ch/event/23022/>.
- [58] S. Rey. Broadband phase & amplitude modulator. EDMS, CERN, EDA-02198-V2-0, 2011. <https://edms.cern.ch/item/EDA-02198-V2-0/0>.
- [59] TKE-180-4-X-X phase shifter. SHX-SH, China. <http://www.shx-sh.com/en/upfiles/201266859173582.pdf>.
- [60] 5C45-2998.6/T10-0/0 bandpass filter. K&L Microwave. <http://www.klmicrowave.com/>.
- [61] AQA-1933 RF / mixrowave amplified quadrupler. Marki microwave. [http://www.markimicrowave.com/Multipliers/Amplified\\_Quadruplers/AQA-1933.aspx](http://www.markimicrowave.com/Multipliers/Amplified_Quadruplers/AQA-1933.aspx).
- [62] ZVE-3W-183+ high power amplifier. Mini-Circuits. <https://www.minicircuits.com/pdfs/ZVE-3W-183+.pdf>.
- [63] ADS5474 14-bit, 400 MSPS analog-to-digital converter with buffered input. Texas Instruments. <http://www.ti.com/product/ADS5474>.
- [64] SIS3320-250 8 channel 250 MHz 12-bit ADC/digitiser. Struck Innovative Systeme. <http://www.struck.de/sis3320.htm>.
- [65] L. Timeo. Baseband x10 amplifier block. EDMS, CERN, AED-00209, 2014. <https://edms.cern.ch/item/AED-00209/0>.
- [66] MatLab. Curve fitting toolbox user's guide. R2016a, 2016. [http://ch.mathworks.com/help/releases/R2016a/pdf\\_doc/curvefit/curvefit.pdf](http://ch.mathworks.com/help/releases/R2016a/pdf_doc/curvefit/curvefit.pdf).
- [67] J. Roberts. Phase monitor electronics: Output vs. input voltage in both beam and signal generator data. FONT Meeting, 29th October, 2015. <https://agenda.linearcollider.org/event/6914/>.
- [68] G. Christian. private communication.
- [69] R. Corsini et al. Commissioning status of the CTF3 delay loop. Proceedings of EPAC, Edinburgh, MOPLS093, 2006.
- [70] B. Orwiler. Vertical Amplifier Circuits. Tektronix/Beaverton, Oregon, 1st edition, 1969.

- [71] R. Lillestol et al. Experimental results from the Test Beam Line in the CLIC Test Facility 3. Proceedings of IPAC13, TUPWA046, 2013.
- [72] J. Roberts. Phase feedforward: Update & plans. FONT Meeting, 26th August, 2016. <https://agenda.linearcollider.org/event/7344>.
- [73] L. Lyons. A Practical Guide to Data Analysis for Physical Science Students. Cambridge University Press, 1991.
- [74] L. Malina. Recent improvements in drive beam stability in CTF3. Proceedings of IPAC16, WEPOR007, 2016.
- [75] C. Milardi. CTF3 transfer line design. CTF3 Technical Note, CTFF3-005, 2001.
- [76] L. Rinolfi. TL1 transfer line between Delay Loop and Combiner Ring. EDMS, CERN, 687849, 2009. <https://edms.cern.ch/document/687849/21>.
- [77] T. Persson. private communication.
- [78] D. Bett. The Development of a Fast Intra-train Beam-based Feedback System Capable of Operating on the Bunch Trains of the International Linear Collider. PhD thesis, University of Oxford, 2013.
- [79] Virtex-5 FPGA user guide, v5.4 edition. Xilinx. [http://www.xilinx.com/support/documentation/user\\_guides/ug190.pdf](http://www.xilinx.com/support/documentation/user_guides/ug190.pdf).
- [80] N. Blaskovic Kraljevic et al. Development of a low-latency, micrometre-level precision, intra-train beam feedback system based on cavity beam position monitors. Proceedings of IPAC16, THPOR035, 2016.
- [81] R. Apsimon et al. Design and performance of a high resolution, low latency stripline beam position monitor system. Phys. Rev. ST Accel. Beams 18, 032803, 2015.
- [82] CG635 2 GHz Clock Generator. Stanford Research Systems. <http://www.thinksrs.com/products/CG635.htm>.
- [83] B. Constance. Design and beam testing of a fast, digital intra-train feedback system and its potential for application at the International Linear Collider. PhD thesis, University of Oxford, 2011.
- [84] G. Christian. Phase feed-forward system: amplifier & controls. CLIC Workshop, CERN, 2013. <https://indico.cern.ch/event/204269/>.
- [85] C. Perry. private communication.
- [86] E. Joffe. Grounds for Grounding: A Circuit to System Handbook. Wiley-IEEE, 2010.
- [87] DE150-201N09A RF Power MOSFET. IXYS RF. [http://ixapps.ixys.com/Datasheet/de150\\_201n09a.pdf](http://ixapps.ixys.com/Datasheet/de150_201n09a.pdf).
- [88] C2M0160120D 2nd-Generation Z-FET. Wolfspeed. <http://www.wolfspeed.com/c2m0160120d>.